PB86-175692

Preliminary Evaluation Studies with the Regional Acid Deposition Model (RADM)

National Center for Atmospheric Research
Boulder, CO

Prepared for

Environmental Protection Agency
Research Triangle Park, NC

Mar 86

U.S. Department of Commerce
National Technical Information Service
NTIS

PB86-175692

EPA/600/3-86/024
March 1986

PRELIMINARY EVALUATION STUDIES WITH THE REGIONAL ACID DEPOSITION MODEL (RADM)

By

The Acid Deposition Modeling Project
National Center for Atmospheric Research
P.O. Box 3000
Boulder, Colorado 80307

Interagency Agreement No. DW930144-01-3

Project Officer

John F. Clarke
Meteorology Assessment Division
Atmospheric Sciences Research Laboratory
Research Triangle Park, N.C. 27711

ATMOSPHERIC SCIENCES RESEARCH LABORATORY
OFFICE OF RESEARCH AND DEVELOPMENT
U.S. ENVIRONMENTAL PROTECTION AGENCY
RESEARCH TRIANGLE PARK, N.C. 27711

REPRODUCED BY
NATIONAL TECHNICAL
INFORMATION SERVICE
U.S. DEPARTMENT OF COMMERCE
SPRINGFIELD, VA. 22161

TECHNICAL REPORT DATA

(Please read Instructions on the reverse before completing)

1. REPORT NO. EPA/600/3-86/024	**2.**	**3. RECIPIENT'S ACCESSION NO.**

4. TITLE AND SUBTITLE
PRELIMINARY EVALUATION STUDIES WITH THE
REGIONAL ACID DEPOSTION MODEL (RADM)

5. REPORT DATE
March 1986

6. PERFORMING ORGANIZATION CODE

7. AUTHOR(S)
The NCAR Acid Deposition Modeling Project

8. PERFORMING ORGANIZATION REPORT NO.

9. PERFORMING ORGANIZATION NAME AND ADDRESS
National Center for Armospheric Research
P.O. Box 3000
Boulder, Colorado 80307

10. PROGRAM ELEMENT NO.
CCVNIA/05, TASK 3109 (FY-86)

11. CONTRACT/GRANT NO.
Interagency Agreement No.
DW930144-01-3

12. SPONSORING AGENCY NAME AND ADDRESS
Atmospheric Sciences Research Laboratory-RTP, NC
Office of Research and Development
U.S. Environmental Protection Agency
Research Triangle Park, N.C. 27711

13. TYPE OF REPORT AND PERIOD COVERED
Interim / 1/1/85-12/31/85

14. SPONSORING AGENCY CODE
EPA/600/09

15. SUPPLEMENTARY NOTES

16. ABSTRACT

This report focuses on the findings of preliminary evaluation studies of the NCAR Regional Acid Deposition Modeling System (RADM). Current efforts in evaluating the gas-phase chemistry submodel have met with significant success. An understanding of the smog chamber databases has also been developed. Due to the lack of adequate observation data, evaluations of aqueous-phase chemistry and dry deposition submodels have not been possible. The cloud process submodel is consistent with the available but small data set. Preliminary evaluation of the full RADM system, meteorology and chemical deposition using OSCAR data has achieved initial success, though it is far from being conclusive. Much larger and extensive databases are required to thoroughly test this system. MM4 has shown considerable skill in forecasting the OSCAR IV meteorology. RADM forecasts of sulfate and nitrate wet deposition for the first day of OSCAR IV are also quite good. The RADM-simulated three-dimensional chemical species distributions are very consistent with preliminary data measured by NCAR under a separate program. The first test of RADM's ability to analyze "what if" studies with hypothetical reductions in sulfur emissions is demonstrated. The findings confirm the complexity of directly observing potential benefit from emissions reductions.

17. KEY WORDS AND DOCUMENT ANALYSIS

a. DESCRIPTORS	b. IDENTIFIERS/OPEN ENDED TERMS	c. COSATI Field/Group

18. DISTRIBUTION STATEMENT RELEASE TO THE PUBLIC	**19. SECURITY CLASS** *(This Report)* UNCLASSIFIED	**21. NO. OF PAGES** 207
	20. SECURITY CLASS *(This page)* UNCLASSIFIED	**22. PRICE**

EPA Form 2220-1 (Rev. 4-77) PREVIOUS EDITION IS OBSOLETE

DISCLAIMER

The information in this document has been funded wholly or in part by the United States Environmental Protection Agency under Interagency Agreement No. DW930144-01-3 to the National Science Foundation. It has been subject to the Agency's peer and administrative review, and it has been approved for publication as an EPA document. Mention of trade names or commercial products does not constitute endorsement or recommendation for use.

ABSTRACT

This report focuses on the findings of preliminary evaluation studies of the NCAR Regional Acid Deposition Modeling System (RADM). Current efforts in evaluating the gas-phase chemistry submodel have met with significant success. An understanding of the smog chamber databases has also been developed. Due to the lack of adequate observation data, evaluations of aqueous-phase chemistry and dry deposition submodels have not been possible. The cloud process submodel is consistent with the available but small data set. Preliminary evaluation of the full RADM system, meteorology and chemical deposition using OSCAR data has achieved initial success, though it is far from being conclusive. Much larger and extensive databases are required to thoroughly test this system. MM4 has shown considerable skill in forecasting the OSCAR IV meteorology. RADM forecasts of sulfate and nitrate wet deposition for the first day of OSCAR IV are also quite good. The RADM-simulated three-dimensional chemical species distributions are very consistent with preliminary data measured by NCAR under a separate program. The first test of RADM's ability to analyze "what if" studies with hypothetical reductions in sulfur emissions is demonstrated. The findings confirm the complexity of directly observing potential benefit from emissions reductions.

CONTENTS

Abstract iii

Acknowledgement vii

1. INTRODUCTION 1

    1.1 Background Information on Model Evaluation 1

    1.2 Background Information on RADM 3

    1.3 Preliminary Evaluation of the RADM System 4

2. MAJOR FINDINGS 6

3. RADM SUBMODEL VERIFICATION STUDIES 10

    3.1 Gas-Phase Chemistry Submodel Evaluation 10

    3.2 Cloud Processes and Aqueous-Phase Chemistry Submodel Evaluation 35

    3.3 Dry Deposition Submodel Evaluation 45

4. PRELIMINARY EVALUATION OF RADM WITH THE OSCAR DATABASE 48

    4.1 The OSCAR Database 48

    4.2 Meteorological Model Evaluation 57

    4.3 Statistical Comparisons of RADM with OSCAR Data 73

    4.4 Three-Dimensional Distributions of Chemical Trace Species 79

5. SENSITIVITY STUDIES AND APPLICATIONS 98

5.1 Developing Experience with and Understanding of RADM Forecasts 98

5.2 Wet and Dry Deposition of SO_x and NO_x 98

5.3 Ohio Valley Reduction Experiments 108

5.4 Computational Performance of RADM 115

6. DATABASES FOR RADM EVALUATION STUDIES 119

6.1 Introduction 119

6.2 Air Quality Databases 119

6.3 Emissions Databases 129

6.4 Precipitation Databases 158

6.5 Limitations and Uses of Smog Chamber Data in Evaluating RADM Chemistry 159

7. REFERENCES 186

APPENDIX A. Relationship Between UV Irradiance and NO_2 Photolysis Measurements 192

ACKNOWLEDGEMENT

Ever since the beginning of the NCAR Acid Deposition Modeling Project, it has been an intense group endeavor. The development of a three-dimensional Eulerian regional acid deposition modeling system is an interdisciplinary research and development effort. Only through mutual respect and friendship, individual dedication, and selfless cooperation have we succeeded in developing the RADM system to where it is today. The research results and technical findings described in this report are based on the work of many people, although not all of them have contributed written material to this report. Following the established procedure of earlier reports, we have not specifically identified individuals with portions of the text. Research interests and recent works of individual members of our group can be found in the scientific literature. The following staff contributed to this report:

R. Anthes
T. Bettge
R. Brost
J. Calvert
J. Chang (editor)
J. del Corral
P. Haagenson
H. Hildebrand
D. Hopkins
E.-Y. Hsie
Y.-H. Kuo
S. Madronich
P. Middleton
J. Rosinski
P. Samson
M. Skumanich
W. Stockwell
C. Walcek

Our Project Officer, Dr. John F. Clarke (EPA), has been most patient and supportive of our project throughout the year, and of course the report would not have been possible without the tireless dedication of Daloris Flaming, Sharon Blackmon, and Jane Vandine, who typed many revisions of the manuscript, always under pressure and always professionally and cheerfully. Finally, we would like to acknowledge the indispensible role of our trusted Macintoshes and Laserwriter without which the figures would not be what they are.

SECTION 1

INTRODUCTION

1.1 Background Information on Model Evaluation

In the study of atmospheric chemistry and long-range transport of pollutants, evaluation of a complex mathematical model of any physical process is an involved and intricate procedure. To start with, the basic concept of "evaluation" or actually the "evaluation process" has never been well defined. The primitive notion of "let's measure the right variables and see if the model can duplicate the observations" is rarely practical or successful. To understand this, we must first recall the role of mathematical models. Mathematical models become necessary when the atmospheric processes under consideration become sufficiently complex that detailed quantifying of the relevant variables is needed. Further, in recent years, mathematical models have become the indispensable tool for projecting into the unknown (or future) from existing knowledge not only in the field of atmospheric pollution but in many other fields of science. Therefore, the concept of evaluation must somehow couple a successful demonstration of a model's ability in describing a set of observations to its ability in extrapolating into the unknown in some direction. The normal procedure in testing a theory such as those embodied in a mathematical model is to actually design an experiment measuring the predictions of the model (theory) on the specific phenomenon of interest. This then provides a direct measure of the model's ability in exploring new territories. Unfortunately, this is rarely possible in the field of atmospheric pollution. For example, in order to test directly the predictions of a regional acid deposition model in assessing the potential impacts of differing emissions scenarios, one would have to modify emissions over a very large part of North America and implement a very extensive observation network. Clearly, such experiments are difficult and expensive. Indirect evaluation procedures are the only viable alternative.

For this preliminary evaluation of the NCAR Regional Acid Deposition Model (RADM), we shall explore the type of indirect evaluation procedure that is currently possible, the availability of data for model evaluation, and the need for improved databases.

Structured statistical analysis such as those recommended by the AMS Workshop on Dispersion Model Performance (Fox, 1981) requires an extensive database compatible to the intended application of the model in question. The extensive network on air quality measurement does not provide the needed chemical species' atmospheric concentration data. The deposition networks such as those discussed in Section 6.4 provide long-term averages which RADM is not yet ready to simulate. The type of model evaluation represented by Endlich et al. (1984), Brodzinski et al. (1984), and Ruff et al. (1985) certainly should be considered eventually. For the present, while we are still exploring the operational and diagnostic characteristics of RADM, it is more informative and constructive to evaluate this model according to the following concepts. Because of the lack of regional-scale acid deposition data with concurrent atmospheric chemical species concentrations and other variables, it is not possible to test the full RADM. The extensive deposition database gathered by the Oxidant Scavenging Characteristics of April Rains (OSCAR) experiment in 1981 is used to develop a first understanding of the general overall "integrated" performance of the RADM system. This involves both the mesoscale meteorological model and RADM. Additional analyses with the major submodels yield further information on the scientific credibility of RADM. In comparing model results with observations, one must first ascertain the quality and appropriateness of the data used in the comparison. This includes both the input data for running the model and the data for comparing the model outputs. Consequently, for the present report and most likely also for the future, the following evaluation procedure will be used:

A. Comparisons with Atmospheric and Laboratory Observations

   (1) The scientific correctness of the individual submodels describing major physical and chemical processes will be evaluated according to the available databases

   (2) The mesoscale model (MM4) simulations of individual meteorological episodes will be compared with observations

   (3) The deposition model (RADM) simulations of individual deposition events and averages of sets of events will be compared with appropriate observations of deposition and three-dimensional distributions of atmospheric concentrations of chemical species

   (4) When available, the same comparisons will be carried out for the Engineering Model(s)

B. Intermodel Comparisons

   (1) Through the NCAR-sponsored Modeling Intercomparison Project (MIP), the mesoscale model (MM4) will be compared to other mesoscale models developed elsewhere both in North America and Europe

   (2) RADM and all the major submodels will be compared to the Acid Deposition and Oxidant Model (ADOM) and other available models under the complementary research projects supported by EPRI

C. Evaluation and Analysis of Databases

   (1) Verification of emissions databases for model evaluation studies and for model executions

   (2) Analysis of laboratory and field databases for evaluation of chemistry and deposition submodels

D. Performance Evaluation of the RADM System

(1) Evaluation of the flexibility and robustness of RADM

(2) Computational capability of RADM and MM4

The submodel and mesoscale model comparisons with observations and intermodel comparisons are designed to establish the fundamental correctness of the basic science included in RADM. Of course, this does not necessarily assure the correct integration of the full RADM model. This is to be established by direct evaluation of RADM predictions against appropriate observations. All the intermodel comparison studies are necessary steps in seeking better understanding of the highly complex models and in developing new concepts and submodels for further improvement of RADM. The databases must also be evaluated independently so that we may properly interpret the differences and agreements found in the model evaluation studies. Since all data have inherent uncertainties or errors, it is essential that we understand how these factors may influence or even dictate the course of model evaluations. Finally, it is essential to understand how well RADM meets its design goals of carrying out assessment studies both from the viewpoint of computation speed and robustness and in dealing with a broad spectrum of input data and emissions scenarios.

1.2 Background Information on RADM

The NCAR Regional Acid Deposition Model (RADM) is an evolving, continuously improving system of computational models describing the major physical and chemical processes relevant to acid deposition on a regional scale. This modeling project is a follow-up to an earlier study evaluating past modeling efforts and resulting in the recommendation of the development of a new comprehensive modeling system (NCAR, 1983a and 1983b). In December 1984, a first version of RADM was completed. The status of this development was reported in NCAR (1985) and reviewed by NAPAP in March 1985.

The objectives of RADM are threefold. First, the RADM system is to be a state-of-the-art modeling system suitable for carrying out source-receptor assessment studies. Secondly, it is to be sufficiently flexible so as to be able to integrate current and developing representations of the relevant physical and chemical processes. Thirdly, RADM is to describe the spatial and temporal distributions of pollutants resulting from known source emissions. With these goals in mind, the RADM system is designed as a hierarchical set of models. Basic research projects on individual physical and chemical processes such as dry depostion, wet scavenging, gas-phase chemistry, etc., form the foundation of this system. These works, funded by NAPAP and other organizations, are synthesized into a set of submodels by a diverse group of researchers for integration into RADM. The core RADM system consists of two comprehensive models--the mesoscale meteorological model (MM4) and the deposition and transport model (RADM). Starting with any given set of meteorological data, MM4 then develops for RADM a self-consistent description of transport and other physical variables such as wind velocity, precipitation, and local thermal structure of the atmosphere. In addition to considering transport of pollutants, RADM includes gas-phase chemistry, aqueous-phase chemistry, cloud processes, and wet and dry deposition. Because of the emphasis on modularity in computer coding so as to preserve flexibility in incorporating new findings and advanced submodels, this first version of RADM was not designed for speed in execution. Consequently, concerns on turnaround time in eventual application of RADM by the assessment group of NAPAP led to the concept of the "Engineering Model." The Engineering Model is based on the concept that, given the results from RADM, one can approximate the response of the chemical system by a set of somewhat simpler mathematical functions. Therefore, a reduced resolution three-dimensional model with these mathematically approximate chemical descriptions can mimic the qualitative features of RADM while providing self-consistent quantified outputs. Selected interesting results from these first-cut studies with the Engineering Model can then be examined by the full RADM, carefully leading to results for assessment and policy uses. In short, the Engineering Model(s) can provide speed in considering many "what-if" scenarios in a relative sense, while RADM can provide the more definitive quantified results for NAPAP.

The physical domains of application for MM4 and RADM are flexible so long as land use, emissions, terrain, and initial meteorological data are available. The basic 80 x 80 km^2 horizontal grid allows MM4 to cover most of North America in any given simulation. Because of the additional computer memory required by RADM to store information on chemical trace species distributions, RADM version 1 can cover only the eastern United States and southern Canada if it is to stay within the limits of the core memory of the CRAY computer, Model 1A. A new version of RADM (an out-of-core version) utilizing disks for storage during execution was recently completed. First tests show both versions of RADM yield identical results.

This report will summarize NCAR's current (admittedly incomplete but improving) experience in developing, testing, and applying MM4 and RADM, including the submodels and databases.

1.3 Preliminary Evaluation of the RADM System

This preliminary study clearly cannot properly cover all the topics outlined in Section 1.1, especially the intermodel comparison studies since these are mostly still in the planning stages. Nevertheless, we believe the following sections will provide an exciting first glimpse of the type of analyses that will eventually lead to a high level of confidence in RADM as an assessment tool. Section 2 summarizes the major findings of this preliminary evaluation study. It is expected that additional studies in the future with more extensive data will most likely strengthen these conclusions rather than alter them. Section 3 focuses on submodel evaluations. It proceeds from submodels with the most available data to the least. The gas-phase chemistry submodel is the most thoroughly evaluated component of RADM. All major findings affirm the state-of-the-art stature of this submodel. The same can be said of the other two major submodels, cloud processes and aqueous-phase chemistry, and dry deposition. Unfortunately, for these two submodels, state-of-the-art does not necessarily mean proven science due to the lack of extensive data, or even good data, in the latter case. Much work still needs to be done in the future. Preliminary evaluation of the full RADM using OSCAR field experiment data is described in Section 4. First the characteristics of OSCAR data relevant to model evaluation are examined, and then a description of the mesoscale meteorological model verification package is described, along with the results from a preliminary application to an MM4 simulation of the OSCAR IV case. A summary of the planned mesoscale model intercomparison program is also included. Section 5 describes the present interpretations of RADM findings on wet and dry deposition during the OSCAR period. First results on demonstrating the robustness of RADM in considering hypothetical scenarios are contained in Section 5.2. The last section of Section 5 briefly summarizes the improvement in computational speed of RADM with possibilities for further advances. Finally, Section 6 of this report summarizes our current understanding of all the relevant databases (except for OSCAR cases), not only for the purpose of model evaluation but also for model execution and interpretation, including limitations of selected experimental results for application in acid deposition modeling.

SECTION 2

MAJOR FINDINGS

This report summarizes current capabilities of RADM, MM4, the gas-phase and aqueous-phase chemistry submodels, the cloud processes submodel, the dry deposition submodel, and the computational performance of the RADM system. One set of relatively inclusive (although still not adequate) observational data was used to perform a preliminary evaluation of MM4 and RADM as an integrated assessment system. Many data from smog chamber experiments and almost all the pertinent and available data on cloud processes and dry deposition were used to evaluate the submodels. It was found that much of the existing data required further work in order to be useful for RADM evaluation. New evaluation procedures are being developed and explored while the applicability of currently suggested procedures are being tested. The major findings of this report are:

(1) Based on comparisons with observations from OSCAR IV and I events, RADM has been shown to be a scientifically credible and operationally flexible model (Sections 4.3, 4.4, 5.1, and 5.2).

(2) MM4 was shown to have considerable skill in forecasting the meteorology of wet scavenging events (OSCAR IV). A new state-of-the-art mesoscale model verification program was developed for this purpose and was shown to perform as expected (Section 4.2).

(3) It is demonstrated that RADM can indeed conduct "what if" analysis with hypothetical emissions scenarios (Sections 5.1 and 5.3).

(4) The gas-phase chemistry submodel compared well with the SAPRC smog chamber data and with other more detailed theoretical models (Section 3.1).

(5) The cloud processes and aqueous-phase chemistry submodel and the dry deposition submodel agree with all the available data. The need for additional well-planned data is discussed (Sections 3.2 and 3.3).

(6) Most of the available data for model and submodel evaluations have been examined and evaluated. Many of the inadequacies of the existing databases have been documented and some suggestions for future improvements stated (Sections 1.1, 3.2, 3.3, 4.2, 6.2, 6.3, 6.4, 6.5, and Appendix A).

These findings, while not conclusive, strongly support the view that the RADM system is a state-of-the-art assessment modeling system. It is well recognized that additional developments for submodels and full model operational characteristics such as execution speed must be continued. It is also imperative that proper observational data be collected in the near future to thoroughly test the capability of the RADM system.

An additional, somewhat speculative, major finding is that direct observation of potential reduction in acid deposition due to changes in multi-state sulfur dioxide emissions will be nearly impossible at distant receptor sites. If confirmed with further studies, this finding would have considerable significance to NAPAP. As will be discussed in Section 5.3, four "what if" studies with SO_2 emission reductions in the Ohio River Valley were carried out. The resulting changes in wet sulfate deposition over the eastern United States are shown in Figs. 2.1 and 2.2. For both cases, only in the immediate neighborhood of the emissions reduction area are the changes higher than 30% for a 50% reduction in SO_2. In New England and Canada, the small changes around 10% would be very difficult to detect given the accuracy of the measurement technique. For the 90% emissions reduction case, these numbers are doubled with approximately the same distributions (contours). The same results averaged over state-size regions are shown in Figs. 5.13-5.20, including dry deposition. The changes in dry deposition in distant receptor areas are even smaller than the changes in wet deposition. If only a few stations can detect changes, these data most likely will be lost in statistical averages. Unless we have a very dense observational network, changes in episodic acid deposition, which are the basis of long-term averages, are difficult to observe directly. In addition, many chemical species and their deposition cannot be reliably and routinely measured. Therefore, models such as the RADM system must be used in tandem with observations to provide the best scientific information.

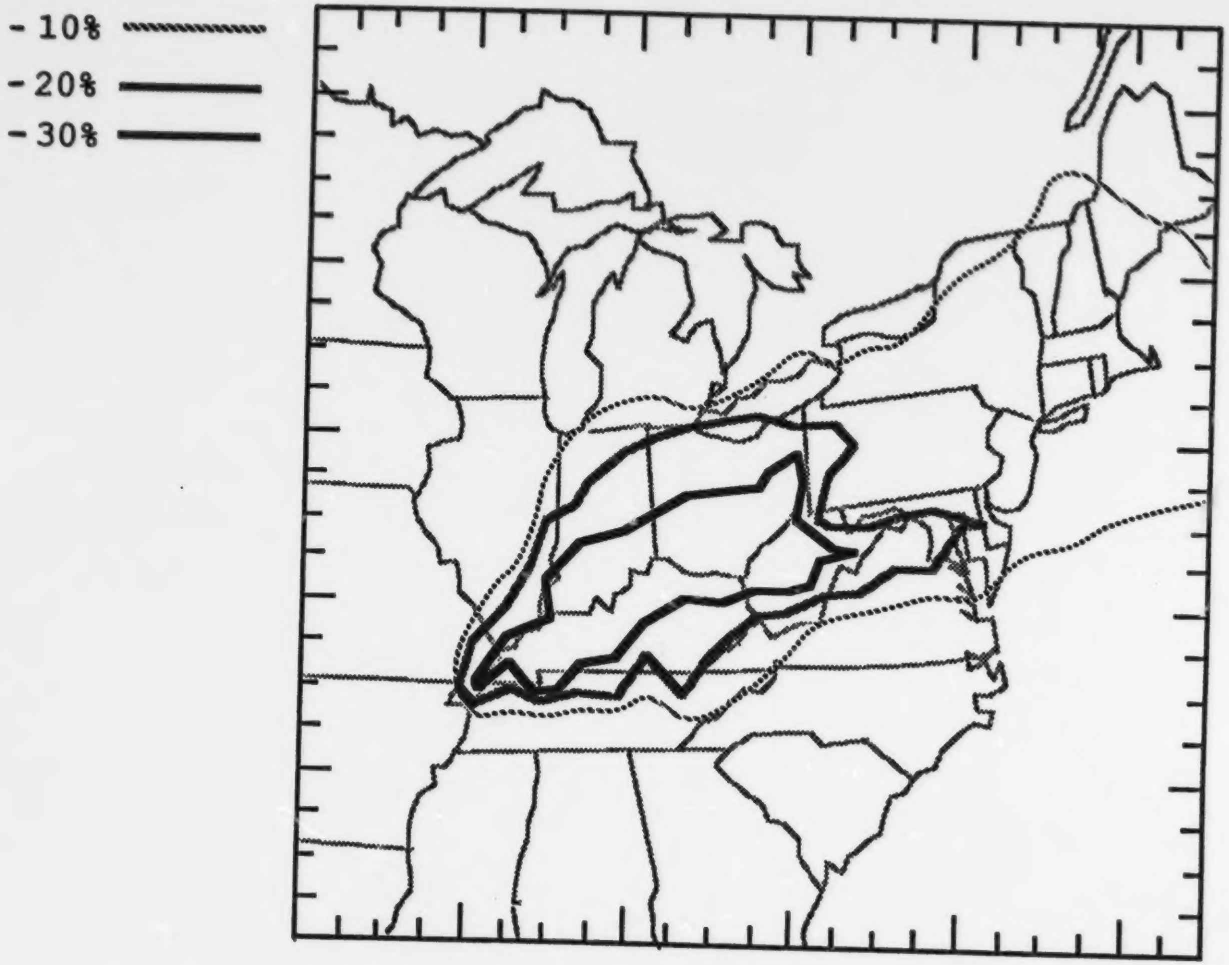

Fig. 2.1 Percent Change in SO_4 Wet Deposition - OSCAR IV (50% reduction of SO_x in Ohio Valley)

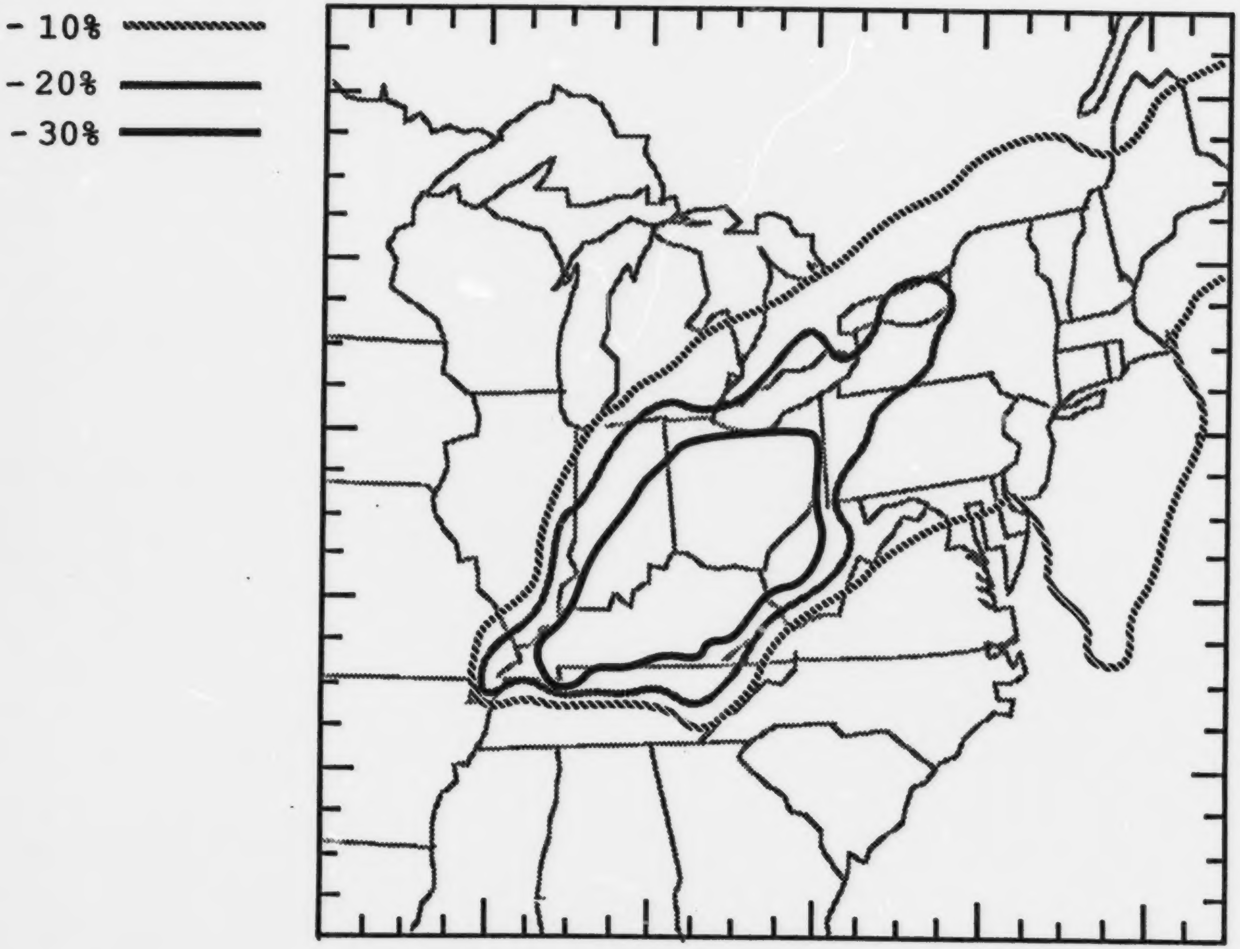

Fig. 2.2 Percent Change in SO_4 Wet Deposition - OSCAR I (50% reduction of SO_x in Ohio Valley)

SECTION 3

RADM SUBMODEL VERIFICATION STUDIES

3.1 Gas-Phase Chemistry Submodel Evaluation

The RADM version 1 gas-phase chemistry mechanism (NCAR, 1985; Stockwell, 1986) has been compared with both smog chamber data and other more complex chemical mechanisms. These tests have shown that the RADM mechanism gives a good representation of those aspects of tropospheric chemistry necessary for the modeling of acid deposition.

3.1.1 Comparison of RADM Version 1 Gas-Phase Chemistry with Statewide Air Pollution Research Center (SAPRC) Data

The initial tests of the RADM mechanism were made with data obtained from the Statewide Air Pollution Research Center (SAPRC) (Pitts et al., 1977). The data from SAPRC were complete and in a format which allowed immediate use. Data sets from most other sources require considerably greater effort to interpret. There have been many characterization studies of the SAPRC chamber. The most important test variables for the comparison of RADM simulation results with SAPRC data are the concentrations of O_3, NO_2, NO, and reactive organics since these species determine HO and HO_2 radical concentrations. The concentrations of HO and HO_2 radicals determine the gas-phase oxidation rates of SO_2, NO_2, and the formation rate of H_2O_2. Hydrogen peroxide is needed for aqueous-phase oxidation of SO_2, and it is a far more important oxidant of SO_2 in aqueous-phase than O_3 (Walcek and Taylor, 1986). The quality of the fit of the simulation results to the concentration profile of the reactive organics is the most important factor, since the concentration of reactive organics is the best available measure of the concentrations of HO and HO_2 in the chamber.

The individual reactive organic species used in the smog chamber experiments were lumped into the RADM reactive classes. This weighting was done according to the chemical class of the individual species and its relative reactivity with HO radical (Stockwell, 1986). The photolysis rate of NO_2 (JNO_2) was taken from the SAPRC data, and the other photolytic rate constants were determined from ratios of these rate constants to JNO_2 according to Leone and Seinfeld (1985). Wall sources and sinks were also taken from Leone and Seinfeld (1985). Uncertainties in these values can lead to uncertainties in the predicted concentration of all of the species of interest. The wall reaction terms were the same for all smog chamber runs and were not tuned for any of the simulations.

A comparison between measured NO, NO_2, O_3, and toluene is shown in Figs. 3.1-3.3 for experiment EC-237. This experiment consisted of the photolysis of a mixture of NO (0.377 ppm), NO_2 (0.106 ppm), ethylene (0.875 ppm), propylene

(0.100 ppm), t-2-butene (0.050 ppm), n-butane (1.025 ppm), 2,3-dimethylbutane (0.463 ppm), toluene (0.086 ppm), m-xylene (0.091 ppm), CO (0.960 ppm), acetaldehyde (0.001 ppm), propionaldehyde (0.002 ppm), and acetone (0.003 ppm). The agreement between the simulation and the experiment for NO_2 and NO is excellent, while the predicted O_3 maximum is about 23% high. This 23% is within the experimental uncertainty of ±30 to 40% for smog chamber experiments (see Section 6.5.2). Fig. 3.3 shows that the predicted toluene agrees well with the measured toluene. Since reaction with HO radicals is the only loss reaction for toluene, the HO levels predicted in the chamber by the mechanism are correct. The results for all SAPRC experiments simulated are summarized in Tables 3.1-3.3. Table 3.1 shows the predicted and observed maximum O_3 and NO_2 concentrations and the times at which they occur. The simulated maximum O_3 and NO_2 concentrations compare well with the smog chamber data, although there is a small bias towards higher simulated values than observed. Table 3.2 shows a comparison of the predicted and observed percent oxidation of the initial concentration of the major reactive organic species for the simple mixtures. Table 3.3 shows a comparison of the predicted and observed percent of the initial concentration of toluene and xylene oxdized for complex mixtures. The agreement between the predicted and experimental values for all of the reactive organic species shown in Tables 3.2 and 3.3 is excellent. Since reaction with HO radicals is the dominant loss process for reactive organics during photooxidation, the agreement between the simulation and the measured concentrations of reactive organic species shows that the RADM mechanism is correctly predicting HO concentrations within the uncertainties imposed by the wall sources.

3.1.2 Comparison of RADM Version 1 Gas-Phase Chemistry with University of North Carolina (UNC) Smog Chamber Data

The testing of the RADM version 1 mechanism against the University of North Carolina (UNC) data is in the beginning stages, since a massive effort was necessary to establish data reduction procedures and to estimate the error bounds of the data. This work is discussed in detail in Section 6.5. These preliminary tests showed apparent inconsistencies in the data, and subsequent analysis showed that the existing data on the absolute magnitude of the JNO_2 values within the UNC chambers appeared to be uncertain by about ±40% (Madronich, 1986) (Section 6.5.3). To determine the effect of this uncertainty in J-values on the predicted concentrations of O_3, NO, PAN, and H_2O_2, we have simulated the experiment UNC 101584 (chamber side R) using the RADM mechanism.

This experiment was a study of acetaldehyde photooxidation in the presence of trace nitrogen oxides in background air. The photolytic rate constants, initial conditions, wall effects, dilution rates, and sample line corrections for NO, O_3, and NO_2 reactions used for the simulations were taken from Whitten (1985). The initial conditions were NO (8 ppb), NO_2 (13 ppb), ALD (1 ppm), H_2O (10^4 ppm), HONO (1 ppb), and CO (300 ppb). The initial HONO concentration assumed by Whitten presumably arose from dark heterogeneous wall processes. The wall effects were represented by loss of O_3 and NO_2, assumed to occur through first-order reactions with rate constants of 2.2×10^{-4} and 1.1×10^{-4} min^{-1}, respectively.

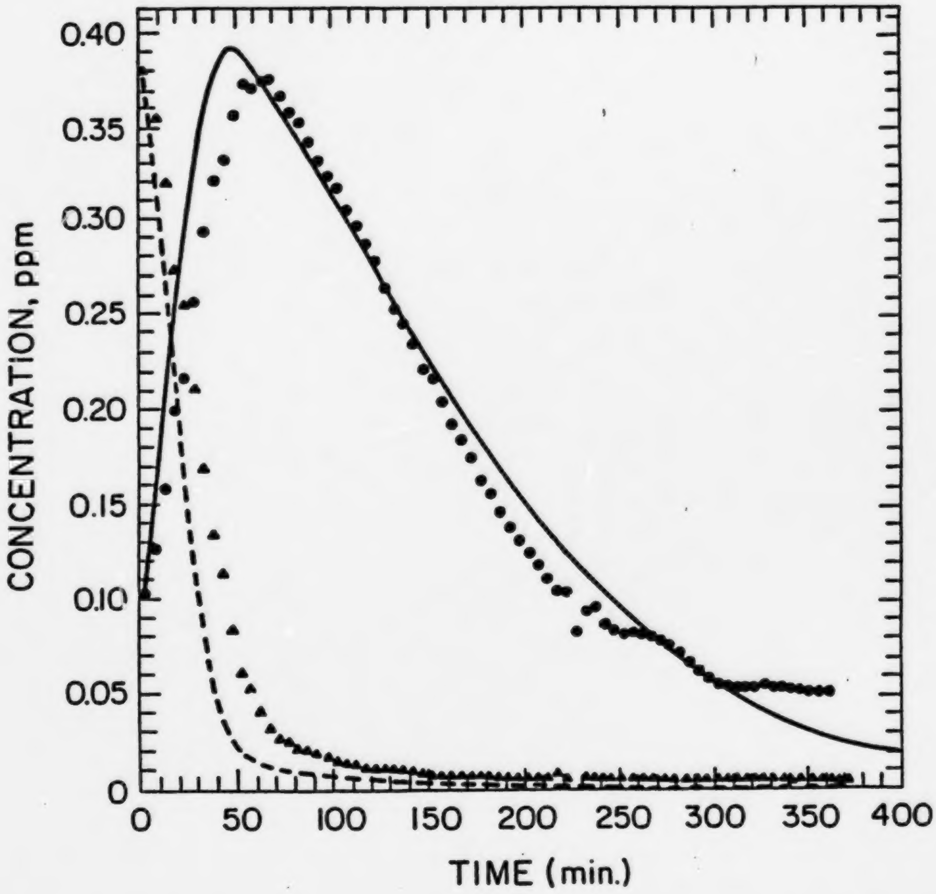

Fig. 3.1. Predicted and observed concentration profiles of NO_2 and NO for SAPRC smog chamber experiment EC-237. Solid circles refer to experimental NO_2; solid line, simulated NO_2; solid triangles, experimental NO; dashed line, simulated NO.

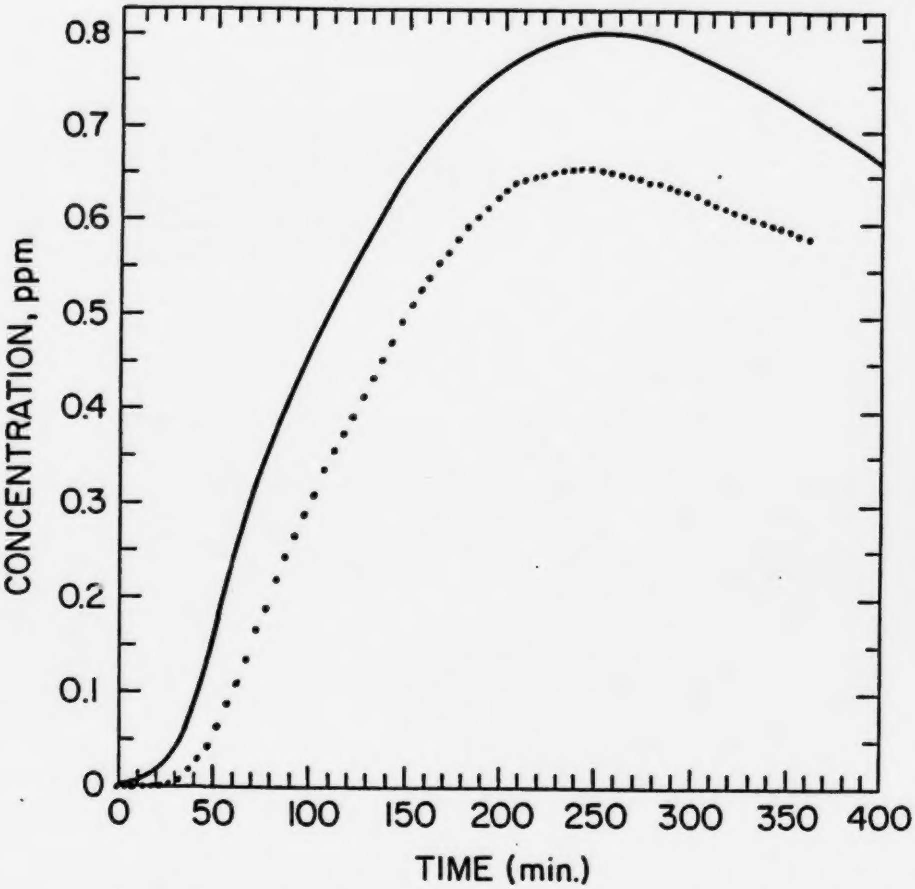

Fig. 3.2. Predicted and observed concentration profiles of O_3 for SAPRC smog chamber experiment EC-237. Solid circles refer to experimental O_3; solid line, simulated O_3.

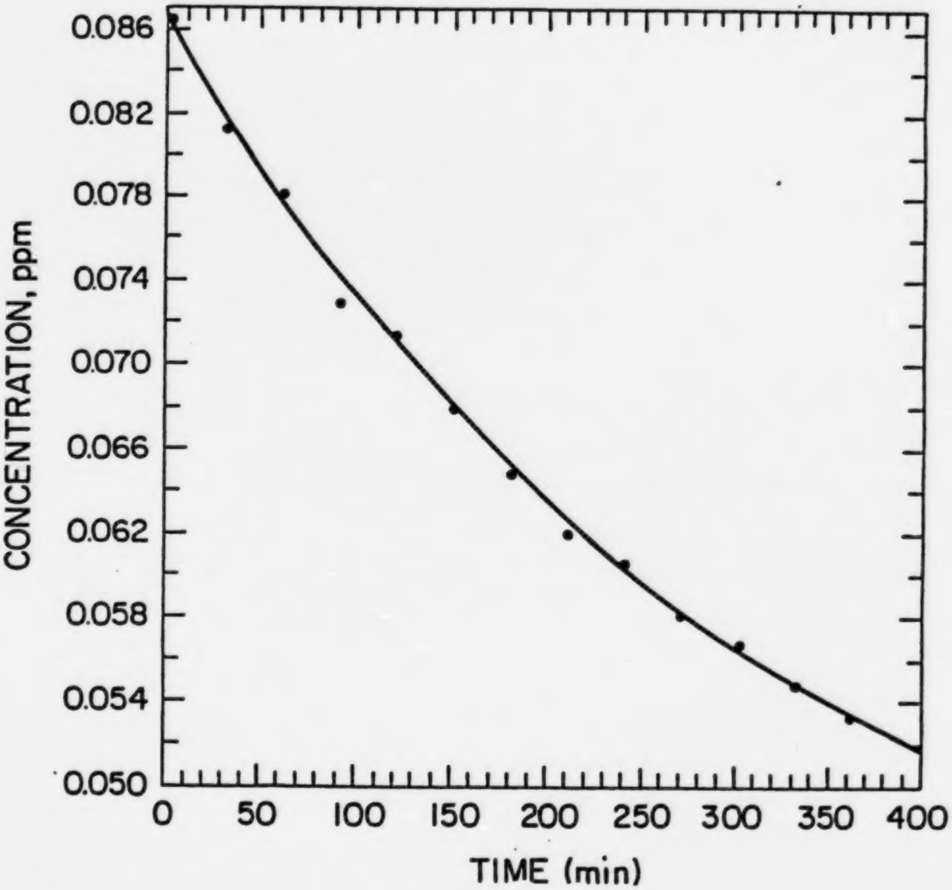

Fig. 3.3. Predicted and observed concentration profiles of toluene for SAPRC smog chamber experiment EC-237. Solid circles refer to experimental toluene; solid line, simulated toluene.

Table 3.1 Predicted and observed O3 and NO2 concentrations for Statewide Air Pollution Research Center (SAPRC) smog chamber experiments.

SAPRC EXPERIMENT	MAXIMUM O3 PPM		MAXIMUM NO2 PPM		TIME OF MAXIMUM O3 MIN		TIME OF MAXIMUM NO2 MIN	
	PREDICTED	OBSERVED	PREDICTED	OBSERVED	PREDICTED	OBSERVED	PREDICTED	OBSERVED
142 ETHENE	0.730	0.782	0.347	0.303	>360	>360	137	105
143 ETHENE	1.070	1.087	0.400	0.375	320	212	97	60
178 n-BUTANE	0.350	0.366	0.075	0.066	>495	>495	109	75
216 PROPENE	0.562	0.564	0.372	0.367	508	465	123	105
231 MULTI-COMPONENT	0.830	0.623	0.401	0.365	218	242	35	80
232 MULTI-COMPONENT	0.417	0.340	0.358	0.344	>390	>390	158	165
233 MULTI-COMPONENT	0.393	0.327	0.083	0.071	222	262	20	35
237 MULTI-COMPONENT	0.800	0.655	0.393	0.368	254	242	43	65
238 MULTI-COMPONENT	0.915	0.694	0.720	0.663	492	435	129	125
241 MULTI-COMPONENT	0.490	0.408	0.357	0.347	>360	>360	118	140
242 MULTI-COMPONENT	0.940	0.682	0.502	0.400	88	105	<10	25
243 MULTI-COMPONENT	0.920	0.716	0.420	0.397	133	132	13	35
245 MULTI-COMPONENT	1.180	0.894	0.830	0.761	154	175	13	55
246 MULTI-COMPONENT	0.492	0.574	0.361	0.373	>575	>575	190	148
254 ACETALDEHYDE	0.240	0.264	0.079	0.068	>370	>370	76	55
305 n-BUTANE	0.430	0.398	0.077	0.076	>360	>360	84	65
306 n-BUTANE	0.565	0.534	0.144	0.146	>405	>405	110	95
331 TOLUENE + n-BUTANE	1.060	0.523	0.466	0.334	103	125	5	45
340 TOLUENE	0.576	0.346	0.290	0.250	>330	>330	32	112
344 m-XYLENE	0.790	0.586	0.670	0.454	277	172	<10	45
345 m-XYLENE	0.700	0.396	0.279	0.192	98	70	<10	25

Table 3.2 Predicted and observed percent major organic species oxidized for simple mixtures in SAPRC smog chamber.

SAPRC EXPERIMENT	PREDICTED	OBSERVED
142 ETHENE	71.7%	78.6%
143 ETHENE	80.2%	80.2%
178 n-BUTANE	27.0%	26.5%
216 PROPENE	100.0%	100.0%
254 ACETALDEHYDE	54.0%	50.6%
305 n-BUTANE	18.3%	18.3%
306 n-BUTANE	15.3%	15.9%
340 TOLUENE	50.7%	60.2%
344 m-XYLENE	89.2%	95.8%
345 m-XYLENE	79.2%	83.1%

	TOLUENE		n-BUTANE	
	PREDICTED	OBSERVED	PREDICTED	OBSERVED
331 TOLUENE + n-BUTANE	32.3%	33.9%	20.1%	20.1%

Table 3.3 Predicted and observed percent xylene and toluene oxidized for multi-component mixtures in SAPRC smog chamber.

SAPRC EXPERIMENT	XYLENE		TOLUENE	
	PREDICTED	OBSERVED	PREDICTED	OBSERVED
231 MULTI-COMPONENT	75.9%	77.8%	35.7%	44.6%
232 MULTI-COMPONENT	62.1%	69.0%	29.7%	31.3%
233 MULTI-COMPONENT	65.2%	63.6%	29.7%	29.4%
237 MULTI-COMPONENT	79.1%	76.9%	38.1%	38.4%
238 MULTI-COMPONENT	84.5%	84.5%	44.9%	45.8%
241 MULTI-COMPONENT	79.5%	77.3%	36.8%	37.5%
242 MULTI-COMPONENT	72.2%	71.9%	33.7%	35.6%
243 MULTI-COMPONENT	63.6%	60.4%	25.8%	25.2%
245 MULTI-COMPONENT	82.0%	79.5%	40.2%	41.7%
246 MULTI-COMPONENT	79.6%	82.6%	40.9%	47.8%

The dilution rate was taken to be 2.2 x 10^{-4} ppm min^{-1}. Following the procedures employed by Whitten et al. (1985), the sample line corrections for NO, NO_2, and O_3 reactions in the dark line were made through the following reactions:

	k
NO ---> NO + NOC	6 min^{-1}
NO_2 ---> NO_2 + NO_2C	6 min^{-1}
O_3 ---> O_3 + O_3C	6 min^{-1}
NOC ---> loss	6 min^{-1}
NO_3C ---> loss	6 min^{-1}
O_3C ---> loss	6 min^{-1}
O_3C + NOC ---> NO_3C	100 ppm min^{-1}

The simulations were started at sunrise and ran for 640 min. Three simulations were run--one with the J-values of Whitten, one with J's 40% greater, and one with J's 40% lower. The photolytic rate constants for NO_2 of Whitten are shown in Fig. 3.4. The remaining photolytic rate constants were calculated from known ratios of these constants to JNO_2. Variation of the ratios for JO_3, JHCHO, and JALD with solar zenith angle was taken into account. The time of sunrise was uncertain from the UNC data; therefore, its timing was determined from data plots supplied by Whitten. The plot for O_3 is shown in Fig. 3.5, and the measured O_3 is in the range predicted by the RADM mechanism. The range for O_3 is rather wide--±30 ppb at the end of the simulation. Nitric oxide is shown in Fig. 3.6, and the agreement is very good, although there is a great deal of scatter in the data towards the end of the experiment. Predicted PAN is shown in Fig. 3.7, and the agreement with the data is very good. Variation in the photolytic rate constants causes very little variation in the final predicted PAN concentrations. The H_2O_2 concentrations were measured by Gervase Mackay of Unisearch Corporation (Jeffries, 1986). Fig. 3.8 shows that there is a great sensitivity of predicted H_2O_2 concentrations to photolysis rates. This figure shows that variations of 40% in the photolytic rates can cause the predicted H_2O_2 concentrations to vary by more than ±40%. Therefore, for definitive tests of chemical mechanisms for the production of H_2O_2 in the atmosphere, the photolytic rate constants must be known very accurately.

3.1.3 Comparison of RADM Version 1 Mechanism Against Other Mechanisms

Most good smog chamber data are limited to a narrow range of highly polluted chemical conditions and to short time durations. Acid generation occurs under much cleaner conditions than found in smog chambers. Most smog chamber experiments last several hours and not the several days needed to simulate air undergoing long-range transport. Therefore, it was necessary to extend the testing to include comparison with more complex chemical mechanisms. These comparisons were made for conditions ranging from very clean to highly pollu-

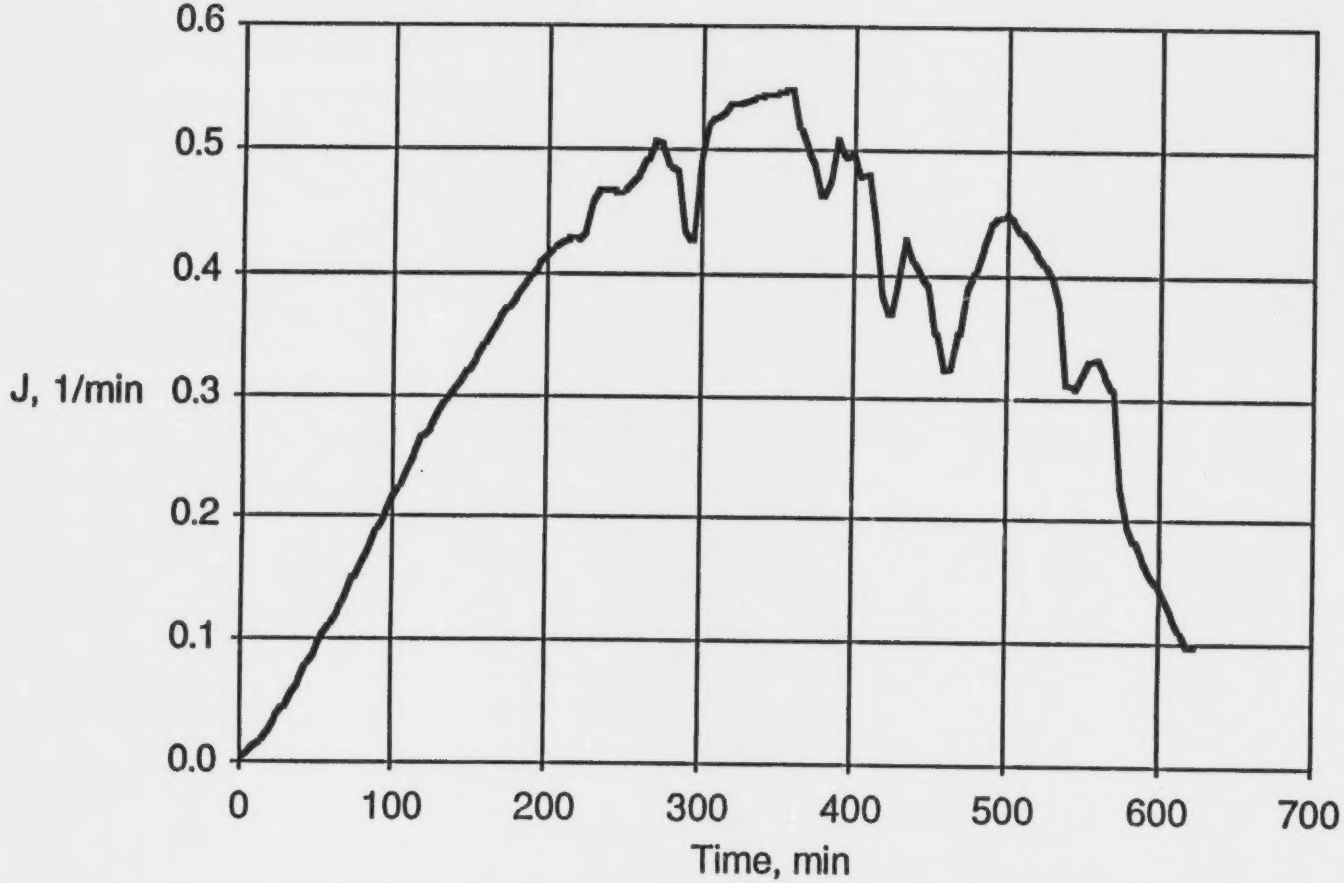

Fig. 3.4. Photolysis rates of NO_2 for UNC 101584 (Whitten, privite communication 1985).

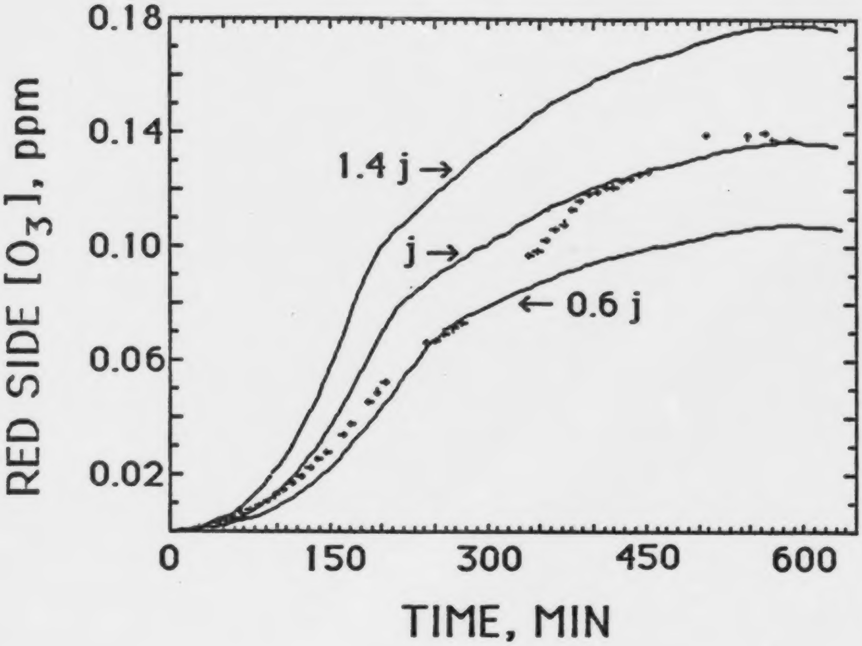

Fig. 3.5. Predicted and observed concentration profiles of O_3 for UNC smog chamber experiment 101584. Points refer to experimental O_3; solid line, simulated O_3 for three different sets of j values.

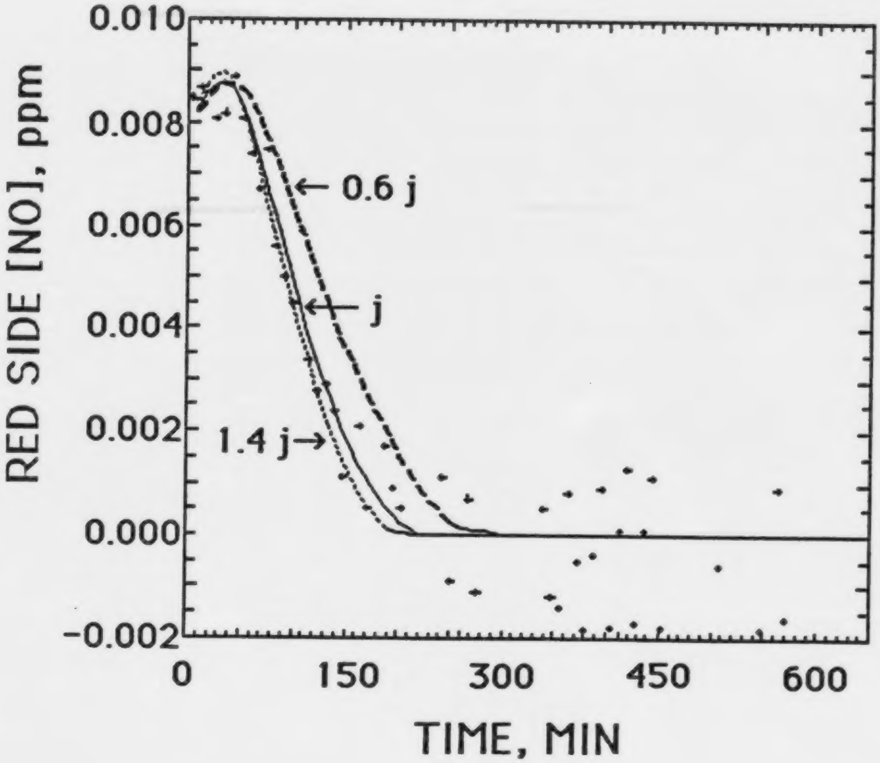

Fig. 3.6. Predicted and observed concentration profiles of NO for UNC smog chamber experiment 101584. Points refer to experimental NO; solid line, simulated NO for three different sets of j values.

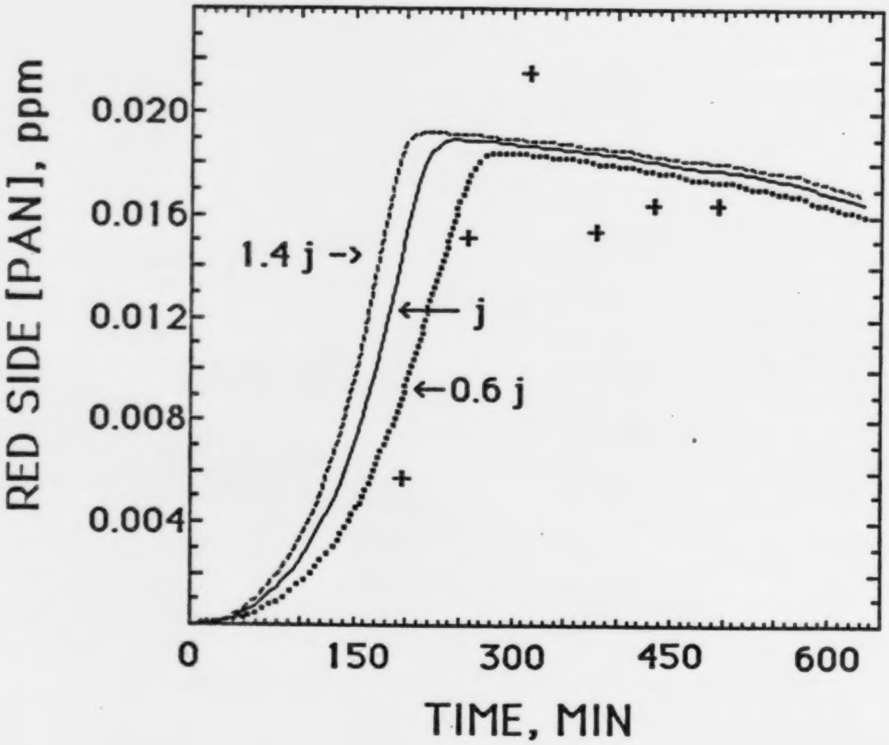

Fig. 3.7. Predicted and observed concentration profiles of PAN for UNC smog chamber experiment 101584. Crosses refer to experimental PAN; solid lines, simulated PAN for three different sets of j values.

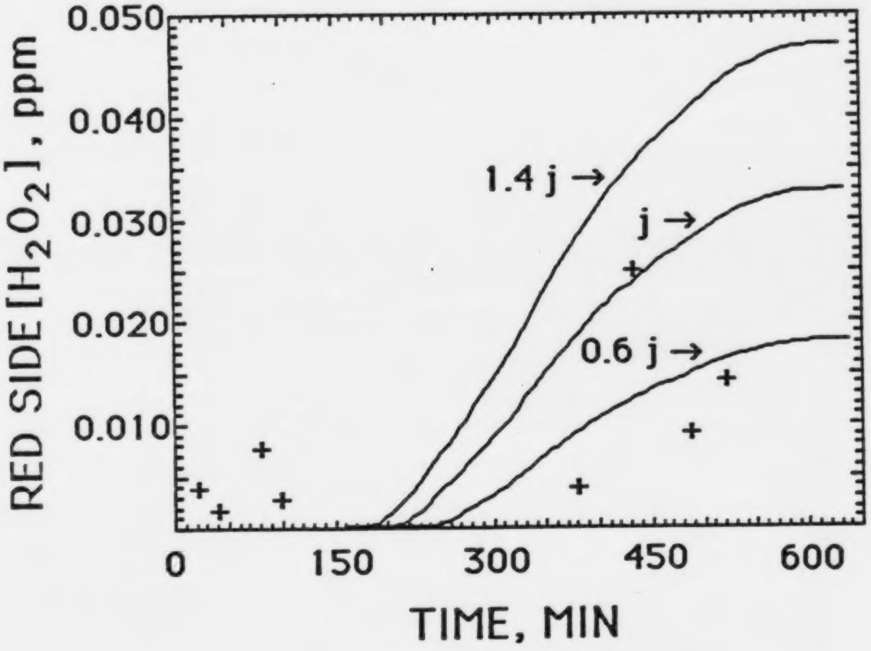

Fig. 3.8. Predicted and observed concentration profiles of H_2O_2 for UNC smog chamber experiment 101584. Crosses refer to experimental H_2O_2; solid lines, simulated H_2O_2 for three different sets of j values.

ted air. The initial NO_x to reactive organic ratio was also varied in these tests. The explicit mechanism (Leone and Seinfeld, 1985) includes explicit organic chemistry for twelve initial stable species. It is an updated version of that of Atkinson et al. (1982). Leone and Seinfeld tested their mechanism against SAPRC smog chamber data and used it as a standard of comparison for other atmospheric chemical mechanisms. The carbon bond mechanism (Whitten et al., 1985) uses a very different approach to atmospheric organic chemistry. Organic species are grouped according to the type and number of carbon bonds in the molecule, irrespective of the species in which the carbon bond is found. The organic classes used by the mechanism were determined through the use of structural reactivity analysis. The carbon bond mechanism has several advantages over other mechanisms, including the conservation of carbon, the range of values over which rate constants need to be averaged is narrowed, and the reactivity of the organic component of the gas mixture changes in a natural way. The mechanism has been extensively tested against both SAPRC and UNC outdoor smog chamber data.

Both mechanisms had to be modified to include sulfur chemistry. The reactions of SO_2 with HO radical and with Criegee intermediates were added to the complex mechanisms. These mechanisms were tested against SAPRC smog chamber experiment EC-237 with and without a fictitious initial SO_2 concentration of 1 ppm. The presence of SO_2 did not appreciably affect the simulated concentrations of O_3, NO_2, NO, and reactive organic species. This result is in agreement with the experimental work of Stockwell and Calvert (1983).

A parametric study was conducted in which eight cases were simulated by all three mechanisms. The initial conditions for the explicit mechanism are given in Table 3.4. The initial conditions were used to initialize each chemical mechanism for a 24-hour simulation which was started at sunrise (5:00 am). Case A represents an urban simulation with a relatively high nitrogen oxide to reactive organic ratio, which is typical of early morning air masses. The initial $NO-NO_2-O_3$ ratios are also typical of early morning air masses. Cases F, G, and H represent cases where the initial conditions from Case A are made progressively cleaner by a factor of ten. Cases B through F represent cases where the nitrogen oxide to reactive organic ratio was varied. No source of nitric oxide was included in these simulations. This choice of conditions was made to emphasize differences in the mechanisms' treatment of peroxy radical-peroxy radical reactions. Since these reactions generate peroxides which can oxidize SO_2 in aqueous phase at a rapid rate, the effect of these differences on H_2O_2 production was very important to determine. The initial conditions given for the explicit mechanism in Table 3.4 were lumped into the carbon bond mechanism according to rules provided by Whitten et al. (1985). The initial conditions for the RADM mechanism were obtained from the explicit conditions by the same scheme of lumping used for the smog chamber simulations. The photolytic rate constants used for the diurnal simulations for all three mechanisms were derived from Demerjian et al. (1980) except for formaldehyde, acetaldehyde, and acetone. The photolytic rate constants for formaldehyde and acetaldehyde were taken from Calvert and Stockwell (1983), and the rate constant for acetone photolysis was taken from Gardner et al. (1984). The photolytic rate constants were chosen for a clear summer day (July 1) at 40° N latitude, near sea level, and a temperature of 25° C. A surface albedo of 20% was assumed.

Table 3.4 Initial conditions for mechanism intercomparisons. Concentrations given for explicit mechanism, Leone and Seinfeld (1985).

SPECIES	CONCENTRATION, PPB							
	A	B	C	D	E	F	G	H
NO_2	25	0.25	0.025	2.50	2.500	2.5	0.25	0.025
NO	75	0.75	0.075	7.50	7.500	7.5	0.75	0.075
SO_2	60	6.00	6.000	0.60	0.600	6.0	0.60	0.060
Ethane	100	10.00	10.000	1.00	0.100	10.0	1.00	0.100
Propane	75	7.50	7.500	0.75	0.075	7.5	0.75	0.075
Butane	100	10.00	10.000	1.00	0.100	10.0	1.00	0.100
Toluene	20	2.00	2.000	0.20	0.020	2.0	0.20	0.020
Xylene	10	1.00	1.000	0.10	0.010	1.0	0.10	0.010
Ethylene	70	7.00	7.000	0.70	0.070	7.0	0.70	0.070
Propylene	30	3.00	3.000	0.30	0.030	3.0	0.30	0.030
Butene	10	1.00	1.000	0.10	0.010	1.0	0.10	0.010
HCHO	20	2.00	2.000	0.20	0.020	2.0	0.20	0.020
CH_3CHO	10	1.00	1.000	0.10	0.010	1.0	0.10	0.010
Acetone	5	0.50	0.500	0.05	0.005	0.5	0.05	0.005

H_2O set to 50% humidity, 15,600 PPM, Ozone set to 30 PPB, Methane set to 1.4 PPM, and CO set to 100 PPB for all cases.

A plot of the oxidation rates of SO_2 for the three mechanisms is shown in Fig. 3.9. The SO_2 oxidation rates for RADM and the explicit mechanisms are in very good agreement. The carbon bond mechanism gives higher SO_2 oxidation rates for the cleaner cases G and H. The total sulfate produced over 24 hours for all three mechanisms is given in Table 3.5. Some of the differences are due to differences in the fraction of SO_2 oxidized by Criegee intermediates. For Case A, for example, the carbon bond mechanism predicts that 44.4% of the oxidation of SO_2 occurs by reaction with Criegee intermediates, while only 6% and 7% of the oxidation occurs through this process for the RADM and explicit mechanisms, respectively.

NO_x oxidation rates are shown in Fig. 3.10, and the total nitric acid produced after 24 hours is given in Table 3.6. The rates of nitric generation by all three mechanisms are in good agreement. The total nitric acid concentrations produced by the RADM mechanism and the carbon bond mechanism are higher than those produced through the explicit mechanism. The carbon bond mechanism has higher NO_2 concentrations (and therefore a higher HNO_3 production rate) since it does not include organic nitrates as stable species nor does it have as many peroxyacetyl nitrates as the explicit mechanism. The carbon bond mechanism includes the reaction of N_2O_5 with H_2O to give HNO_3 as a homogeneous gas phase reaction which can produce a great deal of HNO_3 at night. This reaction has been excluded by Kerr and Calvert (1984).

The total production of H_2O_2 for the 24 hour period is shown in Table 3.7. Large differences exist in the total H_2O_2 produced. The carbon bond mechanism can produce more H_2O_2 than the explicit mechanism, as in Case C with low initial NO_x and high initial hydrocarbons, and as little as 1% of that produced for Case D by the explicit mechanism for high initial NO_x and low initial hydrocarbons. These differences result from small differences in the HO_x radical chemistry between the mechanisms.

To determine reasons for these differences in predicted H_2O_2, a sensitivity study of the RADM mechanism was performed to determine the chemical processes which control the hydrogen peroxide production rate in the atmosphere. The decoupled direct method of Dunker (1984) and McCrosky (1985) was used to calculate the first-order sensitivities, $d(\ln[p_i]/d(\ln k_j)$, for all species, p_i, and for all rate constants, k_j, for a modified Case F. This Case F includes sources of NO_x and reactive organic species. The emission rates were set so that in a 24 hour period the total concentration of an emitted species was equal to the initial concentration of that species. The sensitivity calculation was run for six daylight hours with constant photoylsis rates. The photolysis rate constant for NO_2 was set to 0.3 min^{-1}. The sensitivities were ranked according to the following integral:

$$S_j = \int \left| d(\ln[p_i]/d(\ln k_j) \right| dt. \tag{3.1}$$

The ten most important parameter sensitivity coefficients as functions of time for the production of H_2O_2 are plotted in Fig. 3.11. The sensitivity coefficients are normalized so that, for a sensitivity coefficient of 1.0, a 1% change in the rate constant for the given reaction will result in a 1% increase in H_2O_2 concentration. Hydrogen peroxide concentrations have the greatest sensitivity to the rate constant for the reaction of NO_2 with HO.

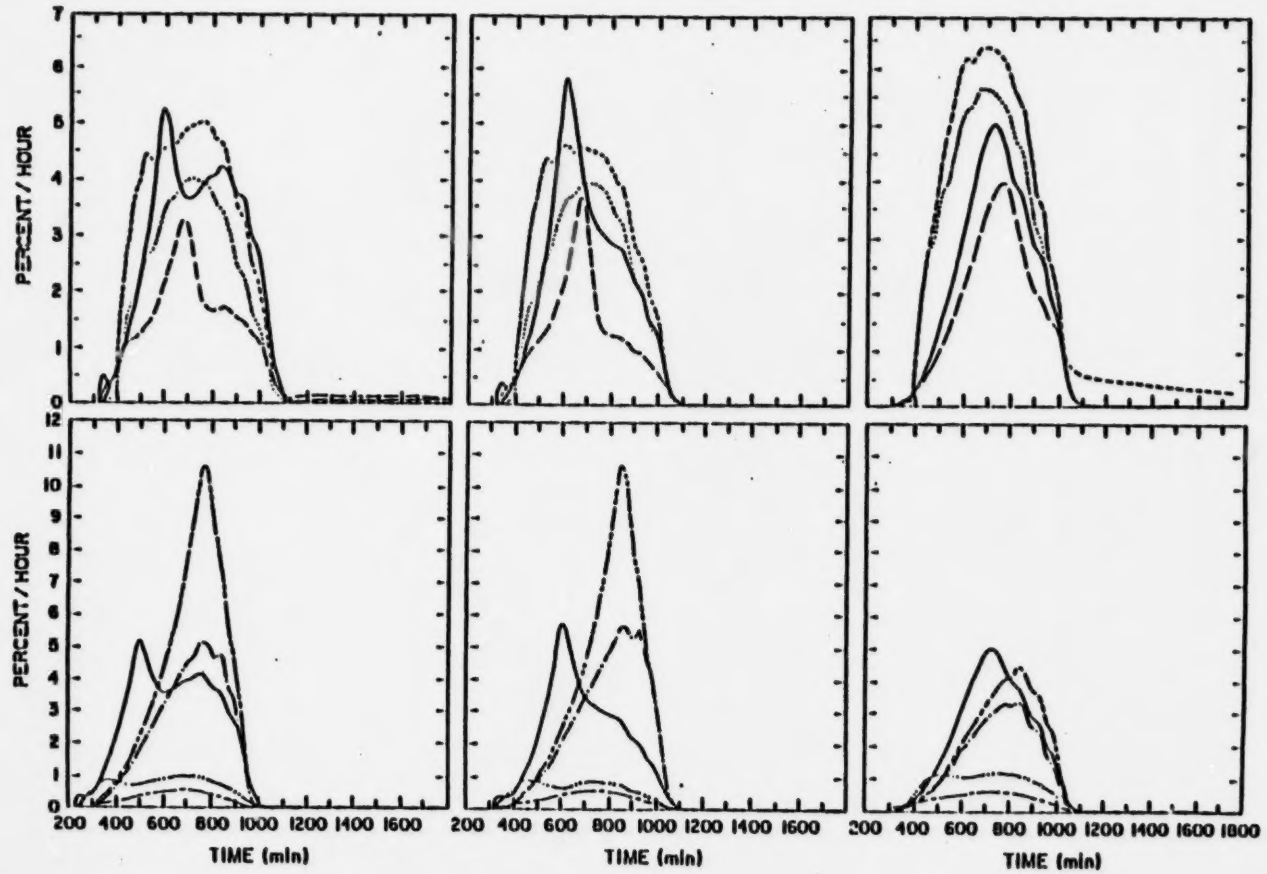

Fig. 3.9 Comparison of predicted SO_2 oxidation rates for RADM, Leone and Seinfeld and carbon bond mechanism, version CBM-X; see next page for full legend.

Legend for Fig. 3.9

Comparison of predicted SO_2 oxidation rates. Top panels show the effect of reducing the initial pollutant concentrations by factors of ten: (top left) RADM; (top middle) Leone and Seinfeld (1985); (top right) carbon bond, version CBM-X, Whitten et al. (1985). Bottom panels show the effect of varying the initial NO_x to hydrocarbon ratio: (bottom left) RADM; (bottom middle) Leone and Seinfeld; (bottom right) carbon bond, version CBM-X, Whitten et al. Sunrise is at 300 min.; noon, 720 min.; sunset, 1140 min. Long dashed line refers to Case A; long dash-two dots line, Case B; long dash-single short dash line, Case C; long dash-two single short dash line, Case D; long dash-single dot line, Case E; solid line, Case F; short dashed line, Case G; dotted line, Case H.

Table 3.5 **Comparison of H_2SO_4 concentrations produced for 24 hour period for three mechanisms: RADM; explicit, Leone and Seinfeld (1985); and carbon bond (CBM-X), Whitten et al. (1985).**

	CONCENTRATION PPM			RATIOS OF RADM & CBM-X TO EXPLICIT MECHANISM	
	RADM	EXPLICIT	CBM-X	RADM	CBM-X
CASE A	1.12E-02	9.15E-03	1.48E-02	1.22	1.62
CASE B	5.51E-04	4.40E-04	6.26E-04	1.25	1.42
CASE C	2.65E-04	2.32E-04	3.17E-04	1.14	1.37
CASE D	2.34E-04	2.27E-04	1.41E-04	1.03	0.62
CASE E	1.61E-05	1.72E-05	1.14E-05	0.94	0.66
CASE F	1.90E-03	1.55E-03	1.58E-03	1.23	1.02
CASE G	2.07E-04	1.90E-04	2.31E-04	1.09	1.22
CASE H	1.54E-05	1.50E-05	2.04E-05	1.03	1.36

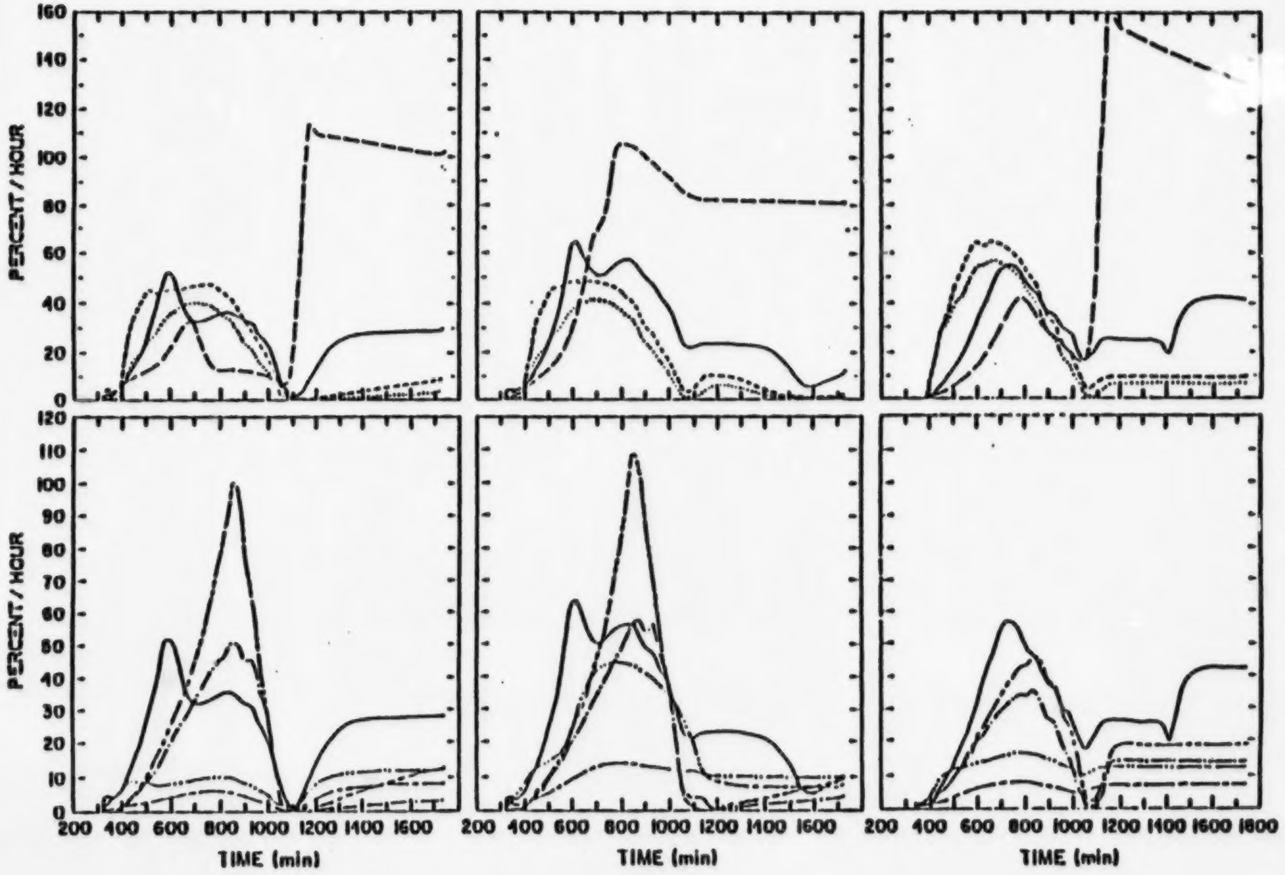

Fig. 3.10 Comparison of predicted NO_x oxidation rates for RADM, Leone and Seinfeld and carbon bond mechanism, version CBM-X; see next page for full legend.

Legend for Fig. 3.10

Comparison of predicted NO_x oxidation rates. Top panels show the effect of reducing the initial pollutant concentrations by factors of ten: (top left) RADM; (top middle) Leone and Seinfeld (1985); (top right) carbon bond, version CBM-X, Whitten et al. (1985). Bottom panels show the effect varying the initial NO_x to hydrocarbon ratio: (bottom left) RADM; (bottom middle) Leone and Seinfeld; (bottom right) carbon bond, version CBM-X, Whitten et al. Sunrise is at 300 min.; noon, 720 min.; sunset, 1140 min. Long dashed line refers to Case A; long dash-two dots line, Case B; long dash-single short dash line, Case C; long dash-two single short dash line, Case D; long dash-single dot line, Case E; solid line, Case F; short dashed line, Case G; dotted line, Case H.

Table 3.6 Comparison of HNO_3 produced over 24 hour period for three mechanisms: RADM; explicit, Leone and Seinfeld (1985); and carbon bond (CBM-X), Whitten et al. (1985).

	CONCENTRATION PPM			RATIOS OF RADM & CBM-X TO EXPLICIT MECHANISM	
	RADM	EXPLICIT	CBM-X	RADM	CBM-X
CASE A	6.22E-02	5.13E-02	7.27E-02	1.21	1.42
CASE B	2.78E-04	2.10E-04	3.51E-04	1.32	1.67
CASE C	8.66E-06	8.48E-06	1.01E-05	1.02	1.19
CASE D	9.32E-03	9.31E-03	9.44E-03	1.00	1.01
CASE E	8.48E-03	8.81E-03	9.21E-03	0.96	1.05
CASE F	6.63E-03	5.12E-03	7.46E-03	1.29	1.46
CASE G	7.39E-04	6.71E-04	7.97E-04	1.10	1.19
CASE H	7.43E-05	7.00E-05	8.47E-05	1.06	1.21

Table 3.7 Comparison of H_2O_2 concentrations produced over 24 hour period for three mechanisms: RADM; explicit, Leone and Seinfeld (1985); and carbon bond (CBM-X), Whitten et al. (1985).

	CONCENTRATION PPM			RATIOS OF RADM & CBM-X TO EXPLICIT MECHANISM	
	RADM	EXPLICIT	CBM-X	RADM	CBM-X
CASE A	2.99E-02	1.73E-02	1.14E-02	1.73	0.66
CASE B	4.68E-03	2.46E-03	4.65E-03	1.90	1.89
CASE C	8.40E-04	1.12E-03	3.58E-03	0.75	3.20
CASE D	7.08E-04	5.15E-04	5.86E-06	1.37	0.01
CASE E	3.86E-05	7.61E-05	5.80E-07	0. 51	0.01
CASE F	7.63E-03	4.45E-03	2.38E-03	1.71	0.53
CASE G	3.49E-03	1.90E-03	2.43E-03	1.84	1.28
CASE H	2.46E-03	1.28E-03	2.78E-03	1.92	2.17

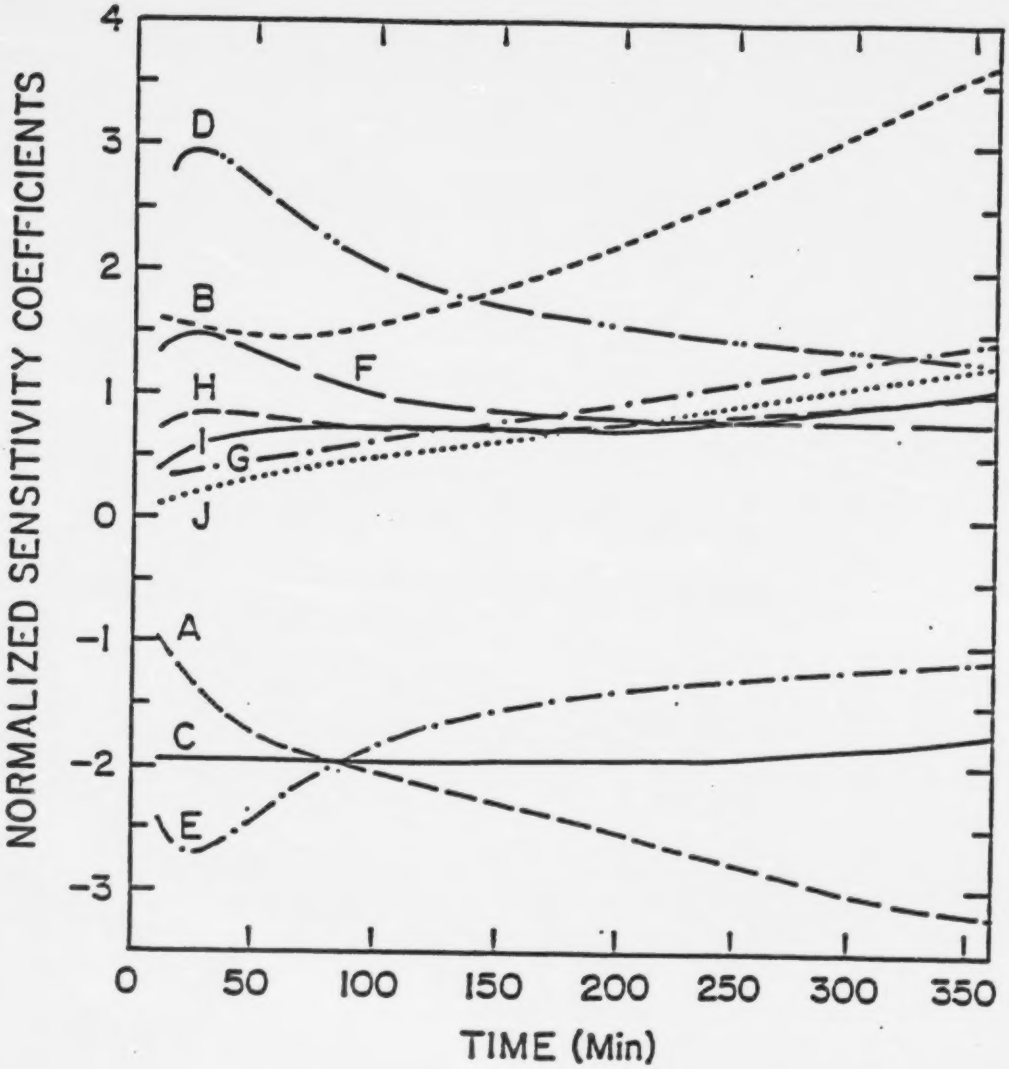

Fig. 3.11 Ten most important sensitivity coefficients of the rate constants in RADM mechanism for hydrogen peroxide concentration (modified Case F). Curve A refers to rate constant for NO_2 + HO --> HNO_3; B to HCHO + hv --> 2 HO_2 + CO; C to HO_2 + NO --> HO + NO; D to OL3P + NO --> 2 HO_2 + 2 NO_2; E to OL3P + NO --> 2 CH_3CHO + 2 HCHO; F to XYLENE + HO --> 2RO_2; G to C_2H_4 + HO --> OL2P; H to TOLUENE + HO --> 2RO_2; I to NO_2 + hv --> O_3 + NO; J to CH_3COO_2 + NO_2 --> PAN: where OL3P and OL2P are the adducts from addition of HO radical to propylene and ethylene respectively.

This reaction removes both HO radicals and nitrogen from the active photochemical system which makes the H_2O_2. The concentration of H_2O_2 is most sensitive in the positive direction to the rate constant for HCHO photolysis to yield HO_2 radicals. Fig. 3.11 shows that the H_2O_2 concentration becomes more sensitive to the HCHO photolysis rate as the simulation progresses. This is due to increases in the concentration of HCHO with time. The third most important parameter is the rate constant for the reaction of HO_2 with NO. Increases in the rate of this reaction lead to decreases in the HO_2 production rate since this reaction competes with the HO_2-HO_2 reaction. The reactions which lead to additional radical production have positive sensitivity coefficients. This is shown by the reaction of the peroxy radical OL_3P (formed from the addition of HO to propylene) with NO which was coded in the mechanism in two parts--a free radical-producing part and a carbonyl-producing part. The sensitivity coefficient is positive for that part of the OL_3-NO reaction with HO_2 radicals as products and negative for the OL_3P-NO reaction which produces carbonyl species. Therefore, increased concentrations of NO_3 result in greater rates of HNO_3 production and lower rates of H_2O_2 production.

The sensitivity analysis has shown that the H_2O_2 concentrations are inversely related to the rate of the HO-NO_2 reaction. The greater the rate of the HO-NO_2 reaction, the greater the concentration of nitric acid. Odd hydrogen radical chains will terminate either by the HO-NO_2 reaction or by the HO_2-HO_2 reaction for most conditions. The ratio of nitrogen oxides to reactive organic species should correlate with the relative number of HO_x radicals terminating with NO_2 or HO_2. Therefore, the ratio of the final concentration of HNO_3 to H_2O_2 will reflect the initial ratio of nitrogen oxides to reactive organic species for similar levels of pollution. A plot of these ratios for all three mechanisms is shown in Fig. 3.12. The HNO_3 to H_2O_2 ratios for the explicit and RADM mechanisms are very similar, while this ratio for the carbon bond mechanism is much higher at high ratios of NO_x to reactive organics. The higher HNO_3 to H_2O_2 ratios for the carbon bond mechanism are consistent with the generally higher average levels of NO_x predicted by this mechanism (Stockwell, 1986).

The sensitivity analysis also shows that the final concentration of H_2O_2 should correlate well with the final concentration of HCHO for a constant ratio of NO_x to reactive organics. This is plotted in Fig. 3.13. The correlation is very good for the RADM and explicit mechanisms, while there is little correlation for the carbon bond mechanism. The explicit mechanism uses explicit organic chemistry, which may predict HCHO more reliably than the highly lumped approach of the carbon bond mechanism for organic chemistry. Since the explicit and the RADM mechanisms show similar behavior with respect to initial conditions for H_2O_2 production, while the highly lumped carbon bond mechanism does not, we conclude that the carbon bond mechanism, version CBM-X, may not accurately predict H_2O_2 concentrations in the atmosphere. This result is not unexpected since the carbon bond mechanism has been highly tuned to fit smog chamber data where H_2O_2 concentrations are not well measured.

3.2 Cloud Processes and Aqueous-Phase Chemistry Submodel Evaluation

Clouds and their associated precipitation will strongly influence the chemical transformation, vertical transport, and wet deposition of numerous

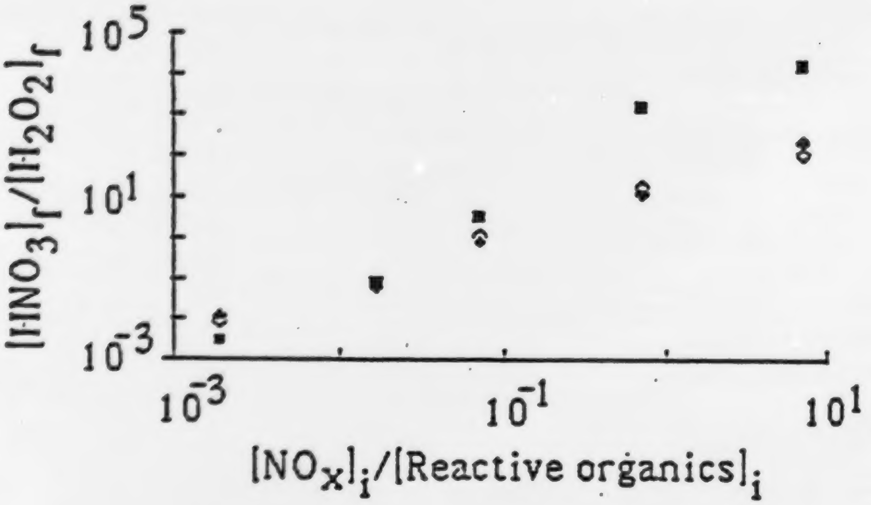

Fig. 3.12 Plot of the final ratio of nitric acid to hydrogen peroxide as a function of the initial ratio of total nitrogen oxides to total reactive organics for RADM, Leone and Seinfeld and carbon bond, version CBM-X, mechanisms; Cases B, C, D, E, and F: Filled diamonds refer to RADM; open diamonds, Leone and Seinfeld; filled squares, carbon bond.

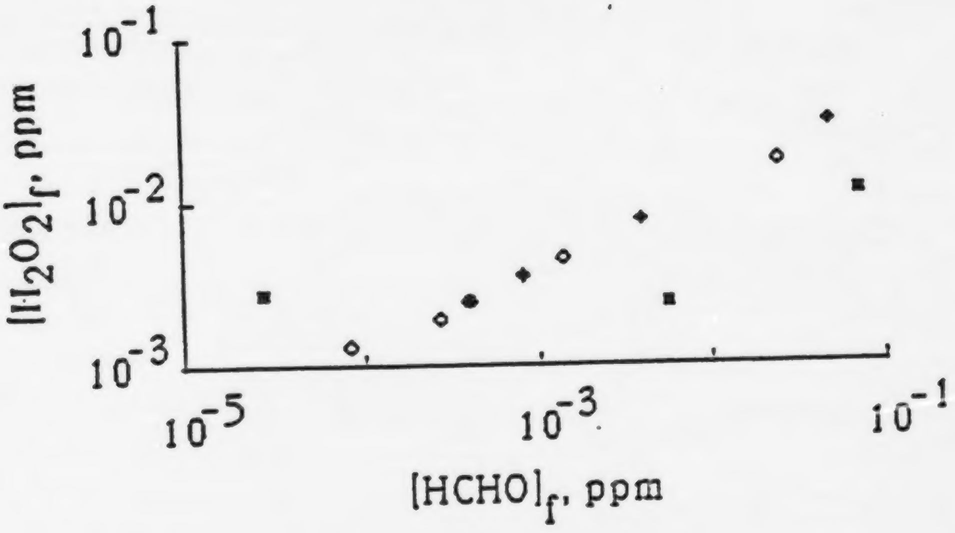

Fig. 3.13 Plot of the final hydrogen peroxide as a function of the final formaldehyde for RADM, Leone and Seinfeld and carbon bond, version CBM-X, mechanisms for a fixed initial ratio of total nitrogen oxides to total reactive organics of 7.12×10^{-2}; Cases A, F, G, and H: Filled diamonds refer to RADM; open diamonds, Leone and Seinfeld; filled squares, carbon bond.

pollutants as they are emitted and transported through the RADM domain. These effects are currently modeled by RADM using a semi-empirical one-dimensional cloud model including an aqueous chemical reaction mechanism. The vertical distribution of pollutants and pertinent cloud microphysical parameters are currently modeled following the approach of Walcek and Taylor (1986). The aqueous chemistry model assumes that an electroneutral solution is maintained at equilibrium with several gaseous pollutants as a series of irreversible reactions modify the composition of the cloudwater, similar to the modeling approach of Jacob and Hoffmann (1983). The aqueous chemical model is initialized with pollutant concentrations and meteorological conditions averaged over the vertical extent of the cloud, weighted with respect to the amount of liquid water present at each cloud level. Pollutant concentration changes predicted by the aqueous chemistry submodel are apportioned to each vertical level of the cloud before being averaged into the RADM grid column. Clouds can thus be treated as subgrid-scale effects if they occur over a portion of a RADM grid. The cloud processes model periodically provides adjustments to the pollutant distributions being analyzed by RADM and also predicts wet deposition for several species.

The RADM cloud processes modeling package is being upgraded to incorporate the one-dimensional reactive scavenging PLUVIUS model developed at Battelle Pacific Northwest Laboratories. This model has been modified (Scott, 1985) to operate in a steady-state mode, initialized with RADM meteorological and pollutant information. The aqueous chemistry incorporated into this version of the cloud model will be equivalent to the current aqueous chemistry submodel described above.

Field data collected to assess these cloud effects tend to be fairly qualitative in nature. For example, field observations of Hegg and Hobbs (1981) and Alkesweeny et al. (1984) show that sulfate may be rapidly produced in cloudy environments, although no accurate quantitative assessment of the numerous factors which determine the rate of conversion can be performed using their data. In another extensive field program utilizing inert tracers, Ching and Alkesweeny (1985) showed that cumulus clouds can rapidly transport trace gases between the boundary layer and free troposphere, although it is difficult to quantify this process from their data. In general, field studies designed to measure these cloud processes have not carefully characterized all of the relevant cloud microphysical, dynamical, and chemical factors which Walcek and Taylor (1986) have shown need to be measured. In the following evaluation, several RADM submodel results will be compared with measurements or more sophisticated models in order to test the performance of the aqueous chemical model and cloud transport parameterization.

Chemical constituents in cloudwater can arise from the soluble portions of aerosols upon which the cloudwater has condensed, and can also originate from gases in the air which dissolve in cloudwater. Subsequent chemical interactions occurring in a cloud will modify the cloudwater composition during its lifetime. The RADM aqueous chemical submodel assumes that an ionic balance is continuously maintained as a set of slower, irreversible chemical reactions convert several chemical constituents in the cloudwater. Given a set of external physical and chemical conditions, hydrogen ion concentration is determined diagnostically from equilibrium and electroneutrality constraints.

Table 3.8 shows a set of environmental conditions measured during April 1981 OSCAR aircraft observations of cloudwater composition over Ohio and Indiana (Dana et al., 1984). These sets of input conditions were fed into the RADM aqueous chemical submodel, and cloudwater pH (= $-\log_{10}[H+]$) predicted by the model were compared with observed pH. As shown in the table, the RADM submodel appears to be capable of inferring cloudwater pH over the range of initial conditions encountered during this observation period.

In addition to predicting cloudwater composition, the RADM aqueous chemistry model predicts the rates of several chemical reactions oxidizing SO_2 to sulfuric acid. Several laboratory investigations (e.g., Penkett et al., 1979) have identified H_2O_2 and O_3 as the primary oxidants responsible for this reaction. Several field studies have attempted to show that SO_2 in clouds is efficiently oxidized into sulfate (Hegg and Hobbs, 1981; Alkesweeny et al., 1984), although SO_2, sulfate, O_3, or H_2O_2 concentrations, as well as cloud liquid water contents, updraft velocities, etc., were not all measured. Until recently, field observations of hydrogen peroxide in clouds were not available, and thus an accurate assessment of its ability to oxidize SO_2 in clouds could not be inferred from field observations.

One method of inferring the occurrence of aqueous oxidation within clouds was proposed by Alkesweeny et al. (1984), by taking the ratio of SO_2 concentrations in air (moles liter^{-1}) to the total sulfur (SO_2 + sulfate) concentration. If no oxidation is occurring, this ratio should remain constant with height in a parcel of air rising through a cloud. On the other hand, if oxidation is occurring, this ratio should decrease significantly with height as SO_2 is converted to sulfate. Alkesweeny et al. found that this ratio was reduced by 20-70% over the vertical extent of several cumulus clouds. Fig. 3.14 plots the ratio of SO_2 to total sulfur concentration (molar concentrations in air) as predicted by the RADM aqueous chemical model applied to a parcel of air rising through a typical cumulus cloud (see Walcek and Taylor (1986) for a further description of this model). The rapid reduction of this ratio with height appears to agree reasonably well with the observations of Alkesweeny et al. (1984).

The current version of RADM predicts rainwater composition by assuming that the concentration of pollutant in rainwater is equal to the average concentration of pollutant in the cloudwater from which the rain originates, since rainwater collects water from many levels of a cloud before exiting the cloud. While this assumption is relatively crude, it was found that rainwater composition predicted using the RADM model agreed reasonably with observations of rain composition during the OSCAR IV event. A parameter frequently measured in field observations of rainwater composition is the scavenging ratio, defined as the ratio of the molar concentration of pollutant in rain to the molar concentration of the pollutant in the air below the cloud. Observations of sulfate scavenging ratio have shown considerable variability over several orders of magnitude, and rarely are other pertinent chemical or physical parameters associated with individual precipitation events measured along with this parameter. The bottom portion of Fig. 3.15 shows an example of the sulfate scavenging ratios compiled by Niemann (1983) as a function of collected precipitation volume. Clearly, there is significant scatter and no clear trend with precipitation volume during a storm event. Since the chemical con-

TABLE 3.8. PREDICTED AND OBSERVED CLOUD pH, OSCAR AIRCRAFT OBSERVATIONS

Environmental conditions[1]								Cloudwater pH	
$[SO_4^{=}]$ (μg m^{-3})	Carbonate[2] (μg m^{-3})	$[SO_2]$ (ppb)	$[HNO_3]$ (ppt)	$[NH_3]$ (ppt)	L (g m^{-3})	P (atm)	T (°C)	Observed	RADM
1.40	0.058	4.3	177.	290.	0.37	0.81	5.	**4.38**	**4.28**
1.08	0.068	4.0	116.	280.	0.62	0.76	2.	**4.63**	**4.61**
0.062	0.140	<0.1	18.	20.	0.13	0.68	-1.0	-.--[3]	**6.30**
0.012	<0.01	<0.1	5.	< 1.	0.04	0.64	-3.0	**5.92**	**5.64**

[1] Environmental conditions inferred from aircraft observations made between 16 - 21 GMT, 22 April 1981. All pollutant concentrations are expressed as sea-level equivalent concentrations in air, and are derived from the aqueous concentrations reported by aircraft, assuming total dissolution of soluble aerosol.

[2] Carbonate aerosol concentrations inferred from observed concentrations of calcium and magnesium, ions assumed complexed with $CO_3^{=}$.

[3] Hydrogen ion concentration too low to detect

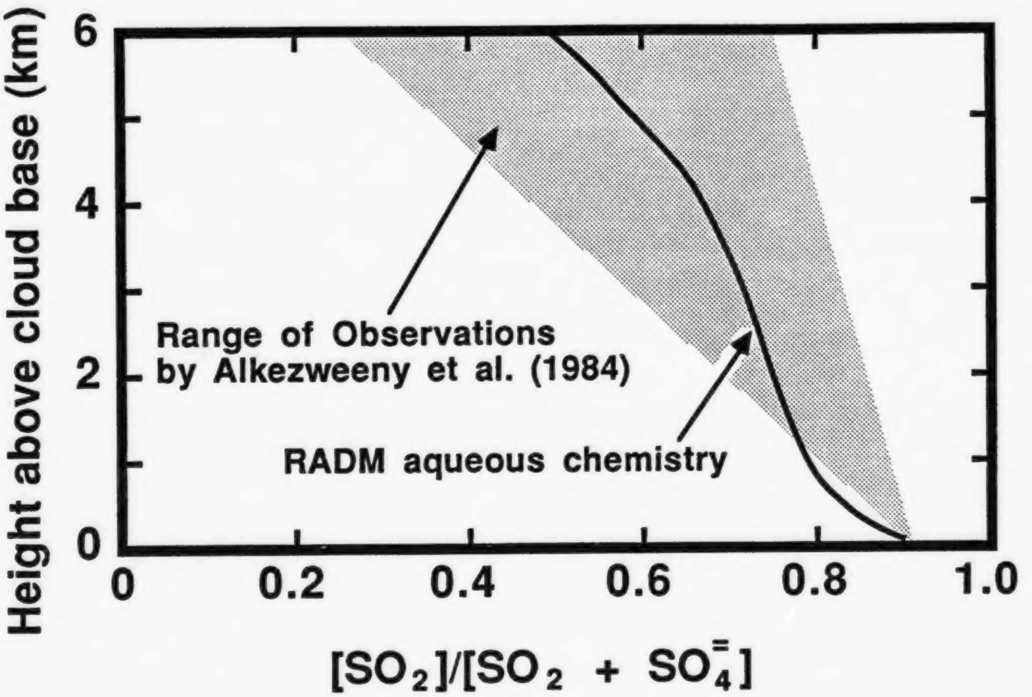

Figure 3.14 Ratio of SO_2 concentration in air to total sulfur concentration (SO_2 + sulfate) in rising, entraining parcel of air. Observations of Alkesweeny *et al.* showing a 20 - 70% reduction in this ratio with height are also shaded. Initial conditions at cloud base are: $[SO_2]=10$ppb, $[HNO_3]=10$ppt, $[NH_3]=0$, $[HCOOH]=50$ppt, $[H_2O_2]=1$ppb, $[O_3]=50$ppb, $[SO_4^-]=5\mu g\ m^{-3}$.

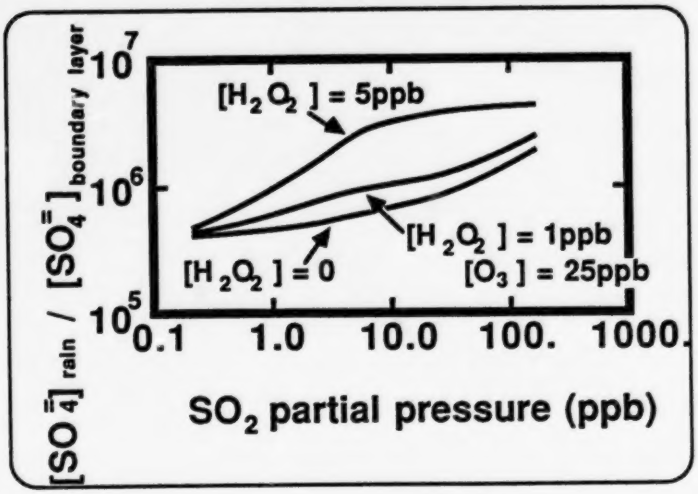

Model predictions

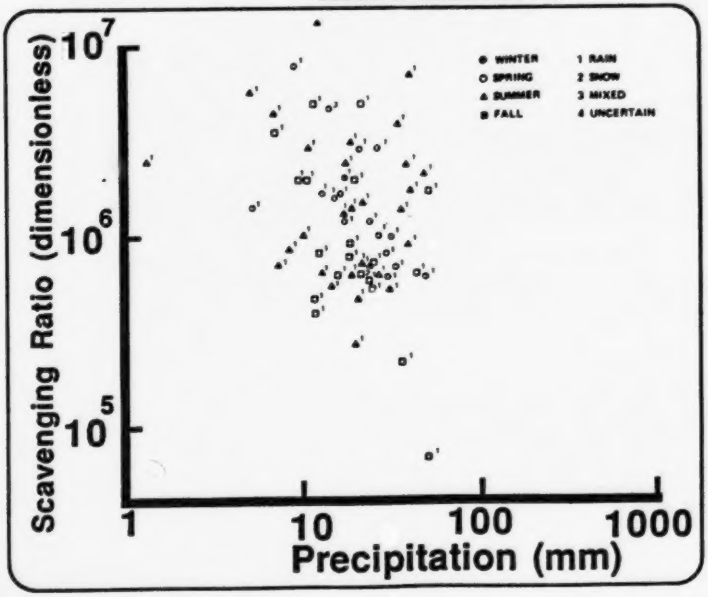

Observations

Figure 3.15 Typical sulfate scavenging ratios predicted using the RADM cloud processes parameterization scheme (top), and the observations of Niemann (1983), (bottom). RADM model conditions: Cloud depth: 6 km, Rainfall rate: 8 mm h^{-1}, storm duration: 1 hour.

ditions under which these observations were obtained were not available, the top portion of Fig. 3.15 shows the scavenging ratio predicted using the RADM cloud processes model for a variety of SO_2 and oxidant concentrations for a typical cloud. The scavenging ratios predicted by the RADM parameterization show that much of the inherent variability in the observations can be explained by chemical variations in the cloudy environment. As shown in Fig. 3.15, scavenging ratios predicted by the RADM model lie between the extremes observed in field observations.

Perhaps the most complete database currently available for cloud processes model evaluation was collected at the OSCAR high density precipitation sampling network in April 1981. The high density sampling network consisted of 47 precipitation sampling sites spread over roughly a (100 km)^2 area near Fort Wayne, Indiana. Several aircraft observations reported pollutant concentrations in and around clouds which subsequently rained in the area for about 4 hours on 21-22 April 1981. Over this area, it was found that 0.2-0.4 kg ha^{-1} of sulfate was deposited during the storm, and 0.07-0.20 kg ha^{-1} of nitrate was reported at the sampling sites. The RADM predictions over the same general area showed 0.40-0.55 kg ha^{-1} sulfate and 0.15-0.25 kg ha^{-1} nitrate. Further analysis and comparisons between OSCAR observations and RADM predictions will be provided in Section 4. Using the high-resolution OSCAR data, Easter and Hales (1982) were able to test the performance of the PLUVIUS reactive scavenging model and to obtain reasonable agreement between observations and model predictions.

In addition to predicting cloud and rainwater composition, the RADM cloud processes model predicts the rate at which pollutants are vertically transported by subgrid-scale cumulus clouds. It is difficult to accurately assess this transport process using field observations. Fortunately, Niewiadomski (1986) has utilized a high resolution (1 km horizontally, 200 m vertically), three-dimensional wind field generated using the cloud model of Clark (1979) to study the redistribution of tracer by a cloud field. Results of his numerical experiments are shown in Fig 3.16. Starting with the initial distribution of passive tracer shown as the grey line, a layer of clouds covering only a fraction of a 50 x 50 km^2 area was found to redistribute the pollutant as shown in the solid line after one hour. The one-dimensional RADM parameterization was applied to the same initial distribution, and the pollutant profile after one hour is shown using a dashed line. Both models predict a significant depletion of passive tracer from the boundary layer and a "venting" of this material to the cloud layer.

Further evaluation of the RADM cloud processes model must rely on additional detailed measurements taken during individual storm events where the physical and chemical environment surrounding the storm is well-characterized. Data available at this time can be only used to qualitatively evaluate the model's performance. In order to assess accurately the performance of a cloud processes model, the following data need to be measured in several individual storm environments:

Chemical (gas phase): SO_2, H_2O_2, NH_3, HCHO, aerosol sulfate, nitrate, ammonia

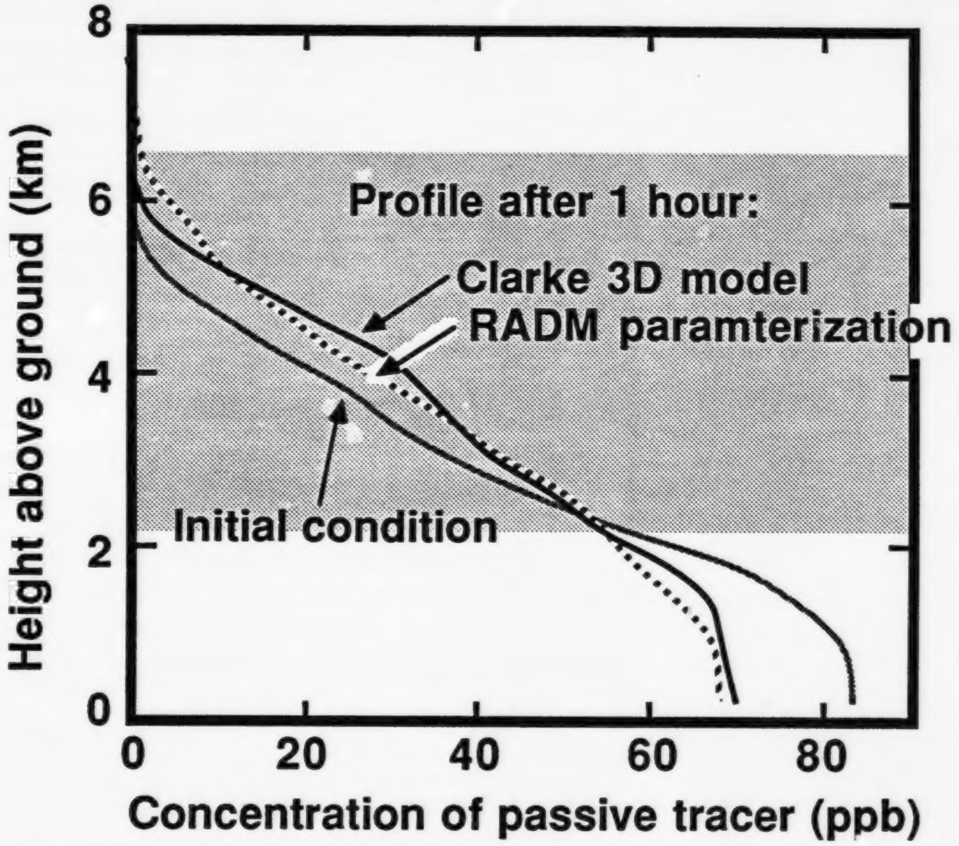

Figure 3.16 Area-averaged (50 x 50 km^2) concentration of passive tracer vs height as predicted using wind fields generated using a 3-D, high resolution cloud field model and the current RADM redistribution parameterization. Initial profile is shown in light grey, and shaded area denotes the layer in which clouds occurred.

Chemical (aqueous phase): $SO_4^=$, NO_3, NH_4^+, H^+, Ca^{2+}, Mg^{2+}, Cl^-, Na^+, trace metals

Supporting environmental data: Temperature, pressure, water vapor, cloudwater, wind speed (vertical and horizontal), cloud top/base heights, degree of coverage, rainfall rate/pattern, insolation flux, surface heat flux

Each of these data should be measured vertically throughout the tropospheric depth several times during a storm event. Only with data such as these can an accurate evaluation of a cloud processes model be performed.

3.3 Dry Deposition Submodel Evaluation

The method used by RADM to model the dry deposition of several trace species follows the approach of Walcek et al. (1986). This dry deposition model was expanded from an earlier model provided to RADM by Argonne National Laboratory. Dry deposition fluxes are computed in RADM by multiplying the ambient concentration of pollutant above a surface by its deposition velocity v_d, which is assumed to vary with time of day, land surface type, season, and several other factors. This deposition velocity is assumed to be composed of a series of three resistances: (1) aerodynamic resistance r_a, proportional to the turbulence level in the lowest atmospheric layer; (2) sublayer resistance r_b, proportional to the trace gas diffusivity in air; and (3) surface resistance r_s, which is determined by biological and physical factors specific to each pollutant and surface type. Deposition velocities are computed as follows:

$$v_d = \frac{1}{(r_a + r_b + r_s)} . \qquad (3.2)$$

This approach represents a highly empirical parameterization, relying heavily on a relatively sparse database of dry deposition measurements. The dry deposition behavior observed at a few sites under specific sets of conditions has been extrapolated over the entire RADM domain. Therefore, it is difficult to evaluate independently the performance of the dry deposition model since any available data on dry deposition has been used to "tune" the current model parameterizations. An additional problem arises since dry deposition measurements are representative of only a relatively small area within a particular land type, while RADM computes dry deposition fluxes over relatively large areas (80 x 80 km) where several land types may be present. Therefore, simple "point by point" comparisons of dry deposition fluxes are inappropriate for model evaluation.

The aerodynamic resistance to pollutant transport has been studied for several years by boundary layer meteorologists interested in the transport of momentum, heat and moisture in the lowest atmospheric layer, and is currently characterized using standard techniques in this field (Sheih et al., 1979). Deposition velocities are usually insensitive to the formulation used to describe the sublayer resistance, since this term is small relative to the other resistance terms. On the other hand, surface resistances are frequently the largest resistance encountered for several trace gases of interest over many surface types. In order to assess this important term in computing deposition velocities, the RADM parameterization utilizes compilations of as many field observations of dry deposition as possible to accurately quantify the numerous factors which influence this resistance. For example, the wide range of values reported for SO_2 surface resistance (McMahon and Denison, 1979) can be attributed largely to variations in land type, season, and time of day during which individual measurements were performed. After noting such correlations, the RADM dry deposition model uses a series of "look-up" tables which categorize SO_2 surface resistance in terms of season, land type, and insolation.

Wesely et al. (1985) have presented results of an extensive field program designed to monitor particulate sulfate deposition to grasslands. Their analysis found that surface and sublayer resistance for sulfate was related to the friction velocity and Monin-Obukhov length scale (two parameters relatively easy to infer from measurements in the atmospheric surface layer) during most of their observational period. Fig. 3.17 shows the data of Wesely et al. as well as the parameterization utilized by RADM to model sulfate deposition. The RADM model applies this parameterization over all areas of the modeling domain, although the validity of this extrapolation will rely on further measurements of sulfate deposition over the wide variety of surface and meteorological conditions encountered by RADM. Unfortunately, for pollutants other than SO_2 and sulfate, relatively little data are available to construct such a generalized treatment of dry deposition, and therefore surface resistances for other gases are currently scaled with respect to those of SO_2. These scaling factors are semi-quantitatively "tuned" to concur with any available dry deposition measurements for each gas of interest.

Comprehensive dry deposition model evaluation will rely most heavily on ongoing measurements of pollutant dry deposition. Due to the parametric nature of the RADM dry deposition model, several meteorological and physical variables must be carefully measured in parallel with future measurements of pollutant dry deposition. These parameters include: heat and momentum fluxes in the surface layer; wind speed, insolation, and land type to which deposition is occurring; surface roughness; and a quantification of surface moisture (i.e., dew or precipitation wetted conditions must be identified). Since the RADM model must appropriately weigh and average deposition velocities over several land types within each grid area of the model, it would be useful to devise a high-density (10-20 measurement sites in a heterogeneous (20-50 km)^2 area) dry deposition measurement experiment to evaluate the effects of heterogeneous land types on area-averaged deposition velocities. In addition, surface resistance measurements for gases such as peroxide, formaldehyde, ammonia, and particulate nitrate, among others, would be useful for future RADM development and evaluation.

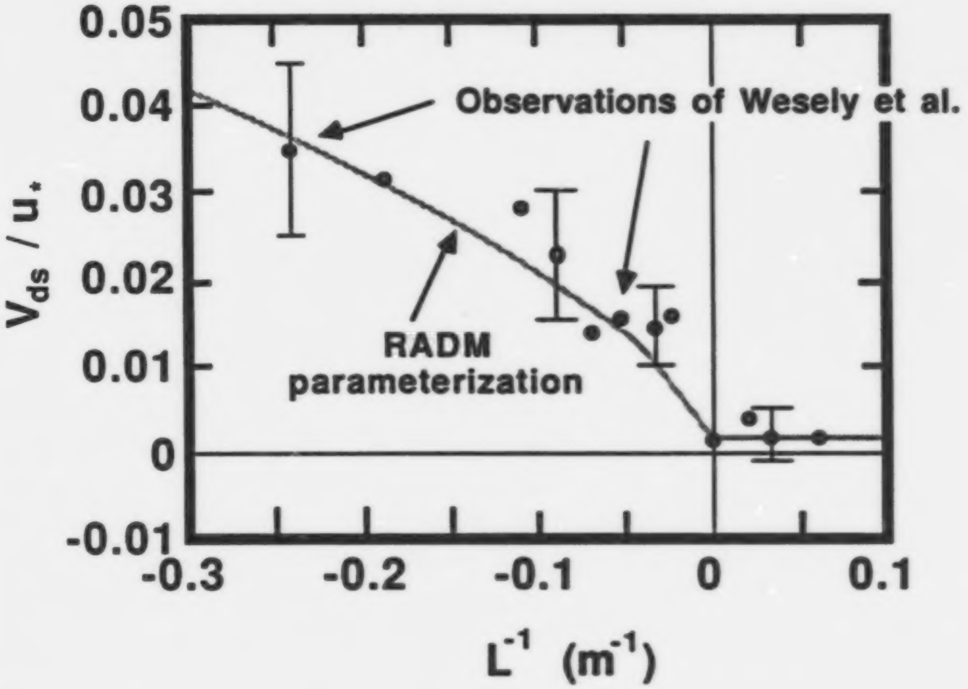

Figure 3.17 Ratio of sulfate surface deposition velocity (aerodynamic resistance removed), V_{ds} and friction velocity, u_* as a function of the inverse Monin Obukhov length scale for the observations compiled by Wesely *et al.*, 1985. RADM parameterization (grey line) is best fit to this data.

SECTION 4

PRELIMINARY EVALUATION OF RADM WITH THE OSCAR DATABASE

4.1 The OSCAR Database

The OSCAR field program has been described extensively in previous reports (OSCAR, 1983). The objective of the program was to study chemical and dynamical features of frontal storms as they traversed the eastern portion of the North American continent. During the April 1981 observational period, four storm systems were examined. Region-wide collection of precipitation for chemical anaysis was carried out for three of the four events observed. One of these storms, the OSCAR IV case, is the basis for much of the analysis presented in this report. A few preliminary studies of OSCAR I are also presented.

Prior to using the OSCAR data for model evaluation, the data were examined to establish the data characteristics and to determine possible sources of error in the data. Analysis of the OSCAR precipitation chemistry database has been presented in more detail elsewhere (Middleton, 1985b).

Differences in field pH and lab pH and the ion balance were the major criteria used to identify suspicious data. Since there was no quality assurance done in the field, the field pH data can only be used as a rough check. Thus, both criteria were used to screen data. A questionable sample was defined as one in which the field pH and the lab pH varied by more than a pH unit and the ion balance was greater than 0.1.

General characteristics of the data obtained using the screened and unscreened data were compared to determine if there were any significant differences. The differences in several general characteristics of the data found using all of the data and only the screened data are illustrated in Fig. 4.1 (a-f) and outlined in Table 4.1. The figures present the characteristic relationships of chemicals in rain and rainfall volume. The table summarizes the location and time of the maximum concentrations for each storm.

The figures present the results of principal components analyses for each of the three events. The principal component eigenvalue which explained a high proportion of the variance (greater than 70%) was selected as a convenient single index describing the change in the set of major variables during each event. For all of the storms, it was found that a principal component based on H, SO_4, NO_3, and NH_4 ion concentrations provided the most appropriate index. A plot of this index versus rainfall volume gives one indication of how closely rain and chemical concentration in raindrops are related.

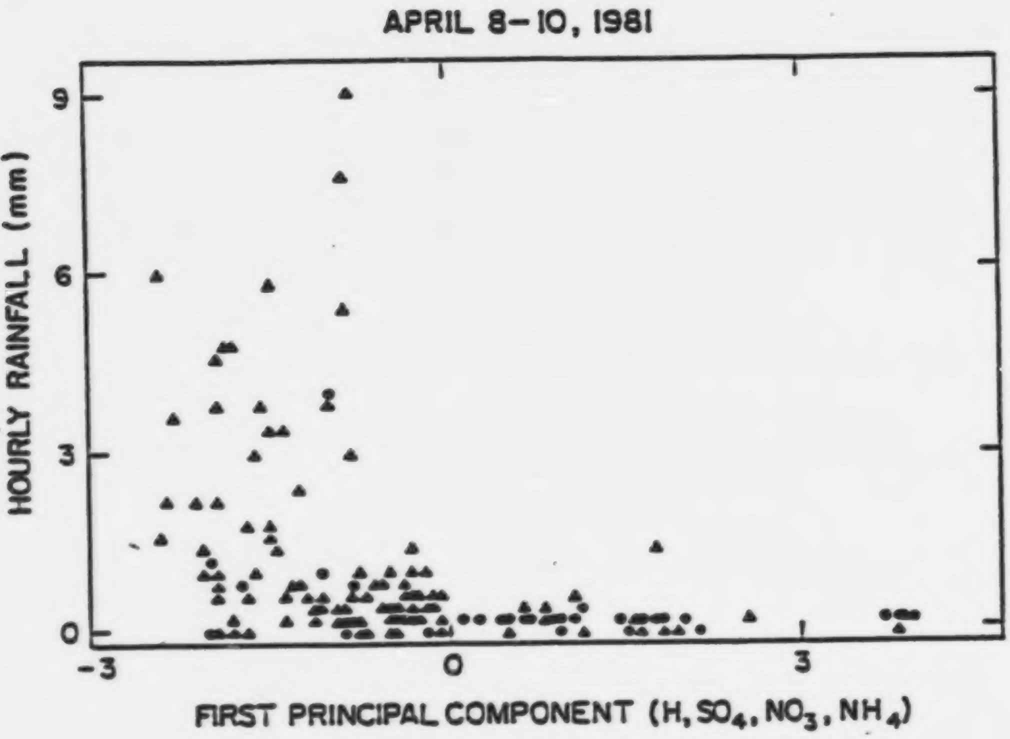

Fig. 4.1a Principal components analysis for three OSCAR events. Principal components included hydrogen, sulfate, nitrate, and ammonium ions. The first three graphs (a–c) depict the first principal component versus rainfall volume for the OSCAR events using all of the data. The next graphs (d–f) depict the first principal component versus rainfall volume for the OSCAR events using only the data which passed the pH and ion balance tests.

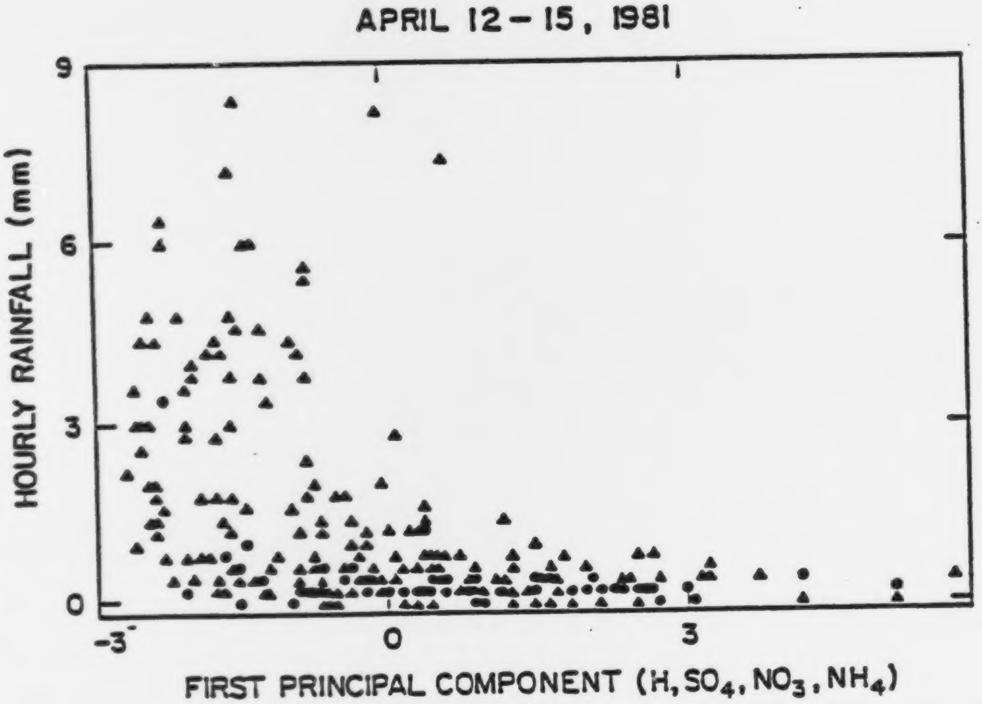

Fig. 4.1b (Same as Fig. 4.1a)

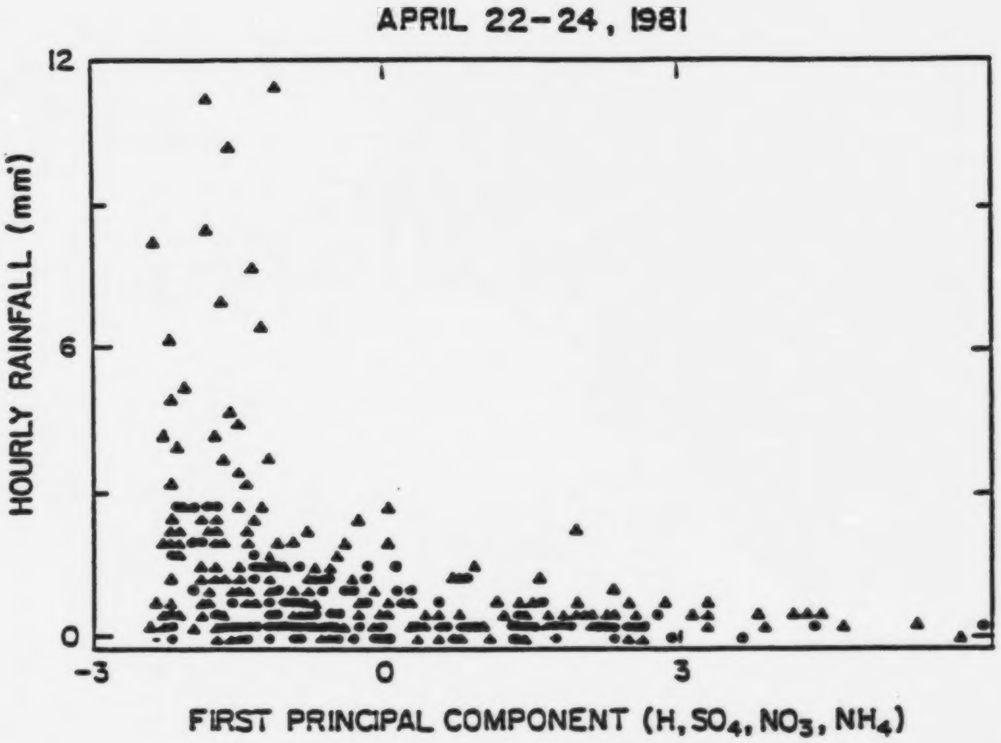

Fig. 4.1c (Same as Fig. 4.1a)

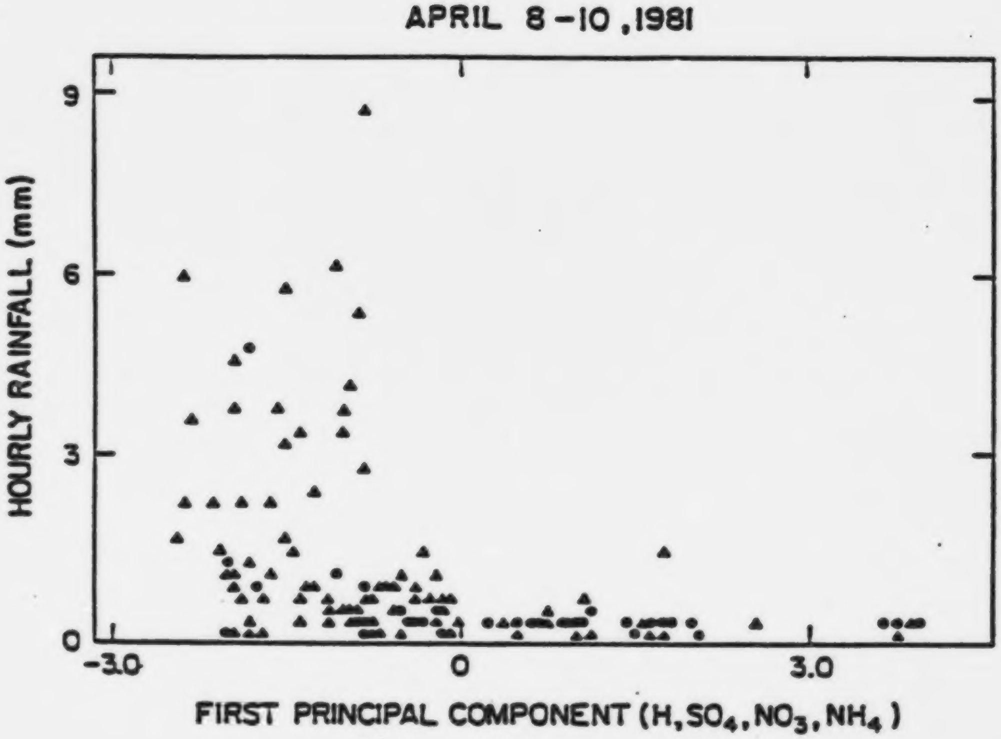

Fig. 4.1d (Same as Fig. 4.1a)

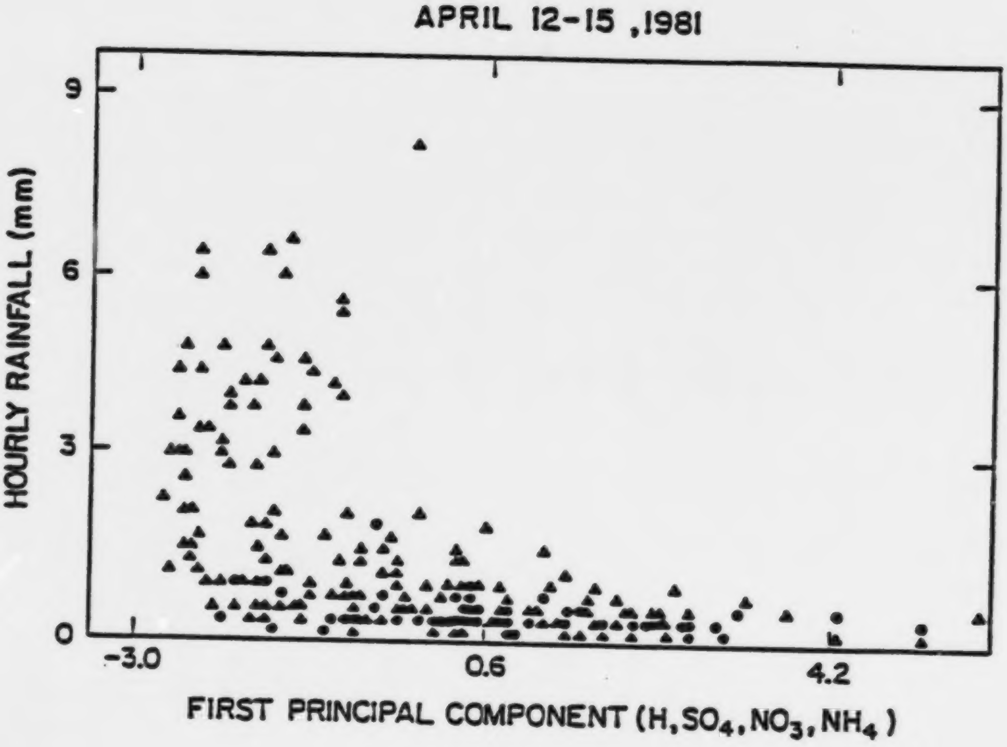

Fig. 4.1e (Same as Fig. 4.1a)

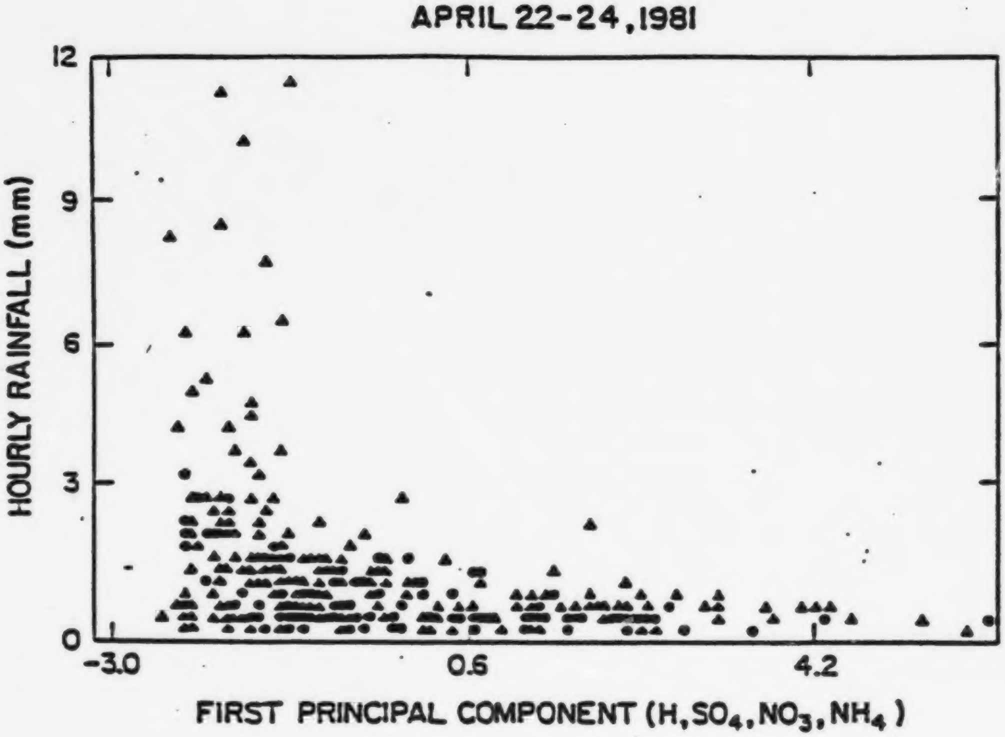

Fig. 4.1f (Same as Fig. 4.1a)

Table 4.1 Comparisons of OSCAR Data Characteristics Using Screened and Unscreened Data*

	Screened			Unscreened		
	Conc	Loc	Time	Conc	Loc	Time
April 8-10						
pH	3.7	E NY	91332 (26)	3.7	E NY	91332 (26)
SO_4	240	E NY	91332 (26)	240	E NY	91332 (26)
NO_3	180	NE Il	9 2 0 (24)	180	NE Il	9 2 0 (24)
NH_4	260	SW Mi	9 0 0 (80)	260	SW Mi	9 0 0 (80)
Na	620	N NY	91138 (21)	620	N NY	91138 (21)
Cl	85	Tn	9 835 (30)	190	S NJ	919 8 (28)
Ca	87	W NY	9 845 (30)	145	C Pa	91438 (6)
Rain	3.3	NE Il	9 224 (1)	3.3	NE Il	9 224 (1)
April 12-15						
pH	3.5	C Pa	14625 (30)	3.5	C Pa	14625 (30)
SO_4	200	C Pa	14625 (30)	200	C Pa	14625 (30)
NO_3	190	C Pa	14625 (30)	190	C Pa	14625 (30)
NH_4	360	SW Mi	14224 (181)	360	SW Mi	14224 (181)
Na	770	LI	141314 (44)	770	LI	141314 (44)
Cl	1080	LI	141314 (44)	1080	LI	141314 (44)
Ca	38	C Pa	14625 (30)	38	C Pa	14625 (30)
Rain	5.8	C Pa	141047 (32)	5.8	C Pa	141047 (32)

Table 4.1 (continued)

	Screened			Unscreened		
	Conc	Loc	Time	Conc	Loc	Time
April 22-24						
pH	3.4	SW Pa	23355 (24)	3.4	SW Pa	23355 (24)
SO_4	190	SW Pa	23355 (24)	190	SW Pa	23355 (24)
NO_3	170	C Pa	23630 (1)	170	C Pa	23630 (1)
NH_4	180	Md	24134 (8)	180	Md	24134 (8)
Na	180	Del	24416 (18)	120	Del	24416 (18)
Cl	120	Del	24416 (18)	120	Del	24416 (18)
Ca	87	W Ont	23 25 (13)	87	W Ont	23218 (13)
Rain	5.3	NC	231010 (16)	5.3	NC	231010 (16)

*Comparisons of maximum concentrations obtained for each OSCAR event using all of the OSCAR data and using only the data screened for anomoulous pH comparisons and ion balances are reported. Concentrations are in units of umoles/liter and rain is in units of mm. Locations follow standard state and direction abbreviations. Times are given in day/hour/minutes with sample duration listed beneath in minutes.

As shown by a comparison of Fig. 4.1 (a-c) with Fig. 4.1 (d-f), there is very little difference in the relationships found using the screened and unscreened data. Comparison of the concentration maxima and their locations and times also show essentially no difference between the screened and unscreened data. As a result of these and related analyses, the unscreened database was used in all of the evaluation studies. Additional probing into the OSCAR database may reveal other problems which need further consideration. At the present time, the data appear to be acceptable for model evaluation studies.

4.2 Meteorological Model Evaluation

4.2.1 Introduction

MM4 is a complex, three-dimensional dynamic model developed to provide high-resolution (in space and time) meteorological data to drive RADM. This model has many optional features (such as planetary boundary layer physics, treatment of clouds and precipitation, analysis and initialization techniques, and horizontal and vertical resolution. We do not know at this time what combination of physics, analysis, resolution, and domain size gives the "best" result. Determination of the "best" model and the sensitivity of the model to these factors is an important goal of the next year's research. A closely related question is how accurate or skillful is the model in predicting or simulating atmospheric flow and precipitation.

The questions of "best" model and accuracy of the various models can be addressed in a variety of ways. Ideally, a complete, high-resolution meteorological data set (horizontal resolution of at least 80 km, vertical resolution 1 km, and temporal resolution of 1 hour) with no errors would be available to verify the model output directly. However, there is little likelihood of obtaining such a data set in the foreseeable future. Therefore, much more limited data sets must be used to estimate the accuracy of the model. For most of the cases to be run, the meteorological data set consists of radiosonde data and surface obervations of pressure, temperature, moisture, and precipitation. The upper-air radiosonde network has an average horizontal spacing of 400 km, root-mean-square (RMS) temperature errors of about 1°C, and RMS horizontal wind errors of about 10%. These errors in the horizontal wind make it practically impossible to estimate the actual vertical motion.

Although mesoscale meteorological models similar to MM4 have shown considerable promise in predicting and simulating three-dimensional atmospheric flows, a systematic, quantitative evaluation of a large number of cases of the type underway at NCAR has not yet been attempted. Such a study is needed to establish the overall accuracy of the model and to avoid false conclusions based on results from a limited number of cases.

We recognize that an ideal validation of the meteorological model from the point of view of how well it performs in the RADM system would be a calculation of the impact on the acid deposition predicted by RADM of errors in the meteorological data. However, not only do perfect meteorological data not exist (so that the true errors in the meteorology are unknown), the chemical data sets for verifying RADM are even more incomplete than the meteorological data. Furthermore, errors in RADM due to imperfect initial chemical data, emissions, and parameterization of the chemistry make it difficult to isolate the impact of errors in the meteorology when using real data. Therefore, simplified approaches must be made to verify the meteorological model and to study the sensitivity of RADM to the meteorological data. NCAR plans to study the problem in two major ways: (1) verifying different versions of the meteorological model against the available meteorological data using a variety of objective measures of accuracy, and (2) testing the sensitivity of RADM to several different meteorological data sets derived from the MM4 system.

The verification of MM4, when done on a large number of cases, will allow definition of a "best" version of the model. It will also provide quantitative estimates of the accuracy of the meteorological data provided to RADM. The sensitivity studies will provide estimates of the uncertainty introduced into RADM acid deposition estimates by uncertainites or errors in the meteorological data. Until more complete meteorological and chemical data sets are available, these results will provide very useful information into the accuracy of the RADM system, as well as provide information concerning the most crucial observations to be obtained in future field programs.

A related study that complements the verification of MM4, supported by non-EPA funds, is the Modeling Intercomparison Project (MIP). In this project, research and operational groups around the world have been invited to run their models on the same cases to be studied as part of ADMP. When verified using the same techniques as applied to RADM, additional information concerning the sensitivity of meteorological models to their components is obtained, as well as more information on the inherent uncertainty in meteorological model simulations.

In the examples to follow, an MM4 simulation of the OSCAR IV case (0000 GMT 22 April to 0000 GMT 25 April 1981) is verified using the objective verification program. The version of MM4 used in this simulation will be designated the "control" version in the series of experiments to be carried out during the next years. It consists of ten layers, a bulk aerodynamic formulation of the planetary boundary layer, and parameterization of convective and nonconvective precipitation and surface fluxes of heat and moisture. The simulation is carried out on a 46x61 80 km grid.

The OSCAR IV case was characterized by rapidly changing weather conditions caused by a developing low pressure system over the upper midwest of the United States. Fig. 4.2 shows the analyses of the 1000 mb geopotential height fields, with the frontal locations marked, for hours 0, 24, 48, and 72. The cold frontal system progressed steadily across the domain and was associated with considerable rainfall.

The forecast 1000 mb geopotential height fields for hours 24, 48, and 72 appear in Fig. 4.3. The initial time is excluded since the differences between it and the observed fields are small, due only to initialization. In general, the forecast is quite good out to 48 hours, with phase, amplitude, and frontal position errors relatively small. As the forecast progresses, the predicted cyclone drifts to the south and west of the observed one, with the predicted values consistently deeper and the circulation more intense than observed.

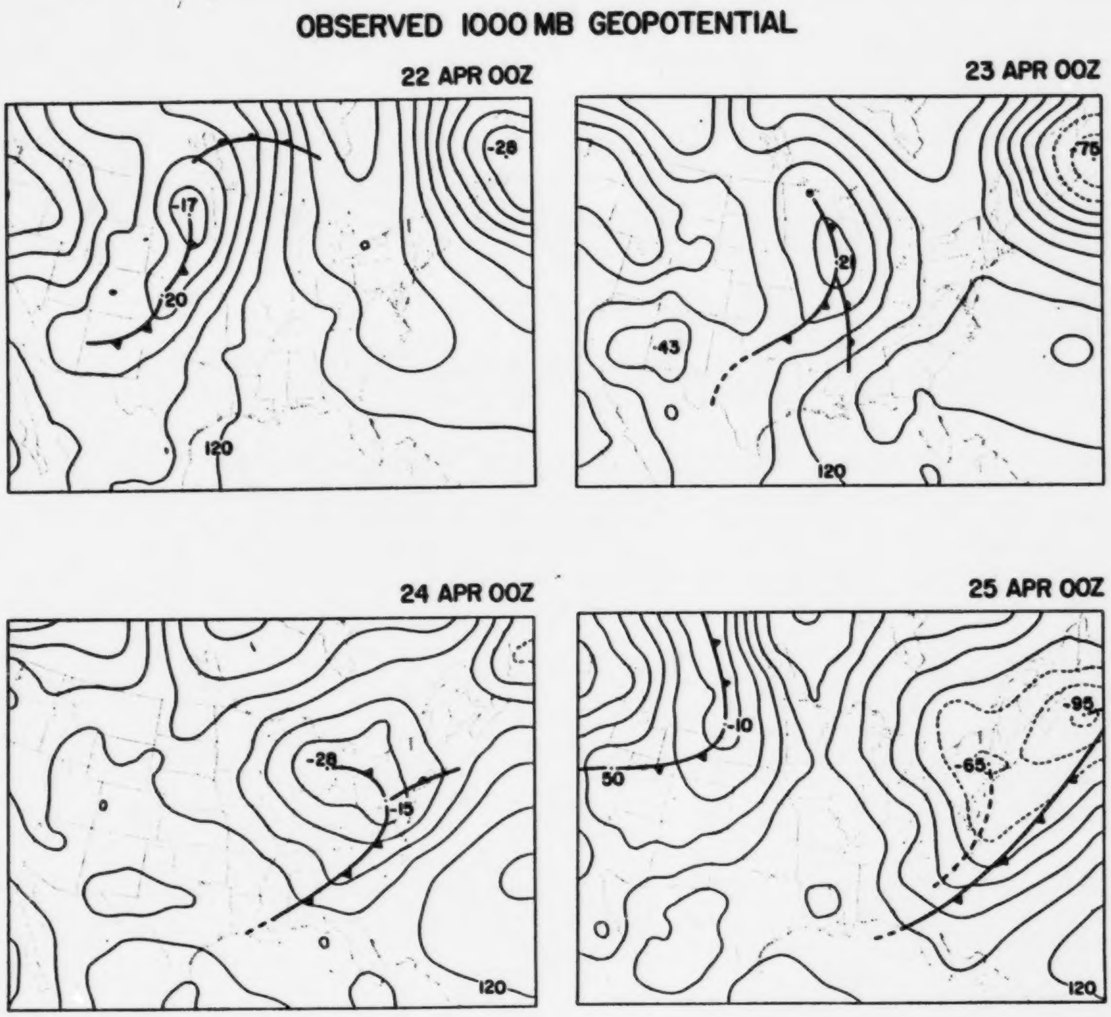
OBSERVED 1000 MB GEOPOTENTIAL
22 APR 00Z
-28
-17
20
0
120
23 APR 00Z
-75
21
-43
0
120
24 APR 00Z
-28
-15
0
0
120
25 APR 00Z
-10
50
-95
-65
0
120

Fig. 4.2 Observed 1000 mb geopotential heights and frontal positions for four time periods during the OSCAR IV period (0000GMT 22 April to 0000GMT 25 April 1981). The contour interval is 30 m.

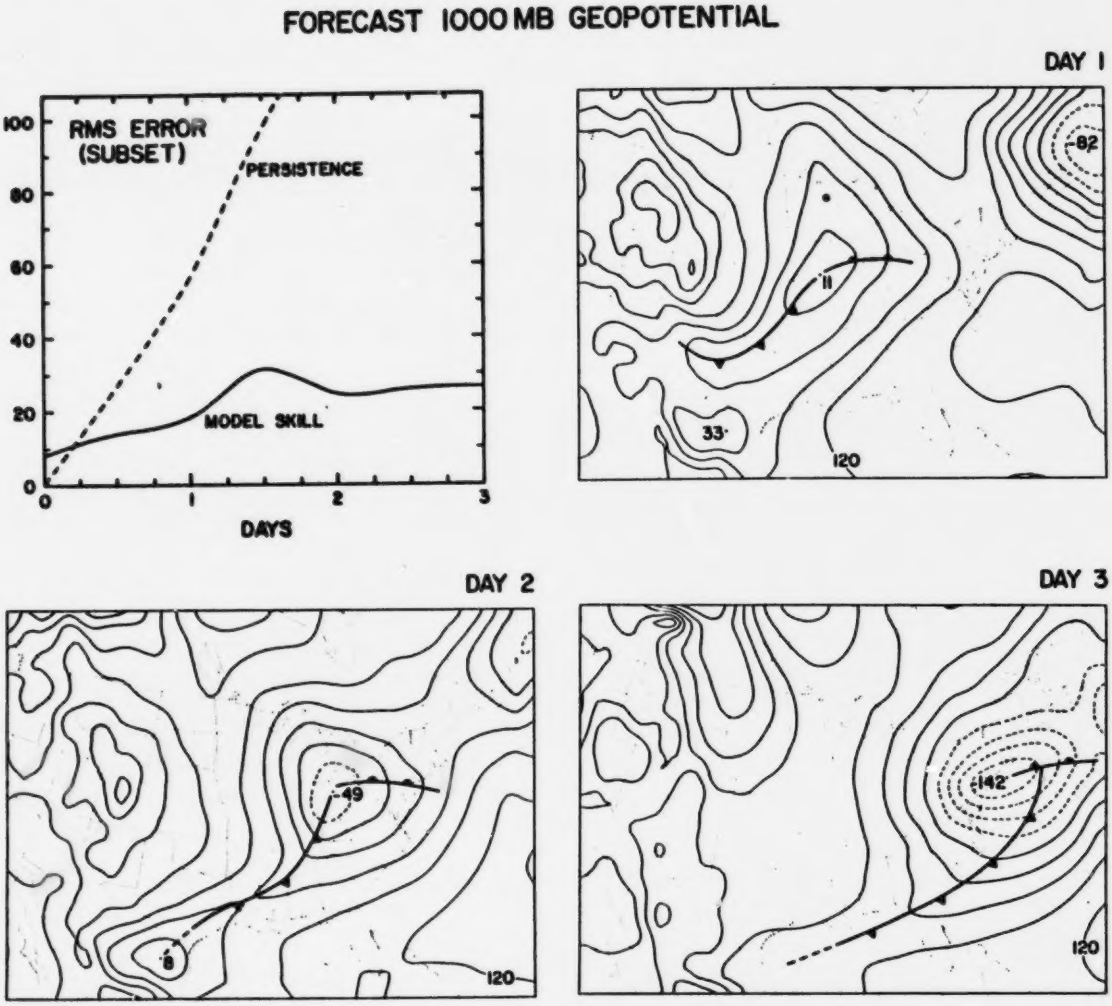
FORECAST 1000 MB GEOPOTENTIAL
RMS ERROR
(SUBSET)
PERSISTENCE
MODEL SKILL
100
80
60
40
20
0
0
1
2
3
DAYS
DAY 1
-82
11
33
120
DAY 2
49
8
120
DAY 3
142
120

Fig. 4.3 Forecast 1000 mb geopotential heights (contour interval 30 m) and frontal positions for 24, 48, and 72 h of the OSCAR IV case. The root mean square error (RMS) of 1000 mb heights for this forecast is shown in the upper left panel.

The RMS error in the 1000 mb height field, evaluated every 12 hours within a subdomain over the eastern United States, is also presented in Fig. 4.3. Compared with the persistence error (a common reference for judging a model's skill), the forecast error grows very slowly in time, again indicating the highly accurate nature of the forecast. Note that the initial error is nonzero. This initial error is a measure of the adjustment produced by initialization and errors produced by vertical coordinate transformations.

4.2.2 Objective Measures of Verification of Meteorological Model

There is no one measure of forecast accuracy or skill that completely characterizes the accuracy of the meteorological data set produced by the model. However, a variety of objective measures of accuracy has been developed by the meteorological community to verify models. Each contributes information about the accuracy of different variables produced by the model. The verification program to be used to evaluate MM4 contains the most complete set of verification measures (or scores) to be systematically computed for a large number of cases studied by a model of this type. This section provides a summary and brief description of the verification methods to be applied to MM4 during the next year. It also provides examples from a preliminary run of one case (OSCAR IV) using the MM4. We emphasize that the scores presented here are only examples and may not be representative of the overall model performance. Additional interpretation of verification methods can be found in Anthes (1983).

Fig. 4.4 shows the portion of the MM4 domain used for computing the verification scores for both the MIP and ADMP studies. This region was chosen to avoid the lateral boundary of the model and much of the data-sparse regions over water and in the western United States. The inner region of Fig. 4.4 shows the portion of the domain used for verifying the precipitation fields.

4.2.3 Root-Mean-Square Errors

A standard measure of accuracy that can be applied to many data sets is the root-mean-square (RMS) error. RMS errors give a good overview of the absolute accuracy of a data set, with a few large errors weighted more than many small errors. RMS errors are computed for temperature, winds, mixing ratio, and sea-level pressure using two methods--comparison against point observations and comparison against analyses derived from the point observations. When compared against observations, the RMS score for a temperature forecast is computed as

$$\mathrm{RMST1} \equiv \left[\frac{1}{N} \sum_{i=1}^{N} (\mathrm{TF}_i - \mathrm{TO}_i)^2\right]^{1/2} , \qquad (4.1)$$

where TF_i is the forecast value of T interpolated to the location of the ith observation of T, TO_i is the observed value of T at this location, and N is the number of observations.

When verified against the analysis, the RMS error in T is computed as

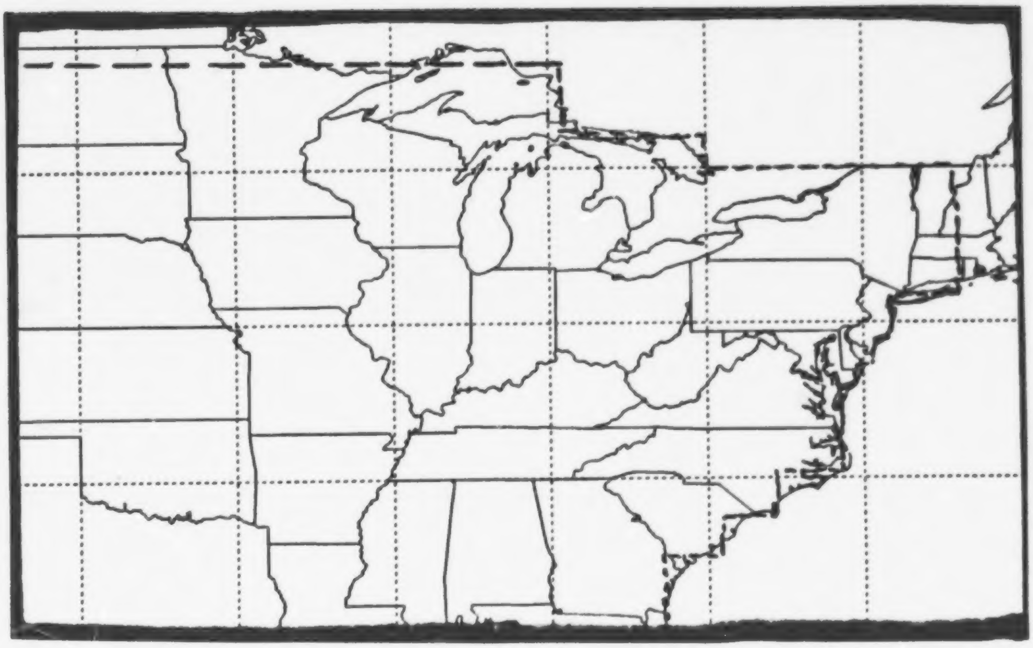

Fig. 4.4 Domain of the MM4 simulations used for computing verification scores and for the ADMP and the model intercomparison project (MIP). The inner portion is used for verifications of the precipitation.

$$\mathrm{RMST1} \equiv \left[\frac{1}{I} \sum_{i=1}^{I} (TF_i - TO_i)^2\right]^{1/2} , \qquad (4.2)$$

where i refers to a grid point in the verification domain, TF_i is the forecast value of T at the grid point, TO_i is the estimate of the observed temperature at that grid point, obtained by analysis of T to the grid, and I is the total number of grid points.

The use of Eq. (4.1) has the advantage that model data are compared directly to observations; there are no analysis errors to contend with. However, there are errors assocated with each observation and with the possibility that the point observation is unrepresentive of the grid average, which is what the model is estimating.

The use of Eq. (4.2) has the advantage that an estimate of the grid average value is used to compare against the model estimate. However, it suffers from the possibility of errors introduced by the analysis technique.

Table 4.2 lists subjective estimates of RMS errors for observations and analysis (denoted E_A). This value represents the observed uncertainty and, therefore, a model cannot be expected to yield errors less than this value. Hence, the values listed may be considered as the minimum value obtainable by any model, or produced by a "perfect" model.

The column listed E_R represents an estimate of the RMS error computed from the difference between two randomly-chosen atmospheric states; E_P approaches E_R as time becomes very large (typically greater than two weeks).

The third column (E_P) gives RMS errors of a forecast based on persistence for a single case (OSCAR IV). Model forecast errors are often compared to persistence errors so that any value less than persistence would be considered to have at least some skill, while a value greater than persistence would indicate a worthless or unskillful forecast.

The column E_F gives a value computed from MM4 at 48 h for the OSCAR IV case. It is considerably less than E_P, indicating the skill of the model for this case.

Finally, the last column S gives an estimate of the skill of the forecast, where S is computed from

$$S \equiv 1 - \frac{\mathrm{Max}\ [(E_F - E_A),\ 0]}{E_R} . \qquad (4.3)$$

According to Eq. (4.3), if the forecast agrees with the analysis within the analysis uncertainty, the forecast is judged to have a skill of 100%. The S score decreases to zero as the forecast error approaches that of two randomly chosen states. The data shown in Table 4.2 indicate that the model shows considerable skill when RMS errors are computed. It must be emphasized, however,

Table 4.2 Estimate of RMS errors.

			OSCAR IV Case - 48 h		
	E_A	E_R	E_P	E_F	S
Temperature (°C) at 850 mb	1.5	16.0	8.0	3.0	0.91
Wind (magnitude of vector wind error, m/s) at 850 mb	3.0	32.0	16.0	9.0	0.81
Specific humidity (g/kg)	2.0	10.0	5.0	3.0	0.90
Sea-level pressure (mb)	1.0	24.0	12.0	3.0	0.92

that this is a single case and the average numbers over many cases could be significantly different.

In the production runs, RMS scores as listed in Table 4.2 will be computed for the 700-, 500-, and 300-mb levels, in addition to the 850-mb level.

4.2.4 Correlation Coefficient Between Observed and Forecast Change

At times, such as when extreme atmospheric events occur, the RMS error of a forecast may appear to be large and yet the forecast may still have value. For example, in a case of explosive cyclogenesis in which the minimum pressure decreases by 50 mb in 24 h, a model which predicts only a 40-mb deepening would show a relatively large error of 10 mb compared to average forecasts, but would clearly have value. The correlation coefficient between observed and forecast changes of a variable is useful in quantifying how well a model predicts changes of a variable from the initial conditions. This measure of skill is easy to interpret--a value of 1.0 indicates a perfect forecast, while a value of 0.0 or less indicates a worthless forecast.

Table 4.3 shows the correlation of observed and forecast change of several variables, computed using forecast values interpolated to observation points. The MM4 for this one case shows considerable skill in forecasting the changes of temperature, mixing ratio, 850-mb height, and sea-level pressure.

4.2.5 S_1 Scores

For some meteorological fields such as pressure or height of the geopotential field, the horizontal gradient is more important than the absolute value. The S_1 score (Anthes, 1983) is a common measure for quantifying the skill of a forecast of sea-level pressure gradient and the gradient of the geopotential height of upper-level constant-pressure surfaces.

Table 4.4 gives examples of S_1 scores for 48-h forecasts of sea-level pressure and 500-mb height. The values listed as "perfect" and "worthless" are based on the experience of many operational forecasters. As shown in Table 4.4, MM4 for this one case shows considerable skill compared to persistence.

4.2.6 Precipitation Verification

Precipitation is an extremely important predicted field in meteorological models. Because observed and model-predicted precipitation is the result of many complex processes and because it often contains very small-scale variations, it is considerably more difficult to forecast than temperature, wind, pressure, and moisture.

We are using a variety of methods to quantify the accuracy of the precipitation forecasts of MM4, including the so-called threat scores, bias score, and categorical forecasts of the occurrence or nonoccurrence of a specified precipitation threshold amount at a given grid point during a specified time period. These scores are discussed in detail in Anthes (1983).

Table 4.3 Correlation coefficients between observed and forecast change of a variable.

	MM4 48 h forecast (OSCAR IV case)
Temperature at 850 mb	0.91
Mixing ratio at 850 mb	0.82
Height of 850 mb surface	0.91
Sea–level pressure	0.91

Table 4.4 S_1 scores.

	"Perfect"	"Worthless"	OSCAR IV Case - 48 h	
			Persistence	MM4
Sea-level pressure	30	80	110	60
500-mb height	30	80	80	38

Fig. 4.5 shows the observed precipitation over the 24-h period ending 0000 GMT 23 April 1981 (OSCAR IV case). Fig. 4.6 shows the MM4 forecast for the same time period. Table 4.5 lists the categorical forecasts, the threat score, and the bias score for precipitation thresholds of 0.025 cm (0.01 inch), 0.254 cm (0.10 inch), 0.635 cm (0.25 inch), 1.27 cm (0.5 inch), and 2.54 cm (1.0 inch). Great caution should be exercised in interpreting the results from this single case, especially for the larger precipitation thresholds which occur over very few model grid points. However, some conclusions that probably have some general validity may be made. The categorical forecasts (yes or no of a grid point receiving a threshold amount of precipitation) indicate that more grid points are correctly forecast (yes or no) at the larger amounts. This is because the correct forecasts of the larger amounts are dominated by "no" forecasts, which are relatively easy to make. However, the threat score, which is a measure of the accuracy of the predicted area receiving a threshold amount, shows just the opposite. As the area diminishes in size (increasing precipitation threshold), it becomes more difficult to forecast.

The bias score indicates whether the model tends to overpredict threshold amounts (bias score greater than 1.0) or underpredict threshold amounts (bias score less than 1.0). The bias scores in Table 4.5 are probably meaningless for the single case presented here. However, this score will be very important when averaged over a larger number of cases, because it will indicate the presence of systematic model errors.

For some purposes, such as estimating annual averages or testing various strategies for control, the details of an individual forecast are not important. It is more important for the model to simulate realistically the structure of the atmosphere. For example, the regional model might forecast the correct intensity and shape of a field, but displace the field by some small distance in space and hence yield large errors at points. A correlation matrix scoring method (Anthes, 1983) is a measure of skill in predicting the intensity and patterns of a field. Fig. 4.7 shows the correlation matrix for the 24-h forecast shown in Fig. 4.6. When the observed precipitation grid (Fig. 4.5) is centered over the forecast grid (Fig. 4.6), a correlation coefficient of 0.65 is obtained as shown by the center value in Fig. 4.7. However, when the observed precipitation field is shifted five grid points (400 km) to the east, a higher correlation of 0.74 is obtained, indicating that the model is predicting a precipitation pattern/intensity with an accuracy of 0.74, but with a displacement error toward the east. A perfect forecast by this method would show a correlation coefficient of 1.0 at the center of the matrix.

4.2.7. Structure (Climatology) of Model Forecasts

As is well known, a general circulation model has no predictive skill (of episodes or events) when integrated beyond about two weeks. However, such models are extremely useful in answering questions like how will the climate change if carbon dioxide is doubled. Similarly, ADMP may have considerable use for evaluating the effects of various emissions reductions, in spite of large errors at points in individual simulations, if the model has the right "climatology." By climatology, we mean that the model, when run over many

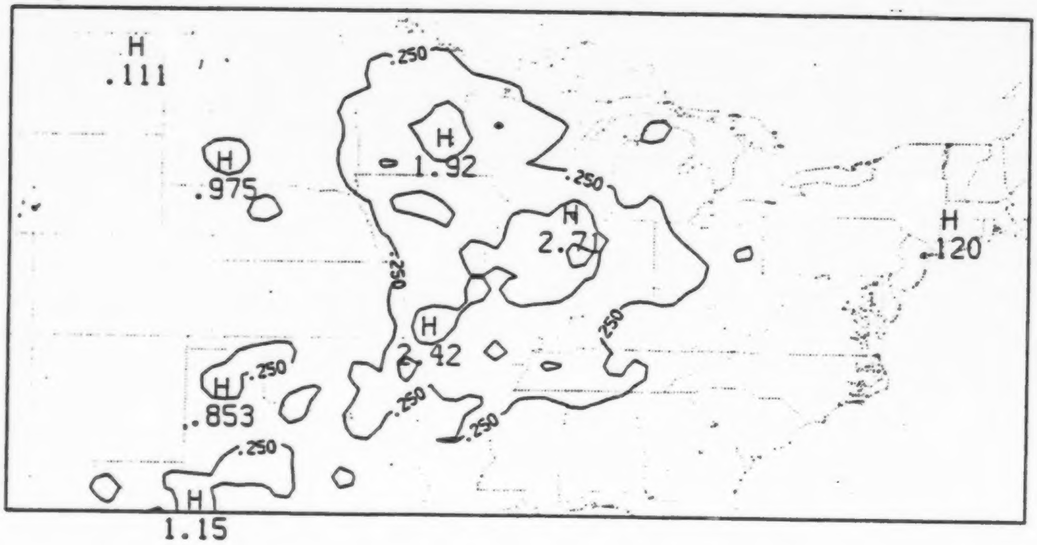
H
.111
H
.975
.250
H
1.92
.250
H
2.71
.250
H
2.42
.250
H
.853
.250
.250
.250
H
1.15
.250
H
120

Fig. 4.5 Observed precipitation for 24-h period ending at 0000GMT 23 April 1981. The contours are 0.25, 1.0, and 2.0 cms.

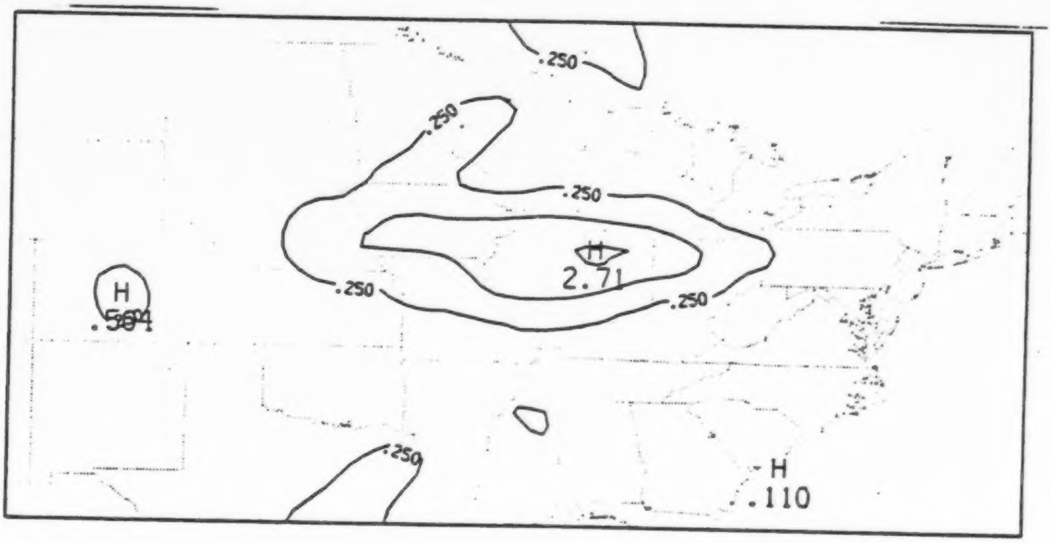
.250
.250
.250
.250
.250
.250
H
2.71
H
.584
H
.110

Fig. 4.6 Forecast precipitation for 24-h period ending at 0000GMT 23 April 1981. The contours are 0.25, 1.0, and 2.0 cms.

Table 4.5 Verification of MM4 prediction of precipitation for 24–h period ending 0000 GMT 23 April 1981.

Precipitation Threshold	Categorical Forecast (% Correct)	Threat Score	Bias Score
0.025 cm	70.0	0.58	1.0
0.254 cm	78.0	0.34	0.75
0.635 cm	88.0	0.34	0.65
1.27 cm	96.0	0.29	1.3
2.54 cm	99.0	0.0	2.5

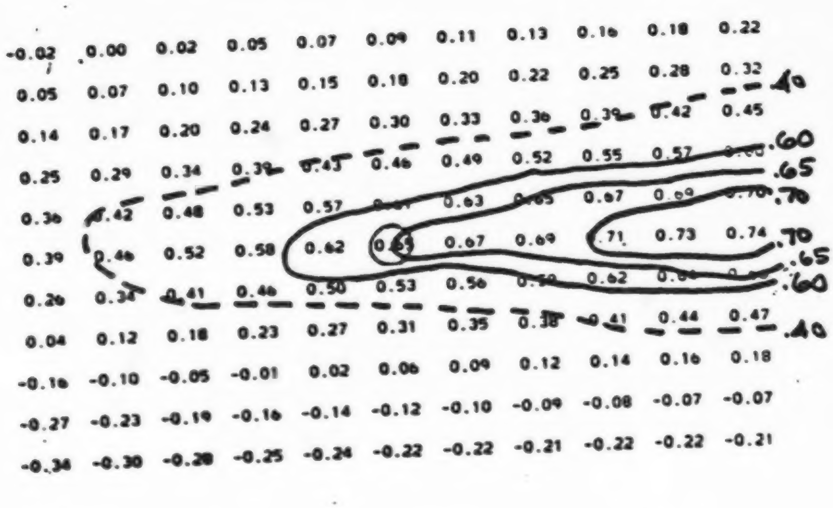

-0.02	0.00	0.02	0.05	0.07	0.09	0.11	0.13	0.16	0.18	0.22
0.05	0.07	0.10	0.13	0.15	0.18	0.20	0.22	0.25	0.28	0.32
0.14	0.17	0.20	0.24	0.27	0.30	0.33	0.36	0.39	0.42	0.45
0.25	0.29	0.34	0.39	0.43	0.46	0.49	0.52	0.55	0.57	[illegible]
0.36	0.42	0.48	0.53	0.57	[illegible]	0.63	0.65	0.67	0.69	0.70
0.39	0.46	0.52	0.58	0.62	0.65	0.67	0.69	0.71	0.73	0.74
0.26	0.34	0.41	0.46	0.50	0.53	0.56	[illegible]	0.62	[illegible]	[illegible]
0.04	0.12	0.18	0.23	0.27	0.31	0.35	0.38	0.41	0.44	0.47
-0.16	-0.10	-0.05	-0.01	0.02	0.06	0.09	0.12	0.14	0.16	0.18
-0.27	-0.23	-0.19	-0.16	-0.14	-0.12	-0.10	-0.09	-0.08	-0.07	-0.07
-0.34	-0.30	-0.28	-0.25	-0.24	-0.22	-0.22	-0.21	-0.22	-0.22	-0.21

Fig. 4.7 Correlation matrix of observed and forecast precipitation fields. Each value in the matrix represents a correlation between observed and forecast precipitation amounts on a subset of the forecast domain for various north-south and east-west lags. The value of 0.65 at the center of the matrix represents no lag. The value of 0.74 in the right column represents the correlation computed when the observed grid is shifted 5 points to the east with respect to the forecast grid.

cases, has no biases and has the correct statistical properties (such as frequencies of extreme events).

A measure of the realism of the model-simulated fields is the normalized correlation function defined by

$$\mu(r_1,r_2) = m(\mathbf{r}_1,\mathbf{r}_2)\,[m(\mathbf{r}_1,\mathbf{r}_1)\; m(\mathbf{r}_2,\mathbf{r}_2)]^{-1/2} \quad , \qquad (4.4)$$

where $\mathbf{r}_1$ and $\mathbf{r}_2$ are position vectors, $m(\mathbf{r}_1, \mathbf{r}_1)$ and $m(\mathbf{r}_2, \mathbf{r}_2)$ are the autocorrelation functions (station variances) and $m(\mathbf{r}_1, \mathbf{r}_2)$ is the cross-correlation function (covariance). For perfect data, $\mu(r_1,r_2)$ varies from 1.0 at zero separation ($r_1=r_2$) to 0 at infinite separation. This function compares the correlation of an anomaly field (departure from the mean) as a function of distance. For fields showing only large-scale features, μ decreases slowly with increasing distance; for fields showing considerable small-scale variation, μ decreases more rapidly. For example, Fig. 4.8 shows the forecast and observed structure of the 500-mb temperature field for the OSCAR IV case over a series of increasingly longer separation distances. Both fields show a decreased correlation with increasing distance. During the 72-h period of this single study, the MM4 (F) is more highly correlated than the observed (O) in the shortest separation distances, is about the same as the observed in the 1000- to 2000-km separation range, and is less correlated for the longer separation distances.

Another way of quantitatively examining the structure of a forecast is to compute the two-dimensional spectra of a field (Errico, 1985). This two-dimensional Fourier decomposition can also be used to measure the errors at various scales of motion. An example of the spectra of the 36-h 500-mb forecast (solid) and observed (long dashed) is shown in Fig. 4.9. The horizontal scale varies logarithmically from 4800 km on the left to 350 km on the right. The MM4 has spectra very similar to the observed although the difference spectra are as large in magnitude at scales of 500 km in length and less. It should be noted that the observed spectra at scales below about 800 km are poorly estimated in this case because of the 400-km spacing of the upper-air observations.

4.2.8 Summary

A number of quantitative measures of the accuracy of the mesoscale meteorological model have been developed. These measures will be used to compare the accuracy of different versions of the model and to provide quantitative estimates of the error in the meteorological data supplied to RADM. Interpretation of the verification scores and methods and examples from one case have been provided. Work in progress will compute these scores for additional cases to increase the reliability of the error estimates.

4.3 Statistical Comparisons of RADM with OSCAR Data

The correlations between OSCAR and RADM precipitation variables over various time scales were used as initial indicators of the performance of RADM. Correlations were chosen since these are good descriptors of the similarity of two variable patterns over the spatial and/or temporal domains of

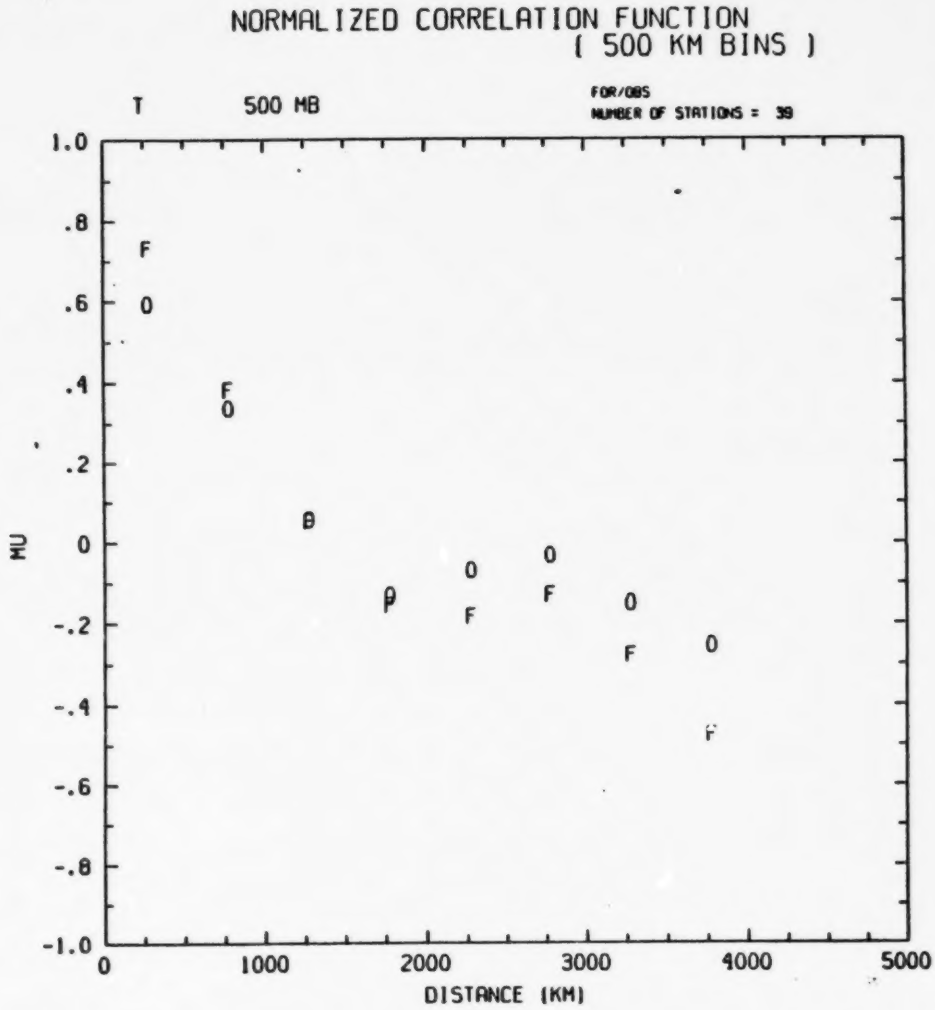

Fig. 4.8 Normalized correlation function for observed and forecast (72 h) 500 mb temperatures as a function of distance. Each point represents the correlation of all points in 500-km bins.

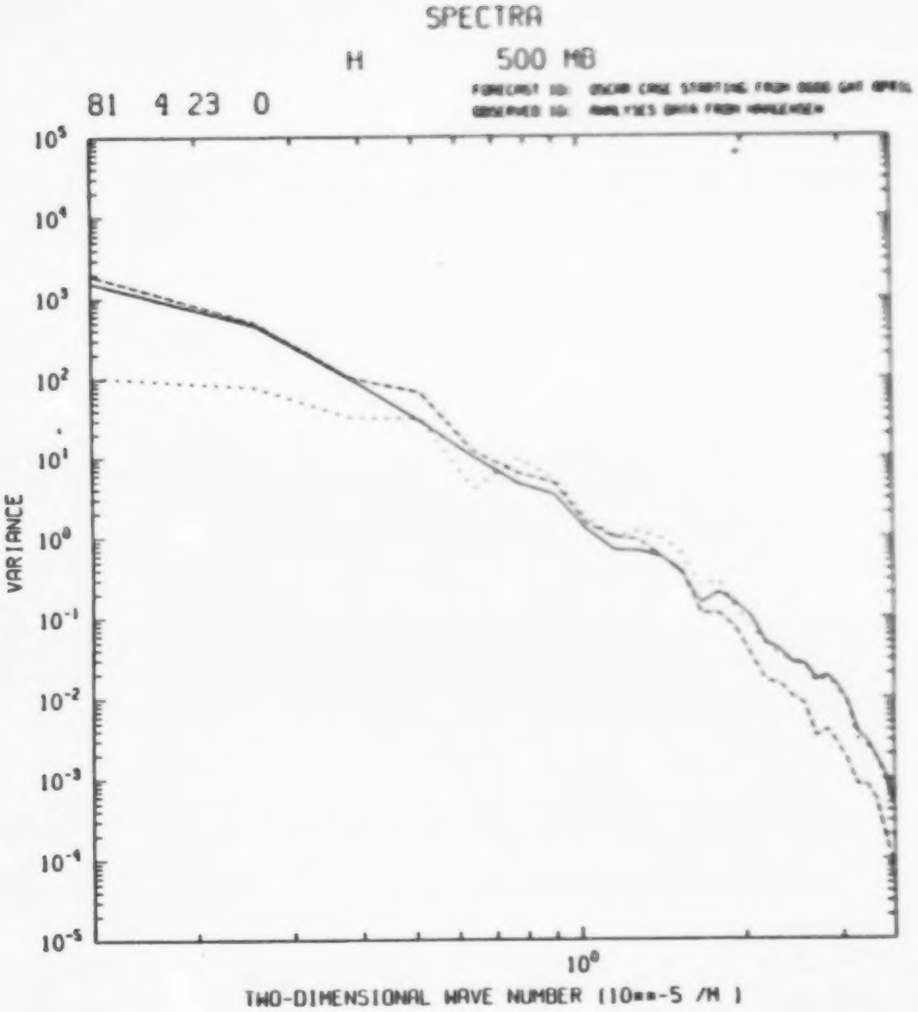

Fig. 4.9 Two-dimensional spectra (variance vs. wave number) of 500 mb heights at 36 h of the OSCAR IV case. The horizontal scale varies from 4800 km on the left to 350 km on the right. The solid line represents the forecast, the long dashed line the observed, and the dotten line the difference.

interest. The goal of these analyses was to compare the regional variability of the model and the observations for all of the major precipitation variables on an hourly and an event total basis. Additional statistical comparisons are being conducted but are not included in this report.

In these studies, hourly and total event depositions and chemical concentrations in rain were compared for OSCAR stations and corresponding RADM grids. The OSCAR station locations and the RADM grid array are depicted in Fig. 4.10.

In order to directly compare the OSCAR and RADM data, the OSCAR data were converted into an hourly average format. The original OSCAR precipitation data were collected on a constant volume basis, resulting in a wide variety of sample periods. Precipitation weighted hourly average concentrations were obtained for each of the precipitation variables. Each sample contribution to an averaging period was multiplied by the rainfall volume associated with that contribution. The total was divided by the entire rainfall volume associated with the averaging period. If the collection time for a sample extended over two or more different averaging periods, it was assumed that the amount collected during each period was proportional to the collection time which overlapped each period. Hourly depositions were calculated by multiplying the volume-weighted hourly concentrations by the total hourly rainfall. Any hourly concentration or deposition variable which had a missing contribution (data should have been present, but there was an error reported in the basic OSCAR data set) was flagged so that missing data could be properly treated in the analysis.

The RADM hourly depositions were directly calculated by the model. The concentrations were calculated by dividing the RADM depositions by the hourly rainfall.

The hourly RADM and OSCAR databases were merged for the statistical analyses as follows. Only OSCAR hourly data which were not flagged as having missing data associated with the hour were used in the comparisons with RADM. In addition, comparisons were made only for times and locations and chemicals where both databases had non-zero values.

The event totals are sums over the hourly concentrations and depositions. If a station had an hourly value for a particular concentration or deposition which was flagged for missing data, then that concentration or deposition variable for that station was omitted from the analysis. There were a possible total of 36 stations. The smallest number of stations used in any of these analyses as a result of this data screening process was 24 stations.

The results of the correlation analysis are presented in Table 4.6. The hourly correlation results represent the correlations for each chemical pair (e.g., OSCAR SO_4 versus RADM SO_4 concentrations correlations are listed under SO_4) for all of the hours for all of the locations. The event correlations represent the correlations between each event sum for each pair of chemicals (e.g., OSCAR SO_4 summed over all hours for each station versus RADM summed over all hours for each corresponding grid). Results obtained for OSCAR IV

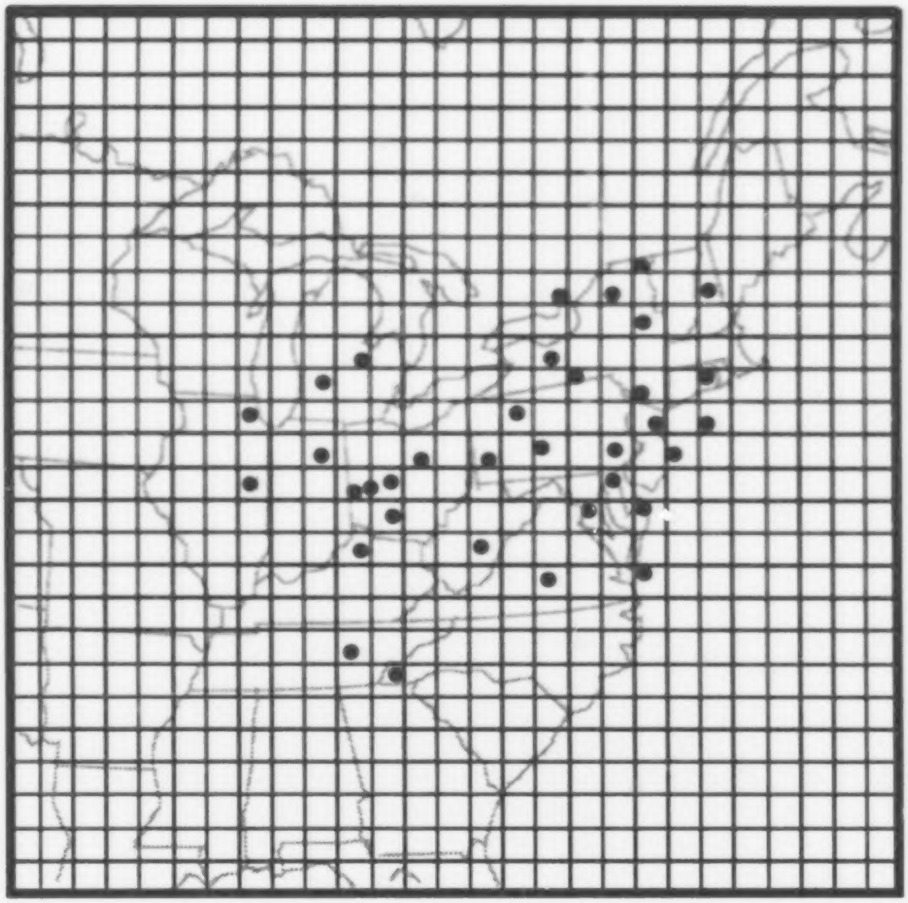

Fig. 4.10 RADM grid with OSCAR station locations noted with ● .

TABLE 4.6 CORRELATION COEFFICIENTS FOR RADM AND OSCAR COMPARISONS*

	H	SO4	NO3	NH4	DSO4	DNO3	DH	DNH4
EVENT								
OSCAR IV								
ND	.89	.86	.85	.40	.51	.47	.75	–
NA	.88	.85	.85	.39	.50	.45	.75	–
ED	.88	.85	.85	.47	.50	.48	.76	–
OSCAR I								
ND	–	.53	.50	.53	–	–	–	–
HOURLY								
OSCAR IV								
ND	.31	.26	.24	–	.12	–	.13	–
NA	.30	.25	.24	–	.12	–	.13	–
ED	.33	.26	.24	–	.12	–	.15	–
OSCAR I								
ND	–	–	–	–	–	–	–	–

*Codes. ND=NAPAP diurnal, NA+NAPAP average, ED=EPRI diurnal. Code distinguishes the emissions inventory used in the calculations. SO4, NO3, NH4, and H refer to the chemical concentrations of sulfate, nitrate, ammonium and hydrogen ions in rain, respectively. DSO4, DNO3, DNH4, and DH refer to the deposition of sulfate, nitrate, ammonium and hyudrogen, respectively. Event refers to total event accumulated concentrations and depositions. Hourly refers to hourly average concentrations. Only statistics which are significant at the .05 or better level are included.

using three different emissions inventories (Section 6.3) are shown to illustrate the sensitivity of the comparisons to variations in emissions, a major driving factor for the RADM experiments. This selection of correlations gives an overall regional description of the variability among chemicals. Correlations on a subevent basis and on a station-by-station basis also are being studied in order to elucidate the variability on a subregional basis.

Selected results from the correlation analysis are presented in Fig. 4.11 (a-f). These scatter plots illustrate hourly and event total sulfate and event total sulfate deposition for the OSCAR IV and the OSCAR I episodes for the RADM experiments carried out using the NAPAP diurnal emissions inventory (Section 6.3). The plots depict the relative amounts of similarity between variables for the different cases. The graphs also indicate the differences in magnitudes between observed and predicted values.

In all cases, the correlations are much higher for the total event comparisons than for the hourly comparisons. In addition, the chemical concentrations in rain are much more highly correlated than the deposition variables which strongly depend on the model predicted rain. The correlations for NH_4 concentration and depositions are consistently lower than those for SO_4, NO_3, and H. Although the general conclusions are similar for both OSCAR cases, the correlations are much higher for the OSCAR IV case than for the OSCAR I case.

These preliminary results suggest that RADM describes the overall variability of the chemical concentrations and depositions with much greater accuracy than the hour-by-hour variability. In addition, RADM predicts the variability of the chemical concentrations in rain more accurately than the variability in the depositions. Additional study is underway to explain these findings in terms of key areas for model improvement. The applicability of other statistical measures is also under study.

4.4 Three-dimensional Distributions of Chemical Trace Species

Initiation of a full three-dimensional model with detailed chemistry requires careful synthesis of several independent sets of very limited data. The data need of RADM far exceeds all the available data. Furthermore, it is very unlikely that sufficient data can be gathered in the future to allow direct initiation from observations. Extensive model aided diagnostics and estimations must be used to establish initial conditions for models such as RADM. At this time, it is common practice to run the model for a few days starting with some, not necessarily very accurate, initial guesses. Because of the strong chemical coupling and short atmospheric chemical lifetime for most of the important chemical species, the full chemical system quickly reaches a state of equilibrium consistent with the local conditions. Therefore, the influence of the initial estimates on the subsequent simulations are minimized. Of course, due to the large variability of local chemical sources (Section 6.3), this assertion of local equilibrium needs to be tested on a case-by-case basis. For some of the longer lived chemical species, we must use critical judgment in estimating their boundary and initial conditions, e.g., O_3, HNO_3, and SO_2. Our current experience indicates that, for a given case, several RADM calculations with differing initial and boundary conditions

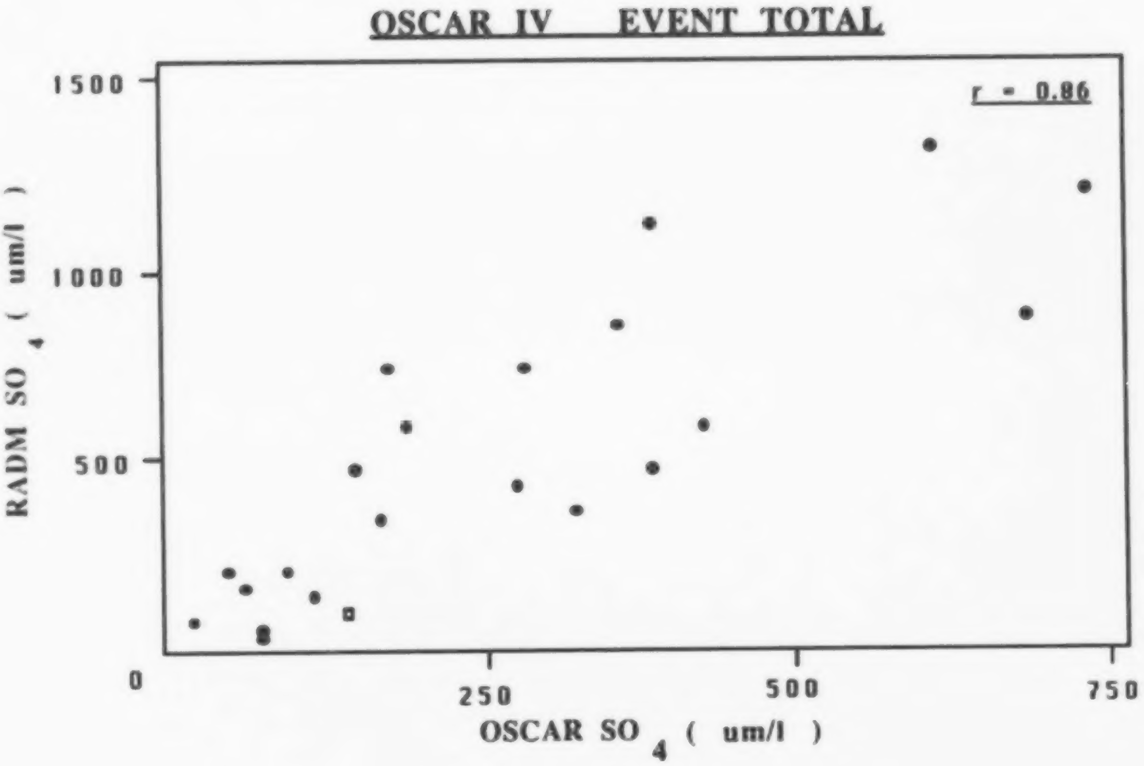

Fig. 4.11a Scatter diagrams of RADM and OSCAR total event accumulated sulfate in rain. Correlation coefficient r is noted.

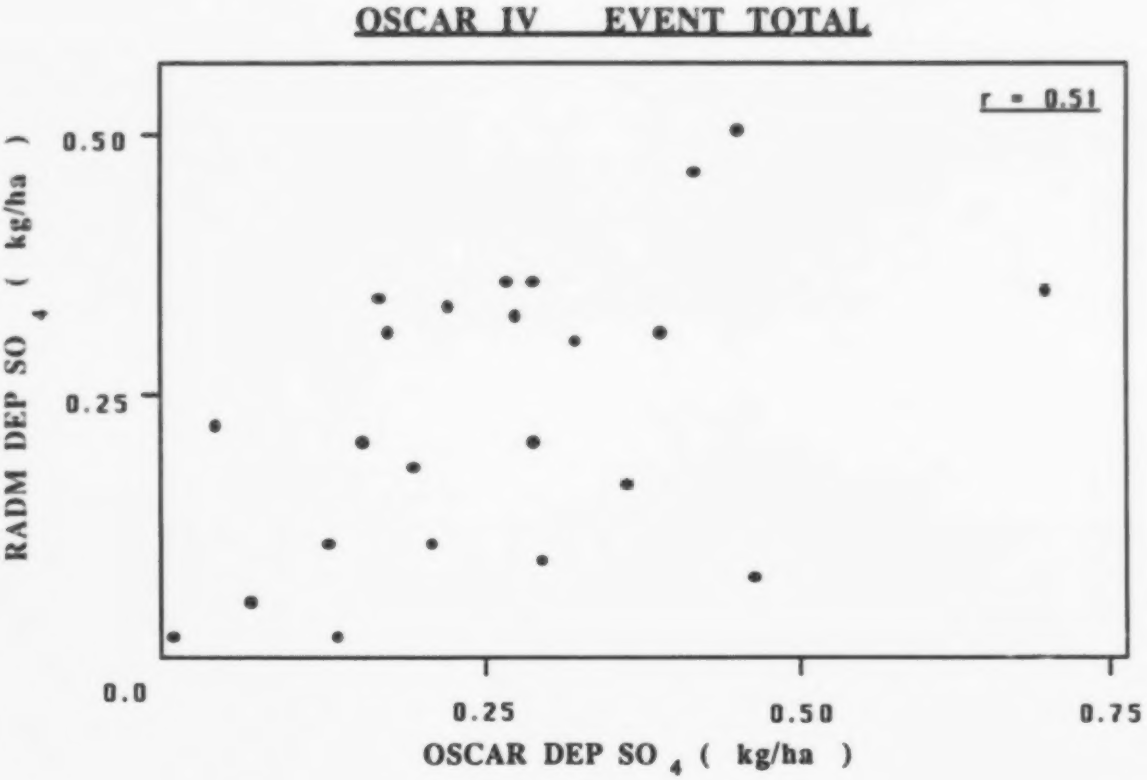

Fig. 4.11b Scatter diagrams of RADM and OSCAR total event accumulated sulfate deposition. Correlation coefficient r is noted.

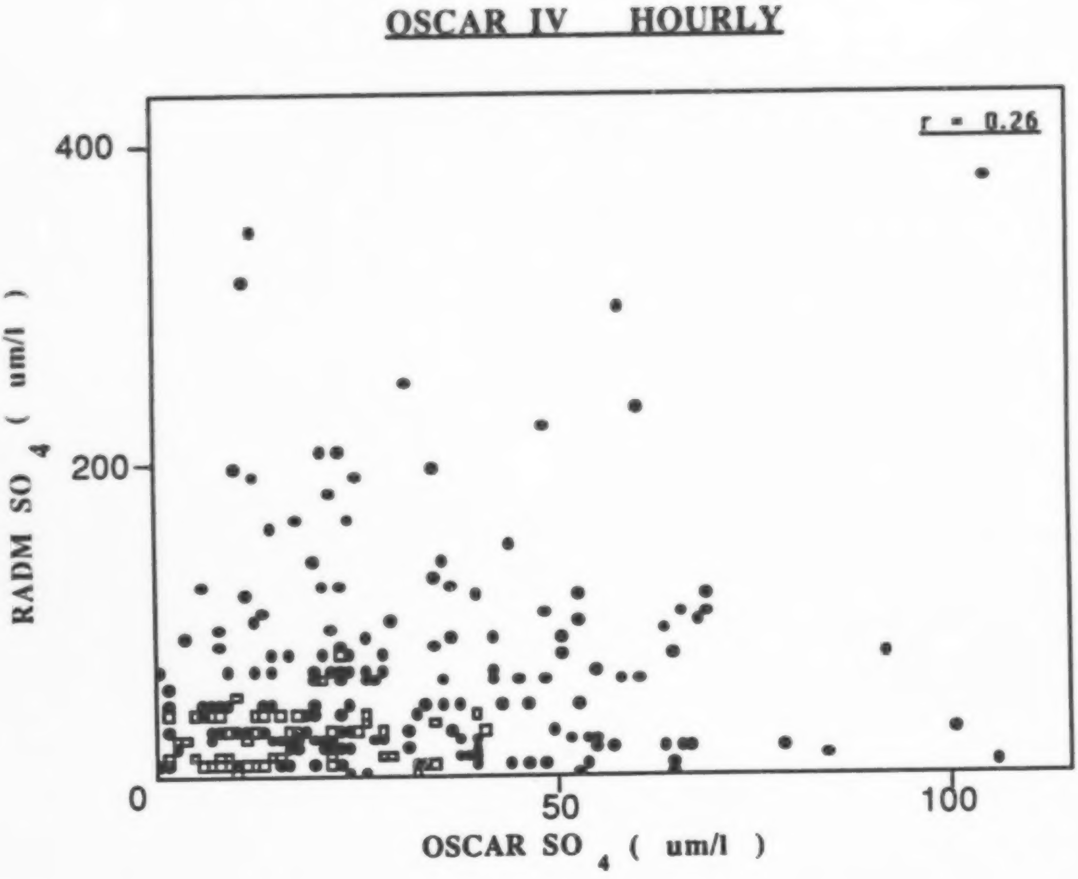

Fig. 4.11c Scatter diagrams of RADM and OSCAR hourly average sulfate rain. Correlation coefficient r is noted. Multiple data points are indicated by □.

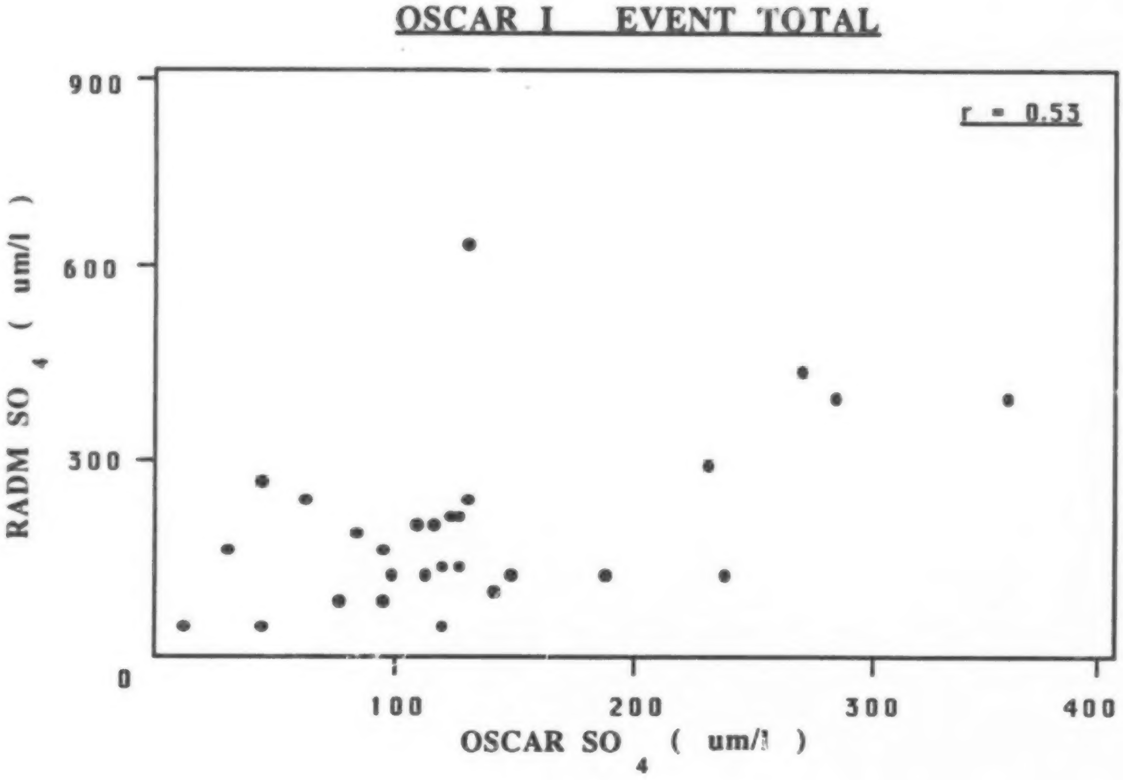

Fig. 4.11d Scatter diagrams of RADM and OSCAR total event accumulated sulfate in rain. Correlation coefficient r is noted.

OSCAR I EVENT TOTAL

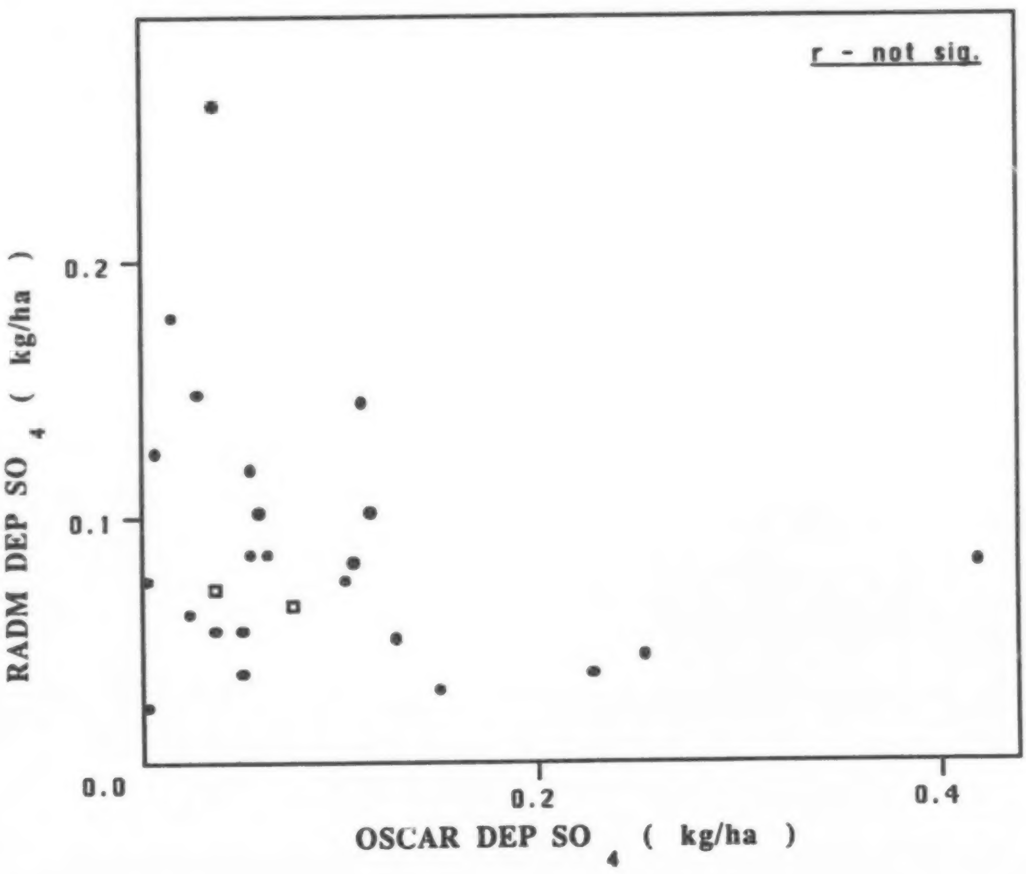

Fig. 4.11e Scatter diagrams of RADM and OSCAR total event accumulated sulfate deposition. Correlation coefficient r is noted.

OSCAR I HOURLY

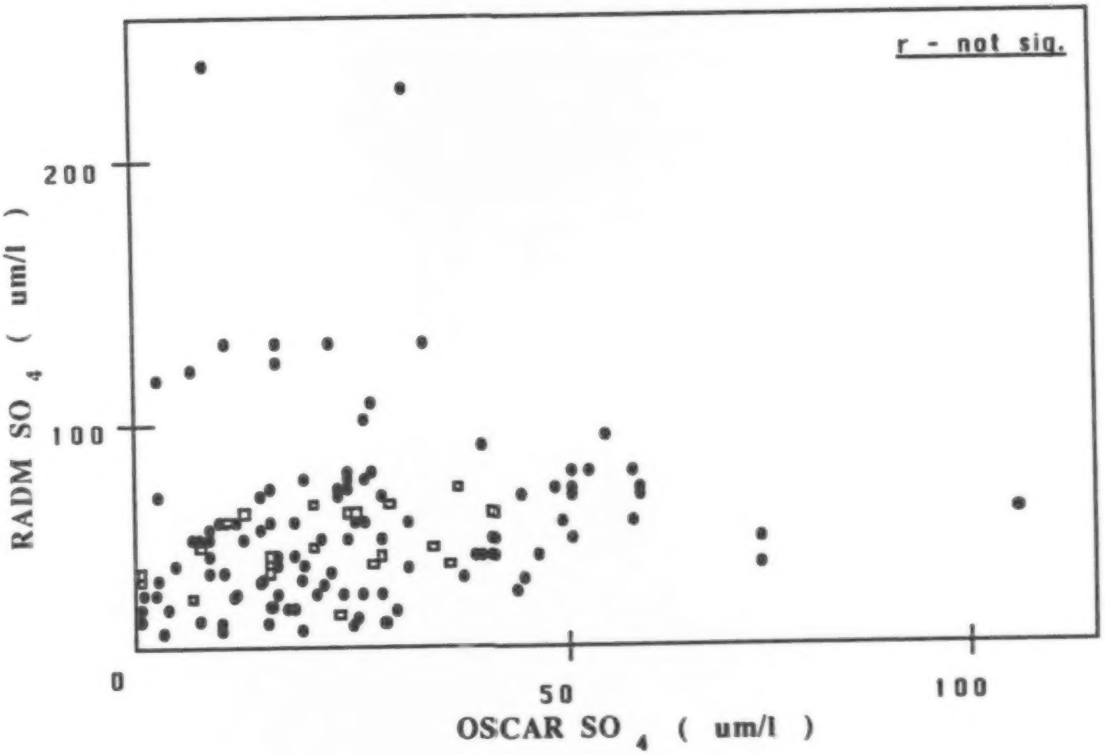

Fig. 4.11f Scatter diagrams of RADM and OSCAR hourly average sulfate in rain. Correlation coefficient r is noted. Multiple data points are indicated by □ .

must be carried out in order to understand their influences on the simulation; hence to choose the appropriate conditions.

The vertical profiles of the 24 prognostic species in RADM are initially horizontally homogeneous and are shown in Table 4.7. These values were determined based on an extensive literature survey and represent relatively clean continental conditions. Then the model simulates one or two days with the first day's meteorology except without wet scavenging. This then produces the horizontally and vertically carrying initial conditions used in model simulations. On the boundary, the concentrations of the following list of species are held constant: SO_2, SO_4, HNO_3, organic acid, PAN, NH_3, CO, ethane, and a lumped hydrocarbon HC. Primarily because they have large diurnal oscillations, the other fifteen prognostic species are allowed to evolve freely on the boundary. Some of the species that are not fixed on the boundaries can drain away and approach very small values. Thus, the boundary conditions are fairly clean and this procedure produces the most realistic results when the lateral boundaries are fairly remote from any polluted region. On the other hand, certain species are free to build up on the boundaries. Hydrogen peroxide particularly has built up on the boundaries to values of the order of 6 ppb along the southern edge of the domain. It is unclear whether this is realistic or not, but it does not seem to cause any great problems.

The most important characteristic of the current boundary conditions is that the inflow of sulfur is exactly specified and that of nitrogen is approximately specified. Ideally, we would prefer to fix as many of the species as possible on the boundaries. If we discover that other species can be fixed on the boundaries without adversely affecting model performance, we intend to do so.

Present choices of boundary conditions correspond to a cleaner atmosphere with many fixed concentrations on the boundary. There is no intrinsic reason why we cannot run the model with dirty boundary conditions, but in the absence of detailed data on the 24 prognostic species for the 700 boundary grid cells, we have decided we prefer to have the concentrations in the model domain dominated by the emissions and chemical reactions in the domain rather than by the flux of pollutants horizontally off the side walls. In the future, the proper way to determine the concentrations on the boundaries of the transport model subdomain will be to run the out-of-core model for the large mesoscale model domain, which has lateral boundaries well away from any polluted region. This forecasts the conditions where the lateral walls would be for the smaller in-core model.

With these initital and boundary conditions and the corresponding three day meteorological variables such as precipitation amounts, 3-D wind velocities, and temperatures, RADM then predicts the time-dependent 3-D distributions of chemical species, wet and dry depositions of sulfate, nitrate, ammonia, and others over the geographic domain as shown in Figs. 4.12-4.19. There is very limited data available for comparison with the detailed chemical species distributions predicted by RADM for the OSCAR cases. Figs. 4.12-4.17, taken from the OSCAR IV simulation, illustrate the essential features of the three-dimensional distributions predicted by RADM at local noon on the first day. On the same figures we have plotted a set of data measured by NCAR in

TABLE 4.7 INITIAL AND BOUNDARY CONCENTRATIONS (ppb)

	Layers					
SPECIES	1	2	3	4	5	6
SO_2	1.0	0.6	0.2	0.1	0.1	0.1
SO_4	0.5	0.3	0.1	0.05	0.05	0.05
NO_2	0.015	0.0225	0.03	0.0525	0.075	0.15
NO	0.005	0.0075	0.01	0.0175	0.025	0.05
O_3	30.0	40.0	50.0	55.0	60.0	80.0
HNO_3	0.005	0.01	0.015	0.02	0.03	0.06
H_2O_2	1.0	1.0	1.0	2.0	2.0	2.0
ALD	0.1	0.1	0.1	0.01	0.01	0.01
HCHO	0.2	0.2	0.2	0.02	0.02	0.02
OP	0.2	0.2	0.2	0.2	0.2	0.2
PAA	0.1	0.1	0.1	0.1	0.1	0.1
ORA	0.0	0.0	0.0	0.0	0.0	0.0
NH_3	1.0	1.0	1.0	0.1	0.1	0.1
N_2O_5	0.0	0.0	0.0	0.0	0.0	0.0
NO_3	0.0	0.0	0.0	0.0	0.0	0.0
PAN	0.03	0.04	0.05	0.1	0.2	0.1
HC	0.2	0.2	0.2	0.2	0.2	0.2
ETH	1.0	1.0	1.0	0.2	0.2	0.2
CO	200.0	180.0	150.0	120.0	120.0	120.0
OL2	0.7	0.7	0.7	0.07	0.07	0.07
OL3	0.3	0.3	0.3	0.03	0.03	0.03
OL4	0.1	0.1	0.1	0.01	0.01	0.01
TOL	0.3	0.3	0.3	0.03	0.03	0.03
XYL	0.1	0.1	0.1	0.01	0.01	0.01

Layer 1 = 0. - 0.150 km
2 = 0.150 km - 0.550 km
3 = 0.550 km - 1.3 km
4 = 1.3 km - 3.8 km
5 = 3.8 km - 8.5 km
6 = 8.5 km - 15 km

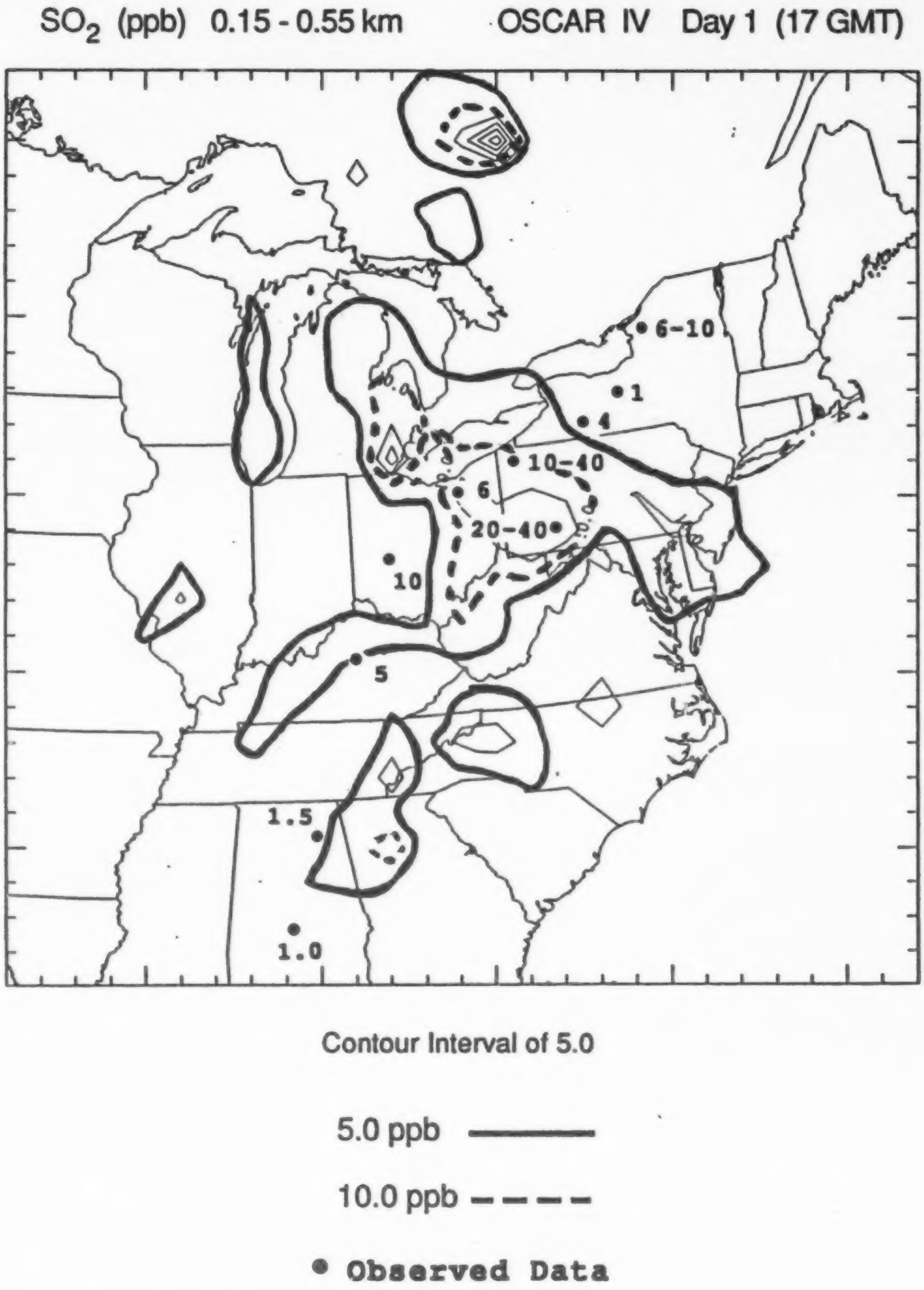
SO2 (ppb) 0.15 - 0.55 km OSCAR IV Day 1 (17 GMT)
6-10
1
4
10-40
6
20-40
10
5
1.5
1.0
Contour Interval of 5.0
5.0 ppb
10.0 ppb
Observed Data

Fig. 4.12 Comparison of boundary layer SO_2 measurements (●) with RADM predicted concentrations (—) at local noon of April 22, 1981 for OSCAR IV.

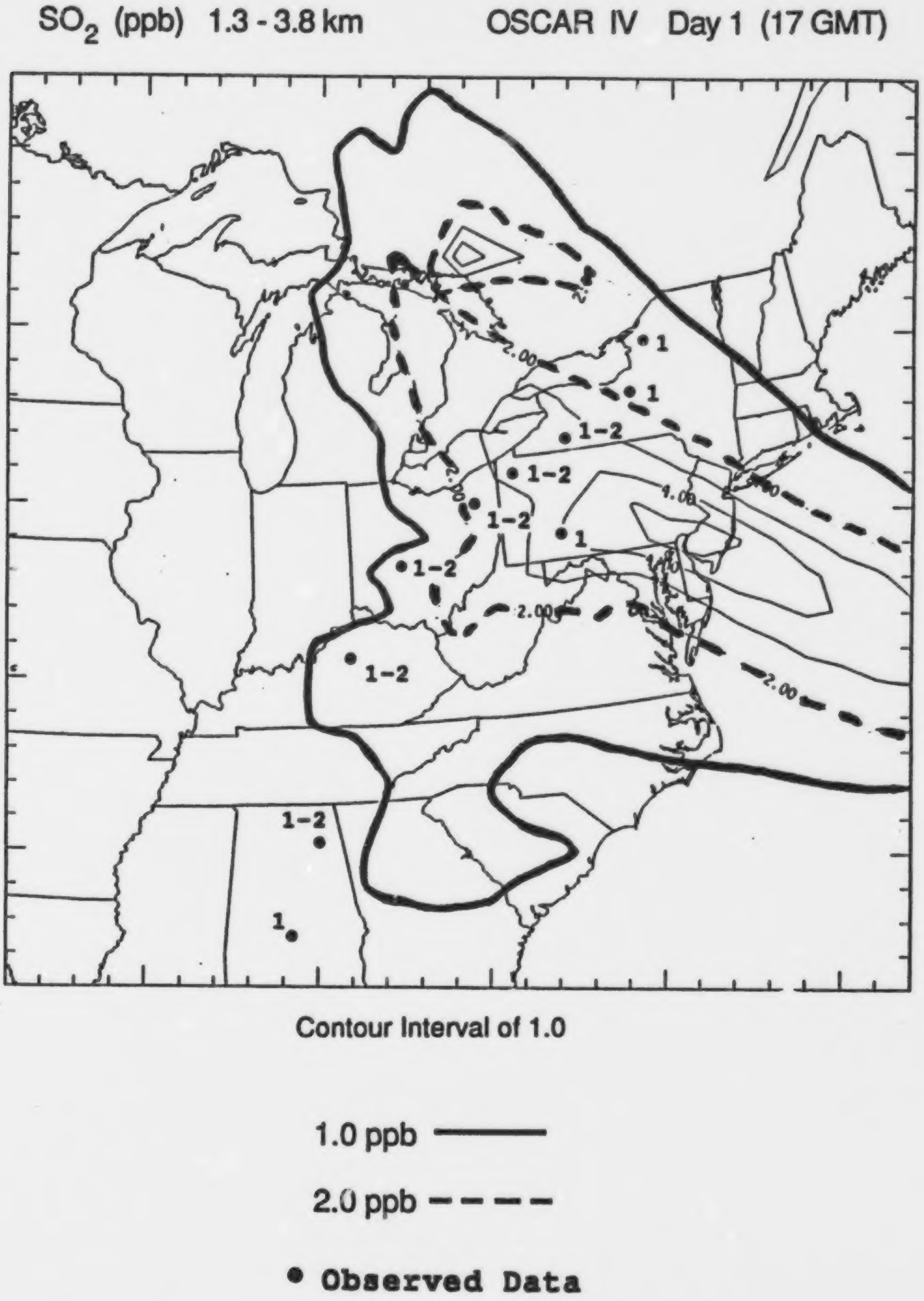
SO$_2$ (ppb) 1.3 - 3.8 km
OSCAR IV Day 1 (17 GMT)
1
1
1-2
1-2
1-2
1
1-2
1-2
1-2
1
2.00
1.00
2.00
2.00
Contour Interval of 1.0
1.0 ppb
2.0 ppb
Observed Data

Fig. 4.13 Comparison of upper layer (2-3 km) SO$_2$ measurements (●) with RADM predicted concentrations (—) at local noon of April 22, 1981 for OSCAR IV.

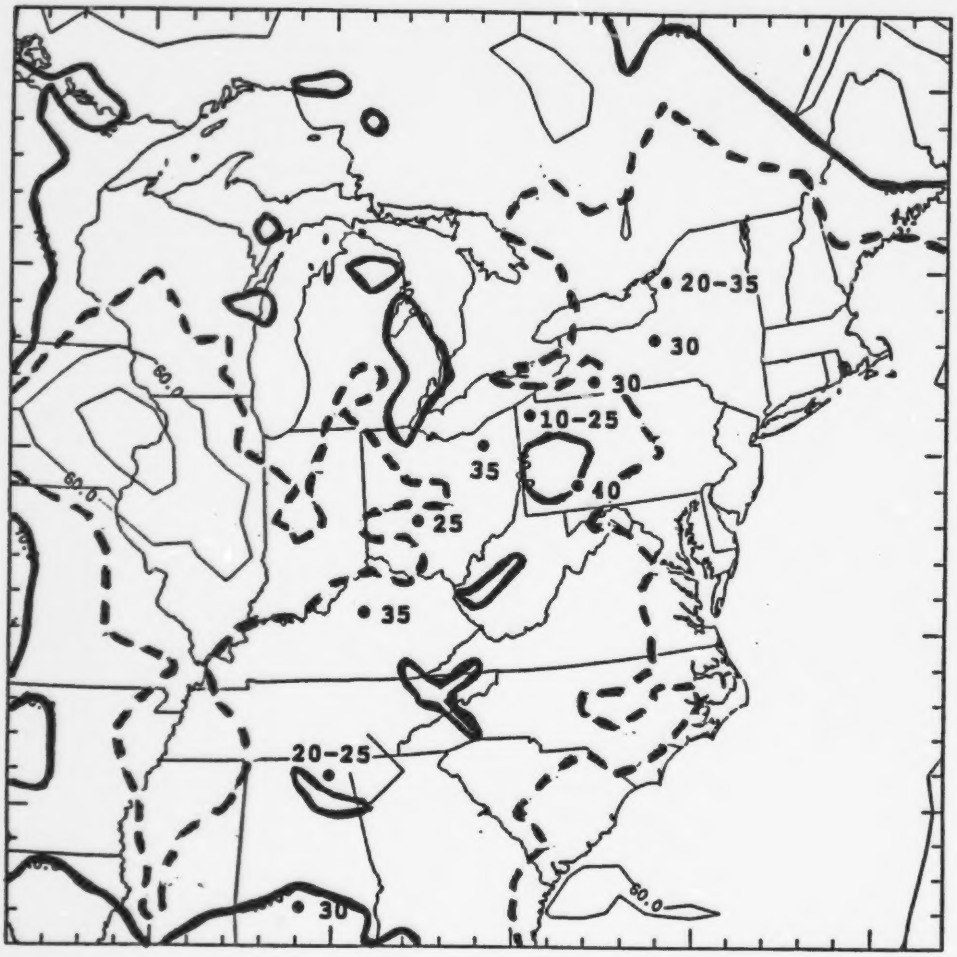
60.0
20-35
30
30
10-25
35
40
25
35
20-25
30
60.0

O_3 (ppb) 0.15 - 0.55 km OSCAR IV Day 1 (17 GMT)

Contour Interval of 10.0

40.0 ppb ———

50.0 ppb - - - -

● **Observed Data**

Fig. 4.14 Comparison of boundary layer O_3 measurements (●) with RADM predicted concentrations (—) at local noon of April 22, 1981 for OSCAR IV.

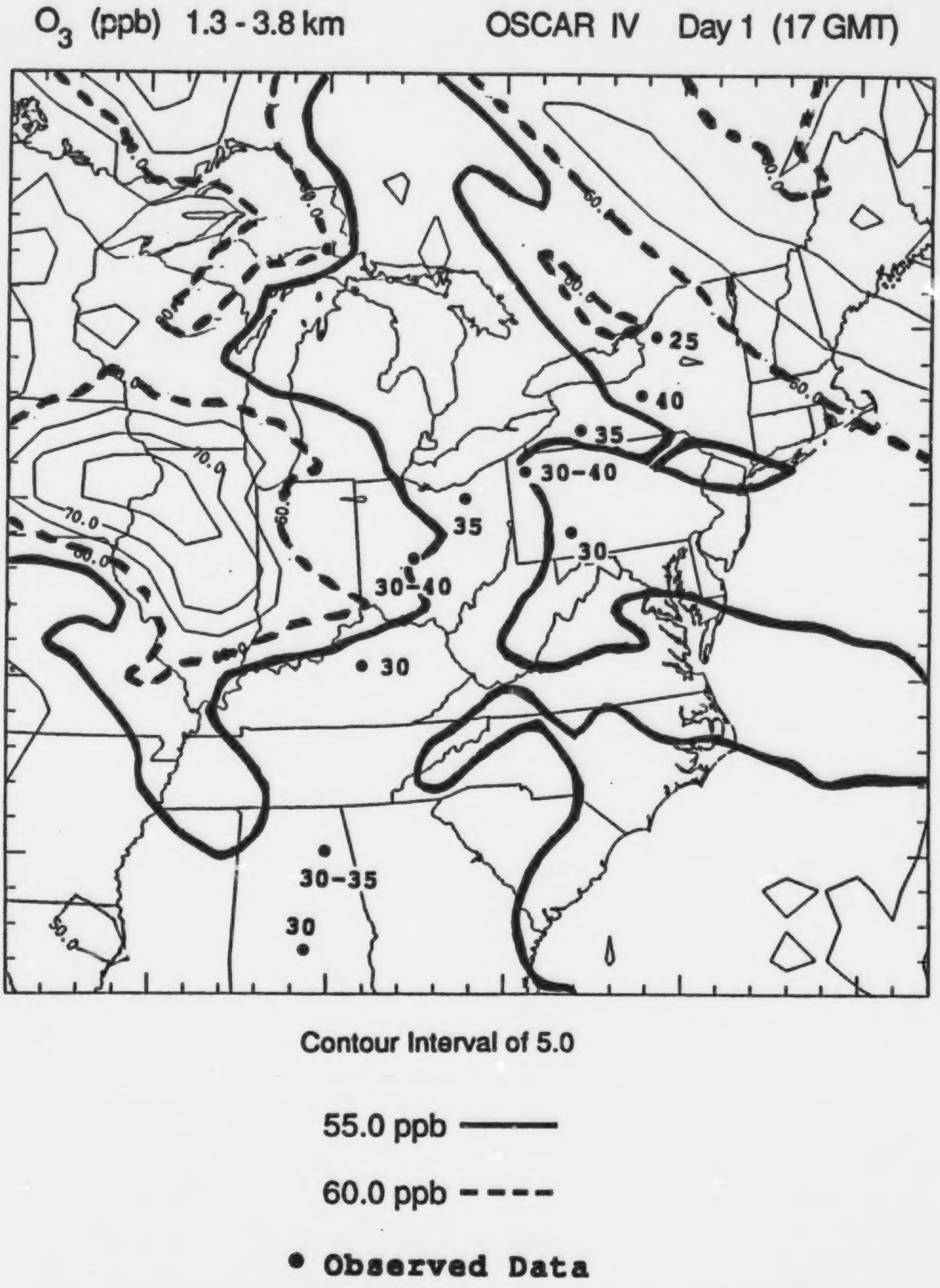

O3 (ppb) 1.3 - 3.8 km
OSCAR IV Day 1 (17 GMT)
60.0
70.0
50.0
25
40
35
30-40
35
30
30-40
30
30-35
30
Contour Interval of 5.0
55.0 ppb
60.0 ppb
● Observed Data

Fig. 4.15 Comparison of upper layer (2-3 km) O_3 measurements (●) with RADM predicted concentrations (—) at local noon of April 22, 1981 for OSCAR IV.

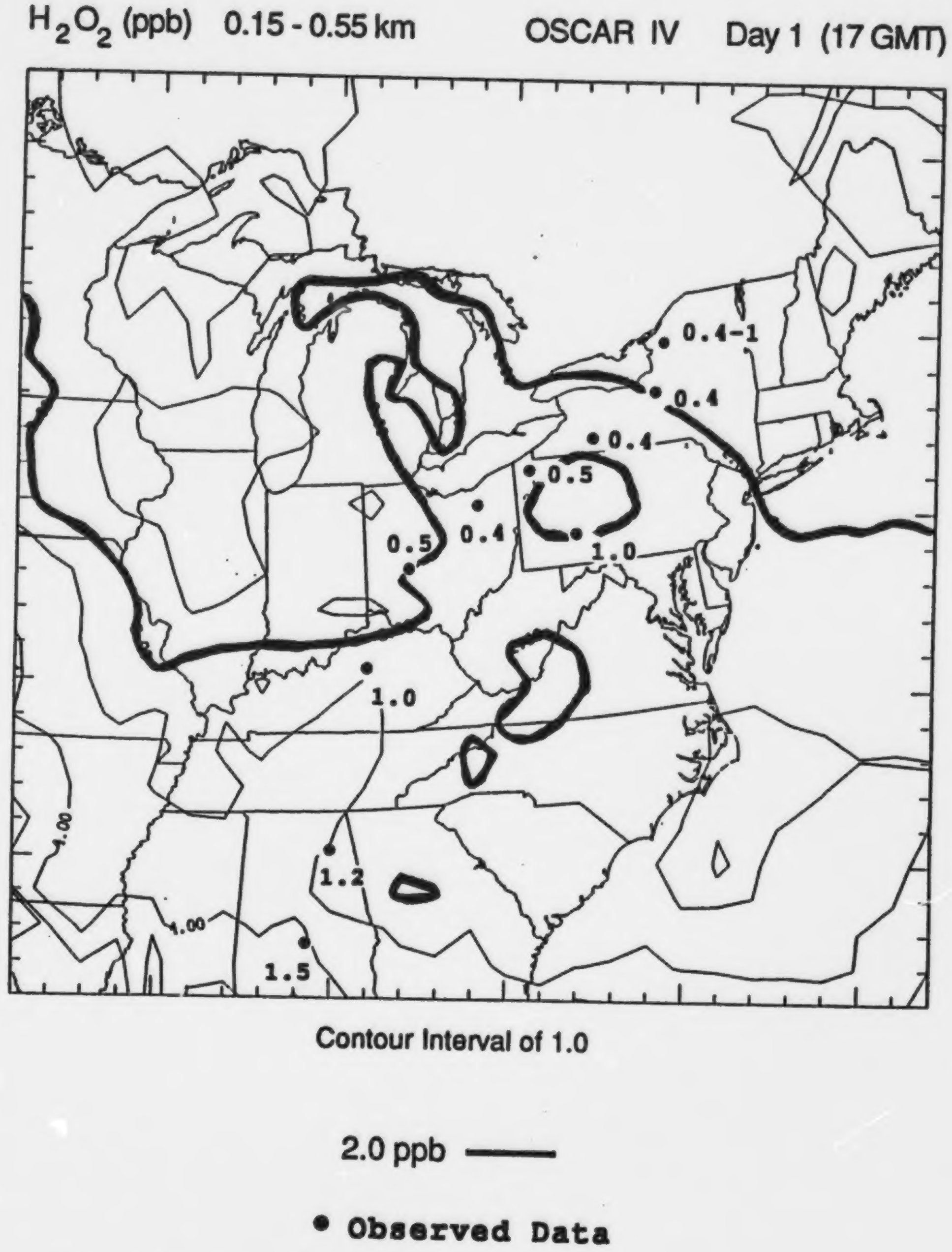
H2O2 (ppb) 0.15 - 0.55 km
OSCAR IV Day 1 (17 GMT)
0.4-1
0.4
0.4
0.5
0.5
0.4
1.0
1.0
1.2
1.5
1.00
1.00
Contour Interval of 1.0
2.0 ppb ——
● Observed Data

Fig. 4.16 Comparison of boundary layer H_2O_2 measurements (●) with RADM predicted concentrations (—) at local noon of April 22, 1981 for OSCAR IV.

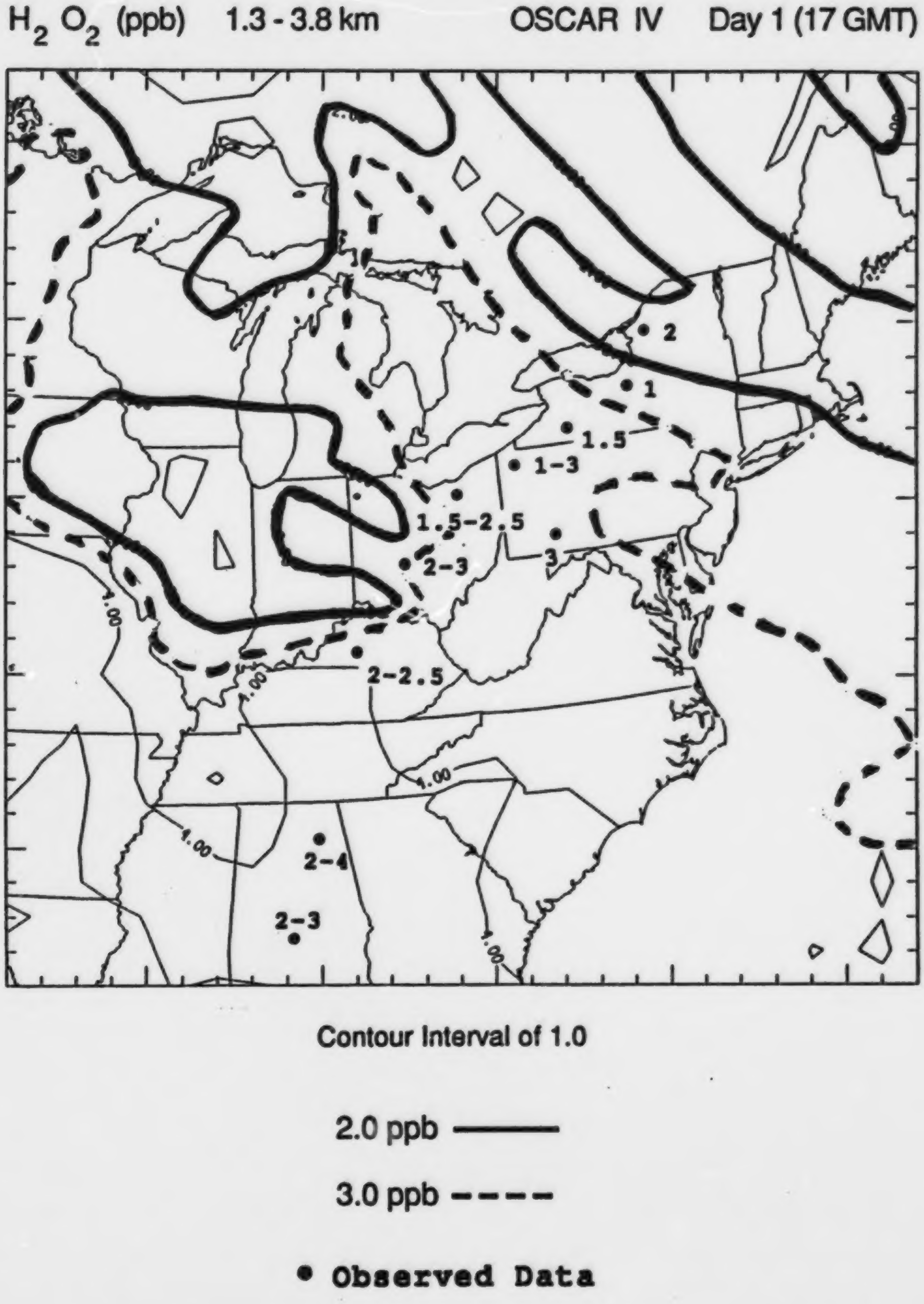
H_2O_2 (ppb) 1.3 - 3.8 km
OSCAR IV Day 1 (17 GMT)
2
1
1.5
1-3
1.5-2.5
3
2-3
2-2.5
2-4
2-3
1.00
Contour Interval of 1.0
2.0 ppb ———
3.0 ppb - - - -
● Observed Data

Fig. 4.17 Comparison of boundary layer H_2O_2 measurements (●) with RADM predicted concentrations (—) at local noon of April 22, 1981 for OSCAR IV.

October 1984 (Heikes et al., 1986). Although the data were gathered during a different period than OSCAR IV, they are under similar meteorological conditions, i.e., ahead of a cold front. The general qualitative and some quantitative agreement shown in these figures are very reassuring. They strongly suggest the general scientific credibility of RADM in representing physical reality. Shortly after noon of the first day and thereafter, precipitation scavenging over the general area significantly alters the chemical species distributions over much of this domain. Therefore, only the first day can be used in the comparison. Most of the horizontal and vertical features of the observed distributions are captured by RADM. For example:

(1) There is a factor of ten or more differences in the SO_2 concentration in the polluted boundary layer (Ohio and Pennsylvania) and the cleaner areas such as New York and Alabama.

(2) In the upper air (2-3 km altitudes), the concentrations of SO_2 stay about 1-2 ppb over the whole domain. This means that over polluted areas the free atmospheric concentrations of SO_2 are at least an order of magnitude less than those in the boundary layer, but over cleaner areas there is little vertical variation in concentration. These highly structured horizontal and vertical variations were well represented quantitatively by RADM (Figs. 4.12 and 4.13).

(3) The general horizontal variation of O_3 over the eastern United States is also well represented (Figs. 4.14 and 4.15). The measured concentration of O_3 (20-30 ppb) appear to be a little less than previously published average surface values of about 30-60 ppb (OTA, 1984; Vukovich et al., 1985). RADM predicted values are in the range of 40-50 ppb. Both the data and the RADM simulation show a small increase in O_3 concentration as we go to the 2-3 km altitude.

(4) The general uniformity of O_3 concentrations over the measurement sites appear also in the RADM predictions. It is interesting to note that the coming storm actually is bringing a higher O_3 concentration toward the measurement area (Fig. 4.15). This suggests that future model and data comparisons must address the detailed time evolution of local meteorological conditions in order to provide proper reference for comparison studies.

(5) The first extensive measurements of H_2O_2 are shown in Figs. 4.16 and 4.17. The decrease of H_2O_2 concentration over polluted areas as compared to cleaner areas is shown by the data and is indeed predicted by RADM. In fact, even the magnitude of local concentrations and the relative changes are in reasonable agreement. RADM predicted higher H_2O_2 concentrations consistent with the higher O_3.

(6) The domain-wide increase of H_2O_2 from the boundary layer to the 2-3 km altitudes is again predicted by the model. The differences in concentrations can be easily corrected when we study in detail the causes for O_3 differences. At this time, it is not clear how or whether we should be concerned about this. Further studies are underway to evaluate these preliminary findings systematically and in greater detail.

Figs. 4.18 and 4.19 further strengthen our faith in RADM. These two figures show a comparison of the observed and model-simulated wet sulfate and nitrate depositions at the end of the first day of OSCAR IV. The close agreement should be considered with some caveats. There is always the question of appropriateness in comparing point measurements with model grid averages. For this case, if we assume the wet deposition from individual cloud systems to have persisted for several hours, then the cumulative total at a given point can be considered as some kind of conceptual spatial average over at least part of a grid. Therefore, direct comparisons can be qualitatively meaningful if not necessarily in a quantified sense. It also must be emphasized that, although the point-by-point comparison shows good agreement, it is the qualitative agreement in general horizontal pattern that is of importance. This suggests the ability of RADM to capture significant regional details in a wet scavenging event. This rather confident statement is also based on results from sensitivity studies not reported here but which will be discussed in forthcoming reports. For example, earlier calculations with vertically stratified, but horizontally uniform, initial SO_2 distributions and different emissions could not predict the relatively higher wet sulfate depositions in southern Indiana and Ohio (Fig. 4.18). Only with the model-generated local high of SO_2 in the Ohio River Valley can we obtain the current result. Further, the wet nitrate deposition was found to be totally dependent on the initial NO_x pattern. The improved, current results use only the NAPAP emissions patterns and OSCAR IV meteorology to establish the proper NO_x distributions.

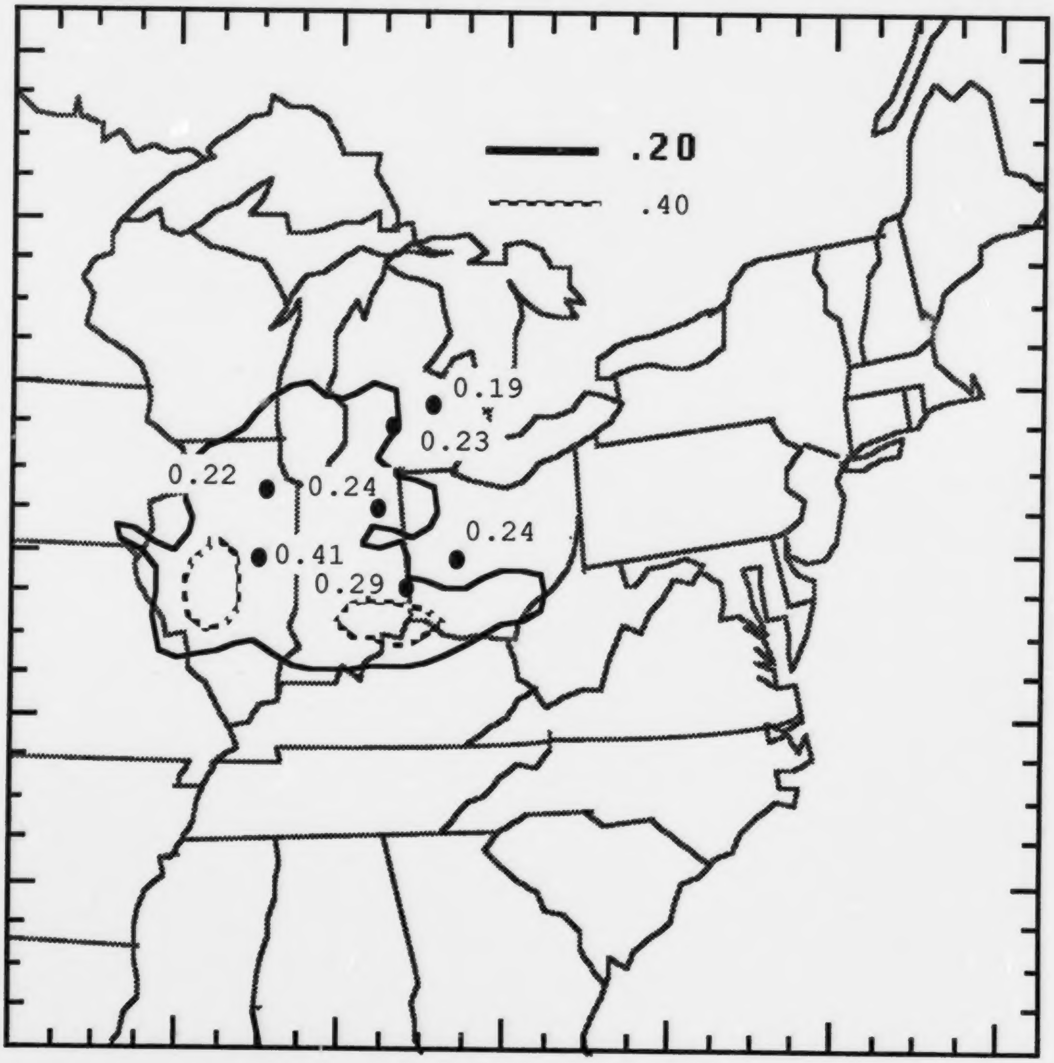
.20
.40
0.19
0.23
0.22
0.24
0.24
0.41
0.29

Fig. 4.18 Comparison of measured cumulated wet sulfate deposition (●) with RADM predictions (—) at the end of April 22, 1981 for OSCAR IV.

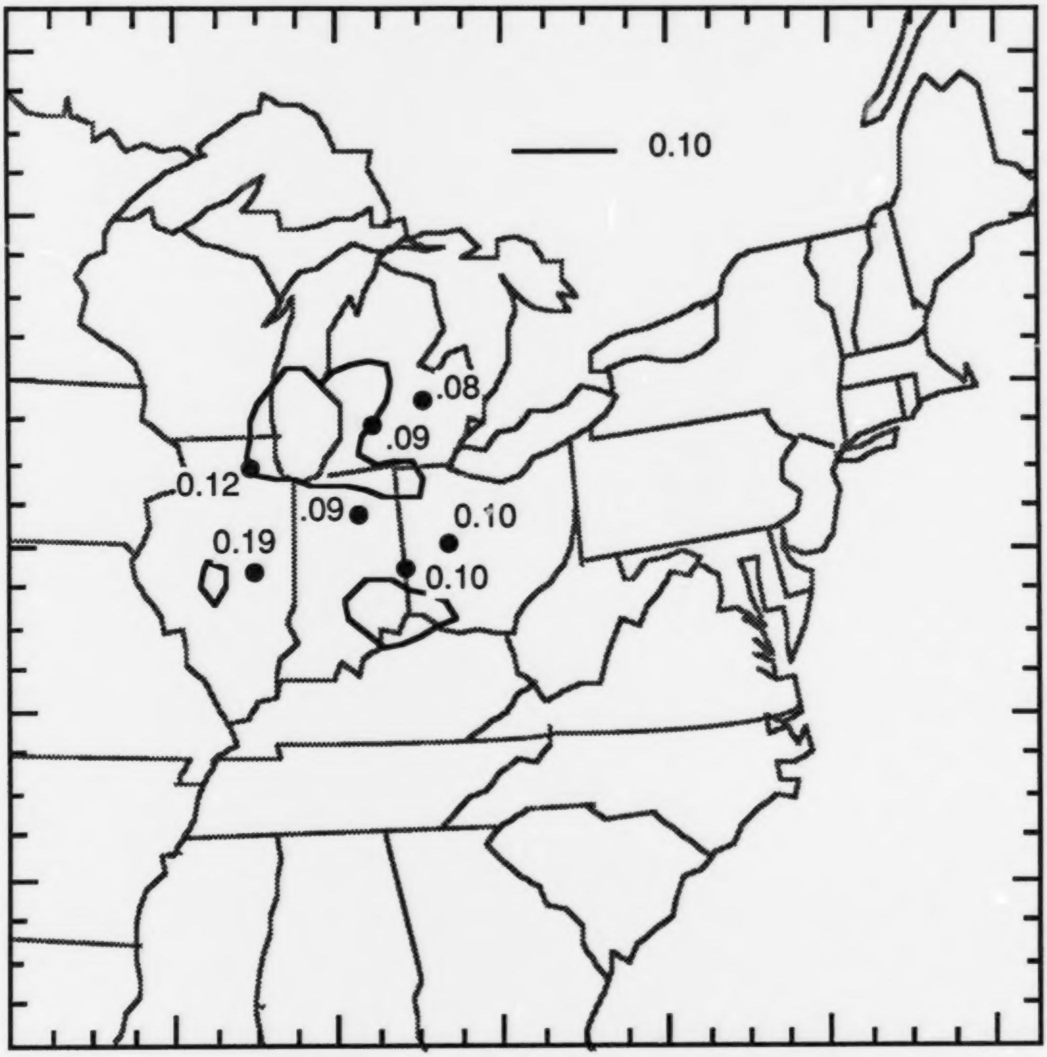
0.10
.08
.09
0.12
.09
0.10
0.19
0.10

Fig. 4.19 Comparison of measured cumulated wet nitrate deposition (●) with RADM predictions (—) at the end of April 22, 1981 for OSCAR IV.

SECTION 5

RADM SENSITIVITY STUDIES AND APPLICATIONS

5.1 Developing Experience with and Understanding of RADM Forecasts

Ultimately RADM will be used to evaluate source-receptor relationships--for example, to study the variation of the emissions at one location and determine its effect on deposition at another location. To work toward this goal, we realize that we need to develop a better understanding of the patterns of concentration and deposition forecast by RADM. We need to understand the normal patterns of deposition for each storm and study the results of many different storms to develop climatologies of deposition. The sensitivity of forecasts to various input parameters and physical parameterizations must be studied. Also, new methods of analyzing and presenting the data must be developed.

MM4 was used to forecast meteorological three-dimensional fields of horizontal wind, temperature, and mixing ratio and other two-dimensional fields such as surface pressure, surface temperature, and rainfall for two three-day episodes: OSCAR I, 00Z 8 April 1981 to 00Z 11 April 1981; and OSCAR IV, 00Z 22 April 1981 to 00Z 25 April 1981 (Section 4.2). These meteorological fields have been used to drive RADM and perform various simulations which will be discussed next. The basic OSCAR I and OSCAR IV runs use the diurnally varying NAPAP emissions inventories for a springtime weekday. First we examine the normal wet and dry deposition patterns for OSCAR I and IV. Then we demonstrate RADM's ability to study "what-if" scenarios by simulating two hypothetical SO_2 emissions reduction strategies, i.e., 50% and 90% SO_2 source reduction in the Ohio River Valley region.

5.2 Wet and Dry Deposition of SO_x and NO_x

Figs. 5.1 and 5.2 show the percentage of the total sulfur deposition which was wet during two different three-day episodes (OSCAR I and OSCAR IV). The values shown are averages over state or multi-state regions in the United States and provincial regions in Canada. In OSCAR I, the percentage of wet deposition was highest where the rainfall was highest for this case, i.e., in Michigan and Canada. The lowest percentages of wet deposition occurred over the low-rainfall region from Missouri to New Jersey. In the OSCAR IV episode, the percentage of wet deposition of sulfur was more uniform, the Canadian regions were not as high and the Ohio Valley not as low, but again the region with the highest percentage of wet deposition was Quebec and Ontario.

Figs. 5.3 and 5.4 show the percentages of wet deposition of nitrogen for the two episodes. For OSCAR I, the percentage of wet deposition of sulfur was almost always greater than the percentage of wet deposition of nitrogen.

Fig. 5.1

Percentage of the sulfur deposition which was wet for the three day OSCAR 1 episode

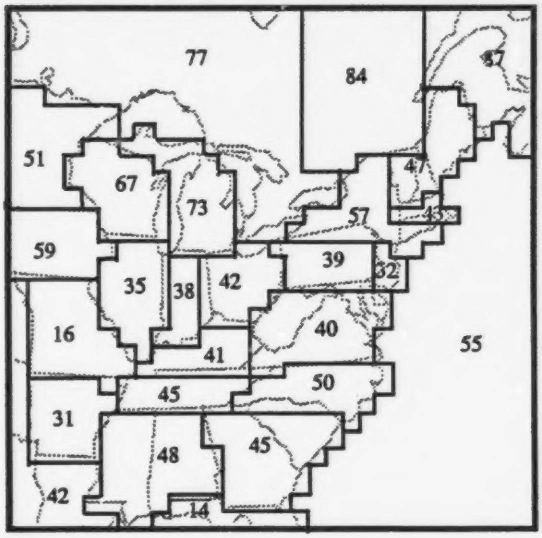
77
84
57
51
67
73
47
57
45
59
39
32
35
38
42
16
40
55
41
50
45
31
48
45
42
14

Fig. 5.2

Percentage of the sulfur deposition which was wet for the three day OSCAR 4 episode

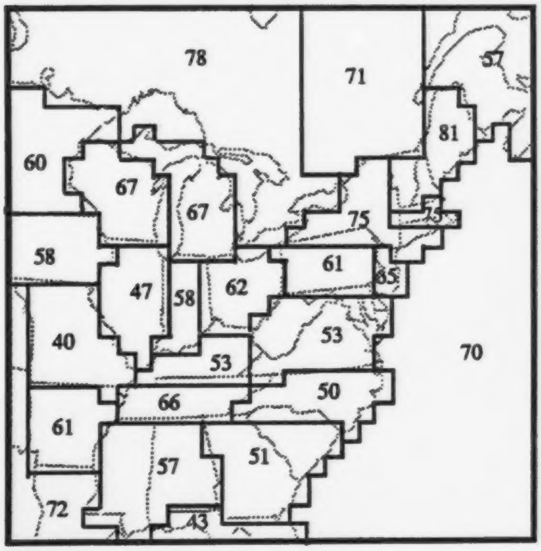
78
71
57
81
60
67
67
75
75
58
61
65
47
58
62
40
53
70
53
50
66
61
57
51
72
43

Fig. 5.3

Percentage of the nitrogen deposition which was wet for the three day OSCAR 1 episode

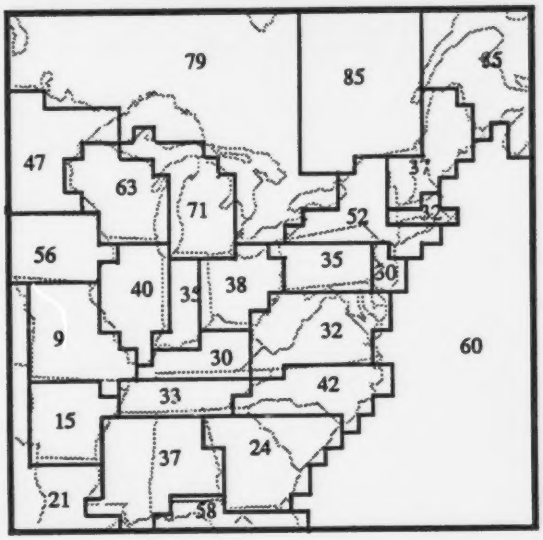
79
85
85
47
63
71
37
52
32
56
35
30
40
35
38
32
60
9
30
42
33
15
37
24
21
58

Fig. 5.4

Percentage of the nitrogen deposition which was wet for the three day OSCAR 4 episode

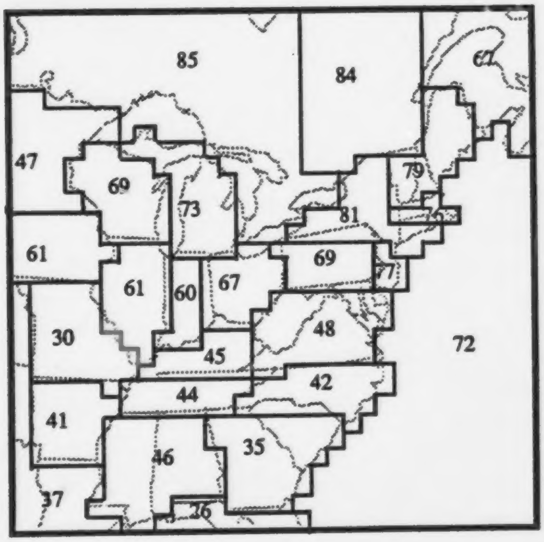
85
84
67
47
69
73
79
81
61
69
77
61
60
67
48
72
30
45
44
42
41
46
35
37
26

For OSCAR IV, the percentage of wet deposition of nitrogen was usually less than the percentage of wet deposition of sulfur in the south but greater than the percentage of wet deposition of sulfur in most northerly locations, e.g., the Ohio Valley and Canada, corresponding to the respective contributions of area NO_x sources. This contrast suggests that, on a local scale, both emission and precipitation patterns are major factors in determining the relative role of wet and dry deposition.

The dry deposition of SO_2 is quite similar in magnitude and distribution in the two episodes, OSCAR I and OSCAR IV (Figs. 5.5 and 5.6). In Canada in particular, the same deposition peaks show up--that is, Sudbury, Noranda, and some others. In the United States, there are three primary deposition areas in both episodes. The first peak area is south-central Illinois, where the peak deposition was 1.08 kg/ha for OSCAR I and 1.14 kg/ha for OSCAR IV. The second area is the conjunction of Ohio, Pennsylvania, and West Virginia, where the peak depositions were 0.502 kg/ha for OSCAR I and 0.626 kg/ha for OSCAR IV. The third region is New Jersey, in which the peak values were 0.488 and 0.460 kg/ha for the two episodes. In OSCAR IV alone, there was a peak of deposition in western North Carolina. Regions with smaller maxima of deposition included the intervening areas in the Ohio Valley and Appalachian Mountains, Green Bay, Wisconsin, northern Georgia and Alabama, and eastern Michigan.

For HNO_3, the accumulated dry deposition for the two three-day episodes are again quite similar (Figs. 5.7 and 5.8), although the mass deposited was less than for SO_2. For OSCAR IV, the Canadian peak was around Windsor, Ontario and the maxima in the United States were in western Kentucky, the Appalachian region from Atlanta to Pennsylvania, and New Jersey. OSCAR I is the same as OSCAR IV, with the addition of a peak near Chicago and the extension of high values up into New England, including a new large peak in New York and Massachusetts, reflecting the contributions of area NO_x sources. It is clear that dry deposition associates strongly with the local area and point sources.

The accumulated wet deposition differs more between the two experiments than does the dry deposition. This reflects primarily the difference in rainfall patterns in the two episodes. In OSCAR I the rainfall maximum and the peak deposition of sulfate is a swath running ENE from Michigan toward Montreal. In Oscar IV both quantities are enclosed within a "triangle" with corners at New Jersey, Atlanta and Sudbury, although the Atlanta-Sudbury side bulges westward to include western Illinois. Figs. 5.9 and 5.10 show the accumulated wet deposition of SO_4 for the two episodes. For OSCAR I, there was relatively little wet deposition of sulfate (0.2-0.4 kg/ha) in the Ohio Valley because little precipitation fell there. But the broad cold front of OSCAR IV gave significant amounts of wet sulfate deposition in this strong source region, 0.4-0.8 kg/ha. The highly varying horizontal distributions of wet sulfate deposition (and nitrate deposition) show the difficulty in conducting episodic observations. These results suggest that, unless the observation network can capture these kind of variations on an episodic basis, many interesting insights on wet depostion processes may not be detected or evaluated with surface data.

Fig. 5.5

OSCAR 1 total SO_2 dry deposition (kg/ha) after 3 days

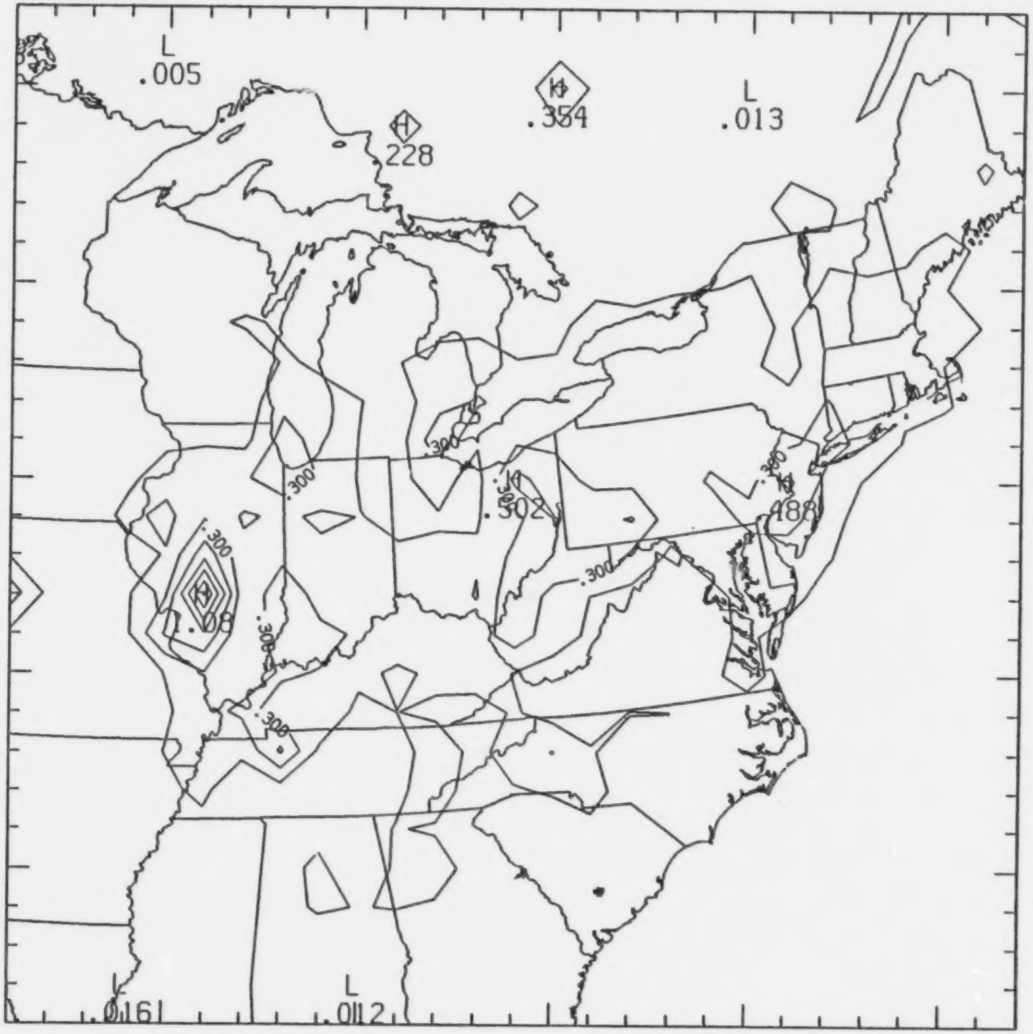
L
.005
H
228
H
.354
L
.013
H
.302
H
.488
H
1.08
.300
L
.016
L
.012

CONTOUR FROM 0.00000 TO 1.2000 CONTOUR INTERVAL OF 0.15000 PT(3,3)= 0.80073E-01

Fig. 5.6

OSCAR 4 total SO_2 dry deposition (kg/ha) after 3 days

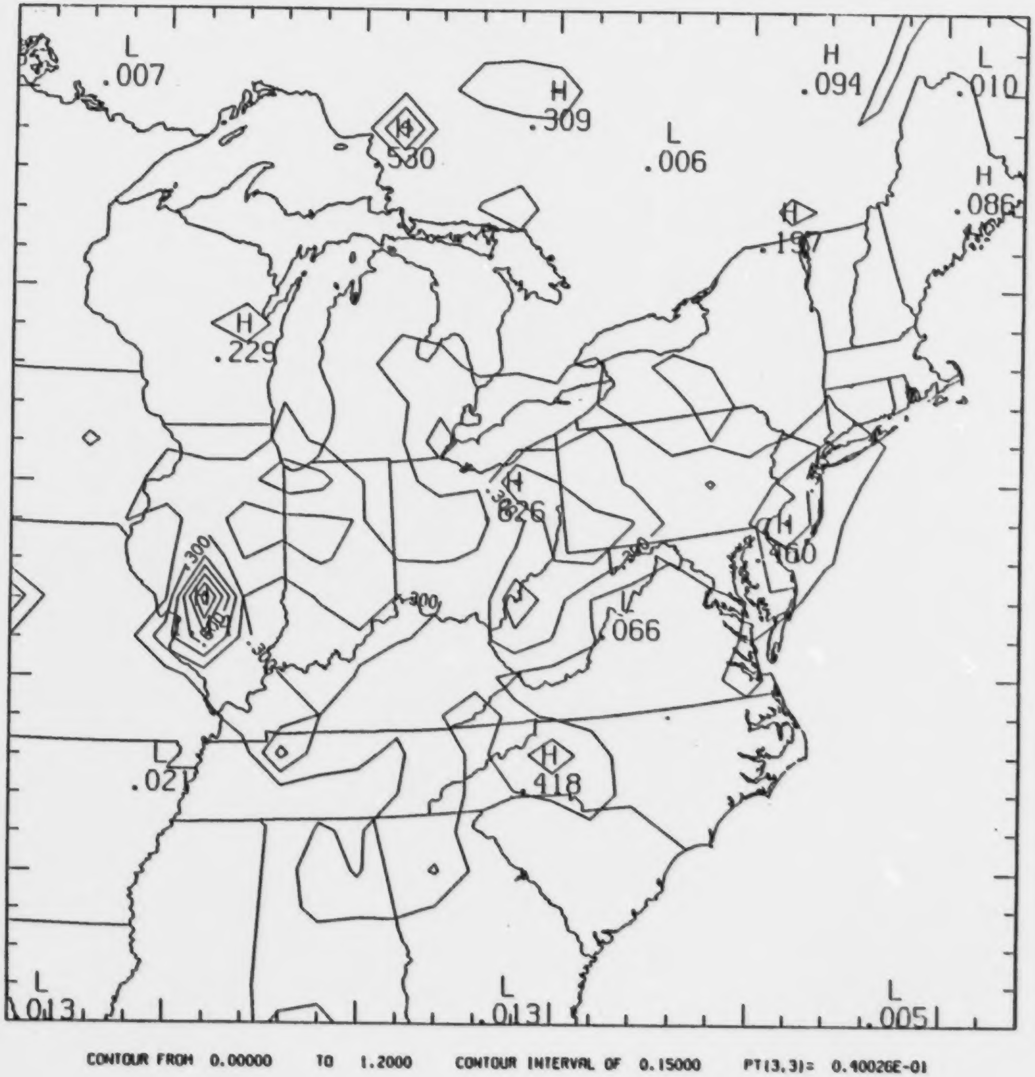
L
.007
H
.530
H
.309
L
.006
H
.094
L
.010
H
.086
.197
H
.229
H
.326
H
.460
.300
L
.066
L
.021
H
.418
L
.013
L
.013
L
.005
CONTOUR FROM 0.00000 TO 1.2000 CONTOUR INTERVAL OF 0.15000 PT(3,3)= 0.40026E-01

Fig. 5.7

OSCAR 1 total HNO_3 dry deposition (kg/ha) after 3 days

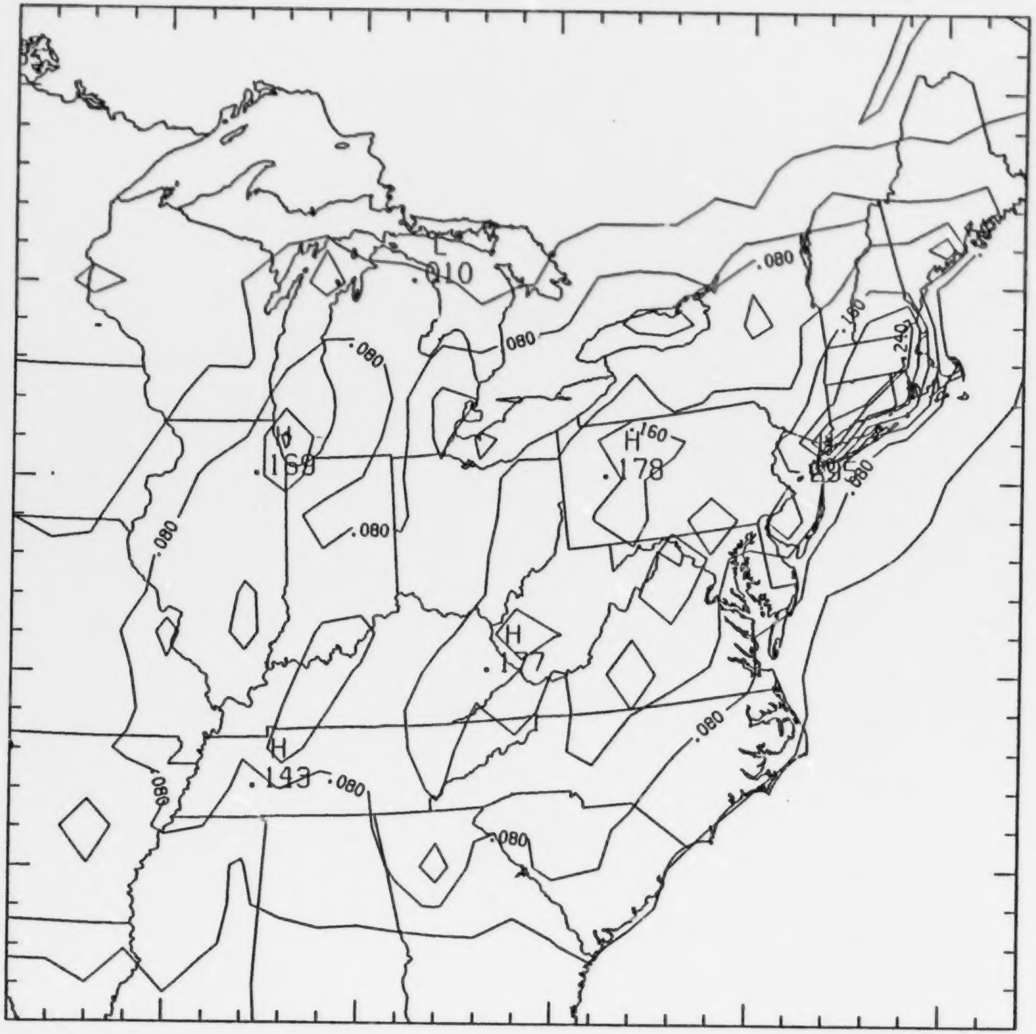

L
.010
.080
H
.168
.080
.080
.080
H
.160
.178
.160
.240
.080
H
.080
H
.143
.080
.080
.080
.080

CONTOUR FROM 0.00000 TO 0.28000 CONTOUR INTERVAL OF 0.40000E-01 PT(3,3)= 0.67286E-01

Fig. 5.8

OSCAR 4 total HNO_3 dry deposition (kg/ha) after 3 days

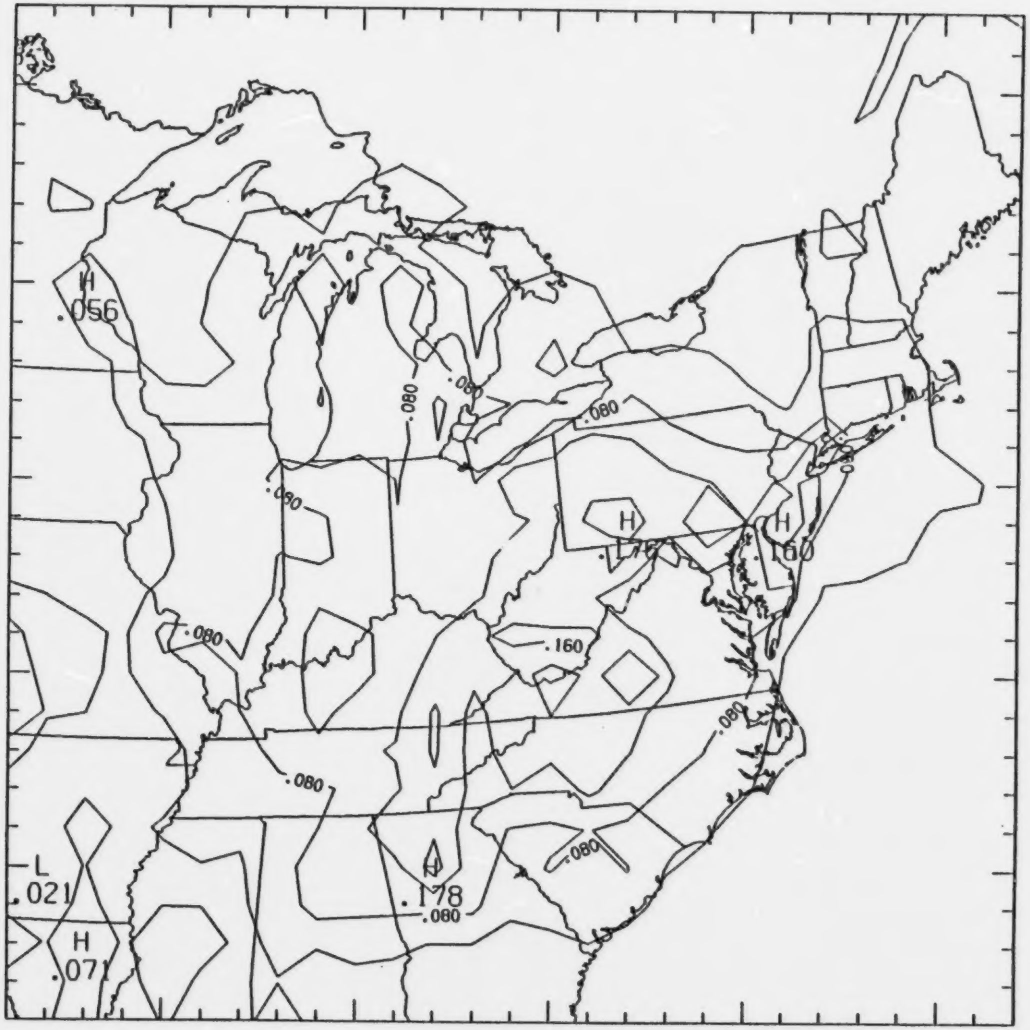
H
.056
.080
.080
.080
.080
H
.176
H
.160
.080
.160
.080
.080
.080
L
.021
H
.071
H
.178
.080

CONTOUR FROM 0.00000 TO 0.28000 CONTOUR INTERVAL OF 0.40000E-01 PT(3,3)= 0.70979E-01

Fig. 5.9

OSCAR 1 total SO_4 wet deposition (kg/ha) after 3 days

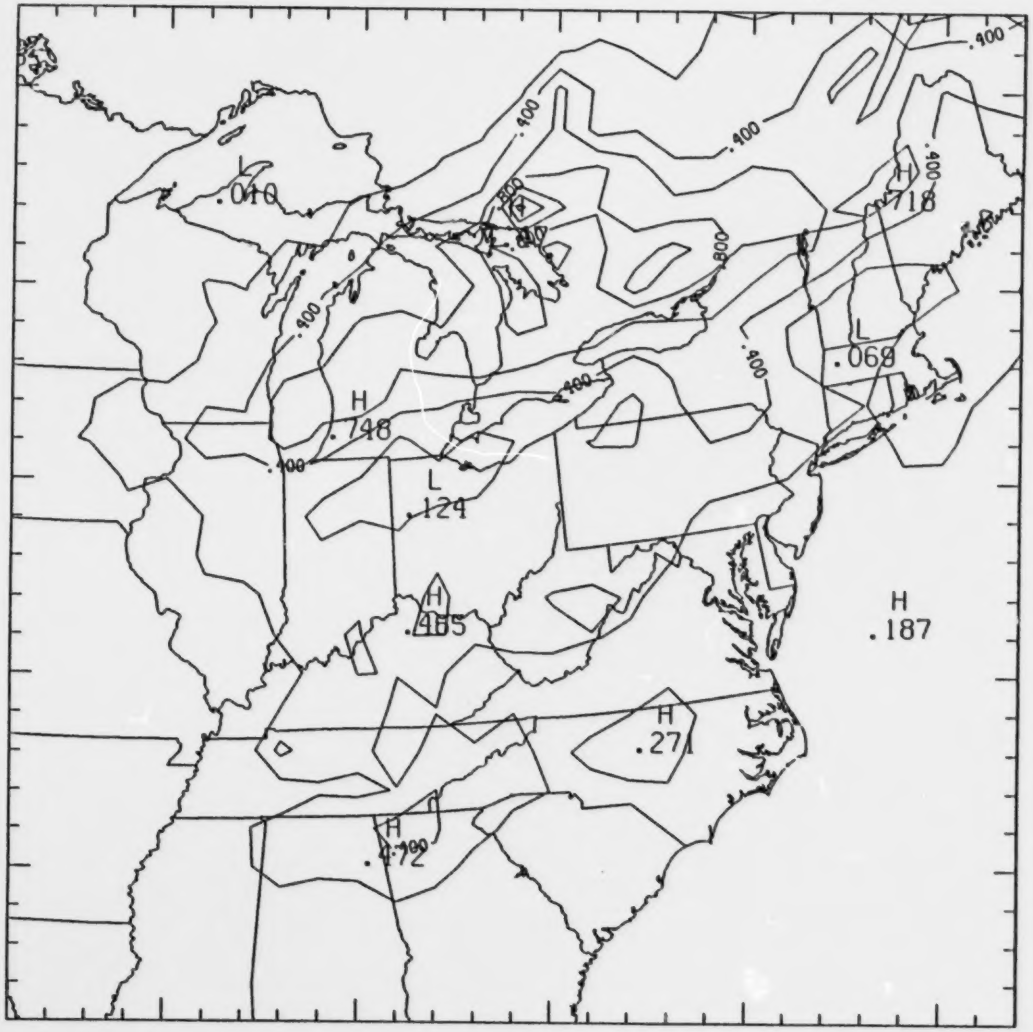
.400
.800
L
.010
H
.718
L
.069
H
.748
L
.124
H
.465
H
.187
H
.271
H
.472

CONTOUR FROM 0.00000 TO 1.4000 CONTOUR INTERVAL OF 0.20000 PT(3,3)= 0.49369E-01

Fig. 5.10

OSCAR 4 total SO_4 wet deposition (kg/ha) after 3 days

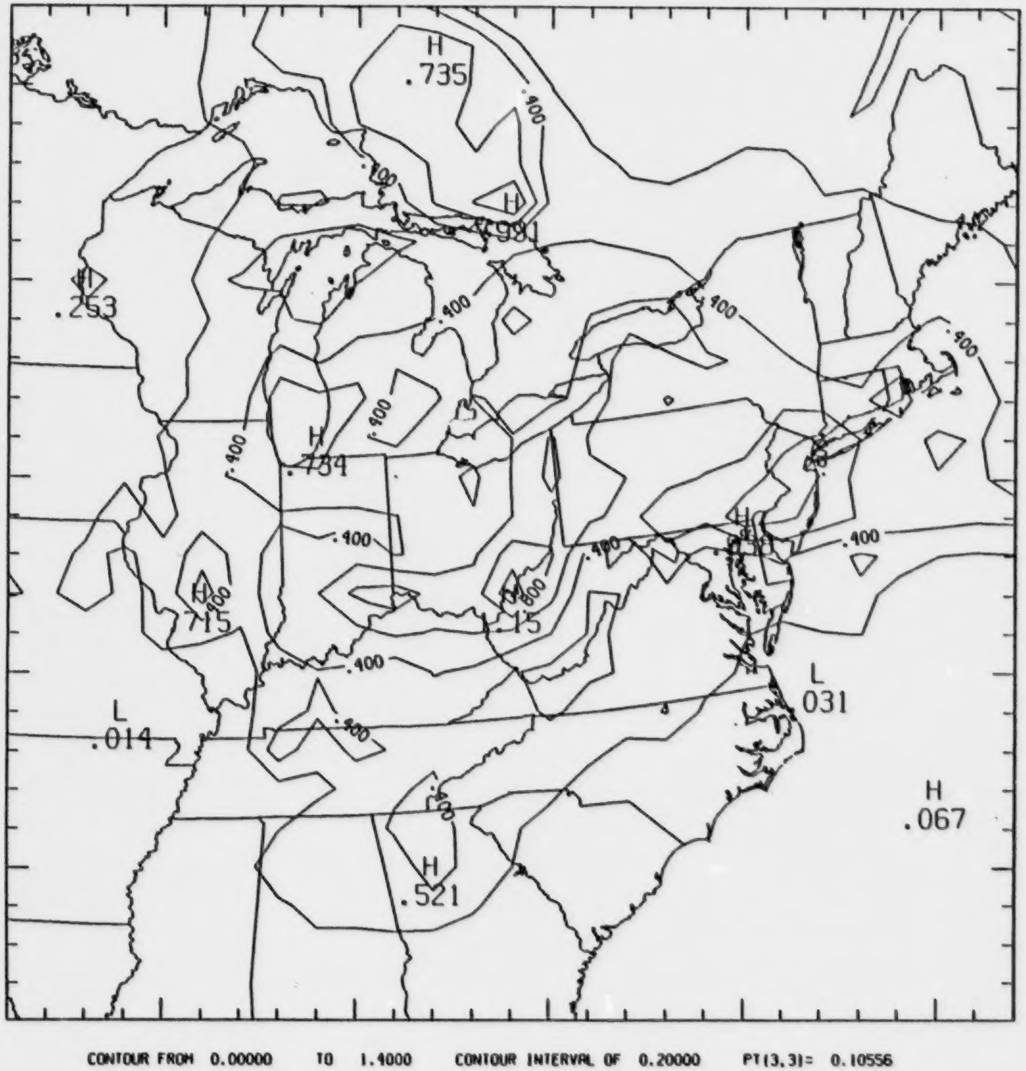
H
.735
.400
H
.253
H
.734
H
.715
.800
L
.014
H
.521
L
.031
H
.067
CONTOUR FROM 0.00000 TO 1.4000 CONTOUR INTERVAL OF 0.20000 PT(3,3)= 0.10556

For the accumulated wet deposition of nitrate, in OSCAR I (Fig. 5.11) the pattern is similar to that for SO_4. For OSCAR IV, the nitrate deposition pattern (Fig. 5.12) is different from that for SO_4, that is, the maximum runs from the upper Great Lakes to New Jersey. Again, this reflects the strong coupling of source distribution and precipitation patterns in determining total wet deposition.

5.3. Ohio Valley Reduction Experiments

Several sensitivity tests were run in which the SO_x emissions were reduced by 50% or 90% in the Ohio Valley--i.e., the states of Indiana, Ohio, Kentucky, Tennessee, and West Virginia. Figs. 5.13-5.20 show the effect on wet deposition of SO_4 and dry deposition of SO_2 for the two OSCAR episodes. The figures show what percentage of the original wet or dry sulfur deposition remain in the experiments with the reduced emissions. We will not show any results for nitrogen deposition because decreasing sulfur emissions has very little effect on nitrogen chemistry or nitrogen deposition.

The largest percentage decrease in deposition occurs in Kentucky, although with OSCAR I meteorology the wet deposition in Ohio decreases relatively as much as in Kentucky. The pattern of changes in wet deposition is similar in the episodes. Likewise, the pattern of changes in dry deposition is similar in the two episodes, although with OSCAR I meteorology the decrease in dry deposition in the Ohio Valley source region is greater than with OSCAR IV meteorology.

In response to a regional reduction in emissions, the maximum regional reduction in deposition occurs locally and in the dry deposition and not in the wet deposition. Dry deposition depends on local sources so that the decrease in dry deposition is greater than the decrease in wet deposition only in the five states with decreased emissions. On the other hand, wet deposition depends on upper air SO_2 concentration, which is more influenced by regional-scale transport, and the decrease in wet deposition exceeds that in dry deposition in all other regions.

Looking in more detail at the wet deposition of SO_4 in the Ohio Valley, for OSCAR I, the peak deposition after three days occurs in the Ohio-Kentucky area and varies in the following ratios for the full, 50%, and 90% reduction experiments: 1.0:0.72:0.49.* For OSCAR IV, the peak deposition in the Ohio Valley is slightly shifted to the Ohio-West Virginia border area and varies in the following ratios: 1.0:0.69:0.26. Thus, a 90% reduction in emissions only decreases the nearby peak in deposition by 51-74%. The reduction for the OSCAR IV case is greater than for the OSCAR I case because the local rainfall in the OSCAR IV case is larger--1.6 versus 0.9 cm.

Let us consider the response in Kentucky, which has the largest average decrease of any region for the emissions experiments considered. Averaging the two episodes and noting that about 1/2 the sulfur deposition in Kentucky

---

* These numbers are derived from detailed results of the simulations not shown here in the figures using regional averaging.

Fig. 5.11

OSCAR 1 total NO_3 wet deposition (kg/ha) after 3 days

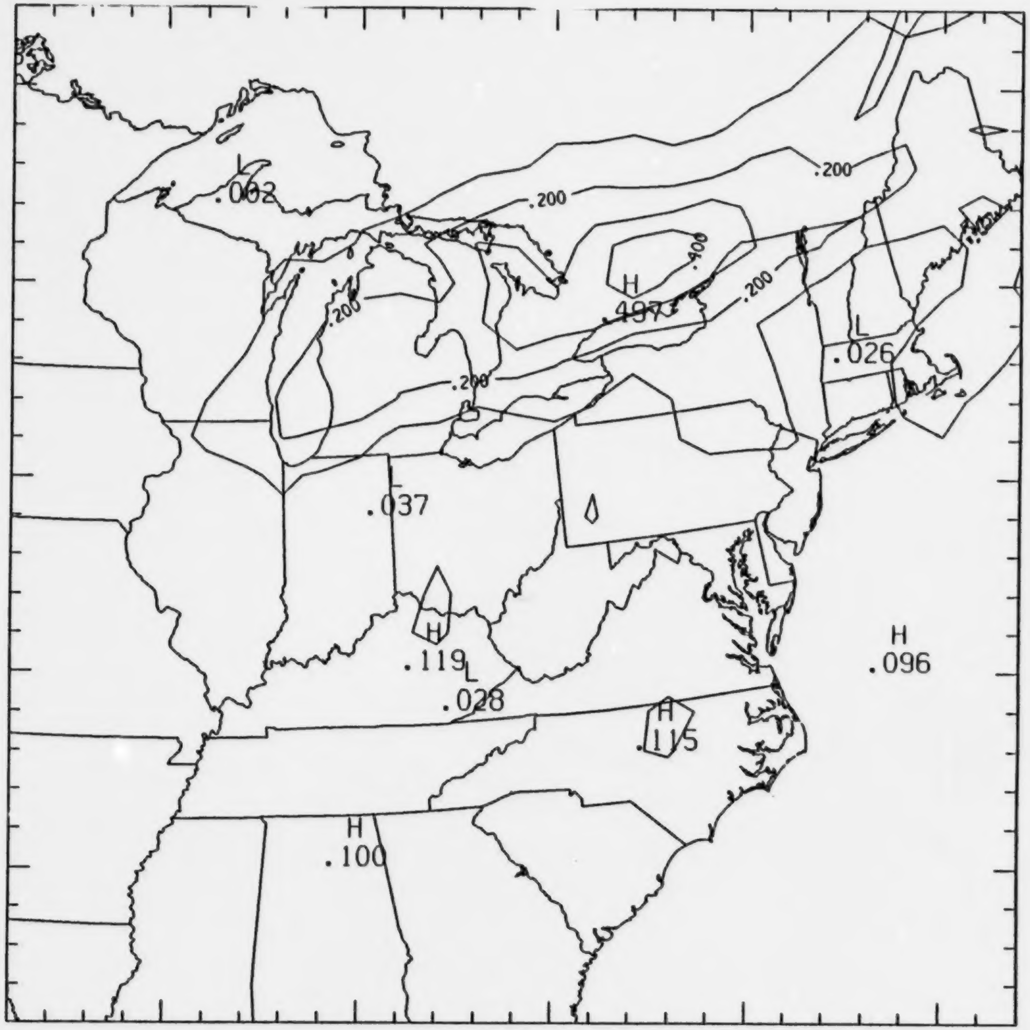

L
.002
.200
.200
.200
.200
.200
.400
H
.497
L
.026
.037
H
.119
L
.028
H
.115
H
.096
H
.100

CONTOUR FROM 0.00000 TO 0.50000 CONTOUR INTERVAL OF 0.10000 PT(3,3)= 0.21268E-01

Fig. 5.12

OSCAR 4 total NO_3 wet deposition (kg/ha) after 3 days

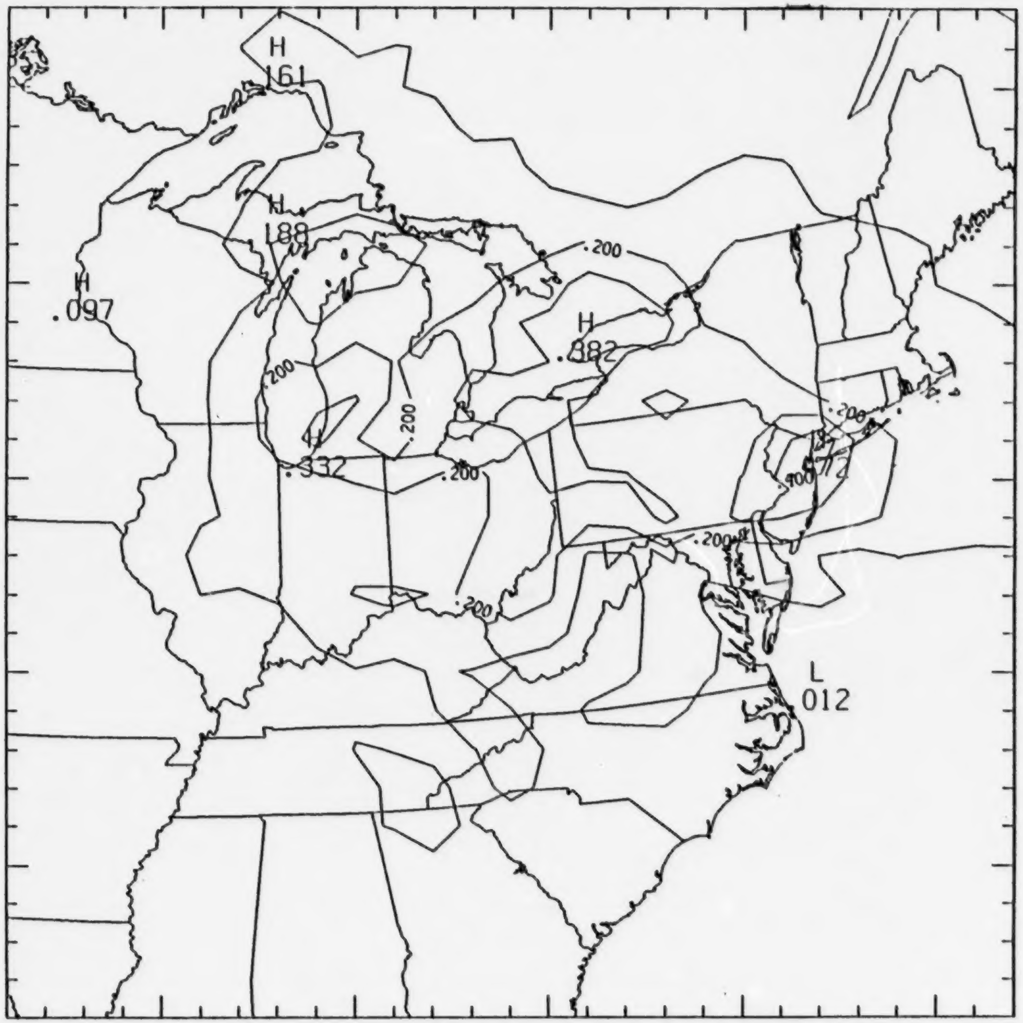
H
.161
H
.188
H
.097
.200
H
.882
.200
.200
.332
.200
.200
.200
.200
.900
.872
L
.012

CONTOUR FROM 0.00000 TO 0.50000 CONTOUR INTERVAL OF 0.10000 PT(3,3)= 0.43943E-01

Fig. 5.13

Percentage of original dry deposition of sulfur which occurs when emissions of sulfur in the Ohio Valley are reduced by 50% (OSCAR 1)

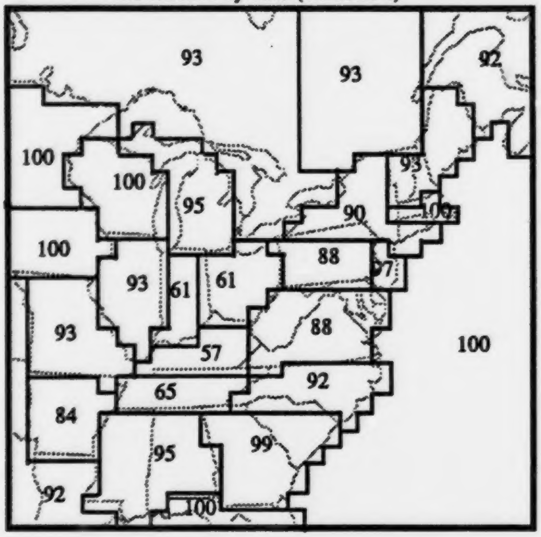
93
93
92
100
100
95
93
90
100
100
88
97
93
61
61
88
100
93
57
92
65
84
95
99
92
100

Fig. 5.14

Percentage of original dry deposition of sulfur which occurs when emissions of sulfur in the Ohio Valley are reduced by 50% (OSCAR 4)

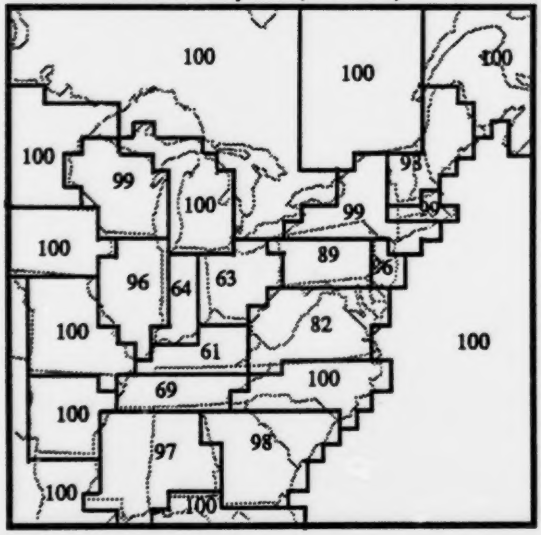
100
100
100
100
99
100
98
99
99
100
89
96
96
64
63
82
100
100
61
100
69
100
97
98
100
100

Fig. 5.15

Percentage of original wet deposition of sulfur which occurs when emissions of sulfur in the Ohio Valley are reduced by 50% (OSCAR 1)

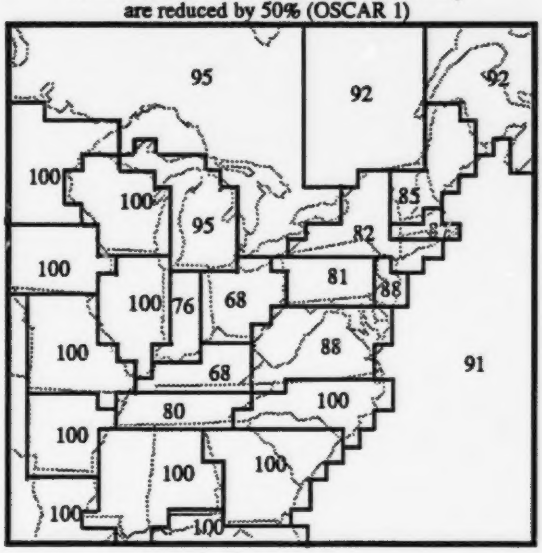
95
92
92
100
100
95
85
82
8
100
81
100
76
68
88
100
88
91
68
100
80
100
100
100
100
100

Fig. 5.16

Percentage of original wet deposition of sulfur which occurs when emissions of sulfur in the Ohio Valley are reduced by 50% (OSCAR 4)

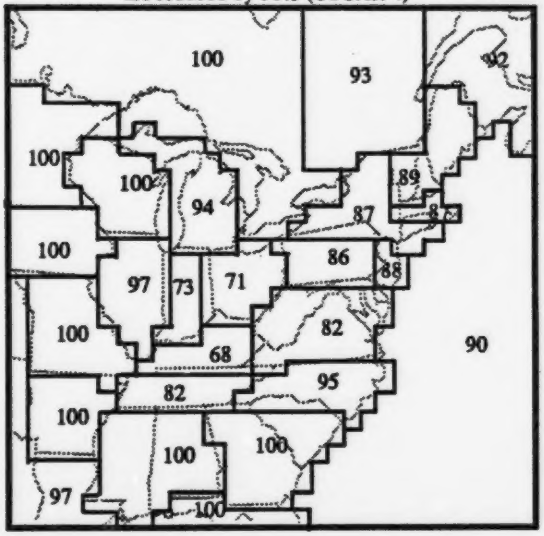
100
93
92
100
100
94
89
87
8
100
86
97
73
71
88
100
82
90
68
95
82
100
100
100
97
100

Fig. 5.17

Percentage of original dry deposition of sulfur which occurs when emissions of sulfur in the Ohio Valley are reduced by 90% (OSCAR 1)

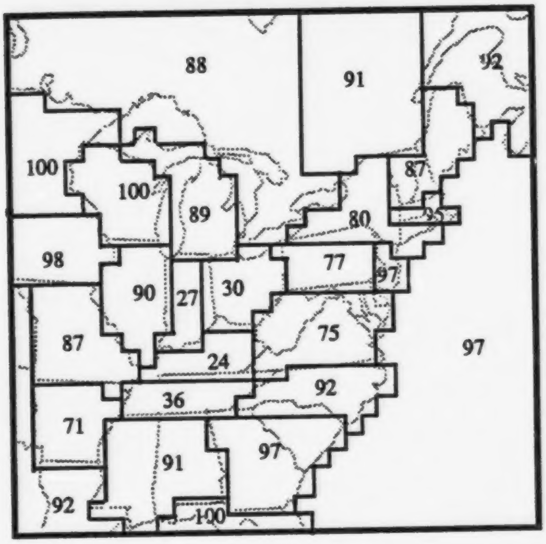

88
91
92
100
100
89
87
80
95
98
77
97
90
27
30
75
87
97
24
92
36
71
91
97
92
100

Fig. 5.18

Percentage of original dry deposition of sulfur which occurs when emissions of sulfur in the Ohio Valley are reduced by 90% (OSCAR 4)

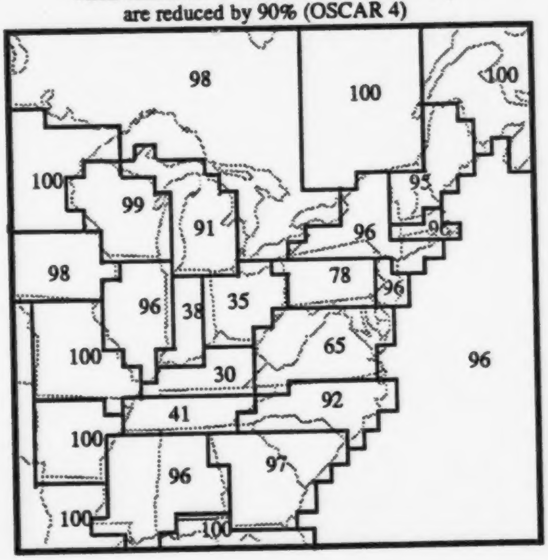

98
100
100
100
99
91
95
96
96
98
78
96
96
38
35
65
100
96
30
92
41
100
97
96
100
100

Fig. 5.19

Percentage of original wet deposition of sulfur which occurs when emissions of sulfur in the Ohio Valley are reduced by 90% (OSCAR 1)

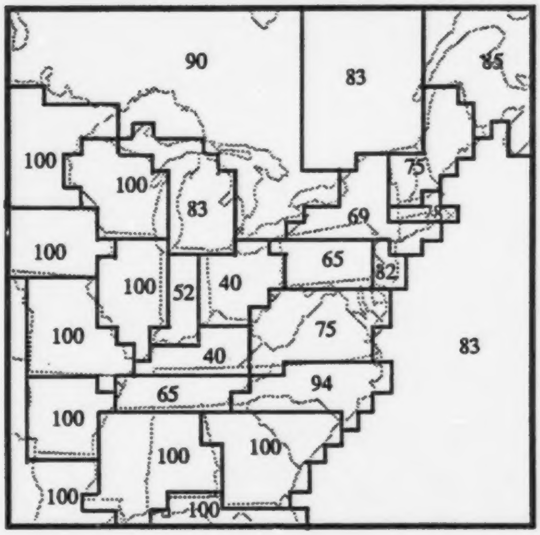
90
83
85
100
100
83
75
69
100
65
82
100
52
40
75
100
40
83
94
65
100
100
100
100
100

Fig. 5.20

Percentage of original wet deposition of sulfur which occurs when emissions of sulfur in the Ohio Valley are reduced by 90% (OSCAR 4)

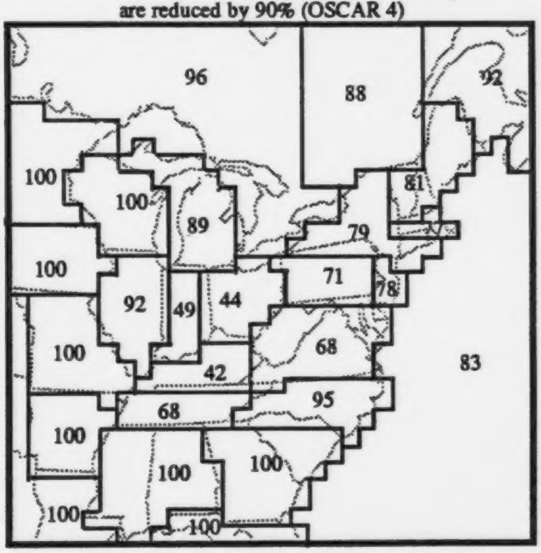
96
88
92
100
100
89
81
79
100
71
78
92
49
44
68
100
42
83
95
68
100
100
100
100
100

is wet (Figs. 5.1 and 5.2), we note that decreasing emissions 90% will decrease the average deposition in Kentucky by only 66%, which is the closest any region approaches linearity. Kentucky approaches linearity apparently because of the meteorological conditions considered. Most of the import of sulfur to Kentucky comes from the neighboring states of Indiana and Ohio which also underwent emissions reductions.

Focusing on the state of New York, and again averaging the two episodes, we note that decreasing the emissions by 90% in the Ohio Valley decreases the dry deposition in New York by 12% (i.e., 20% in OSCAR I and 4% in OSCAR IV) and the wet deposition by 26% (31% in OSCAR I and 21% in OSCAR IV).

5.4 Computational Performance of RADM

The first version of the Regional Acid Deposition Model must reside entirely in the fast or core memory of a computer (for example, the Cray-1 computer at NCAR) and is thus referred to as the in-core model. In RADM I, there are 24 transported species and 5400 grid cells, i.e., 30-by-30 grid cells in the horizontal and six layers in the vertical. As depicted in Fig. 5.21, the first generation RADM operates on a subdomain of the meteorological domain (46x61x15) forecast by the mesoscale model.

To allow for model expansion in terms of adding more complex physical parameterizations and/or enlarging the geographical area of coverage, an out-of-core model was developed which keeps only a portion of the data in core memory and swaps the rest of the data to and from disk as required. For the same grid and chemical mechanism, this model produces identical results to the in-core model, but because of increased I/O, preliminary results show that the out-of-core model costs 70% more than the in-core model based on the charging algorithm of the NCAR Cray 1 computer. However, the out-of-core model allows expansion of the chemical mechanism and/or the domain size. Fig. 5.22 compares the core memory requirements of the in-core model and the out-of-core model for different numbers of grid cells and the same number of transported chemical species. The out-of-core model could expand to the entire meteorological grid with additional space remaining to increase the number of transported species or the complexity of the physical parameterizations.

Current CPU usage on the Cray 1 is about 20 minutes for a one day simulation with in-core model (compared to 40 min/day in Jan. 1985), using 30x30x6 grid cells and 24 transported species. Extrapolation to a 46x61x6 domain yields an estimate of one hour of Cray CPU time per model day of simulation in out-of-core model. The full meteorological domain of 46x61x15 would require 2.5 hours of Cray CPU time. There are steps which may be taken to speed up RADM II without seriously degrading model performance. The advective time step could be increased significantly and still remain well within the stability criteria dictated by the mathematics of finite differencing. It has yet to be determined whether this action would force the chemical time step to become so small as to negate any advantage gained. Possible improvements to the chemical solver could lessen the restrictions posed on the chemical time step. On the other hand, adding chemical species and/or reactions to the chemical mechanism would increase both CPU and core utilization. Furthermore, tests run on a VAX computer indicate that implementation of the more complex PLUVIUS

Fig. 5.21

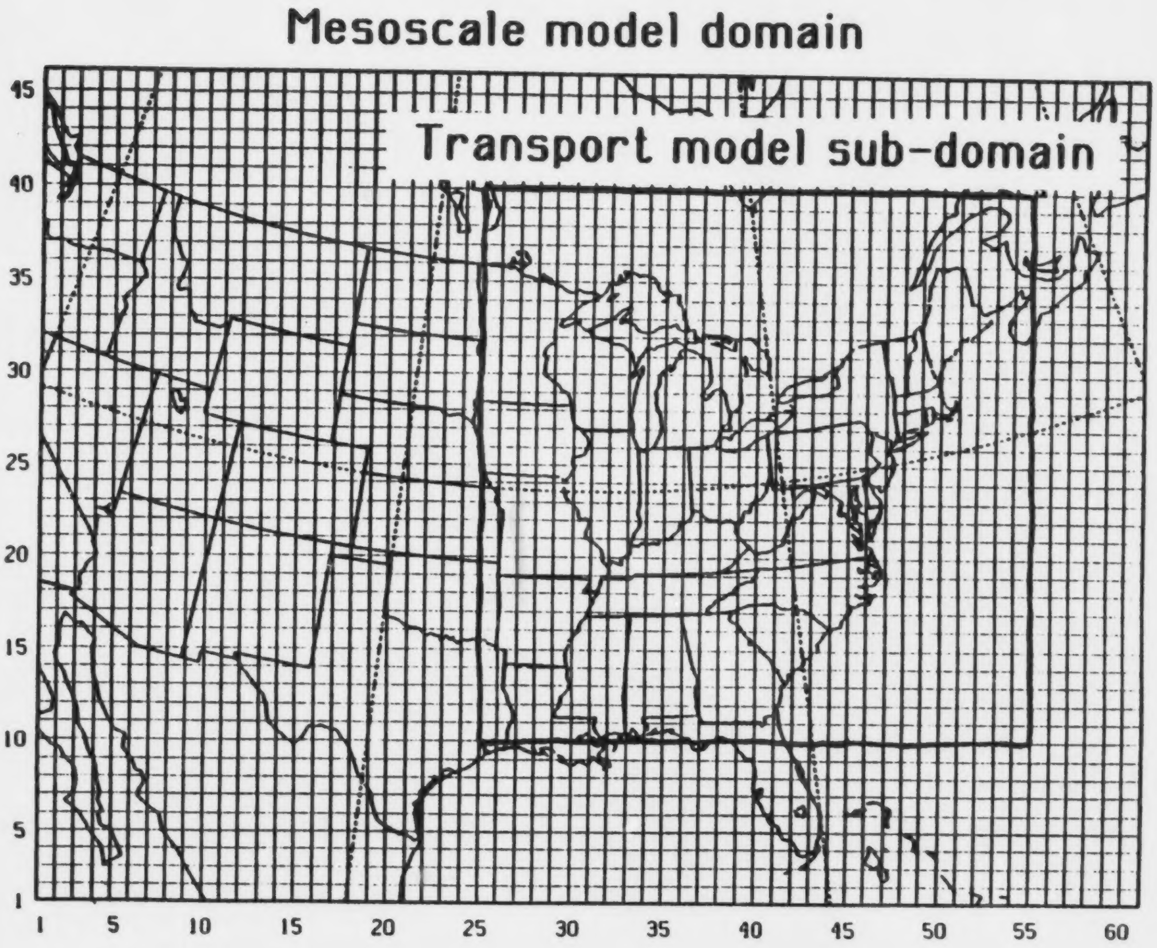

Mesoscale model domain

Transport model sub-domain
45
40
35
30
25
20
15
10
5
1
1
5
10
15
20
25
30
35
40
45
50
55
60

Fig. 5.22

RADM's memory requirements
for various numbers of grid cells

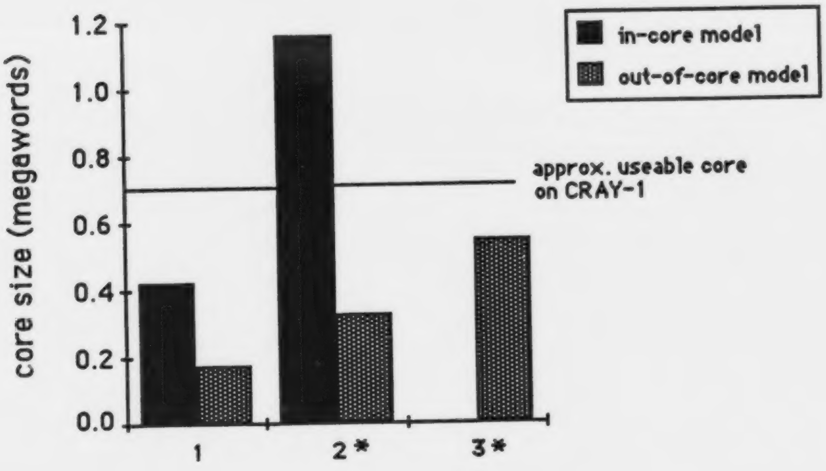

1: 30x30x6 = 5400 grid cells
2: 46x61x6 = 16836 grid cells
3: 46x61x15 = 42090 grid cells
*: in-core model impossible on CRAY 1

scavenging module would have a CPU requirement 3-6 times greater than the current scheme. This factor is not prohibitive, considering that cloud processes and aqueous chemistry currently constitute only about 5% of the total RADM CPU utilization.

The out-of-core model can predict acid deposition over a larger domain with the same 80 km horizontal grid size. In addition, the out-of-core model used with a larger horizontal domain can test the impact of the imperfectly known lateral boundary conditions for chemical species. For example, we could perform equivalent runs with the two models and compare results near the boundary of the smaller subdomain.

SECTION 6

DATABASES FOR RADM EVALUATION STUDIES

6.1 Introduction

The evaluation of RADM involves the assessment of the databases used for model execution and evaluation at each step of the evaluation process from submodels to the complete model. This section focuses on the assessments of databases used for various studies. Included are a description of the air quality databases, the emissions databases, and the precipitation databases. The limitations and uses of smog chamber data in evaluating RADM chemistry are also discussed.

6.2 Air Quality Databases

The chemical data required for RADM execution and evaluation are described in more detail in Middleton (1985a). A summary of these needs is given in Table 6.1. Information on emissions of major gases and aerosols is required to drive the model. Ambient concentrations of major chemicals are required to determine initial and boundary conditions of the model. Concentrations and deposition measurements are needed for model evaluation. Table 6.1 lists only the types of chemical species information required. The optimum feasible spatial domain and resolution and the temporal periods and frequency of the data are still under investigation. The list of chemical species information required may also need to be modified as model studies reveal the relative importance of the different species.

The results of our survey of the major regional scale databases currently available for use in RADM studies are outlined in Table 6.2. These databases are categorized into concentration, deposition, emission, meteorological, and land use databases. Included are databases that are generally recognized as the most comprehensive, up-to-date information for each category.

The potential usefulness of these data for RADM evaluation was investigated on a preliminary basis by comparing the chemical data coverage for different meteorological conditions. The conditions were chosen to represent all of the major conditions thought to occur during the course of a year. A number of candidate case study periods were then chosen based on the availability of meteorological and chemical data for these conditions. The matching of chemical data with the case study periods is summarized in Table 6.3. From this matching, it can be seen that the OSCAR intermediate scale database provides the most comprehensive database for the study of regional scale precipitation chemistry on highly resolved spatial and temoral scales.

Table 6.1 Chemical Data Requirements for RADM*

DATA AVAILABLE (___); DATA NOT YET AVAILABLE (--); DATA NOT NEEDED ( ).

	EMISSIONS	INITIALIZATION AND BOUNDARY CONDITIONS	EVALUATION
Gases			
SO_2	___	--	--
NO_2	___	--	--
NO	___	--	--
Total VOC	___	--	--
Alkanes (not methane)	___	--	--
Methane	___	--	--
Alkenes (not propylene or ethylene)	___	--	--
Propylene	___	--	--
Ethylene	___	--	--
Aromatics	___	--	--
Aldehydes (not formaldehyde)	___	--	--
Formaldehyde	___	--	--
Organic Acids (not formic)	___	--	--
Formic Acid	___	--	--
CO	___	--	--
NH_3	___	--	--
HCl	--	--	--
HF	--	--	--
H_2S	--	--	--
DMS	--	--	--
O_3		--	--
PAN		--	--
HNO_3		--	--
H_2O_2		--	--
OH		--	--
HO_2		--	--
RO_2		--	--

Table 6.1 (continued)

	EMISSIONS	INITIALIZATION AND BOUNDARY CONDITIONS	EVALUATION
Aerosols			
Sulfate	┬	┬	┬
Total Mass	┆	┆	┆
Nitrate	┆	┆	┆
Graphitic Carbon	┆	┆	┆
Organic Carbon	┆	┆	┆
Acidity	┆	┆	┆
Alkaline Dust	┆	┆	┆
Sea Salt	┆	┆	┆
Iron	┆	┆	┆
Manganese	┴	┴	┴
Precipitation and Clouds			
Total Water Content		┬	┬
Nitric Acid		┆	┆
Sulfuric Acid		┆	┆
Organic Acids		┆	┆
Carbon		┆	┆
H^+		┆	┆
Na^+		┆	┆
Ca^{++}		┆	┆
K^+		┆	┆
Mg^{++}		┆	┆
Fe^{+++}		┆	┆
Mn^{++}		┆	┆
$SO_4^=$		┆	┆
NO_3^-		┆	┆
NH_4^+		┆	┆
Cl^-		┆	┆
F^-		┴	┴

*This list is not inclusive. Other chemicals may need to be added or subtracted.

Table 6.2 Summary of Major Regional Chemical Data Bases

WET DEPOSITION	Spatial Domain & Resolution	Time Period	Temporal Resolution	Parameters
APN	Canada 9 stations (Fig. 1)	Nov 78-present	Daily	Field & Lab pH $SO_4^{=}$, NO_3^{-}, Cl^{-}, CA^{++}, NH_4^{+}, MG^{++}, Na^{+}, K^{+}
APIOS	Canada 16 stations (Fig. 1)	July 80-present	Daily	pH, acidity, $SO_4^{=}$, $N\text{-}NO_3^{-}$, $N\text{-}NH_4^{+}$, Cl^{-}, Na^{+}, K^{+}, Ca^{++}, Mg^{++}, conductivity
CANSAP	Canada 53 stations (Fig. 2)	Jan 77-present	Monthly	$SO_4^{=}$, NO_3^{-}, NH_4^{+}, Cl^{-}, Na^{+}, K^{+}, Ca^{++}, Mg^{++}, acidity, alkalinity, pH, conductivity
EPRI/SURE	NE US 9 stations (Fig. 3)	Jan 79-Dec 80	Event	pH, specific conductance, $SO_4^{=}$, NO_3^{-}, Cl^{-}, $PO_4^{\equiv}$, NH_4^{+}, Na^{+}, K^{+}, Ca^{++}, Mg^{++}, Al^{+++}, strong acids, total acids, total organic carbon
MAP3S	NE US 9 stations (Fig. 3)	Sept 76-present	Event	pH, conductivity, $SO_3^{=}$, $SO_4^{=}$, NO_2^{-}, NO_3^{-}, Cl^{-}, $PO_4^{\equiv}$, NH_4^{+}, Na^{+}, Mg^{++}, Al^{+++}, K^{+}, Ca^{++}
NADP	US > 100 stations (Fig. 4)	July 78-present	Weekly	pH, conductivity, $SO_4^{=}$, NO_3^{-}, Cl^{-}, $PO_4^{=}$, NH_4^{+}, Na^{+}, K^{+}, Mg^{++}, Ca^{++}
UAPSP	E US 20 stations (Fig. 3)	Jan 79-present (5 SURE sites) 81-present (other sites)	Event	pH, conductivity, total acidity, strong acidity, $SO_4^{=}$, NO_3^{-}, Cl^{-}, $PO_4^{\equiv}$, NH_4^{+}, Na^{+}, K^{+}, Ca^{++}, Mg^{++}

Table 6.2 (continued)

SURFACE CONCENTRATION	Spatial Domain & Resolution	Time Period	Temporal Resolution	Parameters
NEROS II	NE US State Network sites	14 July-15 Aug 80	Hourly	SO_2, NO, NO_2, O_3
			24-hr	TSP, $SO_4^{=}$, NO_3^{-}
	Columbus OH 4 SURE NECREMP (Examples in Fig. 8)	14 July-15 Aug 80 (Regional missions (1-2, 5-9 Aug 80)	Variable	SO_2, SO_4, NO-NO_x, O_3, b_{scat}, ANC, HC; aerosol $SO_4^{=}$, NO_3^{-} (<3.5 µm); temp, dew pt., light levels
OSCAR	NE US State Network sites (selected semi-rural sites in Fig. 9)	April 81	Hourly	SO_2, NO, NO_2, O_3
			24-hr	TSP, $SO_4^{=}$, NO_3^{-}
	Huntington, IN (Fig. 5)	8-9,13-14, 22-23 April 81	Variable	Aerosol $SO_4^{=}$, NO_3^{-}, NH_4^{+}, Strong acid with variable size discrimination; HNO_3, SO_2, NO, NO_x, O_3, PAN, H_2O_2, b_{scat}, dew pt.
	Long Island (Fig. 5)	10, 11-15, 22-26 April 81	Variable	NO_x, O_3; limited SO_2, NHO_3, Aerosol S
State Network	US mainly urban	1977-present	Hourly	O3,SO2,NO,NO2,CO,TSP

Table 6.2 (continued)

METEORO-LOGICAL DATA	Spatial Domain & Resolution	Time Period	Temporal Resolution	Parameters
SURE	NE US	July 77-Nov 78	Hourly	Standard NWS surface
	NE US	June 77-Oct 78	12-hr	Standard NWS upper air
	2 sites, several tracks	3-7 days during Aug, Oct 77, Jan, Apr, July, Oct 78	Continuous	Standard aircraft
OSCAR	NE US	April 81	Hourly	Standard NWS surface
			12-hr	Standard NWS upper air
	NE ID - NW OH, NJ, WV, OH, DE, PA	8-9, 13-14, 16, 22-23 April 81	Continuous	Standard aircraft
NEROS	NE US	Aug 79, 14 July-15 Aug 80	Hourly	Standard NWS surface
			6-hr	Standard NWS upper air
			Continuous	Standard aircraft
CAPTEX	NE US, SE Canada	Sept-Oct 83	$C_7 F_{14}$ Tracer releases (5 from Dayton, Oh, 2 from Sudbury)	Surface air and aircraft samples, standard NWS data

Table 6.2 (continued)

LAND USE	Spatial Domain & Resolution	Time Period	Temporal Resolution	Parameters
EPA	US and parts of Canada 20×20 km (extension of NEROS land use)	~1980	-	Categories: urban, agricultural, range, deciduous forest, mixed forest, water features, barren, non-forested wetland, mixed agricultural and range, low-growing shrub areas
NASA	1°×1° km	~1980	-	Similar categories to EPA

Table 6.2 (continued)

EMISSIONS	Spatial Domain & Resolution	Time Period	Temporal Resolution	Parameters
SURE	NE US, parts of Canada 80×80 km (Fig. 6)	1977	Diurnal (8 3-hr periods) for each season	SO_x, NO_x, HC, TSP All sources Utilities only
		Aug, Oct 77; Jan-Feb, Apr, Jul 78		Major electric utility sources
NAPAP	US, (parts of Canada by 9/85) 20x20 km	Typical 1980 summer day (seasonal weekend/weekday by 9/85)	Hourly	Human caused SO_4,SO_2,NH_3,NO,NO_2 HC(10 cateogires)
	US (maybe regional)	Annual (maybe seasonal)		Sulfur, Natural Some natural NH_3, natural; VOC maybe from expanded NEROS
EPRI	US, parts of Canada 40×40 km	1982 Seasonal weekday/weekend	3-hour	Human-caused, alkaline dust, sulfate, SO_2, NO, NO_2, NH_3, HC (9 categories) Some natural NH_3, dust

Table 6.2 (continued)

VERTICAL PROFILES	Spatial Domain & Resolution	Time Period	Temporal Resolution	Parameters
SURE	Spirals at 2 sites, several horizontals in NE US	3-7 days during Aug, Oct 77 Jan, Apr, July, Oct 78	Variable	SO_2, NO, NO_2, O_3, CN, b_{scat}, turbulence, temp, dew pt, relative humidity, and aerosol mass, $SO_4^=$ and NO_3^- m size ranges
OSCAR	NE IN - NW OH, NJ, WV, OH, DE, PA	8-9, 13-14, 16, 22-23, April 81	Variable	SO_2, NO, NO_2, O_3, HC, HNO_3, CN, b_{scat} and aerosol H^+, NH_4^+, $SO_4^=$, NO_3^-, S, liq. H_2O content, temp, dew pt, relative hum, solar rad, UV, beta, cloud water pH and major ions
NEROS I	NE US Regional Flights (Fig. 7 for examples)	3-5, 13-14, 15-17, 30-31, Aug 79	Variable	SO_2, 03, NO_x, NO, CN, b_{scat}, UV, solar, RH, dew pt, temp
NEROS II	NE US Regional Flights	24,25,30 July; 1,2, 5-9,10,11 Aug 80	Variable	SO_2, SO_4, NO-NO_x, ANC, HC; Aerosol $SO_4^=$, NO_3^-(<3.5 μm); temp, dew pt, turbulence

Table 6.3 Chemical Data Availability for Candidate RADM Case Study Periods

	1977		1978		1979											1980		1981			
	Aug 3-6	Oct 27-30	Jan 21-24	Jul 17-23	Nov 25-27	Dec 23-25	Jan 12-14	Jan 20-22	Mar 3-5	May 8-10	Jun 28-30	Jul 24-26	Aug 10-12	Aug 3-5	Aug 13-18	Aug 1-2	Aug 5-9	Apr 16-18	Apr 8-10	Apr 12-15	Apr 22-24
GASES																					
SO_2 NO_2 NO O_3 VOC NH_3	SURE Class I & II Surface hourly Vertical variable				Class I Surface hourly					STATE NETWORKS # Surface hourly				NEROS Surface hourly Vertical variable				OSCAR Surface hourly Vertical variable			
PAN HNO_3 H_2O_2 Radicals Others																		OSCAR Surface variable			
AEROSOLS																					
Mass Sulfate Nitrate Ammonium Others	SURE Class I & II Surface 24-hour Vertical variable				Class I Surface 24-hour					STATE NETWORKS Surface 24-hour				NEROS Surface 24-hour Surface & Vertical Variable				OSCAR Surface & Vertical variable			
PRECIP.																					
pH Acidity $SO_4^=$ NO_3^- NH_4^+ Ca^{++} Na^+ Cl^- Others				$MAP3S^{\Delta}$ Event		EPRI/SURE Event UAPSP Event APN Daily					NADP Weekly CANSAP Monthly				$APIOS^{\Delta}$ Daily			High Density	OSCAR Surface sequential Vertical variable High and Intermediate Density		
EMISSIONS																					
SOX NOX VOC NH_3 DUST	SURE '77 Regional															NAPAP '80 U.S. & Canada				EPRI '82	

* Continuous monitoring network data are indicated in solid line boxes. Shorter term measurement programs are indicated in dashed line boxes. Coverage most complete for northeastern U.S. and southeastern Canada.

Daily average values for SO_2, sulfate and nitrate available from Canadian APN network since 1981.

Δ APIO network period is 1980-present. MAP3S network period is 1977-present. All other precipitation networks have periods of

The study of precipitation events was our first priority. Thus, the OSCAR case study periods were selected for our initial evaluation investigations. Investigation into the application of other databases for model evaluation is underway. For example, the SURE and NEROS databases may provide useful information primarily for evaluation of model performance on dry episodes. More localized databases such as the data from the OSCAR high density network could be used for studies of subgrid-scale processes. In addition, future field programs, if carefully designed, could provide more useful data for model evaluation. Similar screening processes to those used for the OSCAR databases will need to be implemented before using these other major databases for model evaluation studies.

6.3 Emissions Databases

The emissions databases developed by NAPAP (1985) and EPRI (1985) were used as the starting points for the development of the RADM emissions databases. These inventories were chosen because both came close to satisfying the spatial, temporal, and chemical species requirements of RADM. The development of these RADM emissions databases has been a major effort during the past year. The details of our investigations are being documented by Middleton (1986) and are summarized in this report. Major consideration regarding the uses of emissions databases in regional modeling has been discussed by Novak and Middleton (1985). A close working relationship with both NAPAP and EPRI has been established to insure that future improvements in the emissions databases will be more useful to the RADM modeling efforts.

The initial translation of these inventories into the model framework included allocation of emissions into the RADM grids, generation of hourly emissions for all of the emitted RADM chemical species, adjustment of the volatile organic carbon (VOC) categories, and allocation of sources into different vertical levels of the model. These translation processes are summarized in Table 6.4.

The resulting RADM emissions databases do not distinguish between point and area sources. Rather, emissions are allocated into different vertical levels of the model. As a result, major point sources are associated with the several upper levels of the model and area sources with the lowest level of the model. RADM requires emissions information at hourly intervals. While the NAPAP inventory supplied emissions on an hourly basis, the EPRI inventory supplied information on a 3-hour average basis. These data were linearly interpolated to derive hourly emissions from the 3-hour averages. Both inventories provided information on grids smaller than the current 80-km RADM grid. The translation of the other grid into the RADM was accomplished by a careful matching procedure based on the latitude and longitude of each individual grid. The conversion of the VOC categories for the two inventories into RADM was based on chemical reactivity similarities among the different species given for the inventories and for RADM.

After the translation process was complete, the two databases were checked for anomalously high values relative to the entire domain, emissions located in the ocean, unusual spatial patterns relative to earlier inventories, and other criteria such as locations of major metropolitan areas,

Table 6.4 Translation of NAPAP and EPRI Inventories into RADM Data Bases

	SPECIFICATIONS			CONVERSION PROCESSES	
	NAPAP	EPRI	RADM	NAPAP → RADM	EPRI → RADM
CATEGORIES	Major Point Gridded minor point Area	Point, Area	Totals	Aggregate gridded minor & area	
				Test points & area separately. Merge points & area.	
SPACIAL Domain	U.S.	U.S. & Canada	NE U.S., SE Canada	Use appropriate regions. Substitute EPRI Canada.	
Resolution Horizon (km)	20x20	40x40	80x80	Aggregate into RADM grids.	
Vertical*	Stack information given.		6 levels	Use stack information to determine point source levels.	
TEMPORAL Periods	Summer day	Day each season	Multiple days each season	Use available days.	
Frequency	Hourly	3-hr Avg	Hourly	Use directly	Linearly interpolate to hourly values
CHEMICALS Units	gm-moles/hr	gm/sec	gm/sec	NAPAP emissions x molecular wt /3600	no unit conversion
Chemicals**	SO_2	SO_2	SO_2	SO_2(64/3600)	SO_2
	SO_4	SO_4	SO_4	SO_4(98/3600)	SO_4
	NO	NO	NO	NO (30/3600)	NO
	NO_2	NO_2	NO_2	NO_2(46/3600)	NO_2
	NH_3	NH_3	NH_3	NH_3(17/3600)	NH_3
	ALK	PB	HC	ALK(.9x115.29/3600)	PB(.462)+>C_3
	OL3	>C_3	ETH	ALK(.1x115.29/3600)	NR(.15)+PB x .538)
	ARO	OL2	OL2	OL2(29/3600)	OL2
	ALD	>C_2	OL3	OL3(42/3600)	>C_2(.475)

Table 6.4 (continued)

	SPECIFICATIONS			CONVERSION PROCESSES	
	NAPAP	EPRI	RADM	NAPAP → RADM	EPRI → RADM
Chemicals**	HCHO	MAky	OL4	OL4(79/3600)	$>C_2$(.475)
	OL4	DTAky	TOL	ARO(.6x119.91/3600)	MAky
	CH_4	HCHO	XYL	ARO(.4x119.91/3600)	DTAky
	OL2	CARB	ORA	OA(111.75/3600)+ FA(49/3600)	$>C_2$(.05)
	OA	NRx	HCHO	HCHO(30/3600)	HCHO
	FA	Dust	ALD	ALD(48.39/3600)	CARB
		TSP			

* Plume height EPRI estimated from stack height, temp, and flow rate. Plume height NAPAP estimated from stack height, temp, exit velocity and stack diameter.

** Nonstandard codes:

ALK - alkanes
OL2 - ethylene
OL4 - other alkenes
ALD - aldehydes
FA - formic acid
XYL - xylene
PB - propane & benzene
$>C_3$ - $>C_3$ alkenes
CARB - other carbonyls
HC - hydrocarbons
OL3 - propyene
ARO - aromatics
OA - other organic acids
TOL - toluene
ORA - organic acids
$>C_2$ - $>C_2$ alkenes
MAKY - monoalklbenzenes
DTAKY - di and trialkylbenzenes
NRx - nonreactive gaseous organic compounds
Dust - alkalini dust

Standard Nomenclature:

TSP - total particulates
HCHO - formaldehyde
NO - nitric oxide
SO_4 - sulfate
CH_4 - methane
NH_3 - ammonia
NO_2 - nitrogendioxide
SO_2 - sulfur dioxide

inconsistent temporal patterns, and unusual balances among the different chemicals. These procedures are listed in Table 6.5.

As outlined in Table 6.5, magnitudes were checked for each category of chemical species. The values for the magnitudes were obtained from data reported by the inventory developers for state totals in each category. The spatial comparisons involved use of previous EPA and EPRI inventories and the inventory developed as part of the U.S.-Canadian Memorandum of Intent. Assessment of the observed temporal variations were based on temporal allocation factors reported by the developers and our previous experience with emissions databases. Assessment of chemical balances also was based in part on comparisons with previous inventory results and with group concensus regarding reasonable relationships among chemicals. More quantitative procedures for investigating the inventories are currently being studied.

Several problems were revealed during the checking process. Some of the more outstanding problems included: (1) exceptionally high values in the point sources for the EPRI inventory, (2) erroneous temporal patterns for VOC area sources in the NAPAP inventory, (3) problems with the Massachusetts emissions in both inventories, (4) missing Canadian data, and (5) unusual temporal patterns in some areas. In cases where the strange features could be traced back to real or strongly suspected errors, modifications were implemented. These corrections are outlined in Table 6.6. In future data screening studies, more detailed grid-by-grid checks on an emissions category-by-category basis should be carried out. This level of more detailed checking would more explicitly identify sources of problems. Such checking was not feasible given the previous structure of the NAPAP and EPRI databases.

Several of these corrections deserve closer inspection by the inventory developers. These include the anomalous points noted in problems (1), (2), and (5). The magnitude of these sources was substantial for some points and therefore could alter even the overall reported annual United States averages for the inventories.

After completing the checking procedures, the two emissions databases were compared with each other to determine the overall differences in the data. Since both inventories are based on similar data, comparison of the two can provide one indicator of uncertainty in the emissions. These comparisons revealed larger differences for VOC and NH_3 than for SO_x and NO_x. Some of the differences are displayed in Figs. 6.1(a-h) - 6.3(a-h) and in Table 6.7.

The overall regional average emissions for the two different inventories do not appear to be substantially different for the total RADM domain for SO_x as shown in Table 6.7. Differences become more pronounced for the other chemicals even at this total domain average level. The differences in VOC and NH_3 in particular are consistent with the fact that emissions for these chemicals are less well known than for SO_x and NO_x.

The spatial differences are illustrated in Fig. 6.1 (a-h). The spatial patterns (Fig. 6.1a and Fig. 6.1e) for daily average emissions of SO_x are quite similar for both databases. The patterns for NO_x (Fig. 6.1b and Fig. 6.1f), while still very similar, do reveal differences in a couple of highs

Table 6.5 Emissions Data Base Checking Procedures

	SOx	NOx	VOC	NH_3
Magnitudes				
1. Individual grids > Region totals				
Total EPRI (gm/sec x 10^5) Point	6.4	2.4	1.0	2.0
Total EPRI (gm/sec x 10^5) Area	.44	2.2	32.0	.66
Total NAPAP (gm/sec x 10^5) Point	6.4	2.4	1.0	2.0
Total NAPAP (gm/sec x 10^5) Area	.45	2.2	32.0	.66
2. Water grids (Figure 1)				
Spatial				
1. Compare to previous inventories	x	x	x	
2. Compare to maps siting urban centers	x	x	x	x
3. Compare to maps showing major SO_2 emissions	x			
4. Compare emissions at different heights	x	x	x	x
Temporal				
1. Domain Avg	x	x	x	x
2. Subdomain Avg	x	x	x	x
3. Individual grids	x	x	x	x*
Chemical Balances				
1. High VOC with SOx=NOx=0 points	x	x	x	
2. High NOx with low SOx points	x	x		
3. NOx/VOC		x	x	
4. Individual VOC/Total VOC			x	
Stack Parameters				
1. Temperature	$288.72°K < T \leq 1366.49°K$			
2. Height	$0 \leq H \leq 305m$			

* Weighting used to determine SOx, NOx and VOC

$$SOx = \frac{32}{64} SO_2 + \frac{32}{98} SO_4 \qquad NOx = \frac{14}{30} NO + \frac{14}{46} NO_2$$

$$VOC = \frac{24}{44} ALD + \frac{12}{30} HCHO + \frac{12}{46} ORA + \frac{48}{58} HC + \frac{24}{30} ETH + \frac{24}{28} OL2 + \frac{36}{42} OL3 + \frac{48}{56} OL4 + \frac{84}{92} TOL + \frac{96}{106} XYL$$

Table 6.5 (continued)

* Four VOC groups also were checked.

$$\text{VOC group 1} = \frac{48}{58}\,\text{HC} + \frac{24}{30}\,\text{ETH}$$

$$\text{VOC group 2} = \frac{24}{28}\,\text{OL2} + \frac{36}{42}\,\text{OL3} + \frac{48}{56}\,\text{OL4}$$

$$\text{VOC group 3} = \frac{24}{44}\,\text{ALD} + \frac{12}{30}\,\text{HCHO} + \frac{12}{46}\,\text{ORA}$$

$$\text{VOC group 4} = \frac{84}{92}\,\text{TOL} + \frac{96}{106}\,\text{XYL}$$

Table 6.6 Major Emissions Inventory Problems and Corrections

	PROBLEM	INVENTORY	CORRECTION
1.	VOC point sources excessive	EPRI	NCAR removed point sources where VOC $\geq 200 \frac{gm}{sec}$ and $SO_x = NO_x = 0$
2.	A few suspicious point sources on IL-IA boundary, southern MI, central MN, ID-IL border, and Cape Cod	EPRI	NCAR omitted suspicious point sources
3.	Eastern Canadian area sources missing from original tapes	EPRI	EPRI corrected
4.	VOC point sources missing from original tapes	NAPAP	NAPAP corrected
5.	Massachusetts sources incorrect	NAPAP EPRI	NCAR replaced Mass. NAPAP emissions with EPRI since EPRI < NAPAP
6.	VOC area sources for 3-9 GMT in eastern time zone erroneously high	NAPAP	NCAR linearly interpolated area sources between 3-9 GMT
7.	Canadian emissions not included	NAPAP	NCAR substituted EPRI for NAPAP emissions in Canadian grids
8.	A few point sources appeared to be slightly mislocated: southern MI, Northern WI, northern NY, and southwest NY	NAPAP EPRI	NCAR moved these point sources to more appropriate adjacent grids (<80 km moves)
9.	A few small, non zero point and area sources located in ocean	NAPAP EPRI	NCAR omitted sources
10.	A few VOC points in excess of domain average	EPRI	NCAR omitted sources (these points already removed in #1)

Table 6.7 Emission Totals (kg/ha/yr)*

	NAPAP			EPRI		
	POINT	AREA	TOTAL	POINT	AREA	TOTAL
SOX	11227.8	7268.4	18496.2	12234.1	5192.5	17426.6
NOX	2087.5	4004.3	6091.5	2387.8	4135.4	6523.1
VOC	40.3	17085.1	17125.3	68.3	13406.9	13475.2
NH3	537.9	3278.2	3816.1	552.8	6575.7	7128.5

*Point sources refer to sources being emitted into the model levels above the ground level. Area sources refer to sources being emitted into the ground level. Total refers to the total amount of substance emitted into the RADM domain. In order to convert daily average emissions in gm/sec into the kg/ha-yr units, emissions are multiplied by 0.049275. SOX, NOX, and VOC are expressed in terms of total sulfur, total nitrogen and total carbon, respectively.

that appear in the Ohio River Valley for EPRI but not for NAPAP. The VOC patterns (Fig. 6.1c and Fig. 6.1g) both capture the major metropolitan area emissions correctly. There are some differences in western Missouri. The magnitude of the St. Louis emissions for VOC also is different for the two inventories. The NH_3 patterns (Fig. 6.1d and Fig. 6.1h) show the greatest differences. Only the highs in the major metropolitan areas appear to be consistently represented in both databases. Other features are not comparable. The pattern of relatively close comparisons for SO_x and NO_x and more differences for VOC and NH_3 is consistent with the fact that VOC and NH_3 emissions are considered by the inventory developers to have the greatest uncertainty.

The temporal differences between the two databases are illustrated in the domain average graphs shown in Figs. 6.2 (a-h). As with the spatial patterns, SO_x and NO_x patterns (Figs. 6.2a,b,e, and f) are more similar than the VOC patterns (Figs. 6.2c and 6.2g). The patterns for NH_3 (Figs. 6.2d and 6.2h) are also more comparable than the VOC patterns. Midday peaks and nighttime lows are shown at basically the same times. A major difference, the appearance of bimodal daytime peaks for VOC in NAPAP but not in EPRI, can be explained in terms of the differences in the temporal patterns of the base inventories. As noted above, EPRI provides 3-hour average values for the emissions, while NAPAP provides hourly values. To convert EPRI data into hourly information, a linear interpolation was used. This results in pseudo-hourly data which cannot reproduce the possibly more realistic bimodal features found in the NAPAP inventory.

The differences between the inventories also are depicted in the VOC/NO_x ratios shown in Fig. 6.3 (a-d). These ratios are given for the first two model levels to illustrate the differences between point and area source ratios. Area and small point sources emit in the first level (k=1), and point sources with taller stacks or greater plume rise emit into higher levels (k=2, 3 and 4). The majority of point sources appear in level two. Considerable differences are revealed for the first level (Fig. 6.3a and Fig. 6.3c). Pronounced differences also appear in the second level. This is consistent with the differences in spatial patterns for VOC shown in Fig. 6.1 (a-h). Such large differences in the VOC/NO_x ratios suggest that the chemical reactivity for experiments using the two different databases could vary considerably at any particular location in the domain.

The sensitivity of RADM to emissions database differences was explored by using the two different inventories for otherwise identical model experiments. A close correspondence between accumulated event and hourly wet deposition patterns for sulfate, nitrate, and ammonium ion concentrations was found. The statistical studies described in Section 4.3 confirmed these observations of the close relationship between results for the model experiments using different emissions inventories. As shown in Table 4.6, the correlations between model and data are very similar for the experiments performed using the two inventories.

Additional studies are needed to further explore the sensitivity of RADM predictions to other important variations in emissions. Some preliminary studies have already been conducted to examine the sensitivity of RADM to

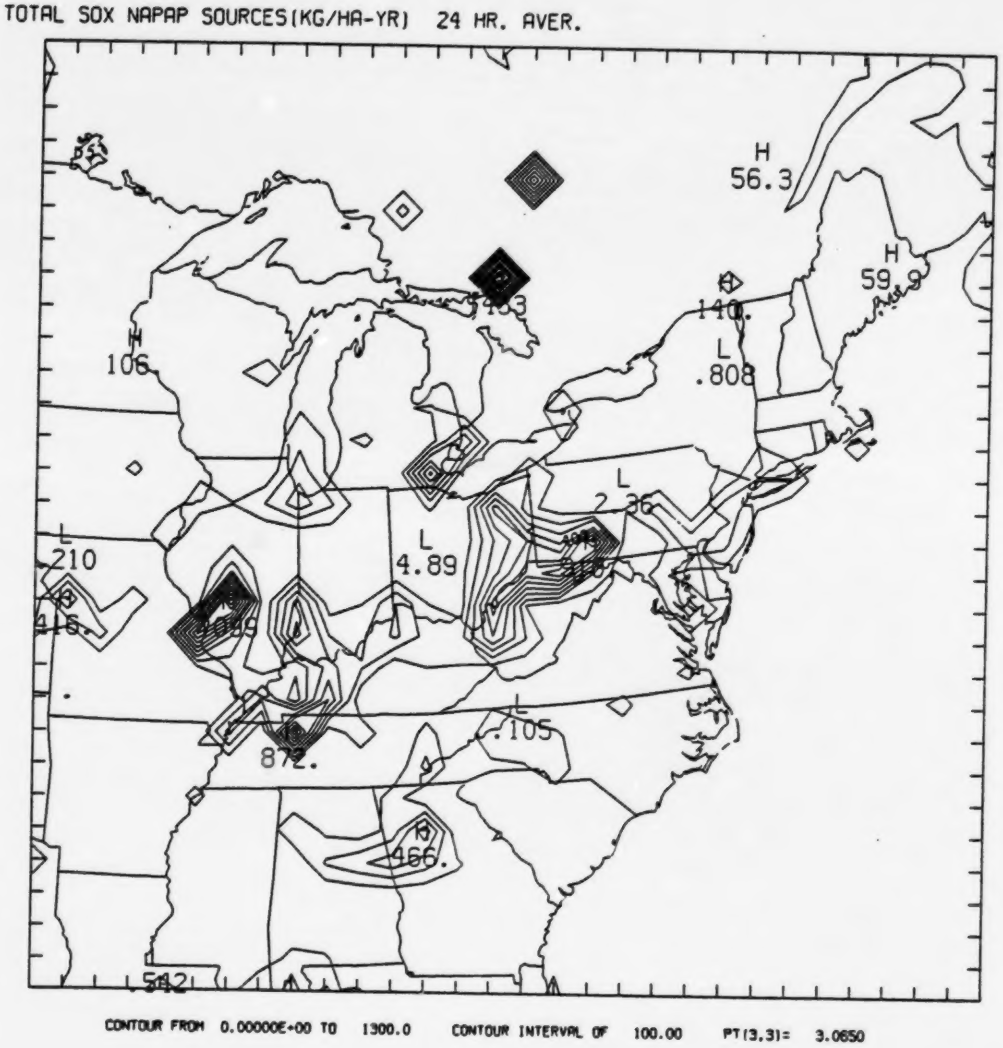
TOTAL SOX NAPAP SOURCES(KG/HA-YR) 24 HR. AVER.
H
56.3
H
59.9
1413
140.
L
.808
H
106
L
2.36
L
4.89
L
210
416.
1009
L
.105
872.
466.
.542
CONTOUR FROM 0.00000E+00 TO 1300.0 CONTOUR INTERVAL OF 100.00 PT(3,3)= 3.0650

Fig. 6.1a Contours of daily average emissions for SOX, NOX, VOC and NH3. SOX, NOX and VOC are expressed as total sulfur, total nitrogen and total carbon, respectively.

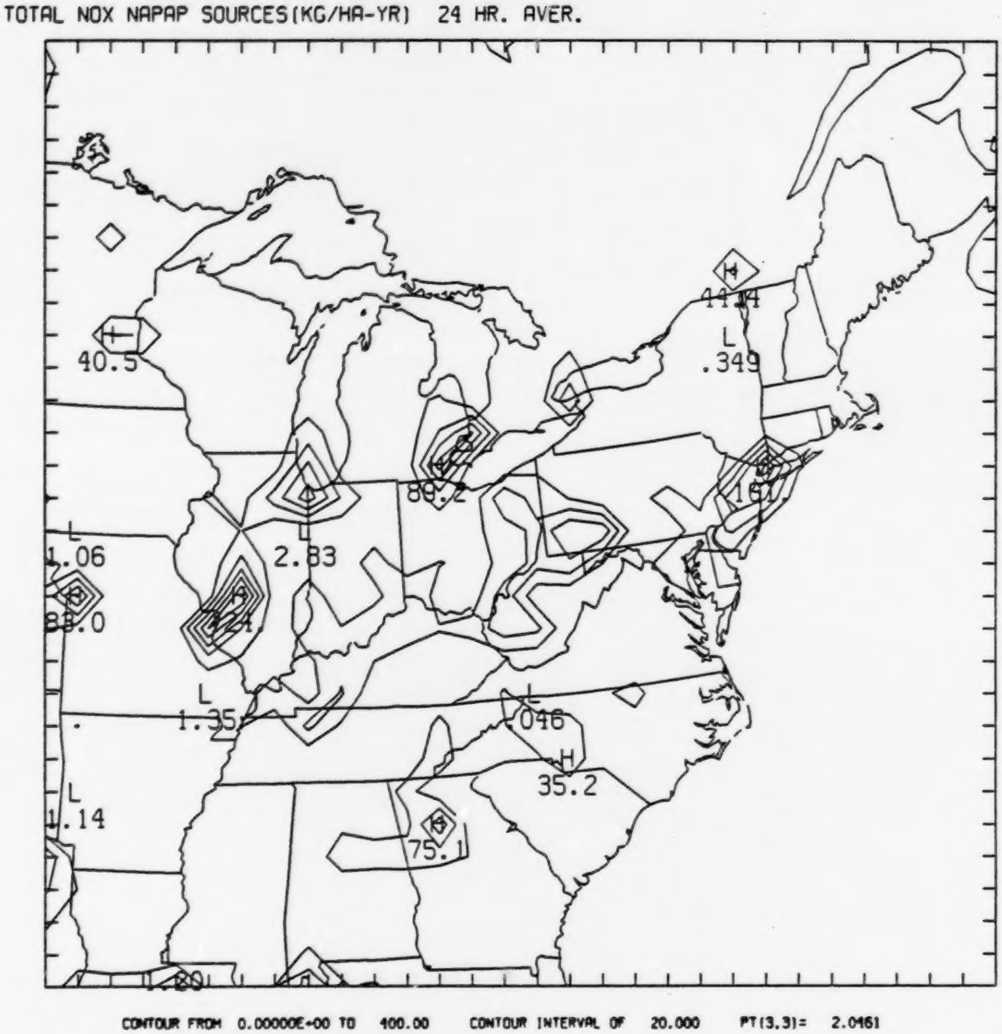
TOTAL NOX NAPAP SOURCES(KG/HA-YR) 24 HR. AVER.
H
414
L
.349
40.5
89.2
161
L
1.06
L
2.83
H
88.0
H
224
L
1.35
L
.046
H
35.2
L
1.14
75.1
1.20
CONTOUR FROM 0.00000E+00 TO 400.00 CONTOUR INTERVAL OF 20.000 PT(3,3)= 2.0161

Fig. 6.1b (Same as 6.1a)

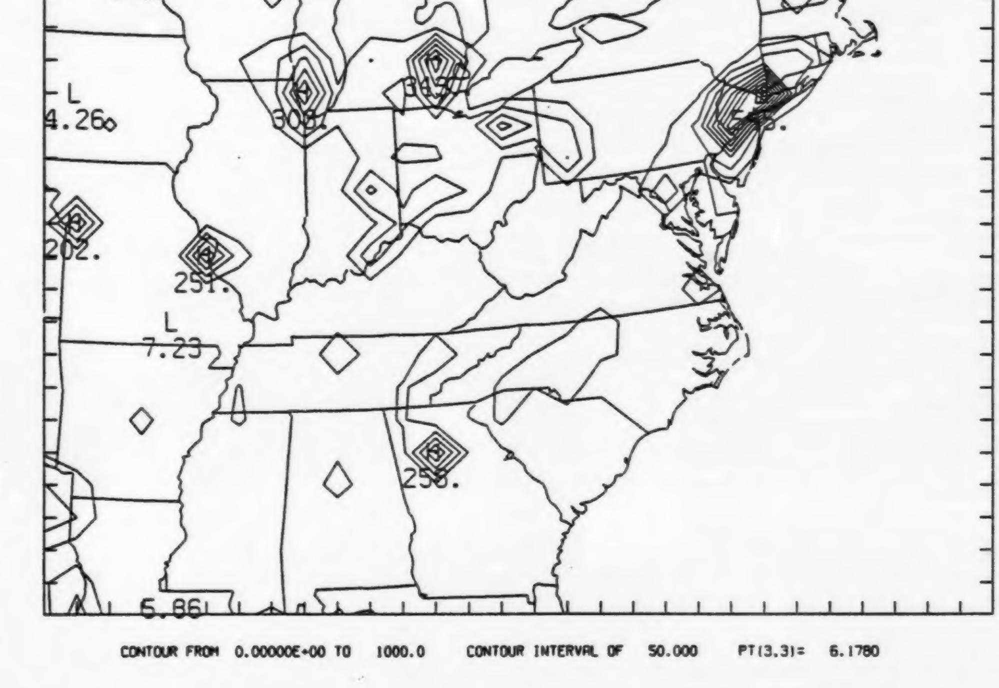
TOTAL VOC NAPAP SOURCES(KG/HA-YR) 24 HR. AVER.
179.
90.3
L
4.26
308.
202.
251.
L
7.23
258.
5.86
CONTOUR FROM 0.00000E+00 TO 1000.0 CONTOUR INTERVAL OF 50.000 PT(3,3)= 6.1780

Fig. 6.1c (Same as 6.1a)

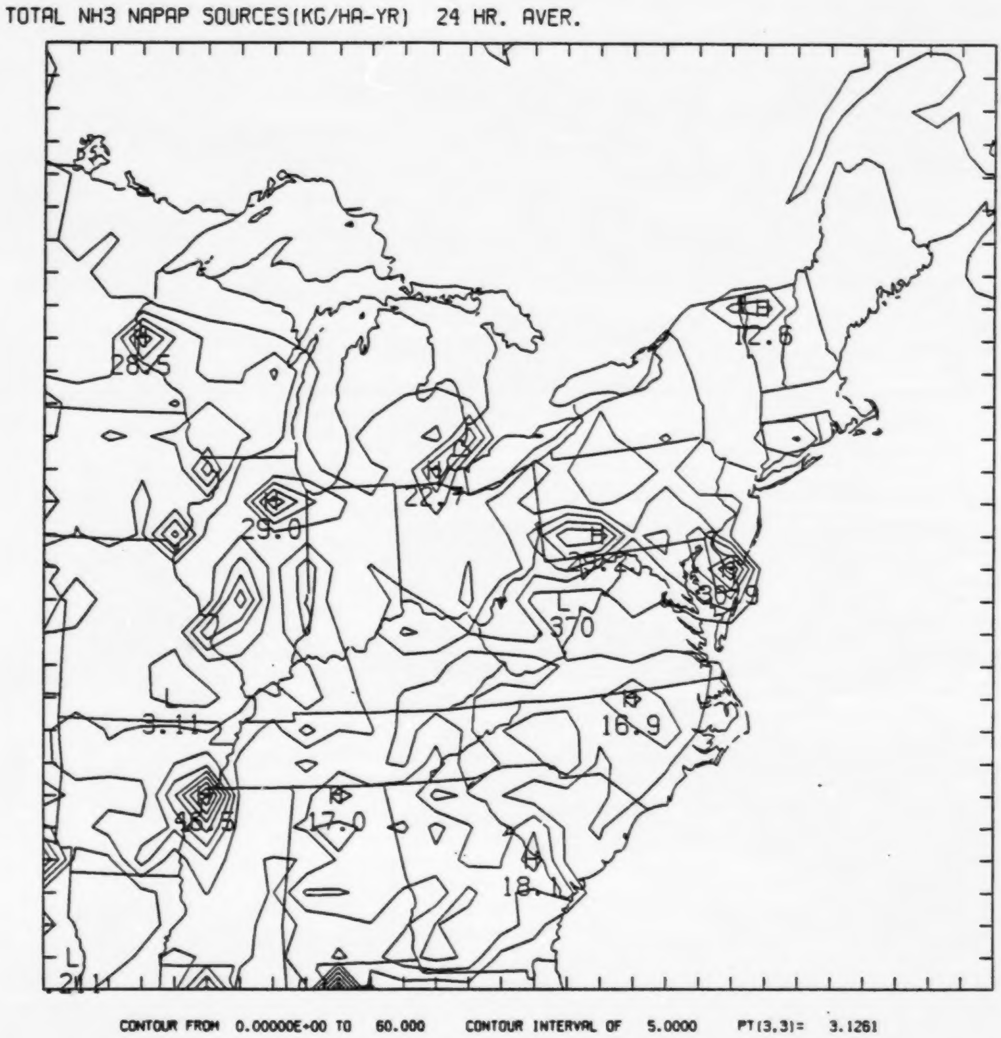

TOTAL NH3 NAPAP SOURCES(KG/HA-YR) 24 HR. AVER.
28.5
29.0
22.7
12.6
L
3.70
L
3.11
16.9
46.5
17.0
18.1
L
2.11
CONTOUR FROM 0.00000E+00 TO 60.000 CONTOUR INTERVAL OF 5.0000 PT(3,3)= 3.1261

Fig. 6.1d (Same as 6.1a)

TOTAL SOX EPRI SOURCES(KG/HA-YR) 24 HR. AVER.

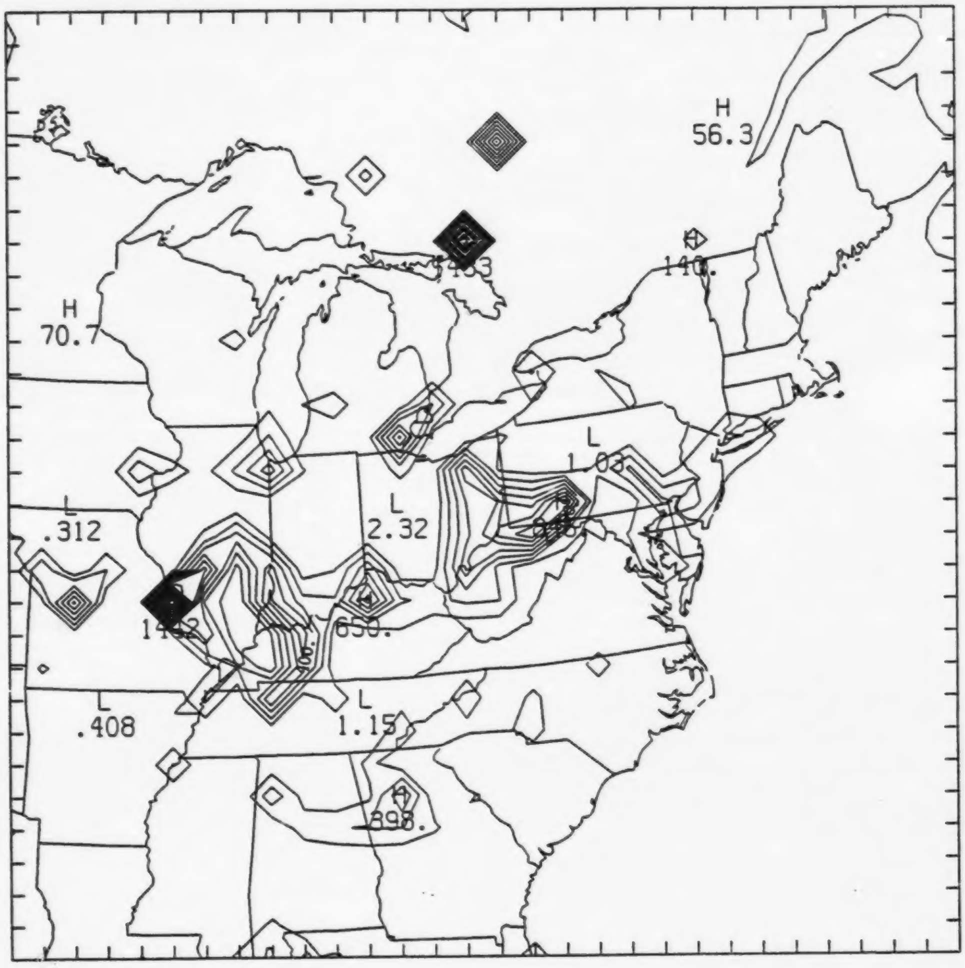
H
56.3
140.
H
70.7
L
1.03
L
2.32
L
.312
650.
L
.408
L
1.15
898.

CONTOUR FROM 0.00000E+00 TO 1300.0 CONTOUR INTERVAL OF 100.00 PT(3,3)= 2.2526

Fig. 6.1e (Same as 6.1a)

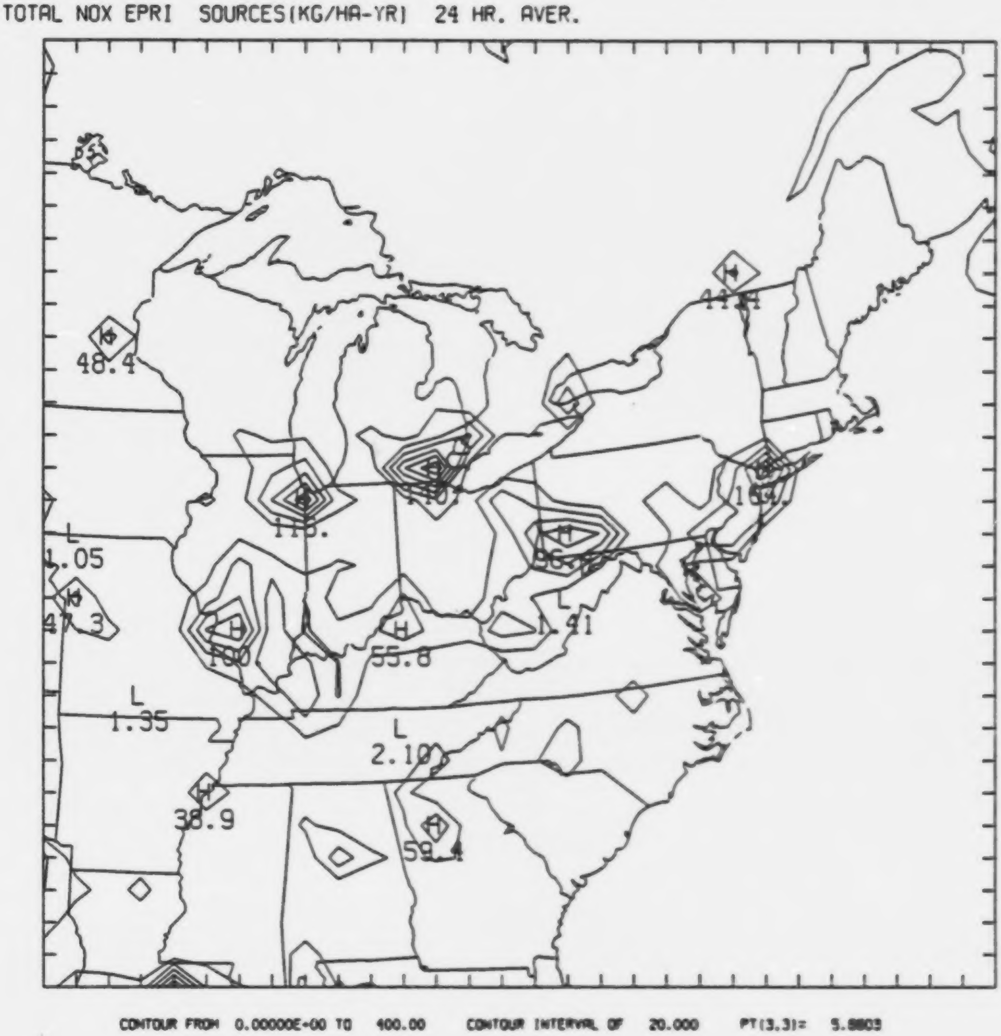
TOTAL NOX EPRI SOURCES(KG/HA-YR) 24 HR. AVER.
H
48.4
L
1.05
H
47.3
L
1.35
H
38.9
H
55.8
L
1.41
L
2.10
H
59.4
CONTOUR FROM 0.00000E+00 TO 400.00 CONTOUR INTERVAL OF 20.000 PT(3,3)= 5.8809

Fig. 6.1f (Same as 6.1a)

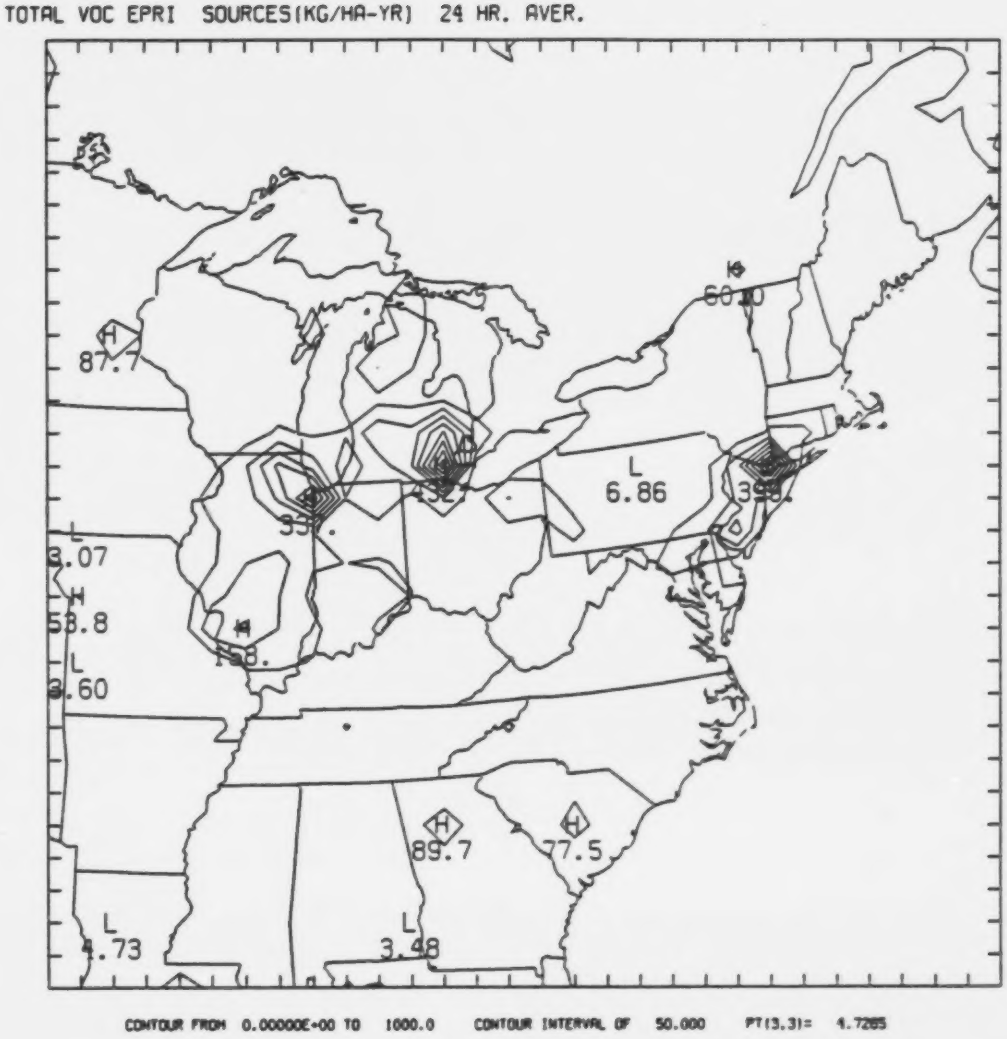
TOTAL VOC EPRI SOURCES(KG/HA-YR) 24 HR. AVER.
H
87.7
H
L
6.86
L
3.07
H
L
3.60
H
89.7
H
77.5
L
L
3.48
CONTOUR FROM 0.00000E+00 TO 1000.0 CONTOUR INTERVAL OF 50.000 PT(3,3)= 4.7265

Fig. 6.1g (Same as 6.1a)

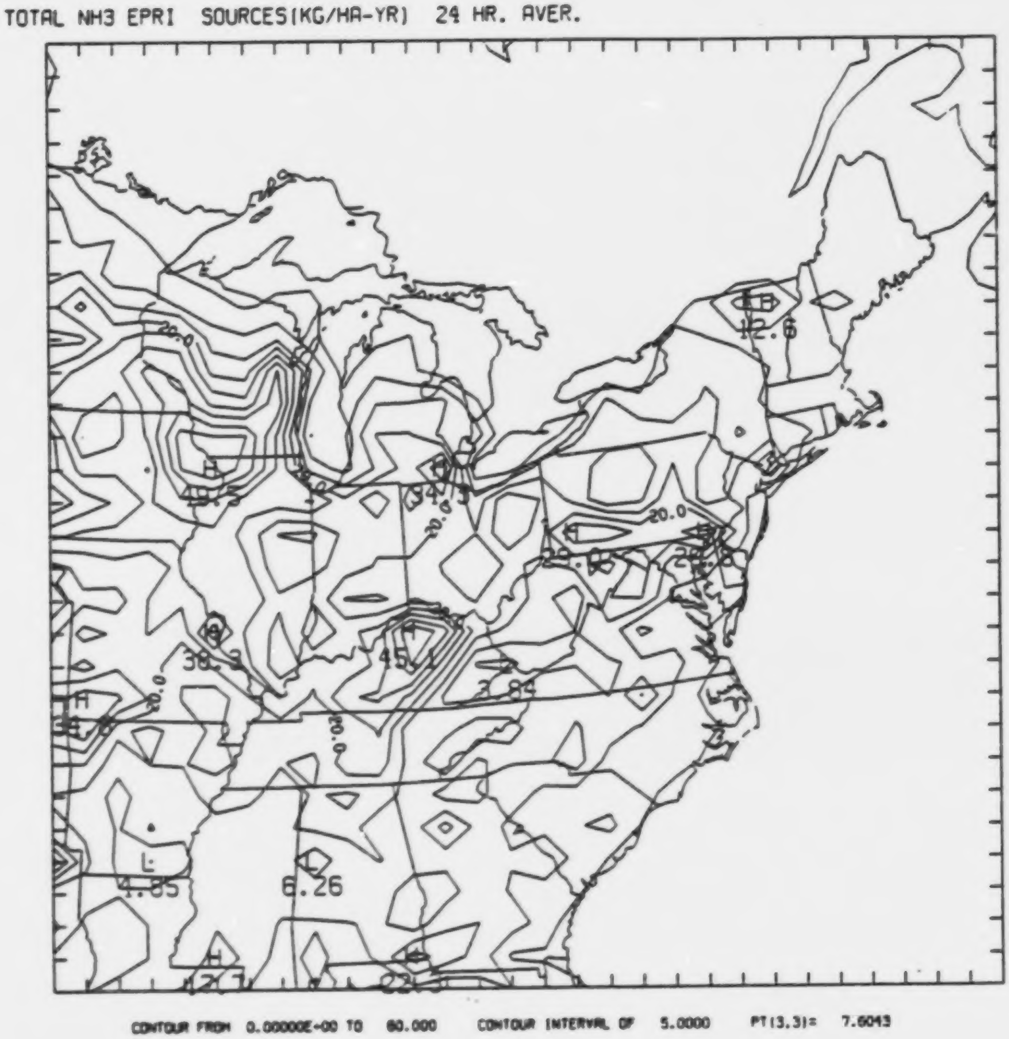
TOTAL NH3 EPRI SOURCES(KG/HA-YR) 24 HR. AVER.
20.0
H
19.3
H
34.3
20.0
20.0
H
12.6
H
38.3
H
45.1
3.84
H
L
4.85
L
6.26
H
CONTOUR FROM 0.00000E+00 TO 60.000 CONTOUR INTERVAL OF 5.0000 PT(3,3)= 7.6043

Fig. 6.1h (Same as 6.1a)

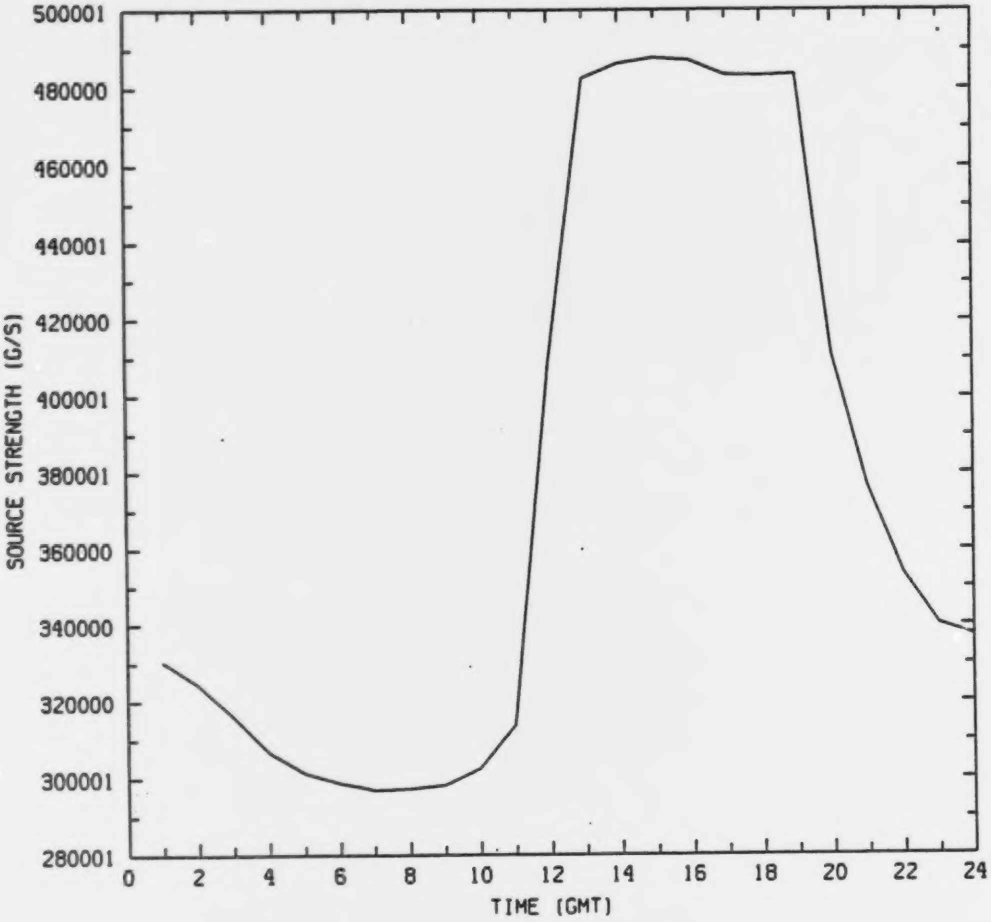

Fig. 6.2a Diurnal variations of RADM domain total emissions for SOX expressed as total sulfur. Data derived from NAPAP inventory.

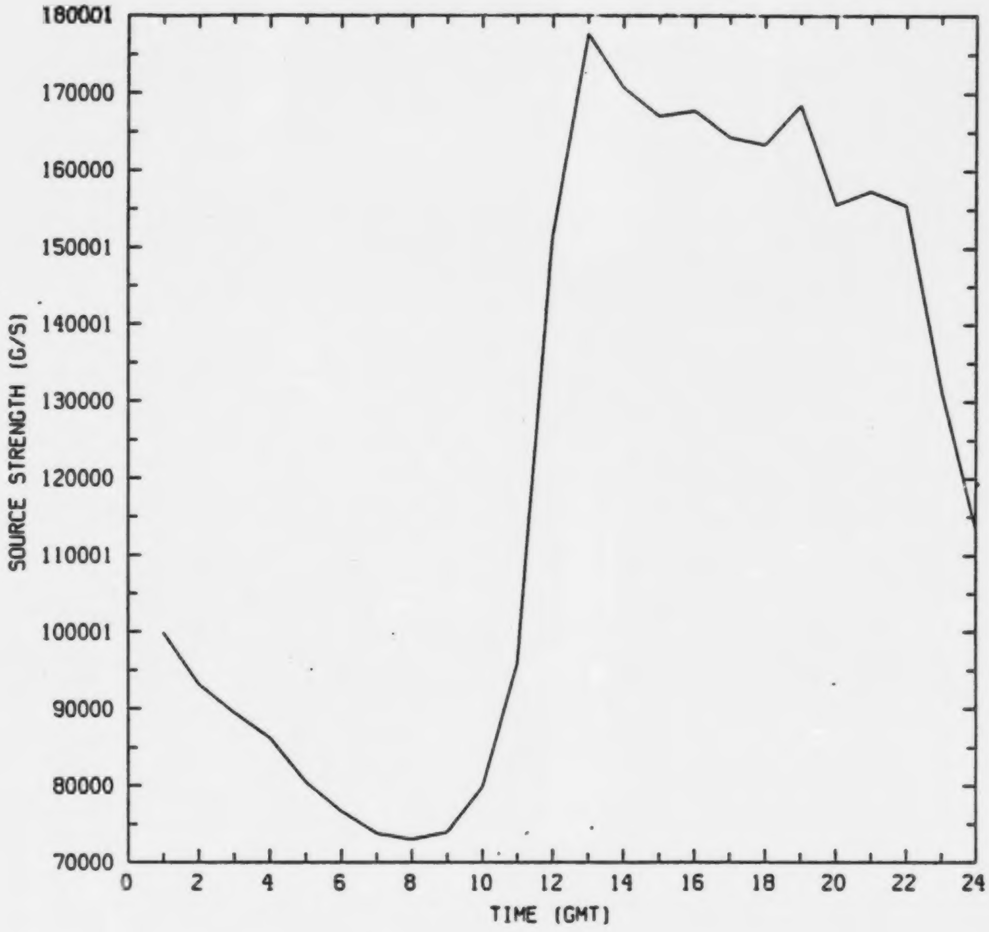

Fig. 6.2b Diurnal variations of RADM domain total emissions for NOX expressed as total nitrogen. Data derived from NAPAP inventory.

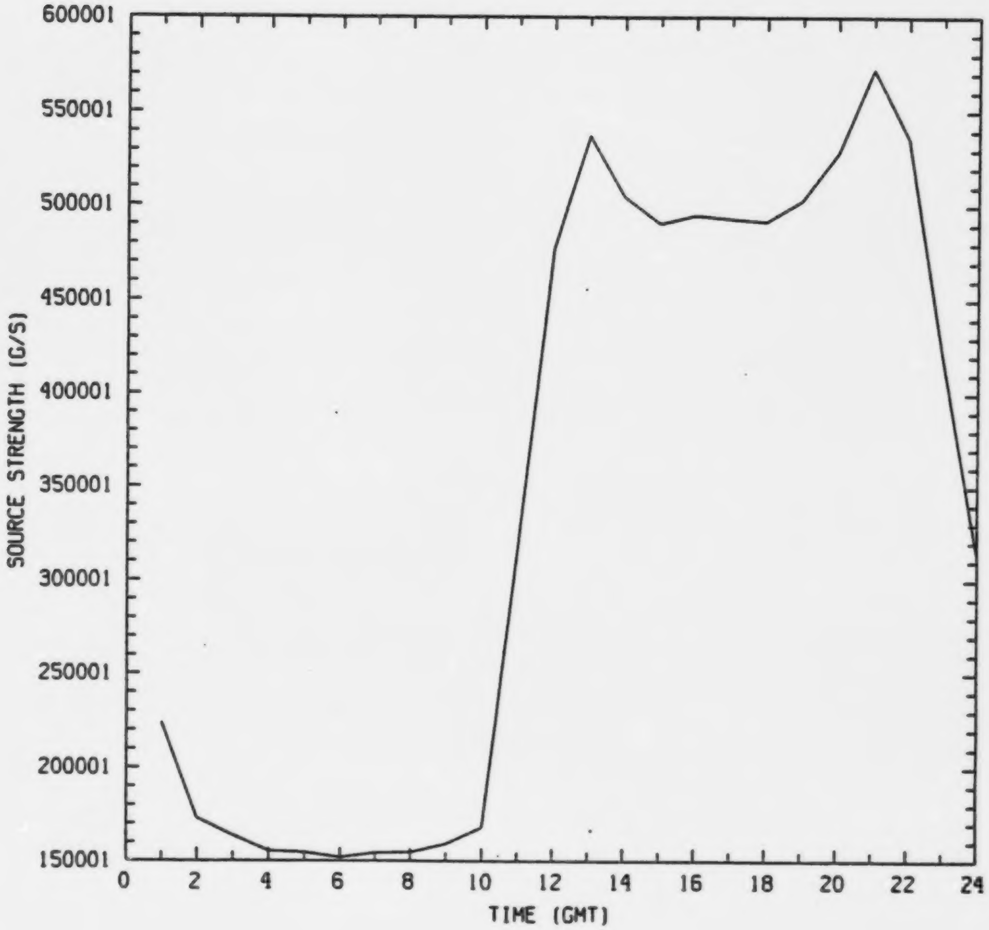

Fig. 6.2c Diurnal variations of RADM domain total emissions for VOC expressed as total carbon. Data derived from NAPAP inventory.

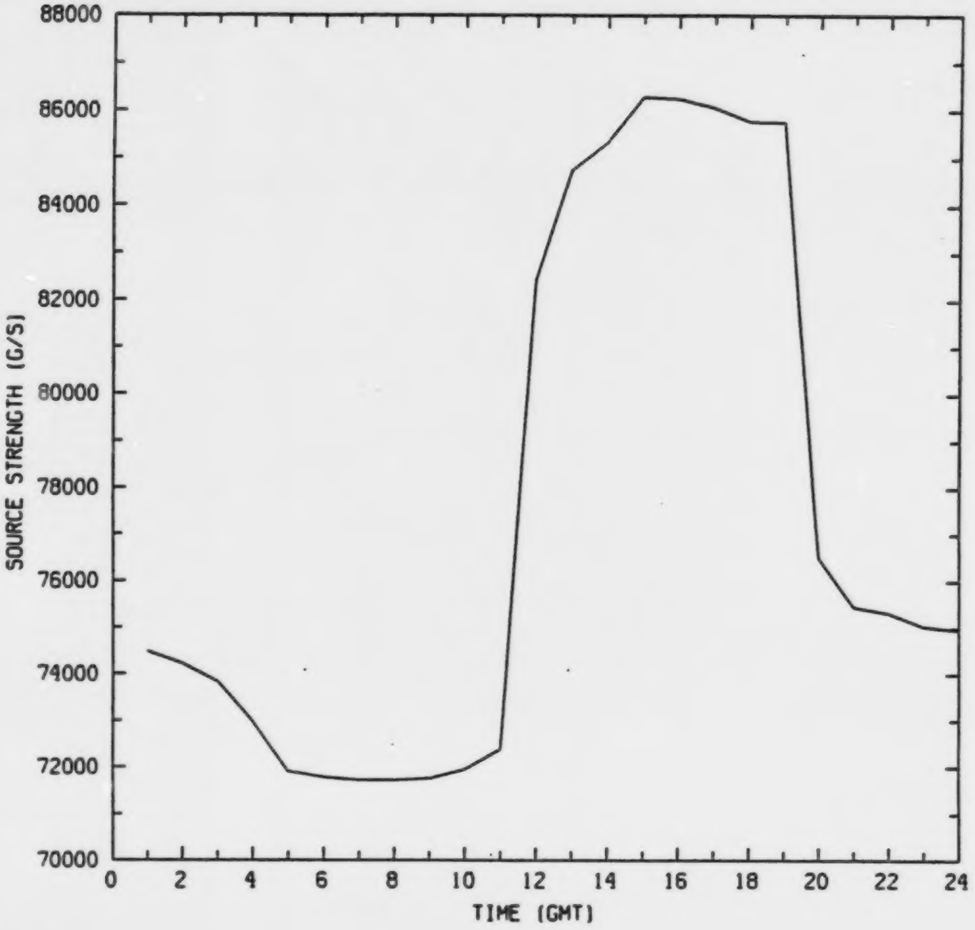

Fig. 6.2d Diurnal variations of RADM domain total emissions for NH3. Data derived from NAPAP inventory.

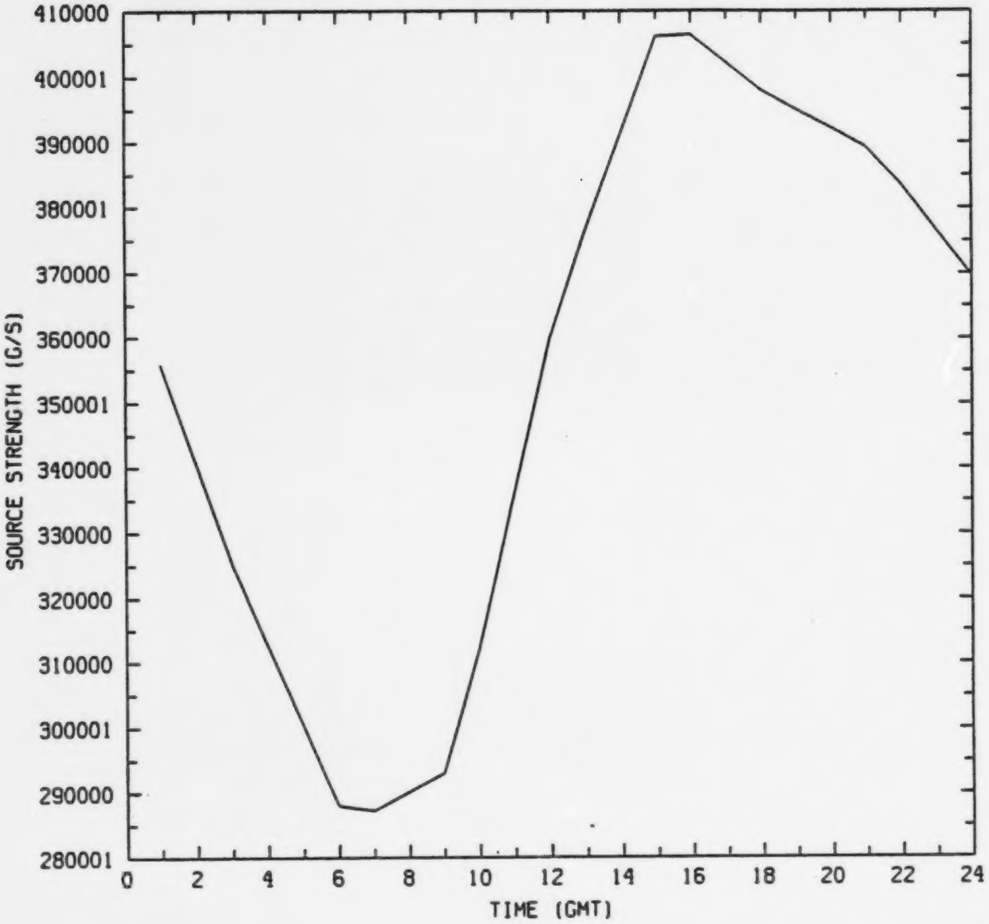

Fig. 6.2e Diurnal variations of RADM domain total emissions for SOX expressed as total sulfur. Data derived from EPRI inventory.

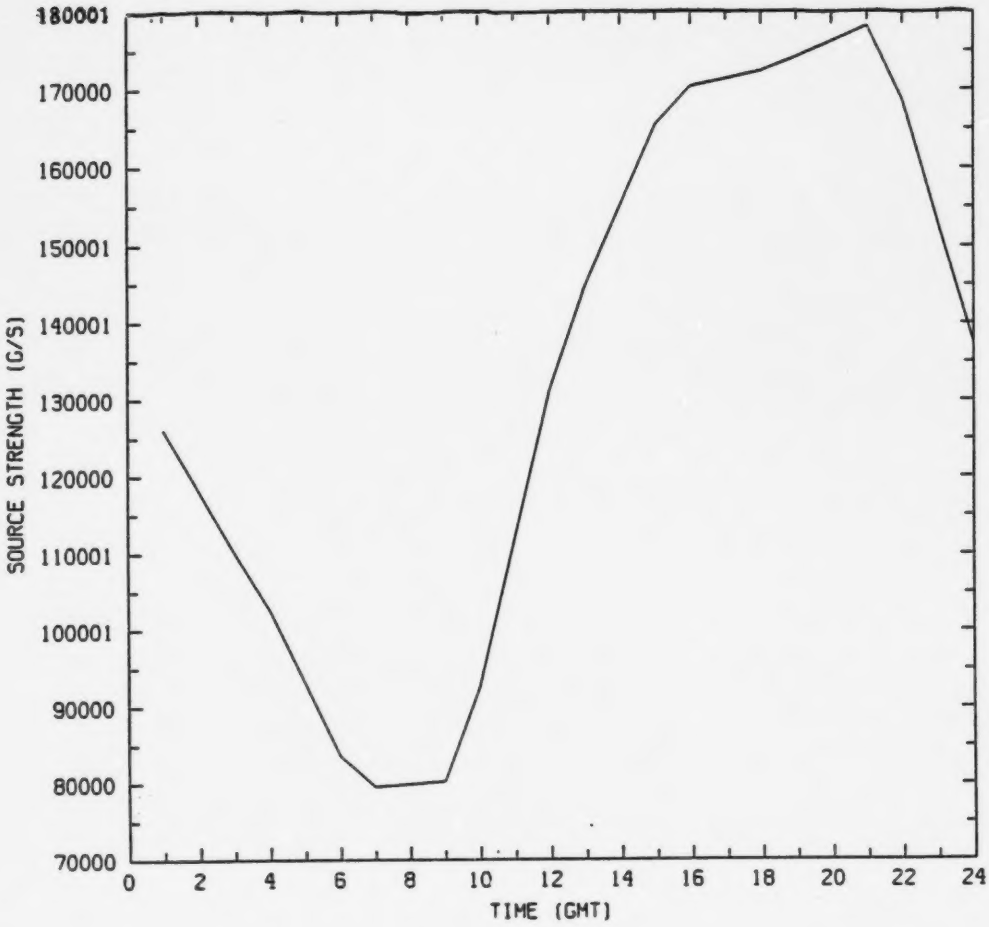

Fig. 6.2f Diurnal variations for RADM domain total emissions for NOX expressed as total nitrogen. Data derived from EPRI inventory.

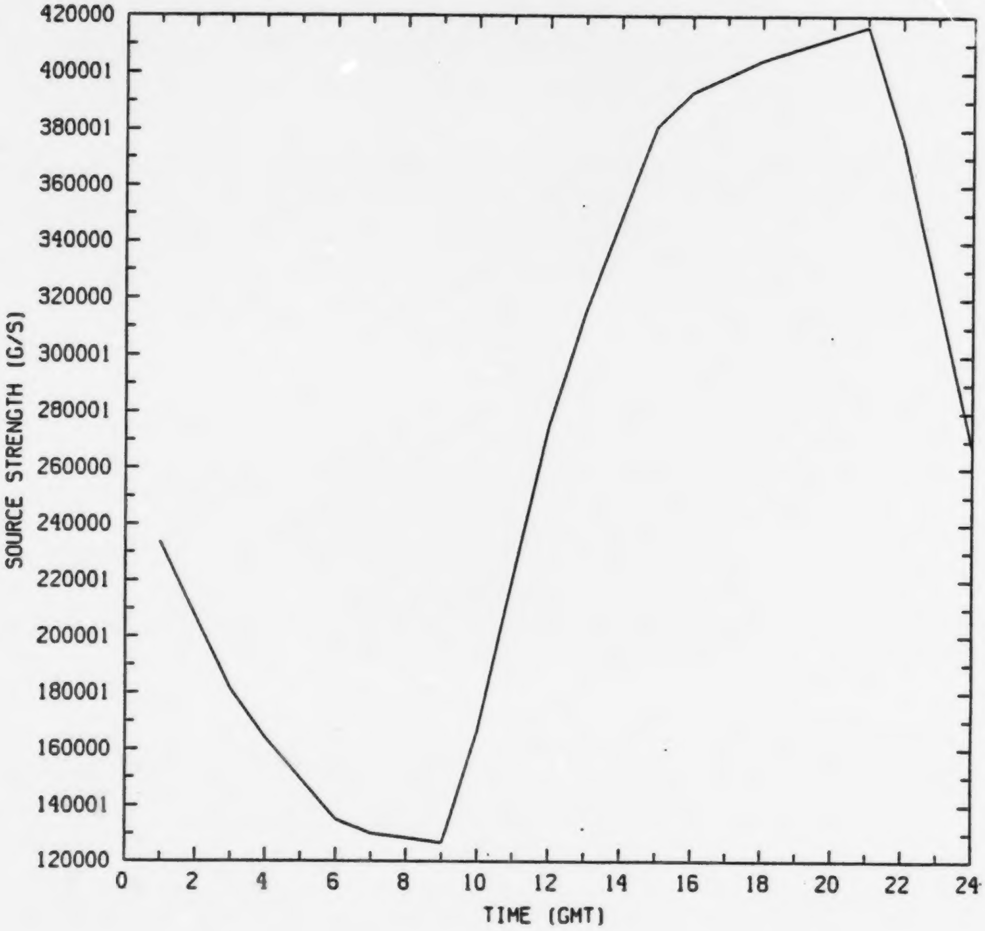

Fig. 6.2g Diurnal variations for RADM domain total emissions for VOC expressed as total carbon. Data derived from EPRI inventory.

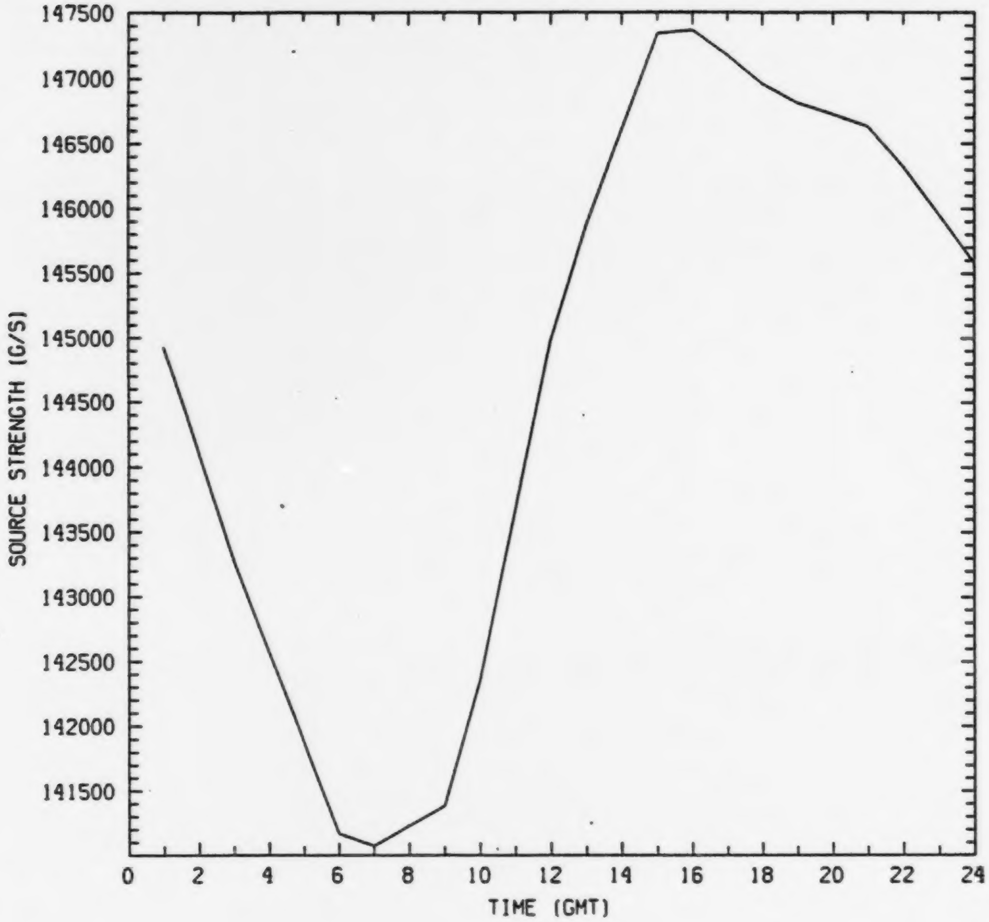

Fig. 6.2h Diurnal variations for RADM domain total emissions for NH3. Data derived from EPRI inventory.

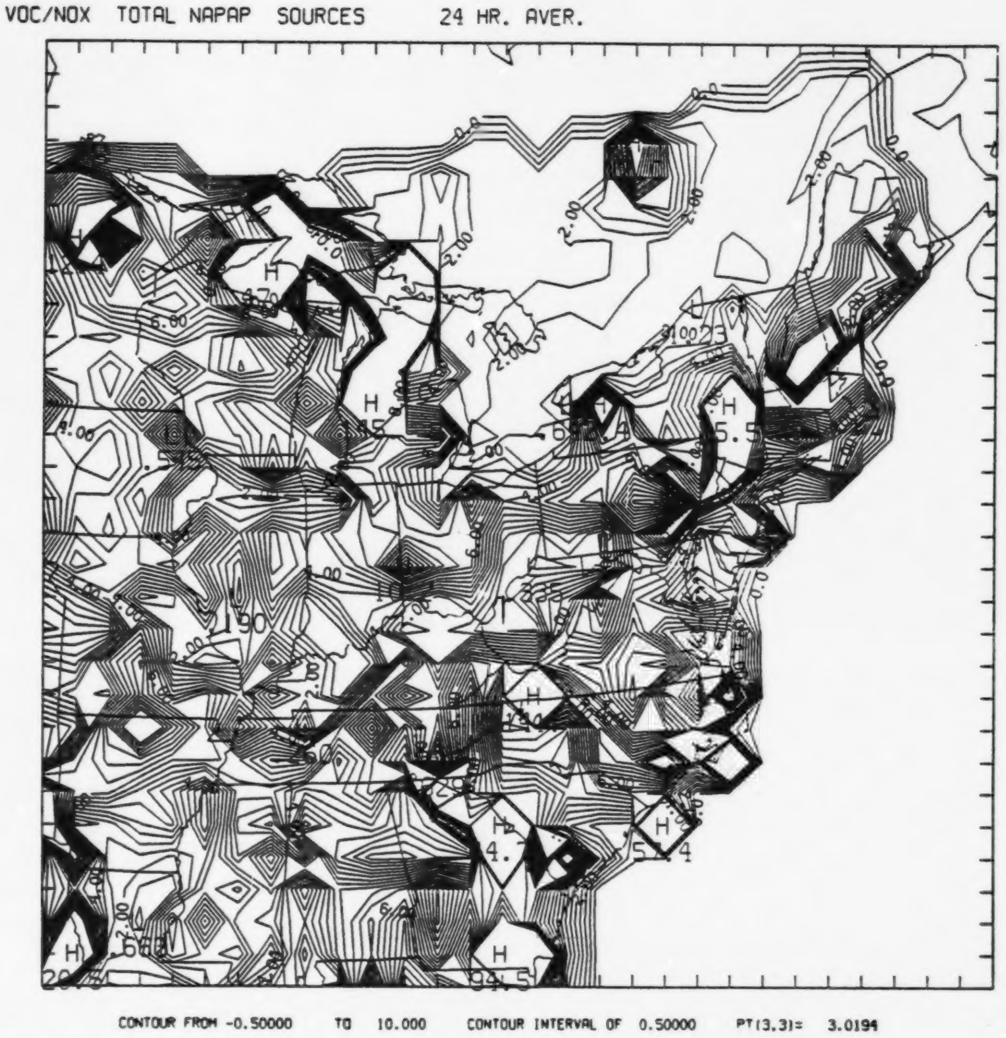
VOC/NOX TOTAL NAPAP SOURCES 24 HR. AVER.
CONTOUR FROM -0.50000 TO 10.000 CONTOUR INTERVAL OF 0.50000 PT(3,3)= 3.0194

Fig. 6.3a VOC/NOX ratios for the first two vertical levels of RADM. Daily average emissions are used. VOC and NOX are expressed as total carbon and total nitrogen, respectively.

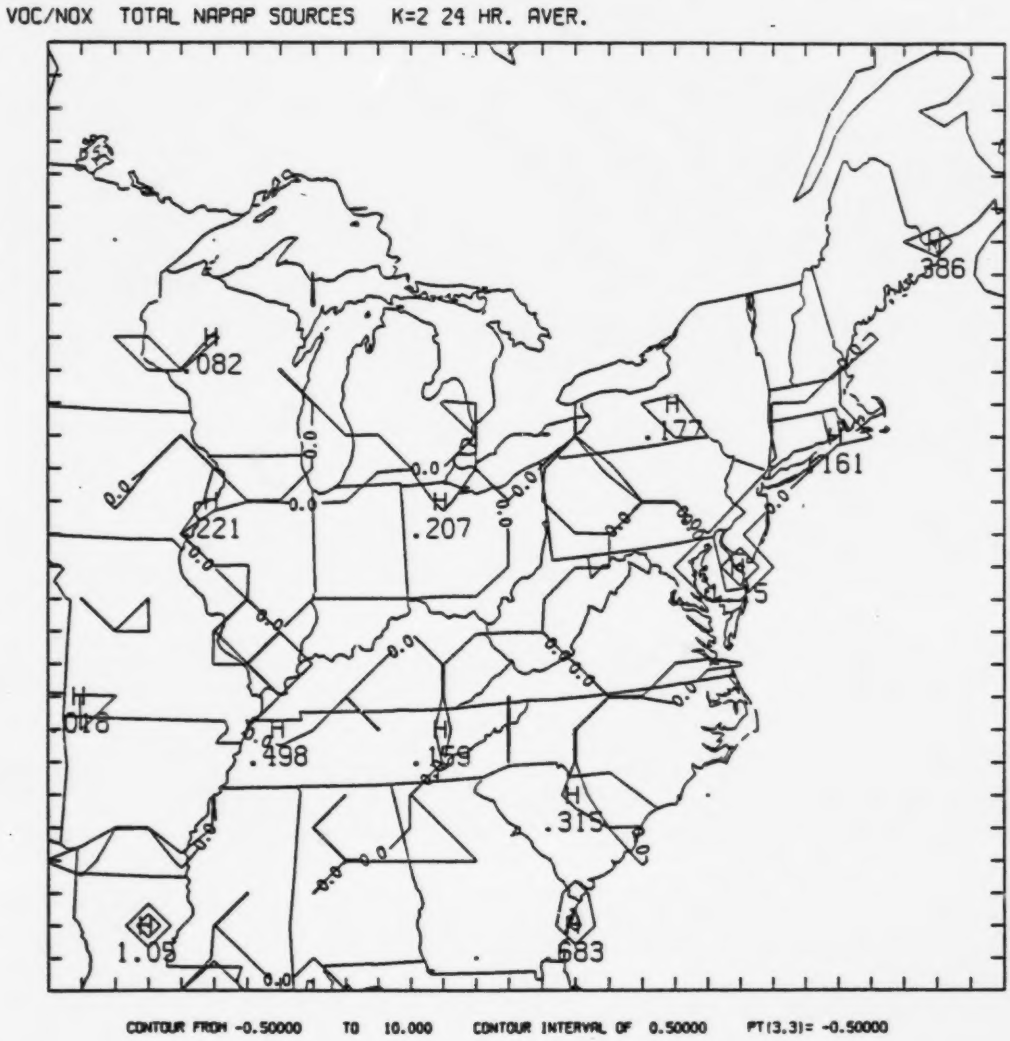
VOC/NOX TOTAL NAPAP SOURCES K=2 24 HR. AVER.

H
.082
H
.177
386
.161
.221
H
.207
0.0
H
.018
H
.498
H
.159
H
.315
H
1.05
H
683
5

CONTOUR FROM -0.50000 TO 10.000 CONTOUR INTERVAL OF 0.50000 PT(3,3)= -0.50000

Fig. 6.3b (Same as Fig. 6.3a)

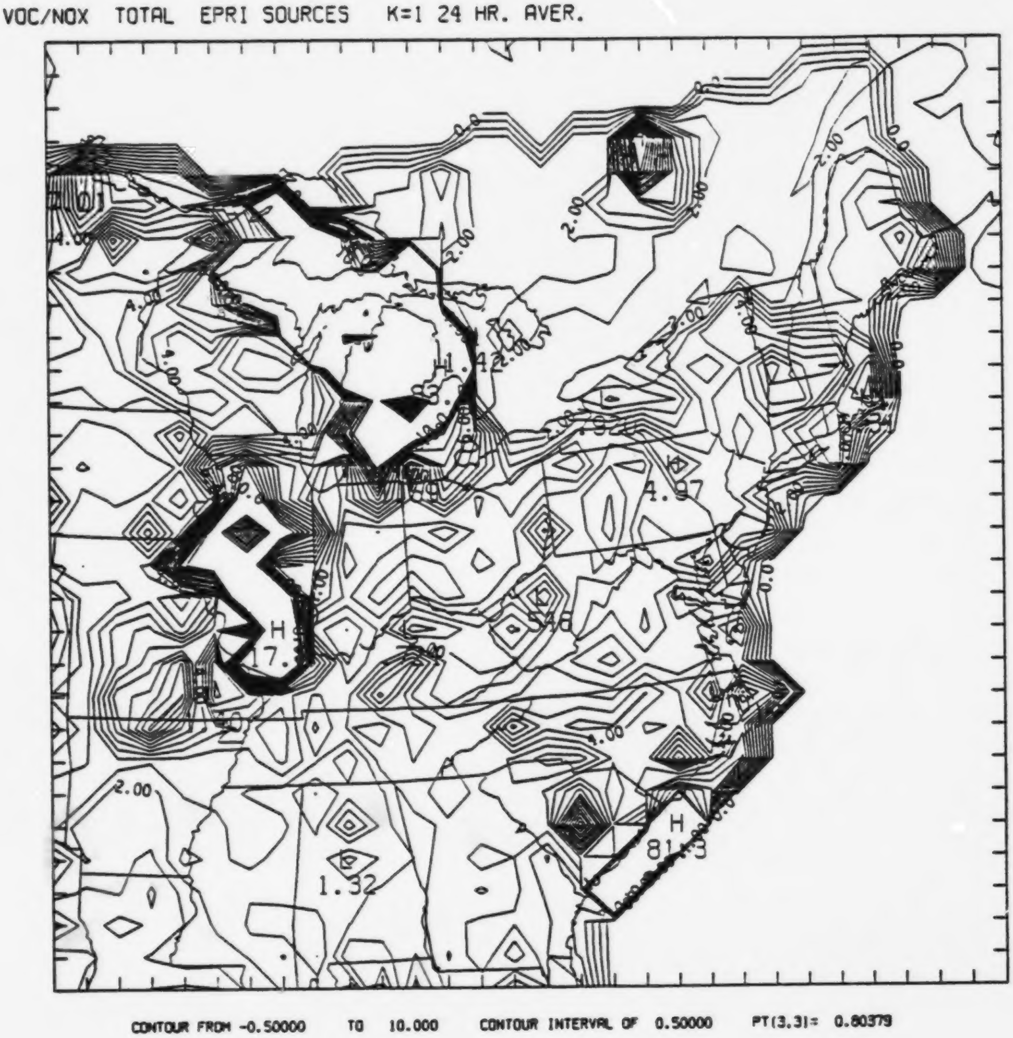
VOC/NOX TOTAL EPRI SOURCES K=1 24 HR. AVER.
2.00
4.00
H 1.42
4.97
H 17.
5.46
H 81.3
1.32
CONTOUR FROM -0.50000 TO 10.000 CONTOUR INTERVAL OF 0.50000 PT(3,3)= 0.80379

Fig. 6.3c (Same as Fig. 6.3a)

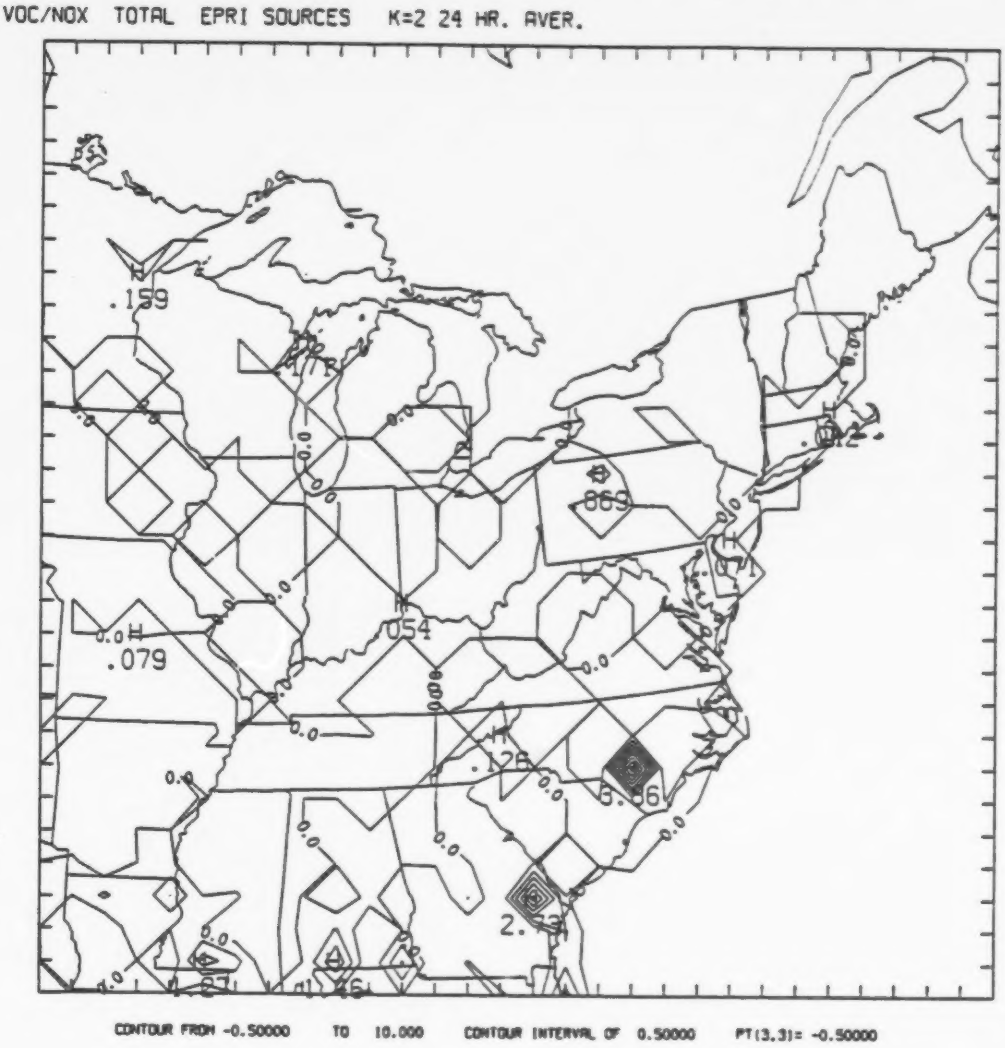
VOC/NOX TOTAL EPRI SOURCES K=2 24 HR. AVER.
.159
.171
.869
.079
.054
.126
3.86
2.33
0.0
CONTOUR FROM -0.50000 TO 10.000 CONTOUR INTERVAL OF 0.50000 PT(3,3)= -0.50000

Fig. 6.3d (Same as Fig. 6.3a)

diurnal variations in emissions. In these studies it was found that the event total wet deposition patterns were not sensitive to the existence of diurnal variations in emissions. The statistical results shown in Table 4.6 demonstrated this correspondance. Experiments performed using the complete NAPAP diurnally-varying database and those done using a diurnally-averaged NAPAP database produced essentially the same correlations for event total deposition. The midday hourly concentrations of major photochemical species, in particular ozone, were more sensitive to temporal variations in emissions. Further examination of the temporal and other emissions features is needed in order to understand the impact of emissions uncertainties and variations on RADM performance.

6.4 Precipitation Databases

Hourly precipitation data, gridded to the RADM domain, was obtained from the University of Michigan Air Pollution Modeling Group. These data were composed of hourly precipitation data obtained for sites in the United States from the National Climatic Center (NCC), Ashville, North Carolina (Form TD-9657) and for sites in Canada from the Atmospheric Environment Service (AES), Downsview, Ontario. In addition to the hourly data, "accumulated" (daily) data were also obtained and used in data-sparse regions of Canada. The Canadian daily accumulation data were used to generate "pseudo-hourly" precipitation in northern latitudes.

To prepare estimates of gridded precipitation, considerable processing of rain gauge data was required (Keeler et al., 1984). The data, which were available in station form (a year of data for each station, station after station), were first sorted, Canadian and United States data separately, into chronological order. The Canadian data were reformatted to correspond to the record format of the United States data and then merged with the United States data in synoptic order (all stations for each hour, hour after hour). At the same time, station latitudes and longitudes are added to the data record. The processed data, in synoptic order, were then written onto monthly files for ease in further analyses.

At those sites where precipitation data were available only for accumulated periods, "pseudo-hourly" values were estimated statistically. Markov chains were used to select the hours of precipitation within the accumulated period. First-order transition probabilities were generated for nearby sites as a function of month and location on the grid.

Normalized precipitation values were chosen for those hours when precipitation was predicted by the Markov chain technique. The values were selected from an exponential distribution, as previous experience had shown that this distribution produced stochastic precipitation statistically consistent with the assumed climatology (Small, 1982). The normalized "pseudo-hourly" precipitation rates were then scaled to the sum of the accumulated period.

The combined United States and Canadian data were gridded using a simple box-sum method. All valid precipitation measurements falling in a RADM grid cell were averaged to produce a grid-average precipitation rate each hour. While there are little independent data to confirm the reliability of this data set, it has been extensively checked as part of the International Sulfur Deposition Model Evaluation (ISDME) being conducted by the EPA in the United States and the AES in Canada (Clark et al., 1985). The database has been compared against some independent meteorological analyses such as that provided by Raynor and Hayes (1982). They illustrated the passage of a frontal system across the United States in April 1979 using the surface map analysis reproduced in Fig. 6.4. Figs. 6.5 to 6.7 depict the same frontal system using gridded data as it moved in three-hour increments towards the east. The outline of the United States is discernable from the large number of areas with missing data, indicated by -1, over the ocean and in Canada. The gridded precipitation values and the surface analysis both show the same temporal movement of the storm.

The precipitation data were gridded into the RADM domain using the method described above. The hourly grids were cumulatively summed over 24-hour periods ending at 00Z for each day encompassing the field experiments OSCAR I, OSCAR II, and OSCAR IV. OSCAR I precipitation, shown in Fig. 6.8, included 9-11 April 1981. OSCAR II precipitation (Fig. 6.9) included 13-15 April 1981, and OSCAR IV precipitation (Fig. 6.10) included 23-25 April 1981. Note that this data set does not include any information over the oceans, in northern Canada, or in Mexico.

The precipitation data were used for qualitative and quantitative comparison of forecast and observed rainfall patterns and amounts. Fig. 6.11 shows the observed and forecast precipitation over the area of interest during the 24-to-36 hour period of study. The forecast rainfall pattern is in good agreement with the observed, particularly along the frontal system.

Quantitatively, the forecast precipitation can be evaluated through a series of scoring computations, one of which is the bias score. The bias score measures the tendency of the model to forecast too small or too large an area of a given amount of precipitation. Fig. 6.12 contains the MM4 bias scores every 12 hours for threshold amounts of 0.01, 0.10, 0.25, 0.50, and 1.00 inches. The MM4 shows the tendency to forecast too little precipitation early in the period and too much later in the period.

6.5 Limitations and Uses of Smog Chamber Data in Evaluating RADM Chemistry

The RADM chemical kinetic mechanism is currently being tested against experimental data from the University of North Carolina (UNC) outdoor smog chamber and the Statewide Air Pollution Research Center (SAPRC) chambers (see Section 3.1). These tests, while useful, must be viewed in light of two limitations: (1) the limited applicability of the smog chamber experiments to the chemical regimes of interest to RADM's acid generation models, and (2) the experimental uncertainties associated with the chamber measurements. The first limitation, discussed in Section 6.5.1, arises because the smog chamber data are designed primarily for simulation of urban pollution, while the RADM chemistry is specifically designed to simulate acid generation occurring mostly in less polluted air. The second limitation arises from the accuracy of the smog chamber data which (as for any experimental study) is necessarily finite. Therefore, agreement or disagreement between RADM chemistry submodel predictions and the chamber measurements is meaningful only to within the

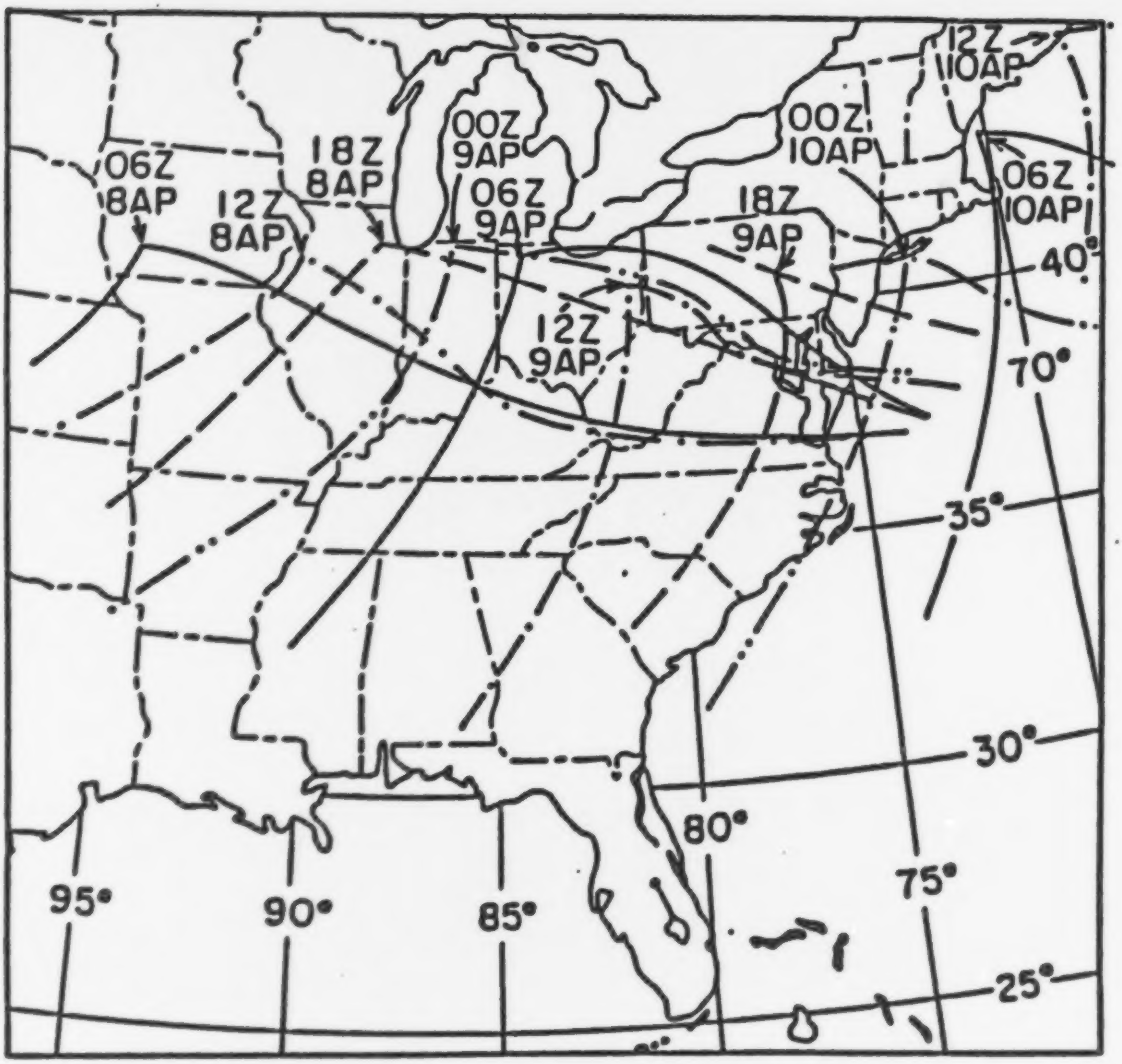
12Z
11AP
00Z
9AP
00Z
10AP
06Z
8AP
18Z
8AP
12Z
8AP
06Z
9AP
06Z
10AP
18Z
9AP
12Z
9AP
40°
70°
35°
30°
80°
75°
25°
95°
90°
85°

Fig. 6.4 Passage of a frontal system across the United States, April 8-10, 1979 as seen on a synoptic map (from Raynor and Hayes, 1982).

```
 -1 -1 -1 -1 -1 -1 -1 -1 -1 -1 -1 -1 -1 -1 -1 -1 -1 -1 -1 -1 -1 -1 -1 -1 -1 -1 -1 -1 -1 -1 -1 -1 -1 -1 -1 -1
 -1 -1 -1 -1 -1 -1 -1    -1 -1 -1 -1 -1 -1 -1 -1 -1 -1 -1 -1 -1 -1 -1 -1 -1 -1 -1 -1 -1 -1 -1 -1    -1 -1 -1
 -1 -1 -1 -1 -1 -1 -1 -1 -1 -1 -1 -1 -1 -1 -1 -1 -1 -1 -1 -1 -1 -1 -1 -1 -1 -1 -1 -1 -1 -1 -1 -1 -1 -1 -1 -1
 -1    -1 -1 -1 -1 -1 -1 -1 -1 -1 -1 -1 -1 -1 -1 -1 -1 -1 -1 -1 -1 -1 -1 -1 -1 -1 -1 -1    -1 -1 -1 -1 -1 -1
          -1       -1    -1 -1 -1 -1 -1 -1 -1 -1 -1 -1    -1 -1 -1 -1 -1       -1 -1    -1    -1 -1 -1 -1 -1
             -1 -1       76 -1 -1 -1 -1 -1 -1 -1 -1 -1 -1 -1 -1 -1 -1 -1             -1 -1 -1 -1 -1 -1 -1 -1
                          4 -1 -1 -1    -1 -1    -1 -1 -1 -1 -1 -1                      -1    -1    -1 -1 -1
                               -1 -1    -1 -1 -1    -1 -1 -1 -1                                  -1 -1 -1 -1
                            -1 -1       -1 -1 -1                                                 -1 -1 -1
                            -1 -1       -1 -1                                           -1          -1 -1 -1
                                                                                     -1 -1       -1 -1 -1 -1
                            50                                                    -1 -1 -1 -1 -1 -1 -1 -1 -1
                        296 93       17       51127 10                            -1 -1 -1 -1 -1 -1 -1 -1 -1
                     457213 25118114229 59           4                            -1 -1 -1 -1 -1 -1 -1 -1 -1
          34          51           6     5           3                      -1 -1 -1 -1 -1 -1 -1 -1 -1 -1 -1
                  385208483 77                                        -1 -1 -1 -1 -1 -1 -1 -1 -1 -1 -1 -1 -1
                        220127 31  3                               -1 -1 -1 -1 -1 -1 -1 -1 -1 -1 -1 -1 -1 -1
              6 25         186       20                            -1 -1 -1 -1 -1 -1 -1 -1 -1 -1 -1 -1 -1 -1
             63102   110152725618                               -1 -1 -1 -1 -1 -1 -1 -1 -1 -1 -1 -1 -1 -1 -1
      122504296291192237609102                                  -1 -1 -1 -1 -1 -1 -1 -1 -1 -1 -1 -1 -1 -1 -1
      110 17285153444 86                                        -1 -1 -1 -1 -1 -1 -1 -1 -1 -1 -1 -1 -1 -1 -1
         102   254                                              -1 -1 -1 -1 -1 -1 -1 -1 -1 -1 -1 -1 -1 -1 -1
       25       32 40       89                                  -1 -1 -1 -1 -1 -1 -1 -1 -1 -1 -1 -1 -1 -1 -1
                         -1 -1102                         -1 -1 -1 -1 -1 -1 -1 -1 -1 -1 -1 -1 -1 -1 -1 -1 -1
                      -1 -1 -1 32 76 11                -1 -1 -1 -1 -1 -1 -1 -1 -1 -1 -1 -1 -1 -1 -1 -1 -1 -1
                  124 -1 -1 -1       13             -1 -1 -1 -1 -1 -1 -1 -1 -1 -1 -1 -1 -1 -1 -1 -1 -1 -1 -1
                   51830 21 25      152 25       -1 -1 -1 -1 -1 -1 -1 -1 -1 -1 -1 -1 -1 -1 -1 -1 -1 -1 -1 -1
                                  16127     4 -1 -1 -1 -1 -1 -1 -1 -1 -1 -1 -1 -1 -1 -1 -1 -1 -1 -1 -1 -1 -1
                                              -1 -1 -1 -1 -1 -1 -1 -1 -1 -1 -1 -1 -1 -1 -1 -1 -1 -1 -1 -1 -1
                         -1 -1 -1                -1 -1 -1 -1 -1 -1 -1 -1 -1 -1 -1 -1 -1 -1 -1 -1 -1 -1 -1 -1
       -1 -1 -1 -1    -1 -1 -1 -1 -1             -1 -1 -1 -1 -1 -1 -1 -1 -1 -1 -1 -1 -1 -1 -1 -1 -1 -1 -1 -1
 -1 -1 -1 -1 -1 -1 -1 -1 -1 -1 -1 -1 -1          -1 -1 -1 -1 -1 -1 -1 -1 -1 -1 -1 -1 -1 -1 -1 -1 -1 -1 -1 -1
 -1 -1 -1 -1 -1 -1 -1 -1 -1 -1 -1 -1 -1          -1 -1 -1 -1 -1 -1 -1 -1 -1 -1 -1 -1 -1 -1 -1 -1 -1 -1 -1 -1
 -1 -1 -1 -1 -1 -1 -1 -1 -1 -1 -1 -1 -1             -1 -1 -1 -1 -1 -1 -1 -1 -1 -1 -1 -1 -1 -1 -1 -1 -1 -1 -1
 -1 -1 -1 -1 -1 -1 -1 -1 -1 -1 -1 -1 -1 -1          -1 -1 -1 -1 -1 -1 -1 -1 -1 -1 -1 -1 -1 -1 -1 -1 -1 -1 -1
 -1 -1 -1 -1 -1 -1 -1 -1 -1 -1 -1 -1 -1 -1 -1    -1 -1 -1 -1 -1 -1 -1 -1 -1 -1 -1 -1 -1 -1 -1 -1 -1 -1 -1 -1
```

Fig. 6.5 Position of the frontal system shown in Fig. 6.4 as seen in the gridded precipitation data at 18Z, April 8, 1979. Units are mm x 100 in each cell; values of -1 indicate no data.

```
 -1 -1 -1 -1 -1 -1 -1 -1 -1 -1 -1 -1 -1 -1 -1 -1 -1 -1 -1 -1 -1 -1 -1 -1 -1 -1 -1 -1 -1 -1 -1 -1 -1 -1 -1 -1
 -1 -1 -1 -1 -1 -1 -1    -1 -1 -1 -1 -1 -1 -1 -1 -1 -1 -1 -1 -1 -1 -1 -1 -1 -1 -1 -1 -1 -1 -1 -1    -1 -1 -1
 -1 -1 -1 -1 -1 -1 -1 -1 -1 -1 -1 -1 -1 -1 -1 -1 -1 -1 -1 -1 -1 -1 -1 -1 -1 -1 -1 -1 -1 -1 -1 -1 -1 -1 -1 -1
 -1    -1 -1 -1 -1 -1 -1 -1 -1 -1 -1 -1 -1 -1 -1 -1 -1 -1 -1 -1 -1 -1 -1 -1 -1 -1 -1 -1    -1 -1 -1 -1 -1 -1
          -1       -1    -1 -1 -1 -1 -1 -1 -1 -1 -1 -1    -1 -1 -1 -1 -1       -1 -1    -1    -1 -1 -1 -1 -1
           8  8     2 -1    -1 -1 -1 -1 -1 -1 -1 -1 -1 -1 -1 -1 -1 -1 -1             -1 -1 -1 -1 -1 -1 -1 -1
             50       13 10 -1 -1 -1    -1 -1    -1 -1 -1 -1 -1 -1                      -1    -1    -1 -1 -1
           3              8 63          -1 -1 -1    -1 -1 -1 -1                                  -1 -1 -1 -1
                         76 35 13       -1 -1 -1                                                 -1 -1 -1
                      13 25 -1 -1       -1 -1                                          -1          -1 -1 -1
                               26    24                                             -1 -1       -1 -1 -1 -1
                                 135 25 13          77457356255102  5             -1 -1 -1 -1 -1 -1 -1 -1 -1
                            11      229103   736965450305229787343    18          -1 -1 -1 -1 -1 -1 -1 -1 -1
                      25 13  0 51471610222 63127711711227 76116101305 30 25       -1 -1 -1 -1 -1 -1 -1 -1 -1
                      26          148183 56 22 51100477       98116 83 46127 -1 -1 -1 -1 -1 -1 -1 -1 -1 -1 -1
                            38102116289 87 51   198 48        4 34 57 -1 -1 -1 -1 -1 -1 -1 -1 -1 -1 -1 -1 -1
                           279432311133    17                      -1 -1 -1 -1 -1 -1 -1 -1 -1 -1 -1 -1 -1 -1
                           524   288 41                            -1 -1 -1 -1 -1 -1 -1 -1 -1 -1 -1 -1 -1 -1
                           524322331 93                         -1 -1 -1 -1 -1 -1 -1 -1 -1 -1 -1 -1 -1 -1 -1
                      38305711661221                            -1 -1 -1 -1 -1 -1 -1 -1 -1 -1 -1 -1 -1 -1 -1
                        170102629285   317                      -1 -1 -1 -1 -1 -1 -1 -1 -1 -1 -1 -1 -1 -1 -1
                         38510436533279 25                      -1 -1 -1 -1 -1 -1 -1 -1 -1 -1 -1 -1 -1 -1 -1
                      15382570406508470 98174 13                -1 -1 -1 -1 -1 -1 -1 -1 -1 -1 -1 -1 -1 -1 -1
                11 25   277   279682007923    38          -1 -1 -1 -1 -1 -1 -1 -1 -1 -1 -1 -1 -1 -1 -1 -1 -1
                   63       50534380703401052          -1 -1 -1 -1 -1 -1 -1 -1 -1 -1 -1 -1 -1 -1 -1 -1 -1 -1
                   89 49  2   361    25      122    -1 -1 -1 -1 -1 -1 -1 -1 -1 -1 -1 -1 -1 -1 -1 -1 -1 -1 -1
                  355242  2                      -1 -1 -1 -1 -1 -1 -1 -1 -1 -1 -1 -1 -1 -1 -1 -1 -1 -1 -1 -1
               152                            -1 -1 -1 -1 -1 -1 -1 -1 -1 -1 -1 -1 -1 -1 -1 -1 -1 -1 -1 -1 -1
                                              -1 -1 -1 -1 -1 -1 -1 -1 -1 -1 -1 -1 -1 -1 -1 -1 -1 -1 -1 -1 -1
                         -1 -1 -1                -1 -1 -1 -1 -1 -1 -1 -1 -1 -1 -1 -1 -1 -1 -1 -1 -1 -1 -1 -1
       -1 -1 -1 -1    -1 -1 -1 -1 -1      406    -1 -1 -1 -1 -1 -1 -1 -1 -1 -1 -1 -1 -1 -1 -1 -1 -1 -1 -1 -1
 -1 -1 -1 -1 -1 -1 -1 -1 -1 -1 -1 -1 -1          -1 -1 -1 -1 -1 -1 -1 -1 -1 -1 -1 -1 -1 -1 -1 -1 -1 -1 -1 -1
 -1 -1 -1 -1 -1 -1 -1 -1 -1 -1 -1 -1 -1          -1 -1 -1 -1 -1 -1 -1 -1 -1 -1 -1 -1 -1 -1 -1 -1 -1 -1 -1 -1
 -1 -1 -1 -1 -1 -1 -1 -1 -1 -1 -1 -1 -1             -1 -1 -1 -1 -1 -1 -1 -1 -1 -1 -1 -1 -1 -1 -1 -1 -1 -1 -1
 -1 -1 -1 -1 -1 -1 -1 -1 -1 -1 -1 -1 -1 -1          -1 -1 -1 -1 -1 -1 -1 -1 -1 -1 -1 -1 -1 -1 -1 -1 -1 -1 -1
 -1 -1 -1 -1 -1 -1 -1 -1 -1 -1 -1 -1 -1 -1 -1    -1 -1 -1 -1 -1 -1 -1 -1 -1 -1 -1 -1 -1 -1 -1 -1 -1 -1 -1 -1
```

Fig. 6.6 Position of the frontal system shown in Fig. 6.4 as seen in the gridded precipitation data at 06Z, April 9, 1979. Units are mm x 100 in each cell; values of -1 indicate no data.

```
 -1 -1 -1 -1 -1 -1 -1 -1 -1 -1 -1 -1 -1 -1 -1 -1 -1 -1 -1 -1 -1 -1 -1 -1 -1 -1 -1 -1 -1 -1 -1 -1 -1 -1 -1 -1
 -1 -1 -1 -1 -1 -1 -1    -1 -1 -1 -1 -1 -1 -1 -1 -1 -1 -1 -1 -1 -1 -1 -1 -1 -1 -1 -1 -1 -1 -1 -1    -1 -1 -1
 -1 -1 -1 -1 -1 -1 -1 -1 -1 -1 -1 -1 -1 -1 -1 -1 -1 -1 -1 -1 -1 -1 -1 -1 -1 -1 -1 -1 -1 -1 -1 -1 -1 -1 -1 -1
 -1    -1 -1 -1 -1 -1 -1 -1 -1 -1 -1 -1 -1 -1 -1 -1 -1 -1 -1 -1 -1 -1 -1 -1 -1 -1 -1 -1    -1 -1 -1 -1 -1 -1
          -1       -1    -1 -1 -1 -1 -1 -1 -1 -1 -1 -1    -1 -1 -1 -1 -1       -1 -1    -1    -1 -1 -1 -1 -1
                            -1 -1 -1 -1 -1 -1 -1 -1 -1 -1 -1 -1 -1 -1 -1             -1 -1 -1 -1 -1 -1 -1 -1
                               -1 -1    -1 -1    -1 -1 -1 -1 -1 -1                      -1    -1    -1 -1 -1
                                        -1 -1 -1    -1 -1 -1 -1                                  -1 -1 -1 -1
                                        -1 -1 -1                     135     1                   -1 -1 -1
                       6    -1 -1       -1 -1                         25    41          -1          -1 -1 -1
                      51       23    17           7 74                   11 15203    -1 -1       -1 -1 -1 -1
                             1   119              4187330686305153143193226   149 -1 -1 -1 -1 -1 -1 -1 -1 -1
                          8  5      258199    51204230   939626114   173181184432 -1 -1 -1 -1 -1 -1 -1 -1 -1
                         29                25126224305530224377374 59 35 71 38102 -1 -1 -1 -1 -1 -1 -1 -1 -1
                                            7253268284203293288165156 53 76 -1 -1 -1 -1 -1 -1 -1 -1 -1 -1 -1
                                        10      455153152470262213219 -1 -1 -1 -1 -1 -1 -1 -1 -1 -1 -1 -1 -1
                                          121251791    93256406483 -1 -1 -1 -1 -1 -1 -1 -1 -1 -1 -1 -1 -1 -1
                                      5 25381533508    59292293 -1 -1 -1 -1 -1 -1 -1 -1 -1 -1 -1 -1 -1 -1 -1
                                          127308    71 40 76102 -1 -1 -1 -1 -1 -1 -1 -1 -1 -1 -1 -1 -1 -1 -1
                                          237 83 82229    50 25 -1 -1 -1 -1 -1 -1 -1 -1 -1 -1 -1 -1 -1 -1 -1
                                                101 11    12    -1 -1 -1 -1 -1 -1 -1 -1 -1 -1 -1 -1 -1 -1 -1
                                            8     8       -1 -1 -1 -1 -1 -1 -1 -1 -1 -1 -1 -1 -1 -1 -1 -1 -1
                                                  1       -1143 -1 -1 -1 -1 -1 -1 -1 -1 -1 -1 -1 -1 -1 -1 -1
                                                          -1 -1 -1 -1 -1 -1 -1 -1 -1 -1 -1 -1 -1 -1 -1 -1 -1
                                                    -1 -1 -1 -1 -1 -1 -1 -1 -1 -1 -1 -1 -1 -1 -1 -1 -1 -1 -1
                                          303359 38 -1 -1 -1 -1 -1 -1 -1 -1 -1 -1 -1 -1 -1 -1 -1 -1 -1 -1 -1
                                          800999 -1 -1 -1 -1 -1 -1 -1 -1 -1 -1 -1 -1 -1 -1 -1 -1 -1 -1 -1 -1
                                              -1 -1 -1 -1 -1 -1 -1 -1 -1 -1 -1 -1 -1 -1 -1 -1 -1 -1 -1 -1 -1
                                              -1 -1 -1 -1 -1 -1 -1 -1 -1 -1 -1 -1 -1 -1 -1 -1 -1 -1 -1 -1 -1
                         -1 -1 -1             -1 -1 -1 -1 -1 -1 -1 -1 -1 -1 -1 -1 -1 -1 -1 -1 -1 -1 -1 -1 -1
       -1 -1 -1 -1    -1 -1 -1 -1 -1         190 -1 -1 -1 -1 -1 -1 -1 -1 -1 -1 -1 -1 -1 -1 -1 -1 -1 -1 -1 -1
 -1 -1 -1 -1 -1 -1 -1 -1 -1 -1 -1 -1 -1          -1 -1 -1 -1 -1 -1 -1 -1 -1 -1 -1 -1 -1 -1 -1 -1 -1 -1 -1 -1
 -1 -1 -1 -1 -1 -1 -1 -1 -1 -1 -1 -1 -1          -1 -1 -1 -1 -1 -1 -1 -1 -1 -1 -1 -1 -1 -1 -1 -1 -1 -1 -1 -1
 -1 -1 -1 -1 -1 -1 -1 -1 -1 -1 -1 -1 -1             -1 -1 -1 -1 -1 -1 -1 -1 -1 -1 -1 -1 -1 -1 -1 -1 -1 -1 -1
 -1 -1 -1 -1 -1 -1 -1 -1 -1 -1 -1 -1 -1 -1          -1 -1 -1 -1 -1 -1 -1 -1 -1 -1 -1 -1 -1 -1 -1 -1 -1 -1 -1
 -1 -1 -1 -1 -1 -1 -1 -1 -1 -1 -1 -1 -1 -1 -1    -1 -1 -1 -1 -1 -1 -1 -1 -1 -1 -1 -1 -1 -1 -1 -1 -1 -1 -1 -1
```

Fig. 6.7 Position of the frontal system shown in Fig. 6.4 as seen in the gridded precipitation data at 18Z, April 9, 1979. Units are mm x 100 in each cell; values of -1 indicate no data.

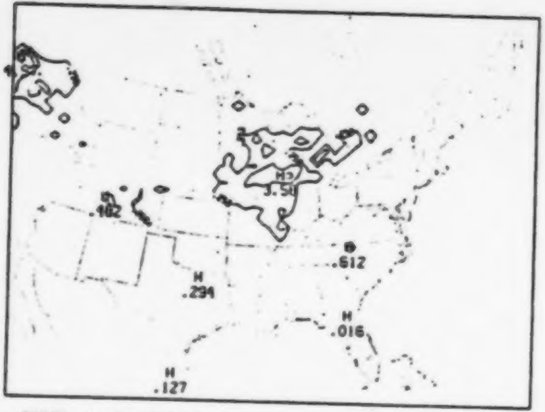
H
3.58
.102
.612
H
.294
H
.016
H
.127

OSCAR I 24 HOUR TOTAL

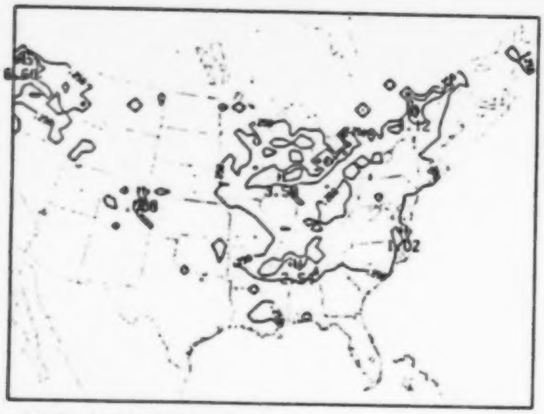

OSCAR I 48 HOUR TOTAL

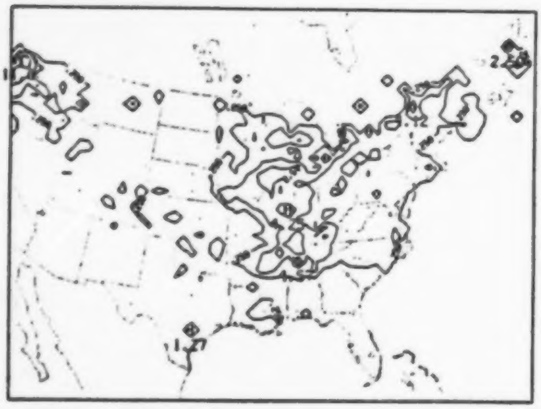

OSCAR I 72 HOUR TOTAL

Fig. 6.8 Cumulative precipitation at 24-hour intervals ending at 00Z over the duration of the OSCAR I field experiment.

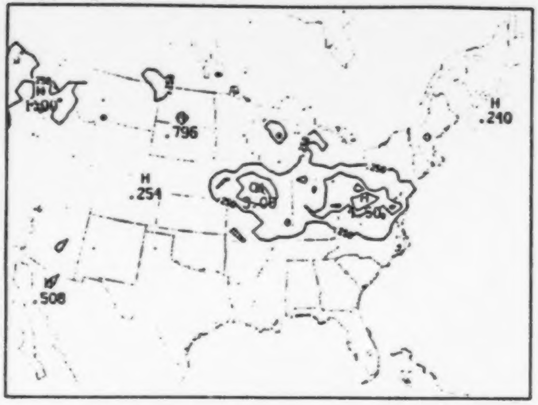
.796
H
.254
H
.240
.508

OSCAR II 24 HOUR TOTAL

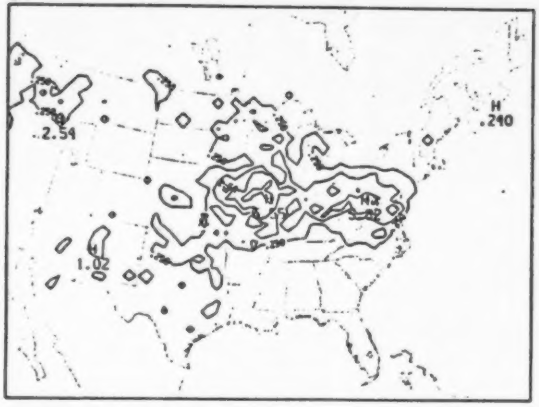
2.54
H
.240
1.02

OSCAR II 48 HOUR TOTAL

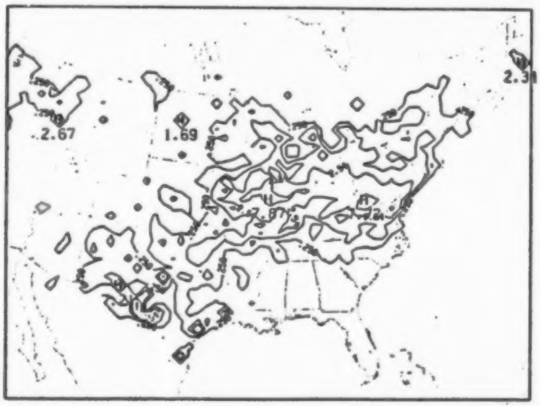

OSCAR II 72 HOUR TOTAL

Fig. 6.9 Cumulative precipitation at 24-hour intervals ending at 00Z over the duration of the OSCAR II field experiment.

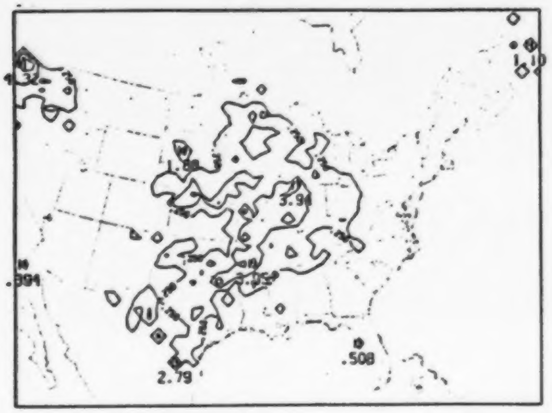
3.94
2.79
.508
.394
1.1

OSCAR IV 24 HOUR TOTAL

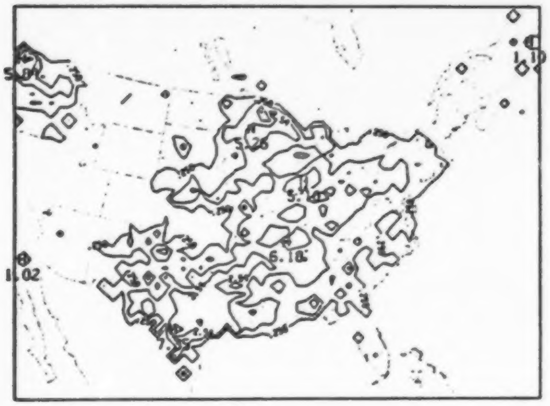
5.0
1.02
6.18
1.1

OSCAR IV 48 HOUR TOTAL

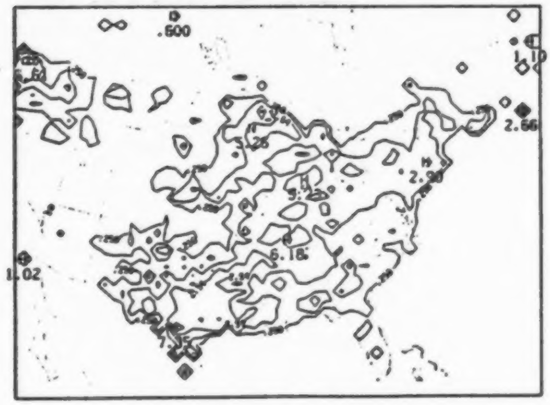
.600
1.02
6.18
2.66
2.98
1.1

OSCAR IV 72 HOUR TOTAL

Fig. 6.10 Cumulative precipitation at 24-hour intervals at 00Z over the duration of the OSCAR IV field experiment.

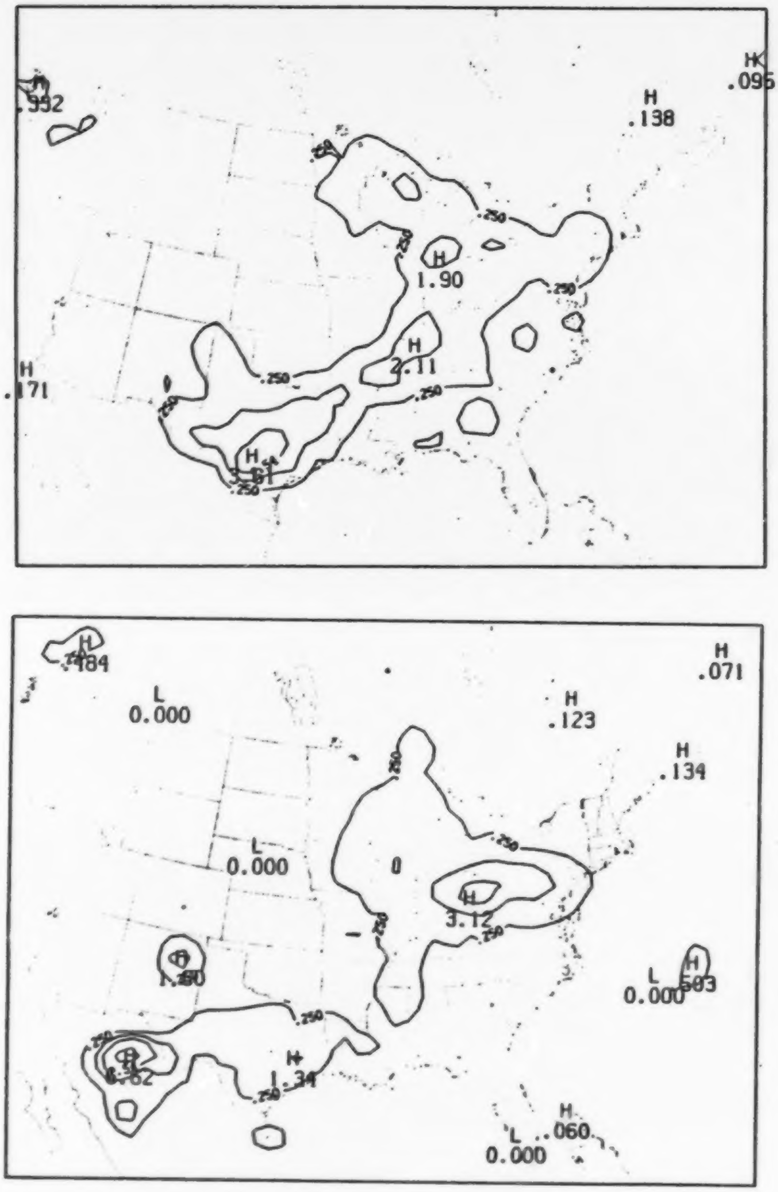
H
.932
H
.096
H
.138
H
1.90
H
2.11
H
.171
H
3.61
.250
H
.184
L
0.000
H
.123
H
.071
H
.134
L
0.000
H
3.12
H
1.80
L
0.000
H
.603
H
6.62
H
1.34
H
.060
L
0.000

Fig. 6.11 The (a) observed and (b) forecast precipitation during the 12-hour period 00Z to 12Z on 23 April, 1981.

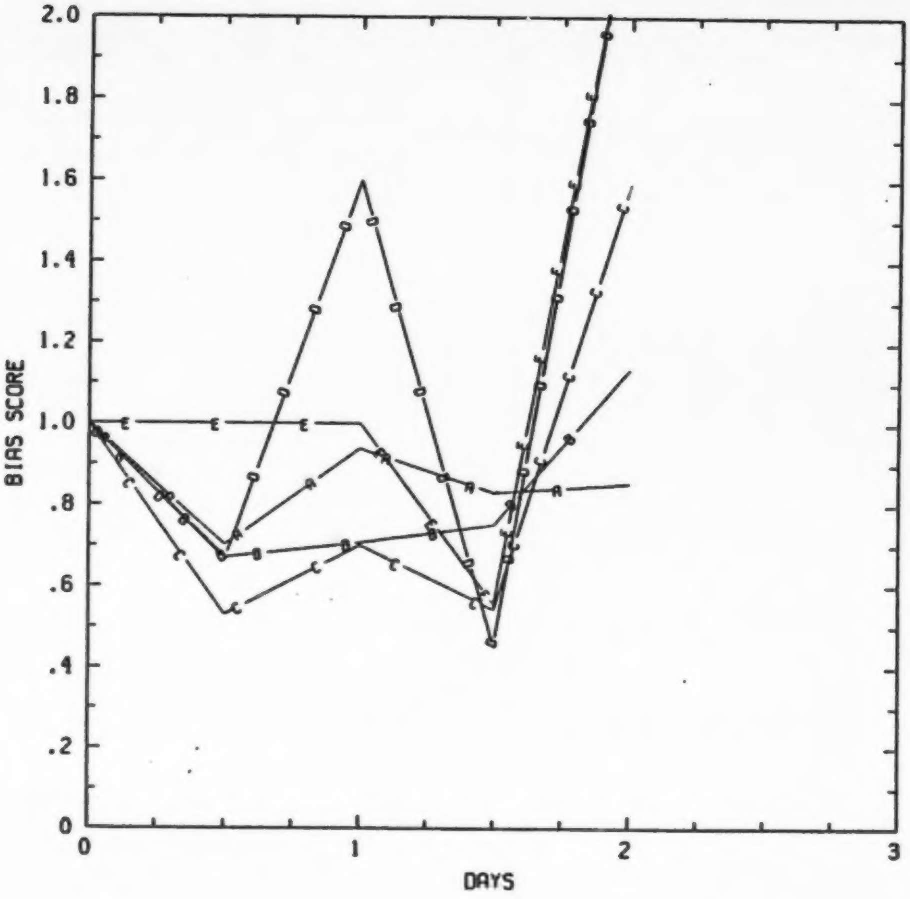

Fig. 6.12 The bias scores of MM4 predictions every 12 hours through the OSCAR IV study period for threshold amounts of 0.01 (A), 0.10 (B), 0.25 (C), 0.50 (D), and 1.00 (E) inches.

estimated experimental accuracy of the measurements. Some of the more important experimental uncertainties associated with the chamber data, and their impact on the testing of RADM chemistry, are discussed in Sections 6.5.2-6.5.4.

6.5.1 Applicability of Smog Chamber Experiments to RADM

A chemical mechanism for the modeling of acid deposition should be evaluated according to its ability to predict the behavior of those species which are required for the production of acids in the atmosphere. The gas-phase chemical mechanism affects the location, chemical form, and concentration of acids in the troposphere since (1) transport times depend on the chemical form of the sulfur and nitrogen compounds in the atmosphere due to differences in deposition velocities, (2) the correct form of sulfur and nitrogen compunds is achieved only if the correct reaction mechanism and rate constants are employed, and (3) gas-phase chemistry supplies important reactants to cloud water where the SO_2 conversion rates can be very high. The key test variable for testing of chemical mechanisms for acid deposition include SO_2 conversion rates, nitric acid production rates, and time dependent concentrations of HO_x radicals, H_2O_2, O_3, organic peroxides, peroxyacetyl nitrate, NO_2, NO, and reactive organic species. Therefore, HO_x, NO_x, hydrocarbons, and SO_x chemistry, aqueous chemistry, and the eventual formation of H_2SO_4, HNO_3, and organic acids are all major components of the RADM model.

In contrast, the majority of smog chamber data is obtained for conditions which typically simulate a heavily polluted urban atmosphere, with NO_x and hydrocarbon concentrations much greater than those applicable to the above-boundary-layer chemistry important to the RADM model. SO_x and acid formation mechanisms have not been studied extensively in smog chambers. Likewise, aqueous chemistry has not been studied in smog chamber experiments.

Because the gas-phase oxidation rates of sulfur dioxide and the formation rates of hydrogen peroxide depend upon the concentrations of HO and HO_2, and because hydrocarbon concentrations are a fair measure of [HO] and [HO_2], the smog chamber data do provide important test variables for comparisons with RADM, specifically in the concentrations of the hydrocarbons and O_3, NO_2, and NO. However, such tests do not apply to those chemical regimes most relevant to acid generation in the atmosphere. Therefore, comparisons of RADM model predictions against smog chamber data are necessary but not sufficient to verify the RADM model.

6.5.2 Limitations Due to Experimental Errors in the SAPRC Chamber Data

The precision of chemical species' measurements at the SAPRC chamber may be estimated from the scatter of the reported data (see, for example, Figs. 3.1-3.3). In the absence of information about possible systematic errors, these precision values are an estimate of absolute accuracy.

Uncertainties in radical fluxes from the SAPRC chamber walls are estimated as ±50%, in accord with the recent evaluation by Carter (1985). In the same evaluation, Carter has estimated that the precision of the photolysis rates measured at the SAPRC chamber is about ±10%. Additional systematic errors may be present in photolysis rates estimated from published absorption cross section and quantum yield data and flux measurements. Thus, for example, the combined uncertainty of the NO_2 absorption cross section and quantum yield data is estimated as ±30% by NASA (1985). Variations in lamp intensity due to aging or electrical supply fluctuations may also contribute. It is therefore likely that the absolute accuracy of the NO_2 photolysis rates at SAPRC is about 20-30%. For other photoactive species, comparable or greater errors are likely.

6.5.3 Limitations Due to Experimental Errors in the UNC Chamber Data

It may be assumed that the precision of these measurements is given by the scatter of the data (see, for example, Figs. 3.5-3.8). Thus, large errors are associated with the measurements of $[H_2O_2]$, [PAN], and $[NO_2]$, while NO and O_3 concentrations are measured with high precision. Some additional errors may be associated with the sampling procedures, e.g., the time delay in the analysis of the O_3, NO, and NO_x (12-20 sec) is somewhat uncertain and a correction for the dark reaction of O_3 with NO and highly reactive alkenes must be made to attempt to reconstruct the actual mixture within the chamber at any time. These errors translate directly to the accuracy with which models and experiments can be compared.

Uncertainties in radical flux estimates from the UNC chamber walls would be expected to be similar to those uncertainties of the SAPRC chamber, i.e., ±50%, in accord with the recent evaluation by Carter (1985). It should be noted that, although the UNC chamber has a greater volume/surface ratio than the SAPRC chambers and may be expected to display lower surface effects, condensation of water on the inner walls in some UNC experiments as well as the practice of rapidly circulating the chamber air will increase the effect of surfaces.

We have recently estimated that the uncertainty in photolysis rates in the UNC chamber is approximately ±40%. Carter has estimated this uncertainty to be at least ±20%. However, Whitten and Gery (1986) have reported that the uncertainty is only ±13%. We have reviewed the analysis by Whitten and Gery, and we believe that they have not fully considered all uncertainties that may contribute to an error estimate. Because of the disagreements in the estimation of these errors, we have included a detailed explanation (Section 6.5.4) of the manner at which we arrived at the approximately ±40% uncertainty in the photolysis rates inside the UNC chamber.

To test the importance of uncertainties in photolysis rates and wall radical fluxes, a sensitivity analysis was performed on the RADM chemical mechanism to arrive at the corresponding uncertainties in the predicted concentrations. These uncertainties represent the "tolerance" of the agreement between model predictions and smog chamber data. The results of this calculation for the conditions given in Table 6.8 are shown in Tables 6.9-6.11. While the uncertainties associated with the UNC data were used, "tolerances" for the SAPRC data are equal for wall effects and somewhat smaller for photolysis rates. For each species listed in the table, we identified the ten reactions most important in determining its concentration. Of the 84 reactions in the

Table 6.8 Conditions for sensitivity analysis of typical smog chamber experiments.

Species	Initial Condition, ppm
NO_2	0.10
NO	0.38
HC	1.50
TOL	0.09
XYL	0.09
OL2	0.90
OL3	0.10
OL4	0.05
H_2O	$2.32 \times 10^{+4}$
J_{NO_2}	0.30 min^{-1}

Table 6.9 Tolerances due to measurement uncertainties in J_{NO_2} measurements*

	Time, Min					
	50		100		300	
Species	Concentration ppm	Tolerance	Concentration ppm	Tolerance	Concentration ppm	Tolerance
NO_2	0.384	± 2.8%	0.285	± 3.2%	0.405×10^{-2}	± 26.0%
O_3	0.164	± 36.0%	0.518	± 12.8%	0.720	± 15.2%
NO	0.236×10^{-1}	± 3.2%	0.494×10^{-2}	± 27.2%	0.315×10^{-4}	± 2.0%
HNO_3	0.405×10^{-1}	± 12.0%	0.898×10^{-1}	± 6.4%	0.177	± 3.2%
HC	$0.145 \times 10^{+1}$	± 0.3%	$0.140 \times 10^{+1}$	± 0.4%	$0.124 \times 10^{+1}$	± 1.5%
OL2	0.810	± 1.6%	0.697	± 2.4%	0.309	± 10.8%
OL3	0.670×10^{-1}	± 4.8%	0.347×10^{-1}	± 10.0%	0.624×10^{-3}	± 54.0%
TOL	0.831×10^{-1}	± 0.8%	0.764×10^{-1}	± 1.0%	0.561×10^{-1}	± 3.6%
XYL	0.667×10^{-1}	± 3.2%	0.488×10^{-1}	± 4.0%	0.153×10^{-1}	± 14.0%

*Tolerance is an estimate of the effect of experimental uncertainties on model concentration predictions. It is the product of the uncertainity in measured J's or wall source rate coefficients, and a model sensitivity coefficient for a given species (McCroskey, 1985).

Table 6.10 Tolerances due to measurement uncertainties in J_{HCHO} measurements[*]

	Time, Min					
	50		100		300	
Species	Concentration ppm	Tolerance	Concentration ppm	Tolerance	Concentration ppm	Tolerance
NO_2	0.384	± 0.0%	0.285	± 4.8%	0.405×10^{-2}	± 38.8%
O_3	0.164	± 16.0%	0.518	± 14.8%	0.720	± 4.0%
NO	0.236×10^{-1}	± 18.8%	0.494×10^{-2}	± 20.8%	0.315×10^{-4}	± 46.0%
H_2O_2	0.126×10^{-4}	± 48.0%	0.572×10^{-3}	± 60.0%	0.809×10^{-1}	± 64.0%
HNO_3	0.405×10^{-1}	± 12.0%	0.898×10^{-1}	± 6.4%	0.177	± 3.2%
HC	$0.145 \times 10^{+1}$	± 0.2%	$0.140 \times 10^{+1}$	± 0.4%	$0.124 \times 10^{+1}$	± 1.3%
OL2	0.810	± 1.2%	0.697	± 2.0%	0.309	± 8.0%
OL3	0.670×10^{-1}	± 2.0%	0.347×10^{-1}	± 8.8%	0.624×10^{-3}	± 40.0%
TOL	0.831×10^{-1}	± 0.5%	0.764×10^{-1}	± 1.0%	0.561×10^{-1}	± 3.2%
XYL	0.667×10^{-1}	± 2.0%	0.488×10^{-1}	± 4.0%	0.153×10^{-1}	± 12.0%

[*] Tolerance is an estimate of the effect of experimental uncertainties on model concentration predictions. It is the product of the uncertainity in measured J's or wall source rate coefficients, and a model sensitivity coefficient for a given species (McCroskey, 1985).

Table 6.11 Tolerances due to measurement uncertainties in wall reactions*

	Time, Min					
	50		100		300	
Species	Concentration ppm	Tolerance	Concentration ppm	Tolerance	Concentration ppm	Tolerance
NO_2	0.384	± 0.6%	0.285	± 7.6%	0.405×10^{-2}	± 28.7%
NO	0.236×10^{-1}	± 22.5%	0.494×10^{-2}	± 17.5%	0.315×10^{-4}	± 18.8%
H_2O_2	0.126×10^{-4}	± 85.1%	0.572×10^{-3}	± 57.2%	0.809×10^{-1}	± 32.0%

---

*Tolerance is an estimate of the effect of experimental uncertainties on model concentration predictions. It is the product of the uncertainity in measured J's or wall source rate coefficients, and a model sensitivity coefficient for a given species (McCroskey, 1985).

RADM model, the NO_2 and HCHO photolysis reactions almost always appeared on this "top ten" list. Radical wall sources are also relatively important for [NO2], [NO], and [H_2O_2]. Large errors in hydrogen peroxide concentrations result from both photolysis and wall source uncertainties. Ozone, NO, and HNO_3 are also affected significantly. Errors in NO_2 and organic species are seen to increase with time, but the absolute value of their concentrations is also lower.

6.5.4 Detailed Analysis of UNC Photolysis Rate Data

Jeffries et al. (1982) have used an actinometer to measure the NO_2 photolysis rate coefficient, J, outside and inside the UNC smog chamber. The objectives were (1) to provide simultaneous J data outside and inside the chamber, in order to "calibrate" the effect of the chamber structure (Teflon film walls, support beams, aluminum foil covered floor) on the actinic flux, and (2) to provide correlations with continuously monitored radiometric data (broadband and UV irradiance measurements), as a substitute for continuous photolysis rate measurements. These measurements are relevant to all photoactive species (not just NO_2), since in practice photolysis rates for the other species are calculated as fractions (zenith angle dependent) of the NO_2 photolysis rate.

The measurements at UNC were made in 1974-1976. Since that time, considerable effort has been expended by several research groups to develop and test different NO_2 actinometers (see Table 6.12), and a large J database is now available. An objective evaluation of the UNC J data is now possible by comparison with this larger J database.

Direct intercomparison of the J data is complicated by the high variability of the natural ambient light, which may mask erroneous measurement resulting from unreliable actinometers. For example, Fig. 6.13 shows representative clear sky J measurements from the seven different measurement programs of Table 6.12. All of the measurements, including the UNC data, seem "reasonable" insofar as they show near-zero values at sunrise or sunset (solar zenith angle $\chi_0 \sim 90°$), and high-sun values not unlike those calculated by, say, Leighton (1961). The variability of the measurements at any fixed zenith angle (e.g., 5 to 9 x 10^{-3} s^{-1} at $\chi_0 = 45°$) can be rationalized by invoking differences in the natural ambient light (e.g., urban, rural, or mountain environments, haze, season, etc.). Yet, at least some of this scatter may be due to experimental problems with the actinometric measurements.

Fortunately, simultaneous measurements of the UV irradiance are available for the studies listed in Table 6.12 (and Fig. 6.13). These measurements allow "normalization" of J measurements to the natural ambient flux, and should therefore give a correlation which emphasizes the actinometer-specific differences. Fig. 6.14 shows typical correlations of the UV irradiance (E) and J measurements for clear sky conditions. On this plot, the UNC data are seen to deviate from the trend of a majority of the studies, but considerable scatter and curvature are still present in all of the measurement. The curvature (and some of the scatter) is now well recognized to result from the cosine response of the standard UV radiometer.

TABLE 6.12. ACTINOMETRIC AND RADIOMETRIC STUDIES OF NO_2 PHOTODISSOCIATION

Reference Year of study	Location Elevation, km(b)	Method, Geometry	Gas Mix	Background(e)
Jeffries et al. (1982) 1974-1976	Pittsboro, NC 0	NO_x . flow(c) sphere	NO_2:1-2 ppm N_2:1 atm	grass
Zafonte et al. (1977) 1975	Los Angeles, CA 0	NO_x, flow cylinder	NO_2:1-2 ppm N_2:1 atm	brown paint
Sickles et al. (1978) 1975	Pittsboro, NC 0	NO_x, flow sphere	NO_2:1-2 ppm N_2:1 atm	black paint
Harvey et al. (1977) 1976	Ann Arbor, MI 0.3	NO_x, flow cylinder	NO_2:25 ppm Air:1 atm	white paint
Dickerson et al. (1982) 1979 (a)	Boulder, CO 1.8 Niwot Ridge, CO 3.0	NO_x, flow cylinder	NO_2:20 ppm O_2:1 atm	black paint
Parrish et al. (1983) 1980	Niwot Ridge, CO 3.0	NO_x, flow cylinder	NO_2: 30 ppm N_2:45.7 Torr	black paint
Madronich et al. (1984) 1980-1981	Toronto, ONT 0.3	ΔP, static(d) double cylinder	NO_2:1-3 Torr	grass, black cloth

---

(a) Radiometer data for 1.8 km taken from Dickerson (1980)

(b) Above sea level, approximate.

(c) Irradiation of flowing gas for various residence times, followed by chemiluminescence detection of NO and/or NO_2.

(d) Pressure change from reaction $2\ NO_2 + h\nu \rightarrow 2\ NO + O_2$.

(e) As reported. True background may differ.

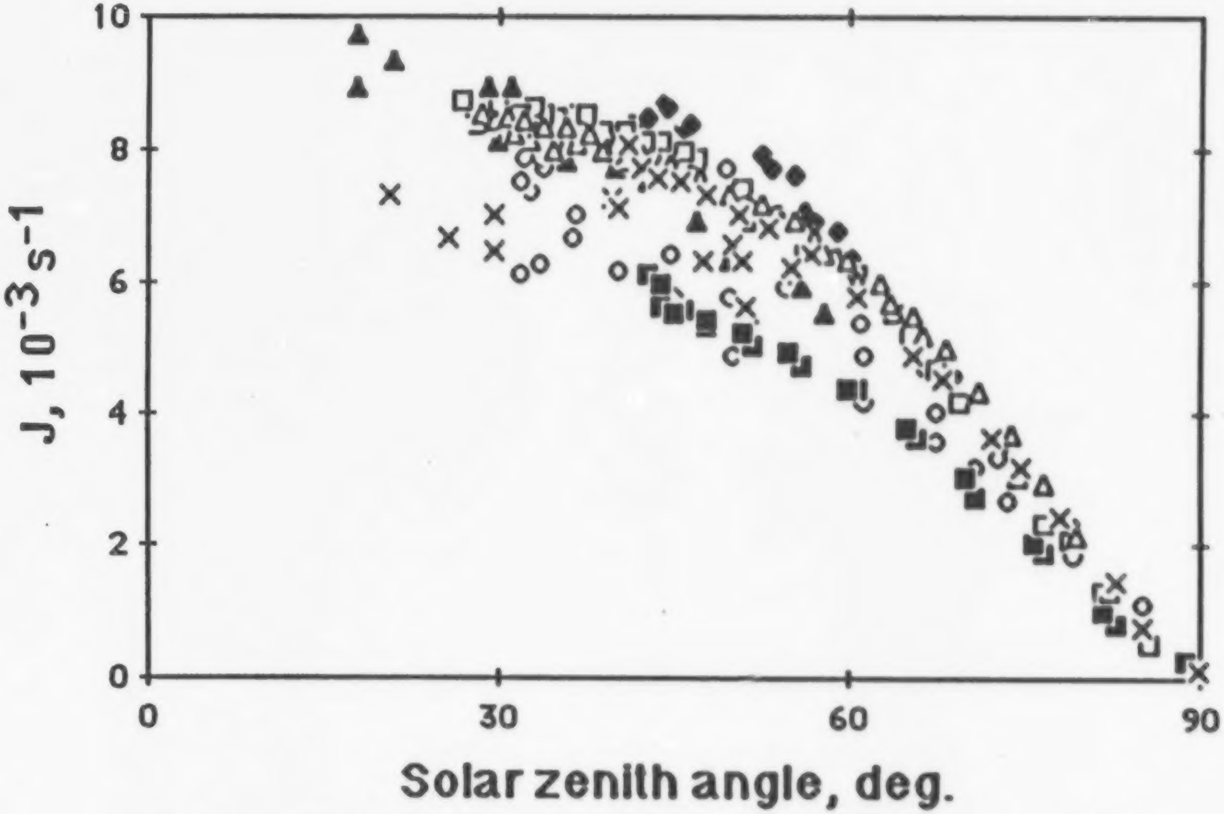

Fig. 6.13 Clear sky J value measurements: ◆ - Jeffries et al., 10/13/76; ○ - Zafonte et al. (9/17/75); ■ - Sickles et al. (10/12/75); □ - Harvey et al. ▲ - Dickerson et al. (3km); △ - Parrish et al. (8/21/80); × - Madronich et al. (see text, pp. 179 and 184, for additional discussion of the Jeffries et al. data).

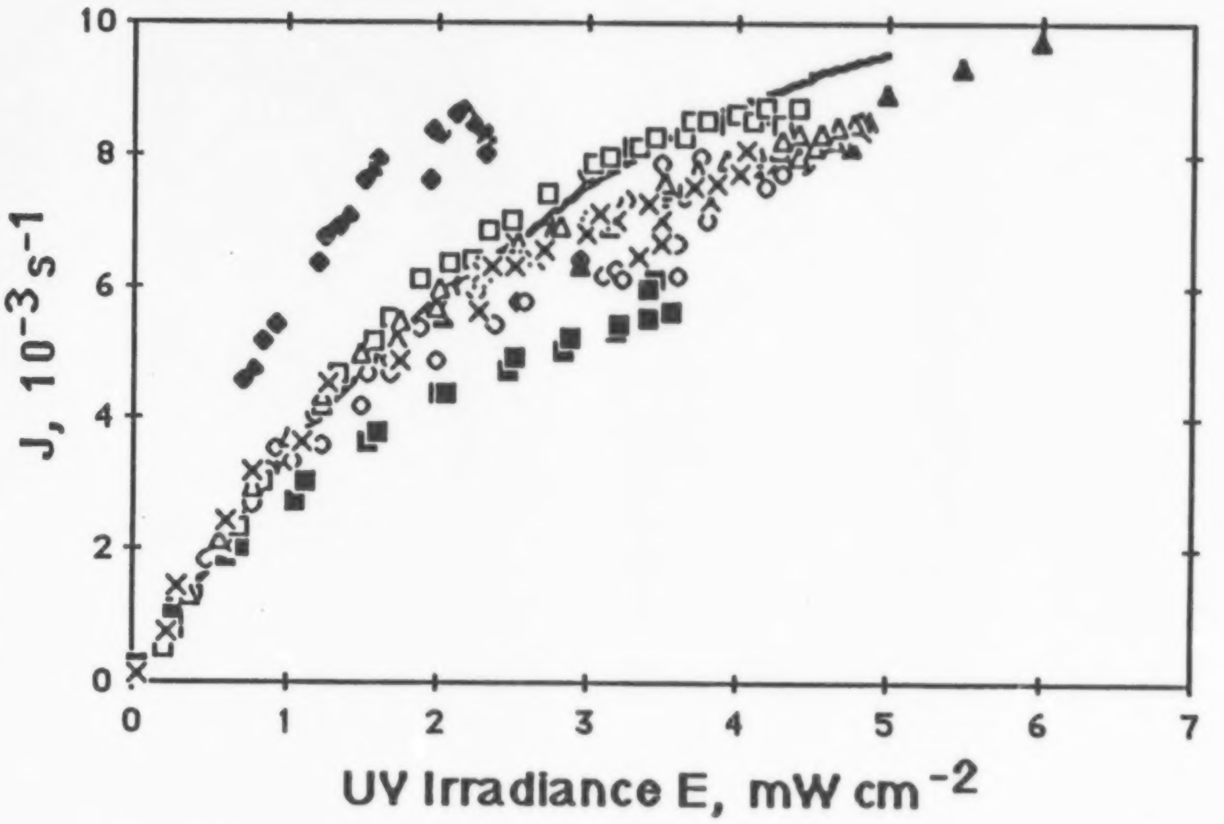

Fig. 6.14 Clear sky correlation between J value measurements and UV irradiance. Symbols as in Fig. 1. Solid line is calculation by Harvey et al. (see text, pp. 179 and 184, for additional discussion of the Jeffries et al. data).

A better correlation between J and E can be obtained by considering in detail the cosine response of the UV radiometer. This is done in Appendix A. Briefly, it is necessary to convert the irradiance (E), measured with a flat plate radiometer, to a quantity proportional to the spherically integrated actinic flux. The resulting expression for clear sky conditions is

$$J/E = C\,[1/f + 2\,A_L]\ , \qquad (6.1)$$

where A_L is the local background albedo, f is a theoretical function given in Appendix A, and C is a constant. Fig. 6.15 shows the J and E measurements plotted according to Eq. (6.1). As predicted, the correlation is much more linear than Fig. 6.14, with a majority of the studies (Zafonte et al., 1977; Harvey et al., 1977; Dickerson et al., 1982; Parrish et al., 1983; and Madronich et al., 1986) lying on a single narrowly defined band. Two sets of measurements (Jeffries et al., 1982; Sickles et al., 1978) both measured at UNC with similar actinometers) are clearly separated from these data, and at opposite extremes.

The constant C of Eq. (6.1) is the ratio of J to the spherically converted irradiance (i.e., the slope of Fig. 6.15), and is predicted to be independent of the solar zenith angle. Values of this ratio are shown in Figs. 6.16 (a-g) for the clear sky data reported by each group (several additional measurements which for clarity were omitted from Figs. 6.13-6.15 are shown here). All but one (panel (a) of Fig. 6.16; Jeffries et al., 1982) of the studies show values of C nearly independent of solar zenith angle, as predicted. For $\chi_0 > 70°$, measured values of both J and the irradiance are smaller and therefore less accurate; the cosine response of the Eppley radiometer is obeyed less accurately; and the calculation of f^{-1} is subject to greater uncertainty from the complexity of modeling multiple scattering in spherical geometry and with greater optical depths. Less accurate values of C are therefore observed.

Table 6.13 gives the average values of the ratio C, measured by each group for $\chi_0 < 70°$. Five of the studies agree within ±2%, and yield an (unweighted) average value,

$$C(\text{clear sky}) \sim 1.35 \pm 0.05\ \text{cm}^2/\text{J}\ . \qquad (6.2)$$

The data of Jeffries et al. (1982) shown in Fig. 6.16a differs from the other studies. The large variations in the value of C observed on any single day cannot be explained by errors in the UV radiometer measurements (calibration drifts of the Eppley radiometer are known to occur, but on a time scale of several years) and must be due to actinometry problems. The deviations in C are therefore direct indicators of errors in the UNC J measurements. The average value of C is $1.73 \pm 0.4\ \text{cm}^2/\text{J}^{-1}$, or about 30% higher than the majority of the studies. Values of C range from 0.8 to 2.8 cm^2/J, i.e., from -41% to +107% of the average value of the majority of studies.

Jeffries (1986) has recently reported a problem with radiometer calibration for the period 1974-1980, and has suggested that all radiometer data be multiplied by a factor of 1.4. If this proposed correction is applied, the difference between the consensus value of C and the UNC value is reduced sig-

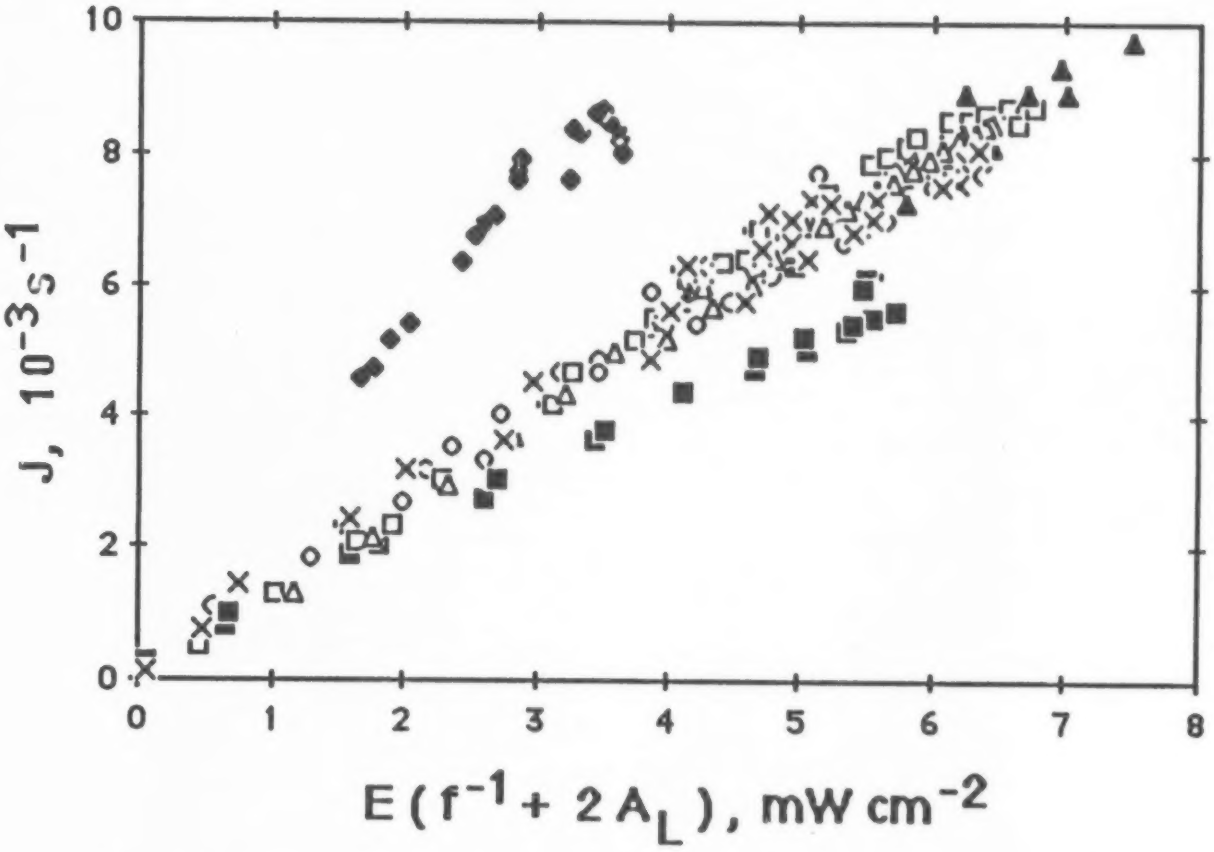

Fig. 6.15 Clear sky correlation of J value measurements with converted irradiance measurements. Symbols as in Fig. 1 (see text, pp. 179 and 184, for additional discussion of the Jeffries et al. data).

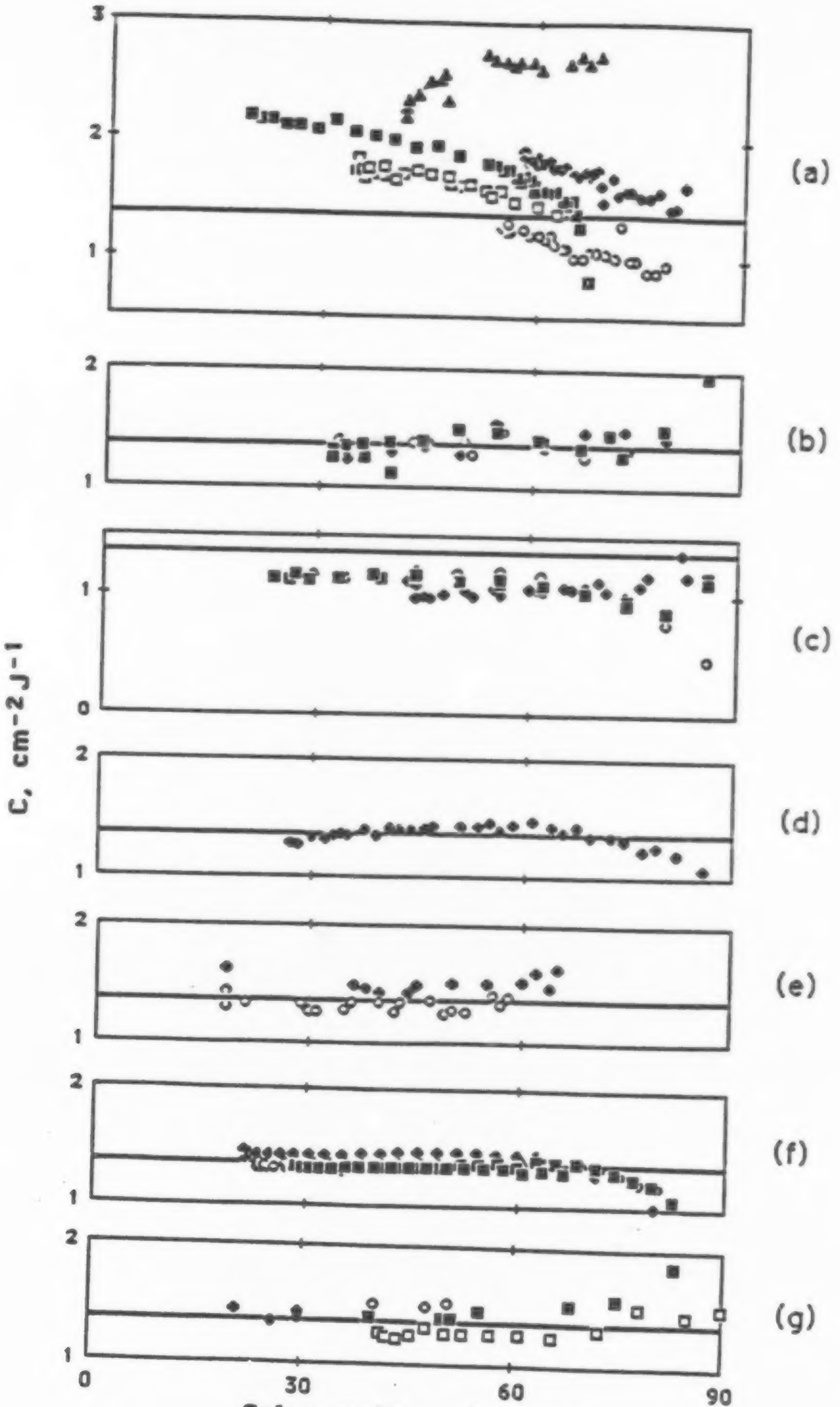
C, cm-2 J-1
3
2
1
(a)
2
1
(b)
1
0
(c)
2
1
(d)
2
1
(e)
2
1
(f)
2
1
(g)
0
30
60
90
Solar zenith angle, deg.

Fig. 6.16

Fig. 6.16 Clear sky ratios of *J* measurements to converted irradiance measurements. Solid line is consensus value, 1.35 cm^2/J.

(a) Jeffries et al., ◆ 12/3/76, ○ 11/19/76, ■ 8/6/76, □ 9/19/74, ▲ 10/13/76;
(b) Zafonte et al., ◆ 9/18/75, ○ 9/19/75, ■ 9/17/75;
(c) Sickles et al., ◆ 10/12/75, ○ 4/21/75, ■ 4/22/75;
(d) Harvey et al;
(e) Dickerson et al., ◆ 1.8 km, ○ 3.0 km;
(f) Parrish et al., ◆ 7/28/80, ○ 8/4/80, ■ 8/21/80;
(g) Madronich et al., ◆ 6/26/80, ○ 8/21/81, □ 8/20/81, ■ 3/27/81.

(see text, pp. 179 and 184, for additional discussion of the Jeffries et al. data).

Table 6.13. Average Value of C over 0-70°

Reference	C (cm^2/J) clear sky	overcast	Deviation$^{(b)}$ (clear sky)
Jeffries et al.	1.73 ± 0.4	1.2 ± 0.1	+ 30 %
Sickles et al.	1.10 ± 0.06	--	- 20 %
Dickerson et al.	1.51 ± 0.07	--	+ 12 % (1.8 km)
*Zafonte et al.	1.35 ± 0.09	--	0 %
*Harvey et al.	1.38 ± 0.05	1.15 ± 0.19	+ 2 %
*Dickerson et al.	1.32 ± 0.06	1.04 ± 0.10	- 2 % (3 km)
*Parrish et al.	1.37 ± 0.06	1.08 ± 0.10	+ 2 %
*Madronich et al.	1.35 ± 0.10	1.30 ± 0.10	0 %
AVERAGE$^{(a)}$	1.35 ± 0.04	1.14 ± 0.08	

(a) average of consensus studies, marked (*).

(b) deviation from consensus average.

nificantly. However, the variations of C observed on any single day in the UNC data (Fig. 6.16a) cannot be explained by this correction factor.

Detailed discussion of the (much smaller) uncertainties involved in the other studies, and of overcast sky data, is given elsewhere (Madronich, 1986).

It should be remembered that, while the UNC measurements shown in Fig. 6.16a were obtained outside the smog chamber, a similar actinometer was used to measure photolysis rates inside the chamber. The ratio of indoor to outdoor measurements was then used to calibrate the effect of the chamber structure on the actinic flux. However, the large scatter in the values of C observed in Fig. 6.16a suggest that even measurements of relative changes in J may be inaccurate. We have analyzed the available simultaneous indoor and outdoor J measurements (three days from Jeffries et al. (1986) and the single day used by Whitten and Gery (1986)). Unfortunately, the measurements are difficult to interpret, since a sizeable fraction of the indoor data may have been obtained with the indoor instrument shadowed from direct sunlight by the support structures of the chamber, and occasionally the outdoor instrument was shadowed by nearby structures, and no record exists which permits the identification of the affected data (Jeffries, 1986). Taking all of the available measurements at face value (i.e., without consideration of shadowing), we find that the ratio of indoor to outdoor J data shows a scatter of ±25% (one standard deviation) about the mean. By comparison, Whitten and Gery (1986) claim ±6% accuracy for the mathematical function which they use to describe the indoor/outdoor ratio. Furthermore, Jeffries (1986) has reported that, although the outdoor measurements were reportedly made over grass (Jeffries et al., 1982), light reflections from nearby buildings may have affected the outdoor measurements significantly and may account for some of the non-horizontal trends seen in Fig. 6.16a. Since these reflections affected only the outdoor J data (and not the indoor J data), a currently unquantified systematic error exists in the indoor/outdoor correction in addition to the ±25% random scatter. Even without considering other uncertainties involved in the determination of JNO_2, the error in the indoor/outdoor ratio alone is much larger than the ±13% total error claimed by Whitten and Gery (1986).

The actinic flux inside the chamber cannot be estimated without reliable measurements. The teflon film walls may attenuate the actinic flux or, by diffusing the solar beam, can increase it; the structures which support the teflon film can cast shadows which, for certain angles of incidence, may obscure large fractions of the chamber volume; the aluminum foil floor may increase the actinic flux by various amounts, depending on its reflectivity and the proportion of specular versus diffuse reflection, which contribute differently to the actinic flux; multiple reflections may also be important. The combined effect of these perturbations can be large, but it is unclear whether the actinic flux is larger or smaller than the outdoor actinic flux.

In summary, we conclude that J values measured with the UNC actinometers are accurate to no better than ±40%. The effect of the chamber structure on the actinic flux inside the chamber was originally estimated using these UNC actinometers and is also estimated to be uncertain by about ±40%. The usefulness of the extensive UNC photochemical smog simulation data for the testing the RADM chemistry could be significantly increased by careful remeasurement of J inside and outside the UNC chamber. Because of the importance of having well-quantified data to assist in the evaluation of chemical mechanisms for acid deposition chemistry, it is esential that this be done in the near future. Of course, as we have stated earlier, this does not necessarily reflect on the use of these data for other purposes such as the ozone control program since the regime of chemical concentrations and the extent of specific nonlinear couplings are different.

SECTION 7

REFERENCES

Alkesweeny, A.J., K.M. Busness, and D.W. Koppenaal, 1984: Contribution of non-precipitating clouds to acid deposition. Preprint, Fourth Joint Conference on Applications of Air Pollution Meteorology, 16-19 October 1984, American Meteorological Society, Boston, Mass., 236-237.

Anthes, R.A., 1983: A review of regional models of the atmosphere in middle latitudes. Mon. Wea. Rev., 111, 1306-1335.

Atkinson, R., A.C. Lloyd, and L. Winges, 1982: An updated chemical mechanism for hydrocarbons/NO_x/SO_2 photo-oxidations suitable for inclusion in atmospheric simulation models. Atmos. Environ., 16, 1341-1355.

Bahe, F.C., U. Schurath, and K.H. Becker, 1980: The frequency of NO_2 photolysis at ground level, as recorded by a continuous actinometer. Atmos. Environ., 14, 711-718.

Brodzinsky, R., B.K. Cantell, R.M. Endlich, and C.M. Bhumralker, 1984: A long-range air pollution transport model for eastern North America. II. Nitrogen oxides. Atmos. Environ., 18, 2361-2366.

Calvert, J.G., and W.R. Stockwell, 1983: Deviations from the O_3-NO-NO_2 photostationary state in tropospheric chemistry. Can. J. Chem., 61, 983-992.

Carter, W., 1985: private communication.

Chandrasekhar, S., 1960: Radiative transfer. Dover Publishers, New York, N.Y., pp. 1-4.

Ching, J.K.S., and A.J. Alkesweeny, 1985: Vertical transport by cumulus clouds. Preprint, Seventh Symposium on Turbulence and Diffusion, 12-15 November 1985, American Meteorological Society, Boston, Mass., 63-66.

Clark, T.L., 1979: Numerical simulation with a three-dimensional cloud model: lateral boundary condition experiments and multi-cellular severe storm simulations. J. Atmos. Sci., 36, 2191-2215.

Clark, T.L., E.C. Voldner, and M.P. Olson, 1985: International sulfur deposition model evaluation program summary. U. S. Environmental Protection Agency, Research Triangle Park, N.C.

Dana, M.T., R.C. Easter, and J.M. Thorp, 1984: OSCAR experiment high density network data report, event 4. PNL report 5152-Pt4, Pacific Northwest Laboratories, Richland, Wash.

Demerjian, K.L., K.L. Schere, and J.T. Peterson, 1980: Theoretical estimates of actinic (spherically integrated) flux and photolytic rate constants of atmpospheric species in the lower troposphere. Adv. Envir. Sci. Technol., 10, 396-459.

Dickerson, R.R., 1980: Direct measurement of ozone and nitrogen dioxide photolysis rates in atmosphere. Ph.D. thesis, University of Michigan, Ann Arbor, Mich.

Dickerson, R.R., and D.H. Stedman, 1980: Precision of NO_2 photolysis rate measurements. Envir. Sci. Technol., 14, 1261-1262.

Dickerson, R.R., D.H. Stedman, and A.C. Delany, 1982: Direct measurement of ozone and nitrogen dioxide photolysis rates in the troposphere. J. Geophys. Res., 87, 4933-4946.

Dunker, A.M., 1984: The decoupled direct method for calculating sensitivity coefficients in chemical kinetics, J. Chem. Phys., 81, 2385-2393.

Easter, R.C., and J.M. Hales, 1984: PLUVIUS: A generalized one-dimensional model of reactive pollutant behavior, including dry deposition, precipitation formation, and wet removal. Pacific Northwest Laboratories Report PNL 4046-ED2.

Easter, R.C., and J.M. Hales, 1983: Interpretations of the OSCAR data for reactive scavenging. In Precipitation Scavenging, Dry Deposition and Resuspension. Coordinated by H.R. Pruppacher, R.G. Semonin, and W.G.N. Slinn, Elsevier, N.Y., 649-662.

Easter, R.C., and J.M. Hales, 1982: Mechanistic evaluation of precipitation scavenging data using a one-dimensional reactive storm model. Pacific Northwest Laboratories Report RP 2022-1 to Electric Power Research Institute, Palo Alto, Calf.

Endlich, R.M., K.C. Nitz, R. Brodzinsky, and C. M. Bhumralker, 1984: A long-range air pollution transport model for eastern North America: sulfur oxides. Atmos. Environ., 18. 2345-2360.

EPRI, 1985: Research project 1630-1623, principal investigator, S.L. Heisler.

Errico, R.M., 1985: Spectra computed for a limited-area grid. Mon. Wea. Rev., 113, 1554-1562.

Fox, D.G., 1981: Judging air quality model performance. Bull. Amer. Meteor. Soc., 62, 599-609.

Gardner, E.P., R.D. Wijayaratne, and J.G. Calvert, 1984: The primary quantum yields of photodecomposition of acetone in air under tropospheric conditions. J. Phys. Chem., 88, 5069-5076.

Harker, A.B., W. Ho, and J.J. Ratto, 1977: Photodissociation quantum yield of NO_2 in the region 375 to 420 nm. Chem. Phys. Lett., 50, 394-397.

Harvey, R.B., D.H. Stedman, and W. Chameides, 1977: Determination of the absolute rate of solar photolysis of NO_2. J. Air Pollu. Contol Assoc., 27, 663-666.

Hegg, D.A., and P.V. Hobbs, 1981: Cloudwater and the production of sulfate in clouds. Atmos. Environ., 15, 1597-1604.

Heikes, B., G. Kok, and A. L. Lazrus, 1986: private communication.

Isaksen, I.S.A., K.H. Midtbo, J. Sunde, and P.J. Crutzen, 1977: A simplified method to include molecular scattering and reflection in calculations of photon fluxes and photodissociation rates. Geophysica Norvegica, 31, 11-26.

Jackson, J.O., D.H. Stedman, R.G. Smith, L.H. Hecker, and P.O. Warner, 1975: Direct NO_2 photolysis rate monitor. Rev. Sci. Instrum., 46, 376-378.

Jacob, D.J., and M.R. Hoffmann, 1983: A dynamic model for the production of H^+, NO_3^-, and $SO_4^=$ in urban fog. J. Geophys. Res., 88, 6611-6621.

Jeffries, H.E., 1986: private communication.

Jeffries, H.E., R.M. Kamens, K.G. Sexton, and A.A. Gerhardt, 1982: Outdoor smog chamber experiments to test photochemical models. EPA-600/3-82-016a, U.S. Environmental Protection Agency, Washington, D.C.

Keeler, G.J., P.J. Samson, and J.J. Small, 1984: Representativeness of precipitation data in regional-scale acid deposition modeling. In The Meteorology of Acid Deposition, P.J. Samson, ed., Air Pollu. Control Assoc., Pittsburgh, Penn., 225-240.

Kerr, J.A., and J.G. Calvert, 1984: Chemical transformations modules for Eulerian acid deposition mdels. I: The gas-phase chemistry. U.S Environmental Protection Agency Report, Interagency Agreement No. DW930237-01-0 to the National Center for Atmospheric Research, Boulder, Colo.

Leighton, P.A., 1961: In Photochemistry of Air Pollution. Academic Press, New York, N.Y., p. 15.

Leone, J.A., and J.H. Seinfeld, 1985: Comparative analysis of chemical reaction mechanisms for photochemical smog. Atmos. Environ., 19, 437-464.

Luther, F.M., and R.J. Gelinas, 1976: Effect of molecular multiple scattering and surface albedo on atmospheric photodissociation rates. J. Geophys. Res., 81, 1125-1132.

Madronich, S., 1986: Intercomparisons of NO_2 photodissociations and UV radiometer measurements (submitted to Atmos. Environ.).

Madronich, S., D.R. Hastie, B.A. Ridley, and H.I. Schiff, 1984: Measurement of the photodissociation coefficient of NO_2 in the atmosphere. I: Method and surface measurements. J. Atmos. Chem. 1, 3-25.

McElroy, M.B., and D.M. Hunten, 1966: A method of estimating the earth albedo for dayglow measurements. J. Geophys. Res., 71, 3635-3638.

McMahon, T.A., and P.J. Denison, 1979: Empirical atmospheric deposition parameters: a survey. Atmos. Environ., 15, 571-585.

McCroskey, P.S., 1985: Direct differential methods for kinetic parameter estimation. Master's thesis, Carnegie-Mellon University, Pittsburgh, Pa.

Middleton, P., 1985a: Chemical data requirements for the NCAR regional acid deposition model. In Proc., Air Pollu. Control Assoc. annual meeting, June 1985, Detroit, Mich.

Middleton, P., 1985b: Chemical characteristics of OSCAR regional precipitation episodes (submitted to Atmos. Environ.).

Middleton, P., 1986: Development of emissions databases for RADM (in preparation).

NAPAP, 1985: Status report on the development of the NAPAP emission inventory for the 1980 base year and summary of preliminary data. EPA-600/7-84-091.

NASA, 1985: Chemical kinetics and photochemical data for use in stratospheric models. Evaluation No. 7, JPL Publ. No. 85-62, National Aeronautics and Space Administration, Jet Propulsion Laboratory, Pasadena, Calif.

NCAR, 1983a: Regional acid deposition: models and physical processes. NCAR/TN-214+STR, National Center for Atmospheric Research, Boulder, Colo.

NCAR, 1983b: Regional acid deposition: design and management plan for a comprehensive modeling system. NCAR/TN-215+PPR, National Center for Atmospheric Research, Boulder, Colo.

NCAR, 1985: The NCAR Eulerian regional acid deposition model. NCAR/TN-256+STR, National Center for Atmospheric Research, Boulder, Colo.

Nader, J.S., and N. White, 1969: Volumetric measurement of ultraviolet energy in an urban atmosphere. Envir. Sci. Technol., 3, 848-854.

Neiwiadomski, M., 1986: A passive pollutant in a three dimensional field of convective clouds: numerical simulations. Atmos. Environ., 20, 139-145.

Niemann, B.L., 1983: Scavenging ratios for exceptional wet SO_4^+ episodes in eastern North America from three network events. In Precipitation Scavenging, Dry Deposition, and Resuspension. Coordinated by H.R. Pruppacher, R.G. Semonin, and W.G.N. Slinn, Elsevier Science Publishing Co., New York, N.Y., 217-227.

Novak, J.H., and P. Middleton, 1985: Application of the NAPAP emissions inventories to Eulerian modeling. In Proc., Second Annual Acid Deposition Emission Inventory Symposium, 12-13 Nobember 1985, Charleston, S.C.

OSCAR, 1983: Overview of the OSCAR experiment. Prepared by R.C. Easter, M.T. Dana, J.M. Thorp, K.M. Busness, J.M. Hales, G.S. Raynor, C.M. Benkovitz, R.L. Tanner and J.D. Shannon.

OTA, 1984: Acid rain and transported air pollutants: implications for public policy. Report No. OTA-O-204, Office of Technology Assessment, U.S. Congress, Washington, D.C.

Parrish, D.D., P.C. Murphy, D.L. Albritton, and F.C. Fehsenfeld, 1983: The measurement of the photodissociation rate of NO_2 in the atmosphere. Atmos. Environ., 17, 1365-1379.

Penkett, S.A., B.M.R. Jones, K.A. Brice, and A.E.J. Eggleton, 1979: The importance of atmospheric ozone and hydrogen peroxide in oxidizing sulfur dioxide in cloud and rainwater. Atmos. Environ., 13, 123-137.

Pitts, J.N., K.R. Darnall, A.M. Winer, and J.M. McAfee, 1977: Mechanisms of photochemical reactions in urban air. II: Smog chamber studies. EPA-600/3-77-0146b, U.S. Environmental Protection Agency, Washington, D.C.

Raynor, G.S., and J.V. Hayes, 1982: Effect of varying air trajectories on spatial and temporal precipitation chemistry patterns. Water Air Soil Poll., 18, 173-189.

Ruff, R.E., K.C. Nitz, F.L. Ludwig, C.M. Bhumralkar, J.D. Shannon, C.M. Sheih, I.Y. Lee, R.Kumar, and D.J. McNaughton, 1985: Evaluation of three regional air quality models, Atmos. Environ., 19, 1103-1115.

Scott, B.C., 1985: Users manual for the cloud scavenging module. Draft manual, Pacific Northwest Laboratories, Richland, Wash.

Sheih, C.M., M.L. Wesely, and B.B. Hicks, 1979: Estimated dry deposition velocities of sulfur over the eastern United States and surrounding regions. Atmos. Environ., 13, 123-137.

Sickles, J.E., III, L.A. Ripperton, W.C. Eaton, and R.S. Wright, 1978: Nitrogen dioxide photolytic, radiometric and meteorological field data. EPA-600/7-78-053, U.S. Environmental Protection Agency, Washington, D.C.

Small, M.J., 1982: Mathematical simulations of Lagrangian precipitation and associated sulfur wet deposition. In Proc., APCA Specfialty Conference on Atmospheric Deposition, E.R. Fredrick, ed., Air Pollu. Control Assoc., Pitssburgh, Pa.

Stockwell, W.R., 1986: A homogeneous gas phase mechanism for use in a regional acid deposition model. Atmos. Environ. (in press).

Stockwell, W.R., and J.G. Calvert, 1983: The mechanism of the $HO\text{-}HSO_2$ reaction. Atmos. Environ., 17, 2231-2235.

Vukovich, F.M., J. Fishman, and E.V. Browell, 1985: The reservoir of ozone in the boundary layer of the eastern United States and its potential impact on the global tropospheric ozone budget (preprint).

Walcek, C.J., R.A. Brost, and J.S. Chang, 1986: So_2 sulfate and HNO_3 deposiition velocities computed using regional land use and meteorological data. Atmos. Environ., 21 (in press).

Walcek, C.J., and G.R. Taylor, 1986: A theoretical method for computing vertical distributions of acidity and sulfate production within cumulus clouds. J. Atmos. Sci., 41, (in press).

Walega, J.G., D.H. Stedman, R.E. Shetter, R.S. Fukuda, and T.A. Bahls, 1980: Final report: Chemiluminescent/laser diode measurement technique intercomparison and captive air measurement program. Coordinating Council Report No. CAPA-17-80.

Weseley, M.L., D.R. Cook, R.L. Hart, and R.E. Speer, 1985: Measurements and parameterization of particulate sulfur dry deposition over grass. J. Geophys. Res., 90, 2131-2143.

Whitten, G.Z., 1985: Private communication.

Whitten, G.Z., and M.W. Gery, 1986: Further development and evaluation of the carbon bond mechanism. Monthly technical narrative No. 1 to EPA for the period 1 October 1985 to 31 December 1985, EPA Contract No. 68-02-4136, U.S. Environmental Protection Agency, Washington, D.C.

Whitten, G.Z., J.P. Killus, and R.G. Johnson:, 1985: Modeling of auto exhaust for smog chamber data for EKMA development. U.S. Environmental Protection Agency Contract No. 68-02-3735, Systems Applications, Inc., San Rafael, Calif.

Zafonte, L., P.L. Rieger, and J.R. Holmes, 1977: Nitrogen dioxide photolysis in the Los Angeles atmosphere. Envir. Sci. Technol., 11, 483-487.

APPENDIX A

RELATIONSHIP BETWEEN UV IRRADIANCE AND NO_2 PHOTOLYSIS MEASUREMENTS

Simultaneous measurements of the NO_2 photolysis rate coefficient J and of the UV irradiance E show that, for clear sky conditions, a strongly non-linear correlation exists between J and E (see Fig. 6.14 of main text). Overcast sky data, on the other hand, result in generally linear correlations.

It is now well recognized that the curved clear sky correlations result from the cosine response of the standard UV radiometers used for the UV irradiance measurements. The radiometers are manufactured by Eppley Laboratory, Inc. of Newport, R.I. and consist of a UV filter and photocell placed behind a flat, opaque quartz diffuser plate. The diffuser plate produces a cosine (Lambertian) response to the directions of the incoming light due to the reduced projected area of the plate for angles of incidence other than 0°. The manufacturer specifies sensitivity over the 295-385 nm wavelength region, with peak response at ~ 340 nm and fwhm of ~ 60 nm, and adherence to the cosine law to within ±2.5% for light incoming at angles less than 70° from the plate normal. During measurements, the radiometer is usually pointed directly upwards.

The parametrization of J versus E correlations has been elusive. Expressing J as a polynomial function of the irradiance (e.g., Walega et al., 1980; Whitten and Gery, 1986) may work on any single day, but different values of the fitting coefficients will be observed on different days. Even for perfectly clear sky conditions, the seasonal variation of the Sun-Earth distance may produce equal J values at quite different values of the solar zenith angle, χ_0 (e.g., 40° on Jan. 1, 30° on July 1, Demerjian et al., 1980); the cosine factor of the radiometer will then be significantly different (e.g., 13% for the above zenith angles), so that two different values of the irradiance are measured for a single value of J. Clouds, variable local background, and station elevation above sea level will have even larger effects on the fitting coefficients. This results in apparent scatter in otherwise accurate correlations of J and E. Zafonte et al. (1977) have attempted to include the effect of the cosine response by correlating J/E ratios with $1/\cos\chi_0$ or with $1-\cos\chi_0$, but the quality of the fit is relatively poor, and there is no theoretical basis for using these zenith angle functions. Harvey et al. (1977) gave a theoretical prediction of the dependence of J on the irradiance (see solid curve of Fig. 6.14). The origin of this calculation is not entirely clear, since, as discussed above, the irradiance alone cannot be used uniquely to determine J. The good agreement between this calculation and their measurements suggests that the calculation was tuned to the conditions of those experiments. Therefore, any discrepancies between this calculation and the other measurements in Fig. 6.14 are difficult to interpret. In addition, since they compute absolute values of J, sizeable errors may be introduced from, e.g., the rather uncertain NO_2 spectral data (estimated as ±30% by the NASA 1985 evaluation).

More recently, a method to convert UV irradiance measurements to spherically (actually, hemispherically) and spectrally integrated actinic flux has been proposed (Madronich et al., 1984). By computing only ratios of the direct and diffuse sunlight contributions to J, this method depends minimally on the NO_2 spectral data and yields a simple and theoretically justifiable correlation. This method will be expanded and presented in detail below.

The spectral radiance, $L(\lambda,\theta,\phi)$, units = mW cm^2 nm^{-1} st^{-1}, is defined (see "specific intensity," Chandrasekhar, 1960) by the expression

$$L(\lambda,\theta,\phi) = dE_\lambda/(\cos\theta\ d\omega\ dt\ d\lambda\ ds), \tag{A1}$$

where dE_λ is the radiant energy in the wavelength interval $\lambda \rightarrow \lambda + d\lambda$ which is transported across a surface element of area ds, in time dt, from a solid angle element $d\omega$ which is at an angle θ to the surface normal.

The UV irradiance, E, measured with the standard Eppley radiometer, can be expressed in terms of the spectral radiance as

$$E = \int A(\lambda) \int L(\lambda,\theta,\phi) \cos\theta\ d\omega\ d\lambda, \tag{A2}$$

where $A(\lambda)$ is the spectral response function of the radiometer, and the angular integration is performed over 2π steradians (overhead hemisphere). The cosine response of the radiometer is shown explicitly in this expression.

The NO_2 photolysis coefficient, J, is related to the spectral radiance by

$$J = \int \sigma(\lambda)\ \phi(\lambda)\ (\lambda/hc) \int L(\lambda,\theta,\phi)\ d\omega\ d\lambda, \tag{A3}$$

where $\sigma(\lambda)$ and $\phi(\lambda)$ are the NO_2 absorption cross section and quantum yield, respectively, and hc/λ is the energy of a single photon. Here, the angular integration is performed over 4π steradians. The cosine factor does not appear in the expression for J, since NO_2 molecules in the atmosphere (and in actinometers) have random spatial orientation.

Because of the factor $\cos\theta$, the expressions for J and for E cannot be related unless the angular dependence of the radiance L is known. It is therefore convenient to separate the radiance into the three components

$$L = L_o + L_u + L_d, \tag{A4}$$

associated with direct sunlight (L_o), and with the diffuse contributions of the upward and downward propagating light (L_u and L_d, respectively). A similar separation can be made for J,

$$J = J_o + J_u + J_d, \tag{A5}$$

where the meaning of the subscripts is as in Eq. (A2.4). If a reflecting background surface of Lambertian albedo A_L is present, an additional relationship exists between the components of J:

$$J_u = A_L \, (J_d + 2 \, J_o \cos\chi_o). \tag{A6}$$

The 2 $\cos\chi_o$ factor ensures conservation of energy, and shows that the photolysis rate can be strongly affected by the local background albedo, e.g., for overhead sun and zero atmospheric optical thickness, changing A_L from zero to unity can increase J by a factor of *three* (McElroy and Hunten, 1966).

To evaluate the angular and spectral integrals which appear in the above equations, two approximations are required. First, by assuming that the diffuse light is isotropic, the angular integrations can be performed, and it is readily shown by combining Eqs. (A2)-(A5) that

$$E = \frac{J_o \cos\chi_o \int A(\lambda) \, L_o(\lambda) \, d\lambda}{\int \sigma(\lambda) \, \phi(\lambda) \, (\lambda/hc) \, L_o(\lambda) \, d\lambda} + \frac{(J_d/2) \int A(\lambda) \, L_d(\lambda) \, d\lambda}{\int \sigma(\lambda) \, \phi(\lambda) \, (\lambda/hc) \, L_d(\lambda) \, d\lambda} \, . \tag{A7}$$

While this assumption is not strictly correct, it has been shown by Luther (1980) that multiple scattering calculations in which the diffuse light is treated as isotropic agree with more detailed calculations (e.g., Luther and Gelinas, 1976) to better than 10% for most altitudes and zenith angles. Second, Eq. (A7) can be further simplified to

$$E \sim C \, [\, J_o \cos\chi_o + J_d/2 \,], \tag{A8}$$

where C is a constant, if the two ratios of wavelength integrals in Eq. (A7) are sufficiently similar. This will certainly be the case (a) if the spectral response of the radiometer, $A(\lambda)$, is similar to the NO_2 photoaction spectrum, $\sigma(\lambda)\phi(\lambda)(\lambda/hc)$, or (b) if the spectral distribution of the diffuse light, L_d, is similar to that of direct sunlight, L_o. To first approximation, both of these conditions (only one is necessary) are satisfied.

Eq. (A8) can be rewritten in terms of the *total* photolysis rate J by using Eqs. (A5) and (A6):

$$J/E = C \, [\, f^{-1} + 2 \, A_L \,], \tag{A9}$$

where

$$f \equiv [\, J_o/(J_o+J_d)] \cos\chi_o + [\, 1 - J_o(J_o+J_d) \,]/2.$$

With experimental values of J and E on the left-hand side, Eq. (A9) provides the desired correlation of J and E measurements, as long as the contribution to J from direct sunlight, $J_o/(J_o+J_d)$ is known. Since only the *fractional* contribution to J is required, errors due to uncertianties in the NO_2 spectral data are largely eliminated.

For clear sky conditions, the ratio $J_o/(J_o + J_d)$ was evaluated using a simplified multiple scattering program (Madronich et al., 1984) based on a two stream successive orders method (Isaksen et al., 1977) but adapted to isotropic scattering and Lambertian ground reflections (Luther, 1980). Values of the direct sun fractional contribution are shown in Figs. A1 and A2 for several values of the regional surface albedo and elevation above sea level. This surface albedo should not be confused with the local background albedo A_L which reflects the immediate surroundings of the experiment and is negligible (dark paint, black cloth) in most experiments considered here. Direct sun contributions are seen to be nearly constant for $\chi_0 < 70°$ and, for moderate regional albedo and surface elevation, vary by only a few percent from an average value of ca. 0.6. The variation of the function f^{-1} with surface elevation and albedo is shown in Fig. A3. The zenith angle dependence of f^{-1} is in qualitative agreement with the data of Nader and White (1969) for the ratio of the total signal from six orthogonal radiometers to that of a single upward looking radiometer obtained in an urban atmosphere. Fig. A3 shows that the function f^{-1} is not very sensitive to albedo or station elevation. For example, at $\chi_0 = 70°$, changing the surface elevation from 0 to 3.0 km increases $J_0/(J_0+J_d)$ by 26%, while f^{-1} increases only by 5%. For each study in the present evaluations of J measurements, values of f^{-1} were calculated at the nearest km surface elevation and a regional surface albedo of 0.15.

For an overcast sky, the direct sun contribution vanishes and Eq. (A9) reduces to

$$J/E = 2\ C\ (1 + A_L), \tag{A10}$$

where C should, at least in principle, have the same numerical value as for the clear sky data. This correlation is linear, in agreement with the observations by Parrish et al. (1983), Dickerson et al. (1982), Harvey et al. (1977), and Sickles et al. (1978).

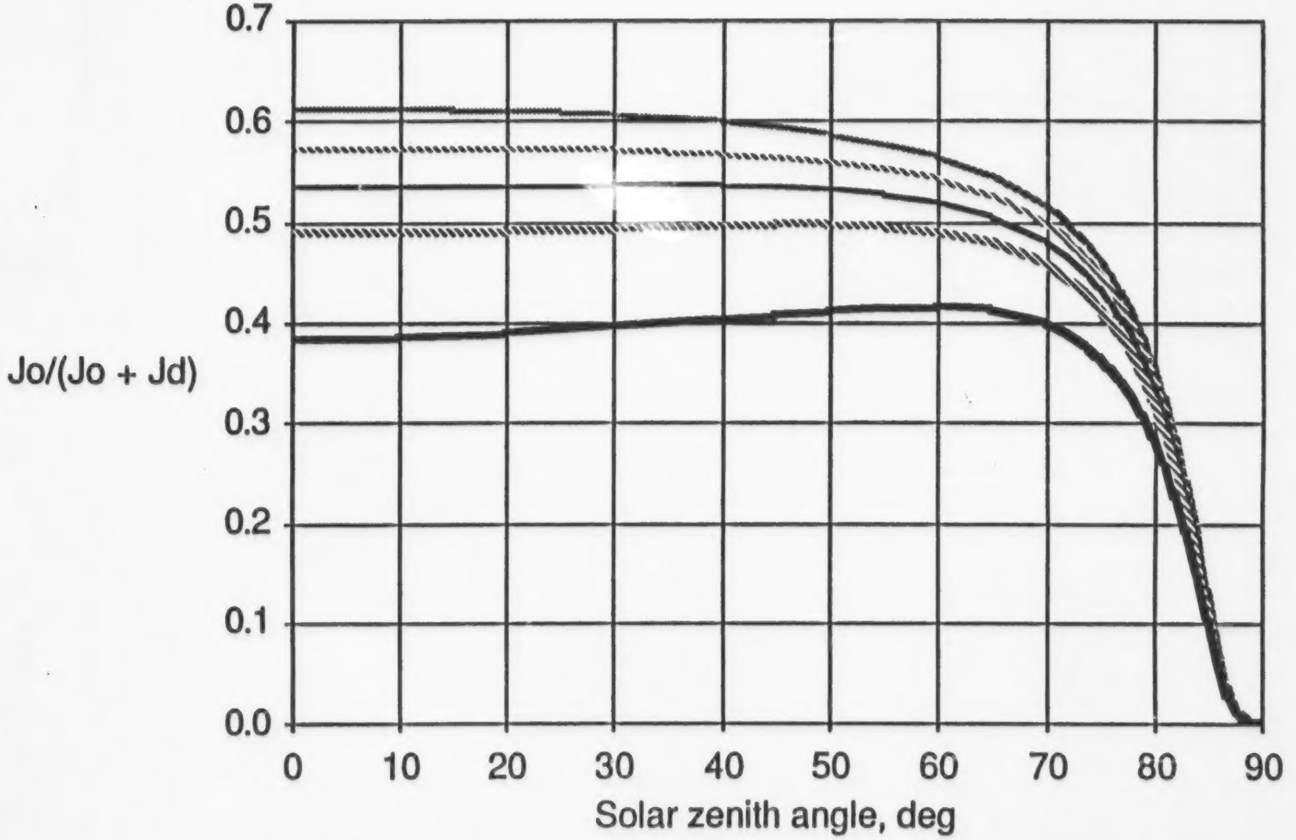

Fig. A1 Clear sky fractional contributions to J from direct sunlight (zero local albedo), for different values of the regional albedo:

— 0.0; ⁓ 0.15; — 0.3; ⁓ 0.5; ▬ 1.0.

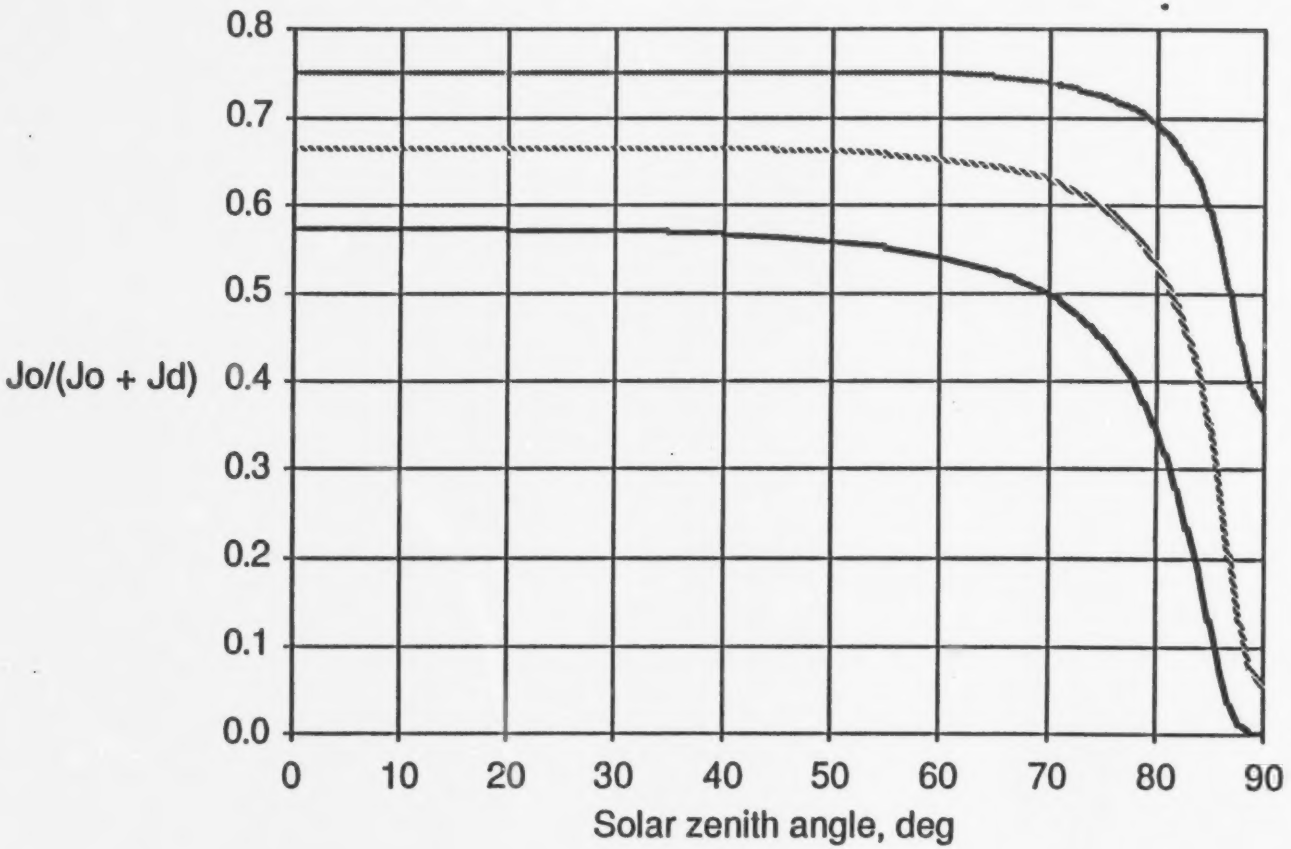

Fig. A2 Clear sky fractional contributions to J from direct sunlight (zero local albedo, 0.15 regional albedo), for different surface elevation above sea level: —— 0 km; ⋯⋯ 3 km; —— 6 km.

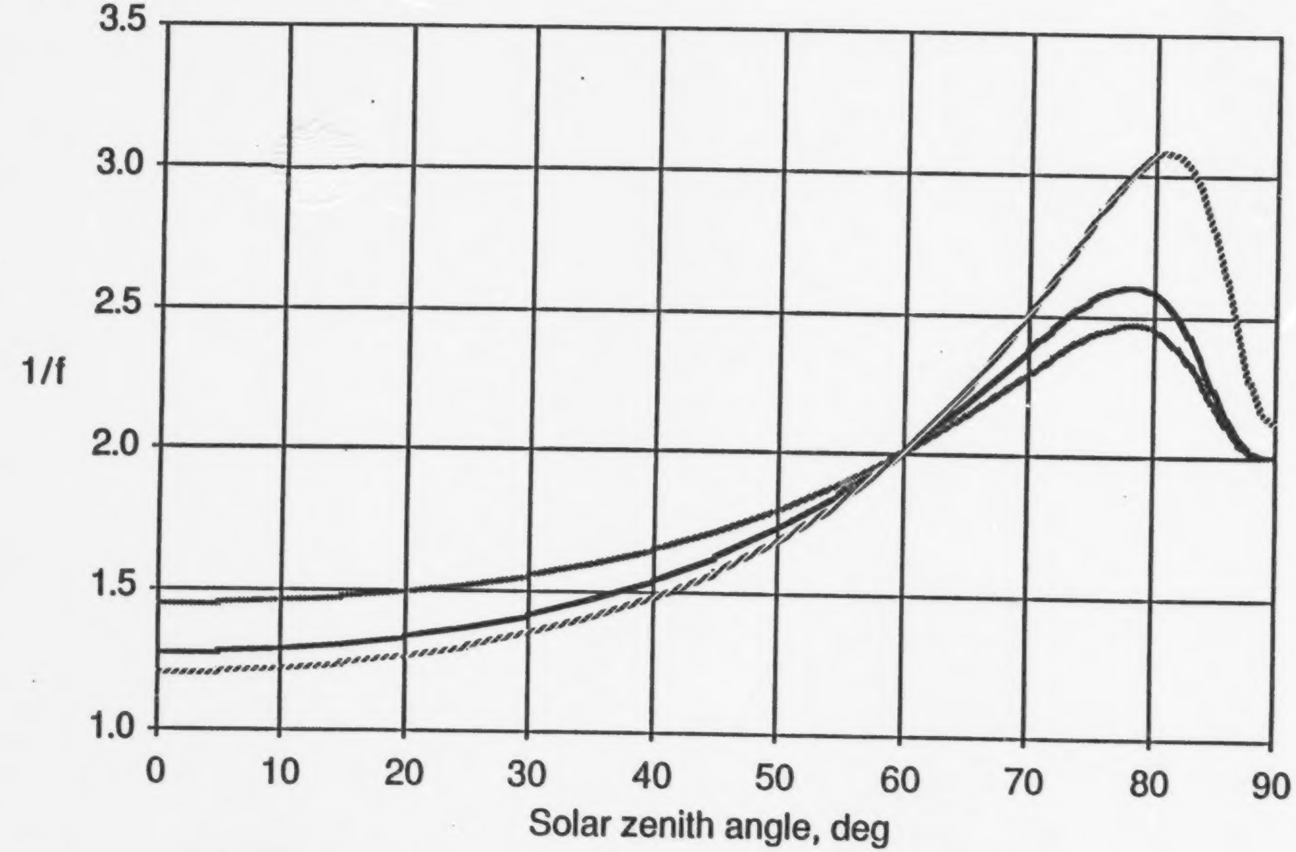

Fig. A3 Clear sky conversion factor for J/irradiance correlations (see text), for different values of surface elevation and regional albedo: — 0 km, 0.15 alb; — 0 km, 1.0 alb; ⋯⋯ 3km, 0.15 alb.